SAPIENZA
UNIVERSITÀ DI ROMA

EXPLOITING THE POTENTIAL OF CHEMICAL LOOPING PROCESSES FOR INDUSTRIAL DECARBONIZATION AND WASTE TO ENERGY CONVERSION

PROCESS DESIGN AND EXPERIMENTAL EVALUATIONS

XXXVI Cycle of the Doctoral School in Energy and Environment

Department of Astronautical, Electrical and Energy Engineering

PhD Candidate: **Orlando Palone**

Tutor: Chiar.mo Prof. **Domenico Borello**

Summary

The impact of anthropogenic activities on the environment is leading to climate changes and exceptional meteorological phenomena all over the world. To address this negative trend, the scientific community agrees that the environmental impact from fossil fuels-based power production must be mitigated by the integration with alternative and sustainable technologies, such as renewable energy. However, the time required for the complete development and diffusion of such technology poses the urgency of finding a midterm solution to significantly reduce CO_2 emissions. Carbon capture, utilization, and storage (CCUS) technologies represent an interesting option to mitigate CO_2 emissions. CCUS involves (among other possible applications) the separation of the CO_2 content from industrial off-gases, its transport and storage or its reconversion to a chemical/fuel. Chemical looping can be considered as an oxyfuel combustion where the oxygen supply comes from the lattice oxygen atoms of a solid. It is based on gas-solid reactions where a solid also known as oxygen carrier, generally a metal oxide, undergoes successive reduction and oxidation steps. In the reduction step, normally occurring at high temperatures (700-1000 °C), the oxygen carrier interacts with a reducing agent, such as coal, natural gas, syngas etc. and loses part of its oxygen atoms. By controlling the degree of reduction of the oxygen carrier is thus possible to achieve a complete oxidation of the reducing agent (the fuel) to CO_2 and H_2O (chemical looping combustion) or a partial oxidation to a syngas (chemical looping reforming and gasification). In these latter case, the introduction of external CO_2 and H_2O can be of help to support the reforming or gasification processes. The oxygen carrier in the reduced phase is then sent to an air reactor, where it reacquires the oxygen atoms by an exothermic reaction with air. This process presents several advantages according to the specific application. In chemical looping combustion, intrinsic separation of N_2 and CO_2 is achieved, because the two streams are involved in two different reaction steps. This largely simplifies the CO_2 separation effort for storage or utilization purposes. On the other hand, in chemical looping reforming it is possible to achieve autothermal operation thanks to the exothermicity of the oxidation step in the air reactor, as well as high reforming efficiencies. Similarly, in chemical looping gasification the resulting syngas is characterized by no N_2 dilution, lower tar release and possibility of autothermal operation. These benefits enhance the energy efficiency of the process, leading to a better energy utilisation.

In this work, strategies for the decarbonisation and circularity of the industrial and power sector are proposed based on the synthesis of hydrogen and hydrogen-derived fuels. In particular, the potential of chemical looping technology is deeply studied aiming at exploiting its ability to reconvert or valorise CO_2 or waste streams to a syngas and then to a liquid fuel/chemical, such as methanol or ammonia. This task is carried out through modelling and experimental evaluations. The modelling activities mainly concern design of

process schemes involving the chemical looping section for waste or CO_2 reconversion and the liquid fuel synthesis section. The experimental evaluations are focused on two crucial that have been limitedly discussed in the literature: the thermochemical syngas production step by oxidation with CO_2 and H_2O streams, the effect of high-pressure operation on the redox abilities of a typical iron and nickel-based oxygen carrier.

In Chapter 1, a general overview on the main research developments on chemical looping technology is provided. A section is reserved for each chemical looping variant, i.e. combustion, reforming and gasification, and a general description of each process is provided along with the summary of the main research achievements. Subsequently, the technology is divided by application in power production and chemicals production. Main findings from techno-economic assessment and process designs are discussed in comparison with benchmark technologies and other clean pathways.

In Chapter 2 steel mills are taken as an example of the hard-to-abate industry. A H_2-based decarbonization strategy is proposed and assessed by Aspen Plus simulation. The strategy starts from an initial configuration that is characterized by a typical blast furnace-basic oxygen furnace steel mill and consider the introduction of direct reduction – electric arc furnace lines, that are more efficient and involve natural gas as reducing agent rather than coke. Sensitivity analyses are carried out to assess the effect of the introduction of H_2/CH_4 blendings in the direct reduction plant and of the utilization of scrap material in the electric arc furnace. The impact of each configuration on the CO_2 emissions and the energy flows of the plant is assessed by mass and energy balances. The results indicate a promising decarbonization potential of the introduced technologies but require large investments to increase the renewable sources penetration in the energy mix and large availability of H_2. Therefore, alternative pathways for an earlier decarbonization of hard-to-abate industries and for large scale syngas/H_2 production need to be considered.

In Chapter 3, a novel process scheme is proposed involving chemical looping for syngas production. The CO_2 content in blast furnace gases is separated with a calcium looping cycle and subsequently injected with H_2O into the oxidation reactor of a chemical looping cycle. Assuming an inlet stream of pure CO_2, mass balances on the chemical looping plant are carried out to compare the performance of nickel ferrites and iron oxides in terms of required oxygen carrier flow rate to process 1 t/h of CO_2. Computational fluid dynamics simulations with integrated reaction kinetics are then carried out to validate the assumptions on the oxygen carrier conversion and syngas compositions.

In Chapter 4 and 5, experimental evaluations are carried out on two crucial aspects for the successful operation of a chemical looping plant aiming at syngas production. In Chapter 4, the syngas productivity by CO_2 and H_2O splitting over a Fe bed is investigated. This is a very important step, and the effect of various parameters was considered. Firstly, the CO_2 splitting is analysed for different temperatures with an inlet flow rate of 1 NL/min to ensure

a substantial dissociation of the CO_2. Subsequently, combined streams of CO_2 and H_2O are evolved in the reactor. The effect of the total flow rate, reactants molar ratio and bed height is investigated and from the results, the optimal syngas composition is identified. SEM and XRD are used to assess the morphological evolution and the phase changes of the material during the test. On the contrary, in Chapter 5 the effect of high-pressure operation on the redox abilities of two NiFe aluminates is assessed. The aluminates present similar Fe loadings, but different Ni loadings. High pressure operation is crucial for the development of this technology because it facilitates downstream processing of the syngas to liquid fuels. For a comparative analysis, preliminary tests at low pressure are carried out at three temperatures. Subsequently, the effect of reactants flow rate, temperature, total pressure, gas composition is analysed at high pressure conditions. Finally, long term tests are performed both at ambient and high-pressure conditions. Material characterization by SEM, XRD and H_2-TPR is used to support the comparative analysis.

In Chapter 6, a techno-economic analysis on a process scheme encompassing methanol and ammonia production from chemical looping gases is carried out. Chemical looping hydrogen production is a very versatile technology and allows for the combined production of power and H_2 or syngas. With proper calibration of the flow rates, a stream of high purity N_2 can also be obtained at the air reactor outlet and used for ammonia synthesis. Back up with an alkaline electrolyser is considered for the supply of the required amount of hydrogen. Sensitivity analyses are carried out on the chemical looping plant to evaluate the effect of fuel flow rate, steam flow rate, and oxygen carrier inlet temperature to the fuel reactor. Subsequently, a techno-economic analysis is carried out evaluating several parameters among which: the specific CO_2 emissions, the energy intensity, and the levelized cost of methanol and ammonia. Finally, a comparison with benchmark technologies and other clean alternatives is presented. In this way, the benefits as well as the drawbacks of chemical looping in terms of environmental and economic parameters are assessed and the missing elements to reach industrial competitivity are clarified.

Contents

List of publications

Journal papers related to this thesis

i. Development of a novel carbon capture and utilization approach for syngas production based on a chemical looping cycle, Hoxha, A., **Palone, O.**, Cedola, L., Stendardo, S., Borello, D., Fuel, 2022, 325, 124760
ii. Assessment of a multistep revamping methodology for cleaner steel production, **Palone, O.**, Barberi, G., Di Gruttola, F., Gagliardi, G.G., Cedola, L., Borello, D. Journal of Cleaner Production, 2022, 381, 135146
iii. Synthesis of Methanol From a Chemical Looping Syngas for the Decarbonization of the Power Sector, **Palone, O.**, Hoxha, A., Gagliardi, G.G., Di Gruttola, F., Stendardo, S., Borello, D., Journal of Engineering for Gas Turbines and Power, 2023, 145(2), 021018
iv. Experimental investigation of thermochemical syngas production in a scrap iron-based oxidizer reactor for industrial decarbonisation, **Palone, O.**, Cava, C., Paris, E., Vincenti, B., Migliarese Caputi, M.V., Gallucci, F., Borello, D., Fuel, 2023, 347, 128436
v. Techno-economic analysis of sustainable methanol and ammonia production by chemical looping hydrogen generation from waste plastic, **Palone, O.**, Gagliardi, G.G., Mechelli, M., Cedola, L., Borello, D., Energy Conversion and Management, 2023, 292, 117389
vi. On the reduction of $NiFe/Al_2O_3$ oxygen carrier in high-pressure chemical looping applications, **Palone, O.**, Ramezani, R., Navarro, C., Di Felice, L., Borello, D., Grasa, G., Gallucci, F., International Journal of Hydrogen Energy, Accepted (In press)

Journal papers out of the scope of this thesis

i. An efficient composite membrane to improve the performance of PEM reversible fuel cells, Gagliardi, G.G., **Palone, O.**, Paris, E., Borello, D., Fuel, 357, 129993
ii. Syngas Quality in Fluidized Bed Gasification of Biomass: Comparison between Olivine and K-Feldspar as Bed Materials, Vincenti, B., Gallucci, F., Paris, E., Carnevale, M., Palma, A., Salerno, M., Cava, C., **Palone, O.**, Agati, G., Caputi, M.V.M., Borello, D., Sustainability (Switzerland), 2023, 15(3), 2600

Conference papers.

i. Methanol production by a chemical looping cycle using blast furnace gases, **Palone, O**., Hoxha, A., Gagliardi, G.G., Di Gruttola, F., Borello, D., Proceedings of the ASME Turbo Expo, 2022, 2, V002T03A010

ii. Analysis of the NOx emissions deriving from hydrogen/air combustion in a swirling non-premixed annular micro-combustor, Mazzotta, L., Di Gruttola, F., **Palone, O.**, Gagliardi, G.G., Borello, D., Proceedings of the ASME Turbo Expo, 2022, 2, V002T03A009

Chapter 1

Introduction

This chapter is based on the following paper under preparation:
Palone, O., Borello, D., Markides, C. Decarbonizing power and fuels production by chemical looping processes: comprehensive review and perspectives

1.1 Climate change and CO_2 mitigation measures

The rapid growth in world population is causing an increase in energy demand and consequently in fossil fuels consumption, with an associated impact on the environment. Without a change of direction, the average temperature of the world in 2060 is going to be more than 2 °C above pre-industrial levels [1]. This would cause the destruction of multiple ecosystems and serious repercussions on the worldwide social and economic fabric. The solution to this problem must come from a collaboration of all the nations of the globe, which is not an easy target considering the contrasting interests of every country regarding their social and economic development. The first step towards the fight against climate change is done in 1997 in the United Nations Framework Convention on Climate Change (UNFCC), when the Kyoto Protocol was signed by 165 nations to reduce greenhouse gas emissions [2]. This agreement was then strengthened by the Paris Treaty, signed on the 21st of April 2016 [3], with the goal of maintaining the temperature difference with pre-industrial levels well below 2 °C and preferably limit it to 1.5 °C. In fact, according to the United Nations' Intergovernmental Panel on Climate Change (IPCC) getting above this threshold could lead to severe and more frequent droughts, rainfalls, and heatwaves [4]. Another step in this direction was taken with the European Green Deal presented by European Union (EU) President Ursula Von Der Leyen in 2019, with the ambitious goal of achieving the climate neutrality in the EU member countries, i.e. zero net anthropogenic CO_2 emissions, before 2050 [5].

1.1.1 Carbon capture, utilization, and storage

In 2022, the total CO_2 emissions associated with energy processes grew by 0.9%, reaching a total of 36.8 Gt/y [6]. Currently, power production is carried out by fossil fuels combustion (coal, oil and natural gas) in three main plant configurations: (1) combined cycle power plants, in which a Rankine cycle (bottoming) recovers the thermal content of the exhaust gases from a Brayton cycle (topping) with net efficiencies above 60% [7]; (2) steam cycle power plants, where water in subcritical (< 22 MPa) or supercritical conditions (> 22 MPa) is heated by coal combustion and then evolved in a steam turbine with net efficiencies up to 47.5% [8]; (3) open cycle gas turbine power plants, which are mainly employed to compensate for the intermittency of the renewable power technologies due to their high flexibility of operation. The adoption of alternative sources and technologies such as renewable or nuclear energy can represent a solution to decarbonize energy production. However, to date the nuclear solution does not seem to be widely accepted by the public opinion, due to waste disposal criticalities, while fusion energy is expected to be demonstrated commercially in 2050 [9]. On the other hand, the renewable energy source is intermittent and requires the integration with high capacity and reliable energy storage systems [10].

The chemical sector is the third largest industrial subsector in terms of direct CO_2 emissions [11] and accounts for 2 Gt/y of CO_2 emissions to the atmosphere (direct and energy emissions) [12]. The chemical industry is heavily reliant on fossil fuels (coal, oil and natural gas) for two main purposes: as carbon feedstock from which syngas (a mixture of H_2 and CO) is produced with significant CO_2 (and other contaminants) emissions and as heat supply for high temperature processes where electrification is not an equally valid replacement. To address the increasing CO_2 concentration in the atmosphere, displayed in Figure 1.1 with the global temperature variation along the years, capture, utilization, and storage (CCUS) technologies appear as the most credible and immediate solution in the short term, involving CO_2 capture and subsequent permanent storage or further reutilization. CO_2 can be captured in several ways: chemical or physical absorption, oxy-fuel combustion, chemical or physical adsorption, membrane separation, cryogenics, calcium looping cycles etc [13]. In CCUS, part of the isolated carbon content of flue gases is employed for other purposes than storage, such as liquid fuels production [14–16] or electric energy production [17]. CO_2 can be further utilized as it is or after a splitting process as CO [18]. However, the high stability of the CO_2 molecule makes the direct thermolysis (i.e. the splitting in CO and O_2) a very energy intensive process, requiring temperatures above 2000 °C to have a significant conversion [19]. However, the ideal processes for the sustainable transition would allow for an almost complete separation of CO_2 from other gases with as low as possible energy and economic penalties. Chemical looping combustion (CLC) is a process in which the oxidizing agent, generally air, and the fuel are never in contact with each other and exchange oxygen with a solid material (oxygen carrier, OC) that is often a metal oxide. The inherent separation of the CO_2 from the N_2 content of air without the need of any energy intensive downstream processing makes chemical looping a promising technology for different applications, such as sustainable power and/or fuels production. Chemical looping processes are also extremely versatile and can be tuned by selecting the proper oxygen carrier, the correct oxygen to fuel molar ratio and the reactor design. In this way, they can be adapted to also perform reforming of hydrocarbons, CO_2 and H_2O splitting, gasification of biomass and/or waste. In chemical looping reforming (CLR) the main advantage is that the heat needed for the endothermic reforming reaction is provided by the exothermic reaction in the air reactor, without energy intensive processes such as air separation, without mixing air with carbonaceous gases, and without burning part of the hydrogen produced in the process [20]. In chemical looping gasification (CLG) the main benefits are the absence of any N_2 dilution with air, the possibility of autothermal operation and the reduction of tar release. Therefore, considering the crucial part that this technology could play in the energy transition, in this paper an overview on chemical looping processes is provided with a focus on the most recent literature works on the subject. Given the extensive research activity on this technology, two scales of analysis have been considered

for the analysis: the laboratory scale, related to material and process development by experimental evaluations; the system-level scale, where chemical looping processes are integrated in conventional power and fuels production sectors and compared with benchmark technologies by environmental and economical assessments. The expected outcome is a synthetic but comprehensive recollection of the main advancements in the field and, based on the main results, the identification of further research pathways that could contribute to reach industrial maturity. The chapter is structured as follows: in the first section a brief description of research progresses on oxygen carrier properties is provided, given the crucial importance that they have in the process. Subsequently, the technology is divided into three main branches, i.e. combustion, reforming, and gasification. Chemical looping combustion is the most developed variant of the three and therefore focus has been given on the most recent advances and still unsolved issues, such as inherent gas cleaning abilities, reactor configurations and waste materials utilization. Chemical looping reforming is also widely investigated in the literature and advances on each variant of the technology (autothermal reforming, H_2 production and CO_2 splitting) are provided, mainly related to material and process development as well as reactor configurations. Chemical looping gasification is also discussed in terms of its benefits and potentials compared to conventional gasification. Then, moving to the system scale, literature works that envisage the integration of chemical looping into power and fuels production scenarios are reviewed, focussing on the comparison with benchmark plants. Finally, a critical discussion on benefits and drawbacks both at the process and system level is carried out, and recommendations for research activities are provided to support the industrial scale up.

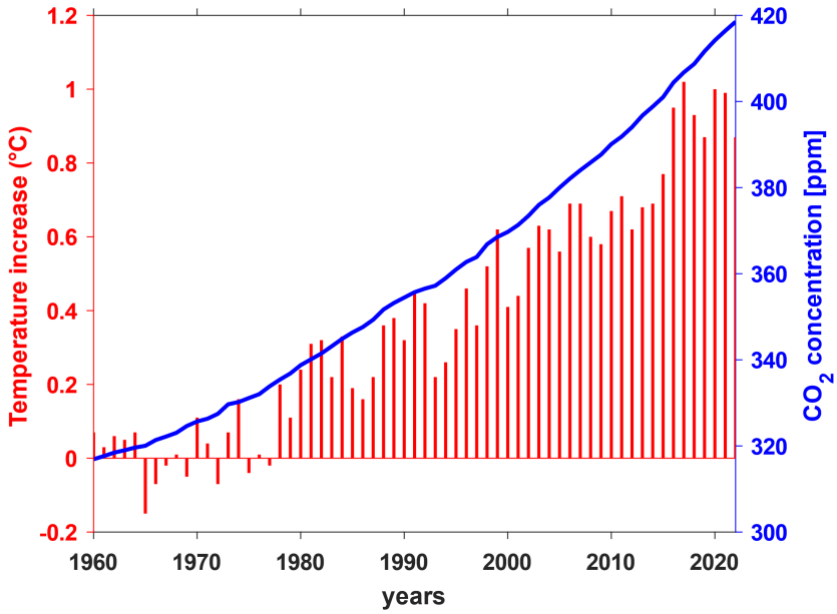

Figure 1.1. Yearly variation of global temperature anomalies with respect to the 1901-2000 average and of CO_2 concentration in the atmosphere. Plotted data retrieved from [21,22]

1.2 Oxygen carriers for chemical looping processes

Research on innovative oxygen carrier materials is at the core of chemical looping development. The most relevant characteristics that an oxygen carrier should have in chemical looping applications are: (1) the ability to transport oxygen, (2) good fuel conversion, (3) high reactivity, (4) high resistance to attrition, (5) low carbon deposition, (6) limited agglomeration, (7) chemical stability, (8) cost-effectiveness, and (9) zero or limited toxicity or other environmental problems. Metal oxides have been selected as the most promising materials for this application, especially Fe_2O_3, NiO, CuO, MnO and MgO. Fe_2O_3 based materials are the most studied oxygen carriers due to their large availability, low toxicity, and relatively high melting temperatures [23]. Iron oxides are also characterized by different chemical phases (Fe_2O_3, Fe_3O_4, FeO and Fe) that ensure flexibility of operation for the different variants of chemical looping [24]. However, they suffer from low cyclability due to agglomeration problems and low reactivity in the fuel oxidation step [25]. Ni-based oxygen carriers are also considered as very promising oxygen carriers because of their catalytic activity for hydrocarbons decomposition, good performance at high temperatures and low attrition rates. The main drawback is their toxicity and the carbon deposition. Mixed oxides with iron and nickel, as well as ferrites [26,27], have been widely investigated to combine the high reactivity of nickel-based materials with the low toxicity and redox properties of iron oxides. CuO-based oxygen carriers are very active materials for complete oxidation of the fuel and present oxygen uncoupling abilities on the redox couple CuO/Cu_2O, but they suffer from serious deactivation due to sintering of CuO above 900/1000 °C, which is associated with its low melting temperature and low mechanical properties. Finally, Mn-based materials provide good oxygen transport capacity, uncoupling abilities between Mn_2O_3 and Mn_3O_4, very high reactivity with CO and H_2 but they are affected by relatively low methane conversion, low mechanical stability and the tendency to form unreactive and highly stable compounds when used as supports [28,29]. Materials of this kinds, that provide good thermal stability and mechanical properties but low activity, are often considered as possible reactive supports for less stable materials. Perovskites have recently attracted attention in several fields (solid oxide fuel cells, oxygen permeable membranes, sensor materials etc. [30]) and represent promising oxygen carriers. They are described by the general formula ABO_3, where A is a rare alkaline earth or lanthanide metal, and B is a transition metal. The main feature of perovskites is their crystalline structure that allows to obtain tailored redox properties by doping and/or partial cation substitution of the A and B sites. Perovskites are also part of the research effort on solar driven chemical looping processes along with iron oxides, zinc oxides, tungsten oxides, ceria oxides and cerium-based oxides. Doped or undoped ceria are promising oxygen carriers for solar chemical looping due to their high oxygen mobility, high oxygen

transport capacity at high temperature, stable crystallographic structure over many cycles and anti sintering properties thanks to significant melting temperatures [31]. Doping of ceria oxides is often considered in solar driven processes to decrease the reduction reaction temperatures below 1500 °C, since in non-doped conditions thermodynamics dictates a reduction temperature of over 2000 °C [32].

To enhance the cyclability of oxygen carriers, they are often supported on ceramic materials such as: Al_2O_3, monoclinic ZrO_2, MgO and $MgAl_2O_4$, CeO_2, partially stabilized tetragonal zirconia (t-PSZ), yttria-stabilized cubic zirconia (c-YSZ), TiO_2, SiO_2, MnO, bentonite, and their mixtures [33]. Among numerous benefits, these structural promoters provide enhanced thermal stability of the particle, higher acidity or basicity of the surface which hinders carbon deposition, improved reactivity, and catalytic activity thanks to optimal dispersion of the active phase. The high temperatures that are necessary for the processes can lead to the formation of new structures by reaction of the active phase with the structural promoter which can preserve the reactivity of the material or make it inert. For instance, materials with SiO_2 supports are shown to form unreactive silicate phases and to suffer from sintering [34], while TiO_2 supports tend to form titanate with low reaction rates, excepts for iron oxides. ZrO_2 and CeO_2 are two promising supports, with limited interactions with the active phase, though both are affected by high costs [34]. Al_2O_3 has been widely investigated as structural promoter, especially for its high thermal and chemical stability combined with low costs [35]. Benefits and drawbacks have been identified, such as improved thermal resistance, especially for Cu-based oxygen carriers that are affected by easy agglomeration [36], and aluminates formation over high temperature cycles, that present lower reaction rates. In the case of $FeAl_2O_4$ formation by reaction with iron oxides, the material becomes an inert when CO_2 and H_2O are used as oxidizing agents [37]. On the contrary, the utilization of aluminates as supports, such as $NiAl_2O_4$, $MgAl_2O_4$, $CaAl_2O_4$ etc., has been demonstrated to prevent interaction with the active phase, improve the thermal stability of the active phase and enhance the catalyst dispersion on the particle [25].

1.2.1 Waste materials

Recently, the research on new oxygen carriers has focused on industrial waste materials (red mud [38][39] , copper slag [40], electric arc furnace dust [41], steel slag [42] and other industrial waste [43–45]) and natural ores (calcite [46], ilmenite [47–49], hematite and manganese ores [49]) for cost abatement of chemical looping processes. Reutilization of waste or direct utilization of natural ores has the advantage of a significant reduction in preparation costs as well as in waste disposal costs and of reduced soil, water and air pollution. The main limitation is represented by lower reactivity towards full fuel oxidation compared to synthesis material [50].

1.3 Chemical looping combustion

This is the first variant of chemical looping process that was proposed for decarbonized power production by the group of Ishida at the Tokyo Institute of Technology in 1994 [51]. In CLC the oxygen carrier undergoes a redox cycle consisting of a reduction step, in which the fuel reacts with the OC and is oxidized to CO_2 and H_2O according to an endothermic reaction (Eq.1.1); and an oxidation step, where the OC is regenerated to the original oxidized phase by interaction with air through a highly exothermic reaction (Eq. 1.2). The main chemical reactions involved in this process are reported in Table 1.1, while a schematic representation is provided in Figure 1.2.

Table 1.1. Main chemical reactions in the fuel and air reactor

Fuel Reactor	$CH_4 + M_xO_y \rightarrow 2H_2O + CO_2 + M_xO_{y-2}$	(1.1)
Air Reactor	$M_xO_{y-2} + O_2 \rightarrow M_xO_y$	(1.2)

The gas products from the reduction reactor are generally treated for contaminants abatement and, after water removal by condensation, a stream of high purity CO_2 is extracted which can be further processed to obtain liquid fuels/chemicals or simply stored. No costly and energy intensive processes for gas cleaning and purification are thus required for CO_2 removal [52]. The net energy released is equivalent to a conventional combustion reaction and can be exploited for combined heat and power conversion, either in a steam cycle or in a Brayton cycle (see following sections). Currently the technology has been proven at laboratory and small pilot plants up to 3 MW [53]. Besides, oxygen carriers have been used in circulating fluidized bed reactors boilers partially replacing the inert bed to enhance combustion (oxygen carrier aided combustion, OCAC) at nominal thermal powers of 75 MW_{th} for more than 12000 h of operation [54]. Further research on the effect of scaling up on CL processes performance is crucial for the development of the technology. Over the years, different types of fuel have been studied in CLC: solid (coal, char, biomass, waste [55] etc), liquid (bioethanol, diesel oil, kerosene), and gaseous (CH_4, H_2, CO, syngas). Less operational experience is recorded for liquid fuels CLC considering the low fuel conversions and the high specific solid inventories, i.e. 1300-2000 kg/MW_{th}, that are excessive for large-scale fluidized beds [56]. Therefore, the following sections will mostly focus on solid and gaseous fuels for CLC.

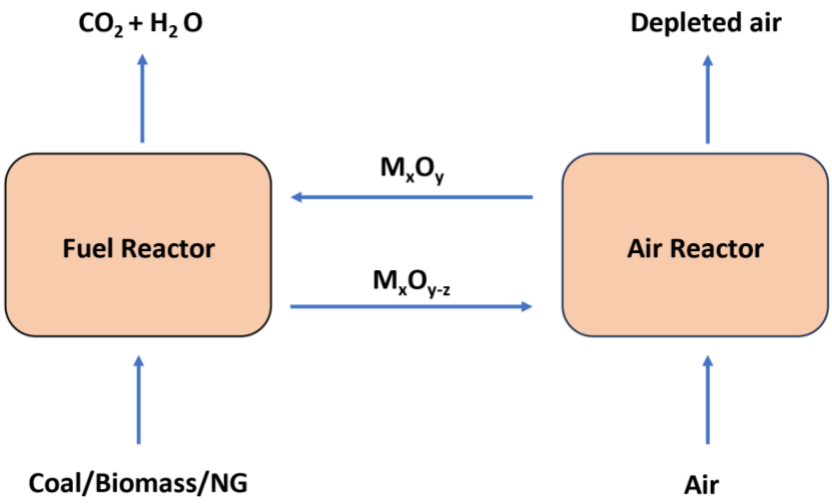

Figure 1.2. Simplified scheme for CL

1.3.1 Advances in solid fuelled CLC

In solid fuelled CLC, coal is the preferred fuel due to its large availability and low cost, though in the close future biomass combustion will be crucial to meet the decarbonization goals through negative CO_2 emissions. Different measures have been put into place to optimize coal combustion, enhance reactivity with the OC and increase the CO_2 purity of the outlet stream. Examples are the selection of the optimal oxygen carrier [57,58], coal ranking and pre-activation [59], tuning of reactor temperature [60] and pressure [61,62], improvement of reactor design [63], use of chemical looping with oxygen uncoupling (CLOU) [64]. Lyngfelt et al. [65] report that most of the operational activities from 2004 to 2018 on solid fuelled CLC have been conducted with iron oxides, ilmenite, and natural ores such as iron and manganese ores, together covering for more than 80% of all operation with solid fuels. This is associated with ash formation during solid fuels combustion that hinders the performance of costly synthetic materials by contamination and active sites blocking.

1.3.2 Contamination in solid fuelled CLC

One of the main problems associated with coal combustion is the presence of sulphur species. In CLC the sulphur content of coal is responsible for contamination of the CO_2 stream from the reducer and the N_2 stream from the air reactor, corrosion of the heat exchangers and atmospheric contamination [66,67]. Higher temperatures promote the oxidation of H_2S to SO_2 and the char consumption in the reducer reactor, preventing the migration to the air reactor [68–70]. In [71] Ma et al. have studied the interaction of Fe_2O_2/Al_2O_3 oxygen carrier with pyrolysis and gasification gases in a two-stage fluidized bed. No sulphur deposition has been detected and the formation of calcium sulphates has suggested a desulphurization effect of the ashes. However, high pressures could be responsible for increased solid sulphur deposition on the OC [72]. Mercury release from

solid fuel combustion is a relevant issue due to its toxicity, and accumulation. Scarce literature works are however available on mercury release from CLC or CLR of solid fuels. In [73] Mendiara et al. have performed the first study on mercury release from CLC of coal, showing that Fe_2O_3 has oxidation abilities on Hg^0 towards the formation of Hg^{2+}. In [74], Xu et al. prepare a magnetic oxygen carrier with a core-shell structure of Co_3O_4@TiO_2@Fe_2O_3. Homogeneous and heterogeneous reaction pathways are identified to justify the increase in mercury removal efficiency in the combined presence of HCl atmosphere and of the OC compared to simply the HCl atmosphere (50 ppm). Higher temperatures (from 800 °C to 900°C) improve the removal efficiency from 45% to 63%, while good stability after 10 redox cycles is observed.

1.3.3 Effect of high pressure on solid fuel CLC

Regarding the effect of high-pressure conditions on CLC with solid fuels, in [62] Wang et al. have analysed pressurized CLC of $CuFe_2O_4$ with a Chinese bituminous coal in a pressure range of 0.1 to 3 MPa. An increase in system pressure has several benefits: (1) OC reaction with pyrolysis volatiles and gasification products is promoted, (2) char consumption is increased, (3) the reduction extent of the $CuFe_2O_4$ is increased. Similarly, in [75] Zhang et al. perform pressurized chemical looping combustion tests of coal observing that up to 5 bar total pressure has a beneficial impact on carbon conversion, while the opposite holds for higher values.

1.3.4 Chemical looping with oxygen uncoupling

CLOU is a reaction mechanism that can occur in parallel with CLC and allows for higher quality combustion [65]. This process is based on materials capable of releasing molecular oxygen at high temperature, thus improving the fuel combustion efficiency especially when solid fuels are used since direct combustion takes place [68]. This configuration also reduces char migration from the FR to the AR and simplifies the engineering complexity of the plant [76]. CLOU materials present additional features with respect to conventional oxygen carriers, such as: the ability to release gaseous oxygen and sufficient equilibrium oxygen partial pressure at the combustion temperatures; low equilibrium partial pressure during oxidation [77]. The main reactions occurring in a CLOU are reported in Table 1.2. Compared to CLC, CLOU systems for coal combustion experimentally reach CO_2 capture efficiencies above 90% and combustion efficiency of 100% in a temperature range between 910 °C and 950 °C, while the former reach 60% and 80% at 920 °C, respectively [78].

Table 1.2. Reaction scheme of CLOU

Fuel reactor	$2M_xO_y \rightarrow 2M_xO_{y-1} + O_2$	(3)
	$Fuel + O_2 \rightarrow CO_2 + H_2O$	(4)

Air reactor	$M_xO_{y-1} + 1/2\ O_2 \rightarrow M_xO_y$	(5)

Recently, materials with CLOU abilities have been considered for thermochemical energy storage applications. Thermochemical storage technologies are particularly attractive because of their geography independency, high energy densities and high discharge temperatures (> 1000°C), which enable the coupling with combined cycle power blocks, and low costs on an energy basis. The most widespread thermochemical energy storage processes are represented by system hydration [79], carbonation [80], redox reactions [81]. In the latter subsector, the most promising redox couples for energy storage applications are: BaO_2/BaO, Co_3O_4/CoO, Mn_2O_3/Mn_3O_4, CuO/Cu_2O, and Fe_2O_3/Fe_3O_4 [82]. Ba oxides present moderate reaction temperatures and energy density but poor reversibility [81], Co oxides are characterized by high energy density and excellent reversibility, but they are expensive and toxic, Mn oxides are low cost but present low oxidation rates, while Cu and Fe oxides are also low cost but are affected by sintering phenomena at the reaction temperatures. To compensate for these drawbacks, mixing of metal oxides has been attempted. To date, research on redox systems for thermochemical energy storage is still at an early stage of development (laboratory scale), where the cycling abilities of different oxygen carriers are compared over successive reduction and oxidation steps. Combinations of Fe and Mn oxides with an optimal composition of about 20 mol% Fe have shown increase in oxidation kinetics, reactive stability and energy storage density compared to Mn_3O_4/Mn_2O_3 [83]. Similarly, mixing of Cu and Mn oxides has yielded promising results due to the formation of spinel phases with high O_2 release during transitions, and higher attrition resistance for higher CuO contents [84]. In [85] Randhir et al. have tested Mn-Mg oxides with different compositions, demonstrating unvaried cycling abilities and fast kinetics over 20 redox cycles between 1200 and 1500 °C at 0.2 bar O_2 partial pressure. Based on these results, Rahmatian et al. [86] have built a 1 kW/0.1 kWh bench-scale demonstration setup operating at industrial conditions, i.e. 20 bar during oxidation, 0.2 bar during reduction, and 1500 °C, over 5 cycles with Mg and Mn oxides pellets (1:1 molar ratio according to King et al. [87]). Calcium manganites ($CaMnO_{3-\partial}$) have been studied at Chalmers University providing higher reactivity with methane than Ni-based OCs by means of the oxygen uncoupling properties [88]. Lanthanum [89] and calcium-based perovskites [90] have also been studied by Babiniec et al. for energy storage applications due to their extremely high oxygen mobility and high melting points, though they require very low oxygen partial pressures for reduction [81].

1.4 Advances in gas fuelled CLC

The combustion of a gas in CLC has received many attentions from the scientific community, with methane being the favourite fuel along with H_2 and syngas. Currently,

research is mostly focused on four main themes: the reduction of gas products contamination by heavy metals, chlorine, and sulphur; the limitation of coke formation during reduction; the testing of new materials combining waste and synthetic oxygen carriers; the analysis of the effect of pressure on kinetics.

1.4.1 Contamination by chlorine and sulphur in gas fuelled CLC

Originally, the CLC technology is not developed to simultaneously operate combustion and purification of the off-gas. However, the increasing interest for the integration of CLC with fuels such as syngas from biomass or waste gasification requires the assessment of possible strategies for inherent reduction of contaminants. For instance, syngas from municipal solid waste gasification is characterized by high concentration of chlorinated compounds (HCl), that eventually can cause corrosion of the heat recovery system as well as contamination to the environment [91]. The modification of iron oxides with alkali or alkaline earth metals (K_2O, Na_2O, CaO, $CaSO_4$, $BaCO_3$ etc.) has provided high dichlorination abilities in several studies where syngas from waste or plastic is employed [92,93]. However, the cyclability of the OC still represents a problem because of the reduction of HCl removing capacities overtime due to consumption of the sorbents. For this reason, it has been suggested the addition of a third step of sorbent regeneration, where HCl desorbs from the particle surface by the injection of water and by temperature increase, depending on the specific sorbent [94]. The presence of the sorbent and its regeneration also have shown improved combustion efficiency. The presence of hydrogen sulphide (H_2S) is another major problem for CLC operation because of its corrosive properties and the formation of sulphur compounds with lower reactivity such as Ni_3S_2 [95] and Cu_2S [96] when nickel and copper oxides are present, respectively. Iron oxides provide unchanged redox performance under reducing gas streams with H_2S concentrations up to 20% in vol and configure as the ideal candidates for an integrated desulphurization process [97]. However, to prevent the presence of SO_2 and H_2S concentrations in the outlet gases, loading with alkaline earth metals as sorbents must be again considered. Among BaO, CaO and MgO, BaO provide significant H_2S sulphur removal properties (around 63% over 10 cycles) by the formation of sulphites and sulphates and the best syngas combustion efficiency [97].

1.4.2 Waste materials for gas fuelled-CLC

Low-cost materials are characterized by low reactivity with methane and therefore are preferred for solid fuels applications. However, recent studies have demonstrated that iron-based waste materials can have promising reactivities, as in the work by Cabello et al. [43] where iron hydroxide residues reach a maximum of 86% combustion efficiency in a continuous CLC unit, high redox stability when completely reduced to Fe and oxidized in air in TGA tests. The combination of waste material and synthesis oxygen carriers can

represent a compromise between cost reduction, fundamental for future scale ups, and high reactivity for CLC. For example, CuO is characterized by extremely high combustion efficiencies and CO_2 yields in the fuel reactor, but also by fast deactivation due to sintering and agglomeration over consecutive cycles. To prevent material loss and extend the lifetime of Cu/Al_2O_3 in methane based CLC, Izquierdo et al. [98] suggest enforcing low reaction extents at operating temperatures below 900 °C. Moreover, the interaction of CuO with the Al_2O_3 support may lead to the formation of $CuAl_2O_4$, which is not characterized by CLOU abilities [99]. On the contrary red mud, a solid waste from aluminium industry with a global production of 120 Mt/y [100], is characterized by relatively low reactivity but high thermal and chemical stability due to the presence of Fe_2O_3 as active component and Al_2O_3, SiO_2 as inerts. In [31], Gu et al. show that by combining red mud and CuO in a 30-70% wt proportion methane conversion increases from an average 67% to 86%, the oxygen carrying capacity rises from 8% to 13%, and cyclability is improved due to $CuFe_2O_4$ spinel formation. Analogously, red mud synergy with MgO and NiO has been demonstrated by Lin et al. [101] in terms of enhanced methane combustion and redox stability over many cycles.

1.4.3 Effect of high pressure in reduction kinetics

In terms of high-pressures effect on reaction kinetics, several works report negative effect of total pressure [47,48,102–105] in gas fuelled CLC, except for the work by San Pio et al [106]. For instance, in [103] Hamers et al. report experimental data at high-pressure conditions on CLC of CuO/Al_2O_3 and $NiO/CaAl_2O_4$. The effect of pressure is detrimental for reaction kinetics and different gas compositions provide different reduction behaviours, likely due to a competitive adsorption mechanism. Garcia-Labiano [107] have tested the reactivity of Cu, Fe and Ni-based oxygen carriers for CLC in the 1 – 30 bar pressure range and have developed a kinetic expression to include the negative effect of pressure. On the oxidation side, Rana et al. have analysed the high-pressure oxidation kinetics (with O_2) of ilmenite ore and confirm the negative effect of total pressure, while constant O_2 volume fractions have shown a positive impact on kinetics up to a certain threshold [108]. Several explanations, though not conclusive, have been provided to justify this negative effect. The most widespread refers to slower products diffusion when the gases leave the particle surface, which then makes it more difficult for the fresh reactants to reach the active sites. In contrast with the presented works, in [109] San Pio et al. carry out high-pressure chemical looping cycles of CuO/Al_2O_3 and demonstrate that total pressure does not impact conversion kinetics nor the morphological and chemical structure of the oxygen carrier. The previous results are thus justified by the presence of mass transfer limitations in the setups. Carbon deposition is strongly affected by high pressure operation, especially during the CLC of methane. The accumulation of carbon on the particle surface hinders the CO_2 capture properties of the process by contaminating the air reactor outlet stream and reduces the

reactivity of the OC by blocking the active sites on the particle. Chemical looping combustion of methane and syngas has been investigated on Ni and Cu oxygen carriers at high pressure conditions (1 - 10 bar) by Nordness et al. [102]. High pressure has led to increased carbon deposition and lower reduction rate. Support with an active material, such as $NiFe_2O_4$, $BaFe_2O_4$ and $MgFe_2O_4$ spinel oxides that stably release oxygen over a long period of time, is shown to attenuate or completely inhibit this drawback [110].

1.4.4 Reactor configurations for CLC

Currently, the interconnected fluidized beds (IFB) configuration is the most widely investigated for large scale operation of chemical looping units, due to the uniform distribution of the solids and of thermal stresses. However, IFB units still present several criticalities in terms of solid attrition with fine formation, gas/solid separations (elutriation of fines from attrition), loop sealing between the fuel reactor and the air reactor, hydrodynamic instability, and power consumption for solid transport [111]. Different kinds of configurations for the FR reactor have been considered in IFB units: bubbling fluidized bed, circulating fluidized bed, fast fluidized bed, spouted bed, and moving bed [112]. In solid fuelled CLC, the fluidized bed configuration suffers from low carbon conversion (generally below 50%) and relevant carbon carryover to the air reactor (49.2%) [113]. The incorporation of a carbon stripper, proposed by Abad et al. [114], Haus et al. [115] and Linderholm et al. [49] has demonstrated of help to reduce the carbon migration to the air reactor and can achieve carbon conversion above 90%. On the contrary, moving bed reactors are characterized by higher fuel and oxygen carrier conversion and limited carbon carryover compared to the fluidized bed configuration, thus reducing the required oxygen carrier circulation and the reactor volume [116]. On the other side, the reduced gas velocity (below the minimum fluidization velocity) involves larger vessels. In [117] Zhang et al. have tested a 250 kW_{th} coal-direct chemical looping system, represented in Figure 1.3-(a), over 1000 h of operation in counter current moving bed mode. Stable temperature and pressure trends along the height of the moving bed reactor can be appreciated in Figure 1.3-(b) over the 288 h of continuous testing. The moving bed configuration is very promising and is often adopted in system-scale analyses of CL processes for power or chemicals production [118–120].

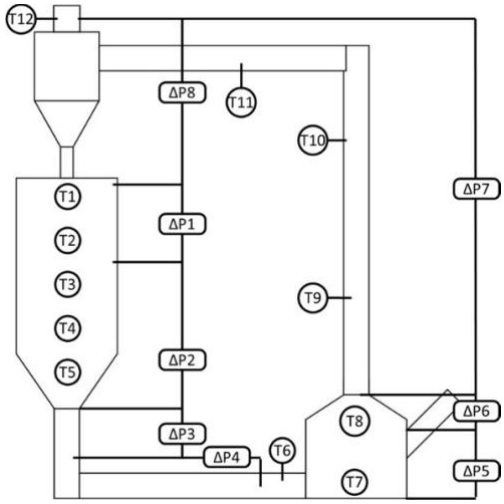

(a)

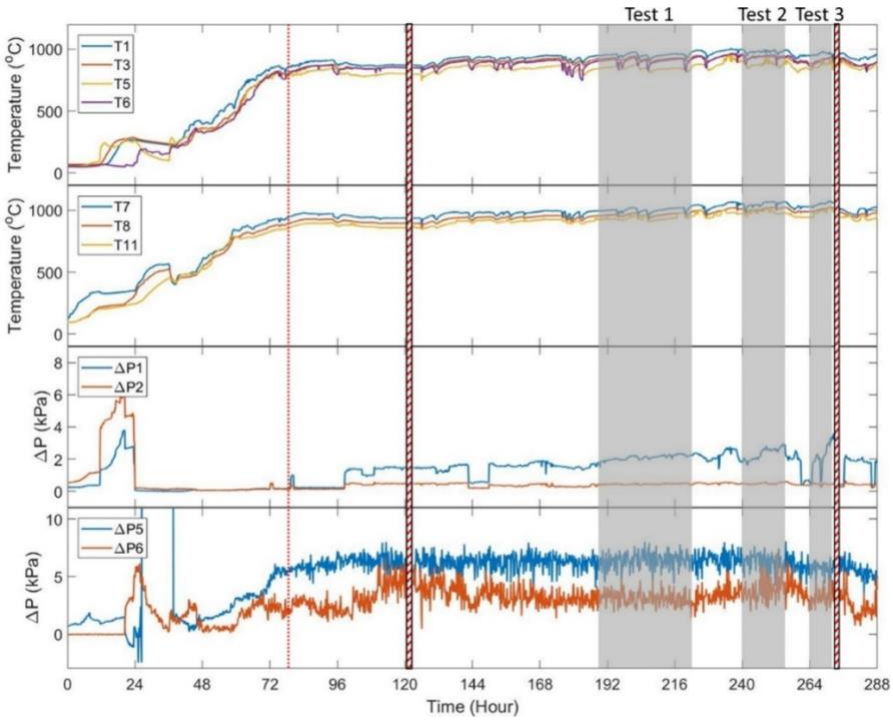

(b)

Figure 1.3. Schematic representation of the CLC system with temperature and pressure sensors (a); temperature and pressure variation along the reactor height over the 288-h of demonstration. Reproduced from [117].

Fixed beds substantially simplify the engineering of the system and reduce the power demand for solid transport [111], but they require greater sizes of the oxygen carrier particles to limit the pressure drop across the reactor. However, greater sizes determine intraparticle diffusion and external transfer limitations that hinder reaction kinetics [111,121]. In [75], Zhang et al. carry out a comparative analysis between fluidized bed and fixed bed operation for CLC of coal. In general, the fixed bed configuration shows the best carbon conversion and CO_2 yield, though the differential thermal stresses over many cycles

in fixed bed mode could lead to sintering and agglomeration. Therefore, fluidized beds are more indicated for long-term operation. Regarding energy storage applications of CLC, in [122] Abanades et al. propose a novel pressurized air reactor replacing the combustion chamber of a conventional Brayton cycle, as shown in Figure 1.4. The reactor is composed of gas conduits that cross a packed bed of oxygen carrier. Air is compressed and heated to about 500—600 °C before entering the reactor. Since the walls of the conduits are porous, but not selective, a small flow of oxygen diffuses through them according to Fick diffusion law and once on the other side reacts with the oxygen carrier in reduced form to regenerate the metal oxide. In this way, the typical temperature gradients and hot spots of fixed bed reactors are prevented and the heat release is adjusted over long period of times, suitable for integration in grid scale electricity supply. The heat release is transferred by conduction through the gas conduits walls to the pressurized depleted air flow. The resulting hot stream is composed of depleted air with 15-18% O_2 content and is sent to an expander for power production. On the contrary, in the charging step the metal oxide bed is reduced by renewable gases such as biomethane, hydrogen etc. which ensure low or negative CO_2 emissions and long-term energy storage of power peaks from renewable sources.

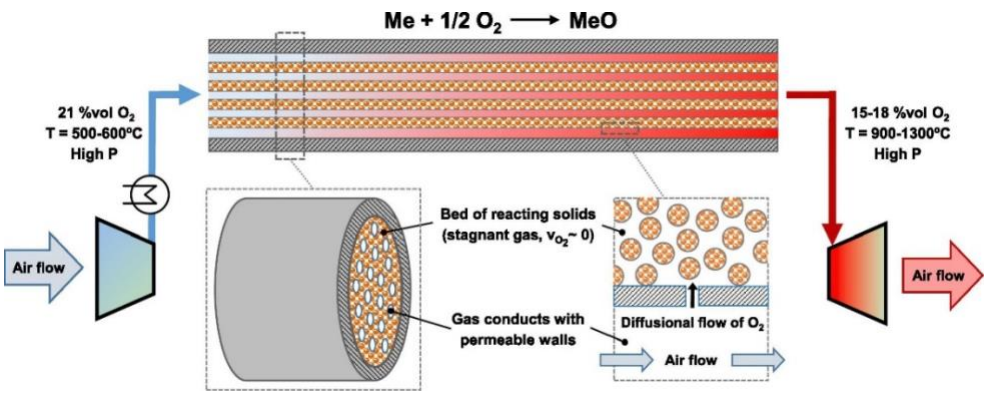

Figure 1.4. Charge and discharge operation for a CLC reactor with slow oxidation. Reproduced from [119].

This configuration has been demonstrated by Diego et al. [123] through thermogravimetric experiments with a graphite powder over times scales up to 8 h and temperatures in the 600-1000 °C range. The effect of different thicknesses and porosities has been assessed. Subsequently, thermogravimetric tests with iron oxides have been carried out by Calvo et al. [124] and the effect of particles sizes on reactivity and final conversion over the expected discharge times has been investigated. Fine particles (d_P = 4 μm) have shown conversions

up to 93% at the end of the oxidation stage at 980 °C and operation of the diffusion-controlled oxidation process has been demonstrated for more than 100 min.

1.4.5 High-pressure operation in reactor design

High temperatures (at least 1200 °C) and pressures (15 bar or higher) are mandatory conditions for industrial scale-up of CLC [125], because of higher efficiencies of the power block. In addition, at high pressures the CO_2 content in the off-gases can be directly sent to the pipeline (35 bar) or to permanent storage (100 bar) without significant compression duties. High pressure operation impacts the process design of the reactors in terms of equipment sizing and design, choice of operating conditions, reaction kinetics. In fluidized bed reactors high pressure leads to: (1) smaller and more frequent bubble formation, (2) lower minimum fluidization velocities and terminal velocities (easier elutriation), (3) higher particles attrition; (4) change in the heat transfer due to the different density and viscosity of the gases [126]. Promising configurations for scale up of CLC, including high pressure operation, are the packed/fluidized gas switching reactors [127] and the rotating reactors configurations [128]. Schematic representation of the two reactor configurations is provided in Figure 1.5-(a) and (b), respectively. With these configurations the pressurized operation is simplified, but new technical difficulties are encountered, such as the transient nature of gas switching processes using costly high-pressure and high-temperature switching valves and the significant gas leaks in the rotary configuration [129]. Recently, a new configuration called internally circulating reactor (ICR) has been developed [130]. In ICR two CFB reactors, together with cyclones and ring seals, are combined into a single reactor that can be pressurized into one pressure shell, as shown in Figure 1.5-(c). The two sections of this reactor, a fuel section (in green) and an air section (in red), are connected with each other by two simple mouths (in blue) that are designed to ensure constant circulation of solids. The circulation is achieved by maintaining a higher surface velocity of the gas in the air section with respect to the fuel section [131]. One drawback is the gas leakage between the fuel and the air section that may hinder CO_2 capture and purity. Numerous experiments on CLC and CLR at have shown that the ICR can be used for practically all chemical looping processes while managing to obtain a CO_2 purity greater than 96%. An exception is represented by the water splitting process in which, however, it is possible to reach a CO_2 purity of 90% [132]. High pressure operation has been demonstrated by Osman et al. with the ICR configuration up to 6 bar for 40 h continuously with CO_2 capture efficiency and purity up to 97% [133]. However, limited operation experience is recorded with this configuration compared to the standard dual CFB.

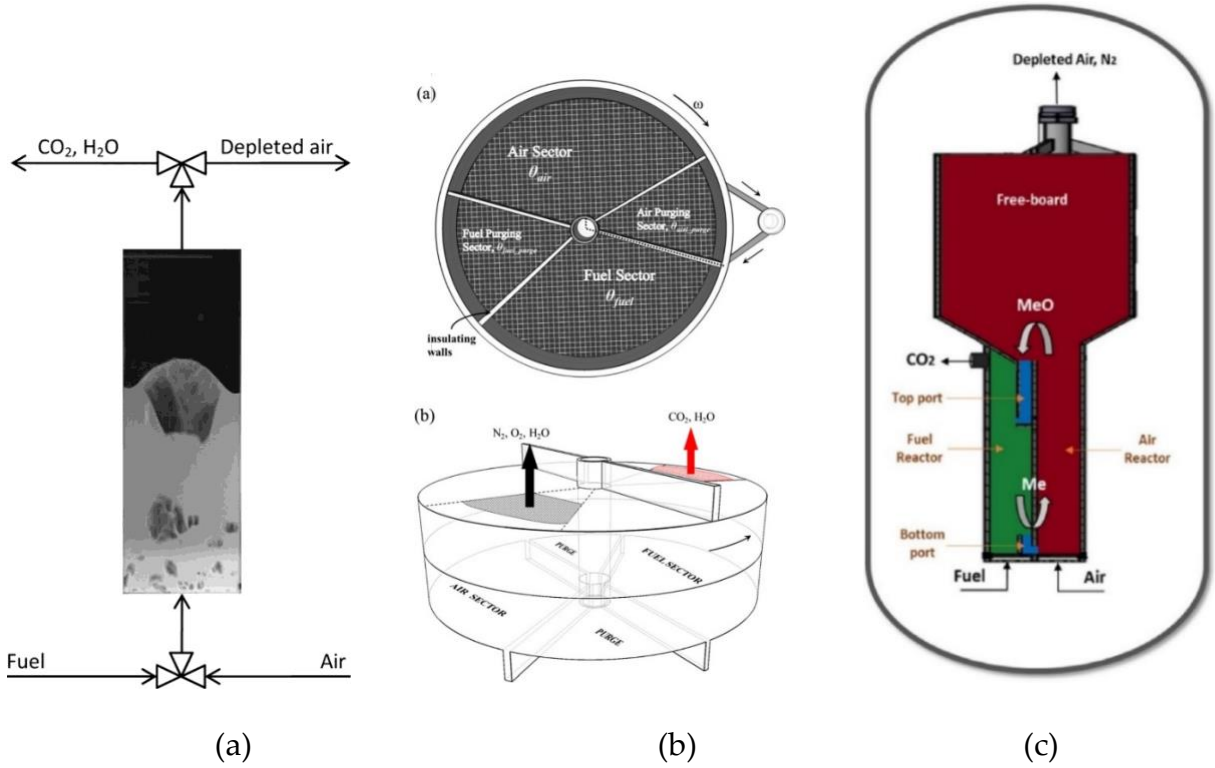

Figure 1.5. Schematic representation of the gas switching reactor, reproduced from [127] (a); of the rotary reactor, reproduced from [128] (b); of the dual ICR configuration, reproduced from [133] (c).

1.5 Chemical looping reforming (CLR)

CLR is an alternative process for syngas production from methane reforming with inherent CO_2 separation. Conventional reforming reactions are based on methane injection in tubes filled with catalyst in combination with H_2O and CO_2. In fired tubular reforming the tubes are located inside a furnace environment where part of the methane is burnt to provide the heat of reaction. Differently, in autothermal reforming oxygen is injected with H_2O/CO_2 and partially burns the methane for internal heat supply. In CLR the principle is similar to CLC, but the fuel to oxygen carrier molar ratio is kept low to prevent full oxidation of the reducing agent. The heat generated in the oxidation reaction is then used for the activation of the reforming reaction. CLR has been also tested with other reactants than methane, especially waste products stream, such as glycerol [134–136], bioethanol [37], biogas [137,138] and pyrolysis gas from plastic waste or biomass [139,140]. The typical reaction occurring in the autothermal CLR are summarized in Table 1.3 [141]. A simplified scheme of the process is reported in Figure 1.6-(a).

Table 1.3. Reactions involved in a CLR process

Fuel reactor	Reactions	
Partial oxidation	$CH_4 + M_xO_y \rightarrow CO + 2H_2 + M_xO_{y-1}$	(1.6)
Full oxidation	$CH_4 + 4M_xO_y \rightarrow CO_2 + 2H_2O + 4M_xO_{y-1}$	(1.7)
Water-gas shift	$CO + H_2O \rightarrow CO_2 + H_2$	(1.8)
Steam CH4 reforming	$CH_4 + H_2O \rightarrow CO + 3H_2$	(1.9)
Dry CH4 reforming	$CH_4 + CO_2 \rightarrow 2CO + 2H_2$	(1.10)
CH_4 decomposition	$CH_4 \rightarrow C + 2H_2$	(1.11)
Air reactor	$M_xO_{y-1} + 1/2O_2 \rightarrow 3M_xO_y$	(1.12)

M_xO_y is the oxidized phase of the OC, while M_xO_{y-1} is the reduced phase. In this case methane undergoes partial oxidation and full fuel oxidation by interacting with the oxygen carrier. At the same time, the addition of steam or CO_2 as enhancers promotes additional methane conversion to syngas by steam or dry reforming, respectively. The water gas shift reaction balances the products composition. To intensify the H_2 content in the gas products, downstream processing with a water gas shift section is generally considered with subsequent separation by pressure swing adsorption or absorption in suitable solvents. In this case, the heat is supplied by both the full oxidation of methane in the fuel reactor and by the exothermicity of the air reactor. Carbon deposition and accumulation is also prevented due to the presence of the air oxidation step. CLR presents several advantages over conventional syngas production pathways, such as for instance the absence of external combustion of part of the reactants or of the tail gas from pressure swing adsorption in a separate unit (as for the SMR), the absence of an air separation unit to produce high purity oxygen because oxygen is directly provided from the solid material. Another interesting concept for decarbonized SMR is the CLC-SMR. In this concept CH_4 is injected in conventional reforming tubes which are located inside a fluidized bed heat exchanger. In this case, when H_2 separation is carried out the tail gases from PSA can be sent to feed the CLC section which is operated at atmospheric conditions. This simplifies the engineering because it does not involve pressurized conditions and low-cost oxygen carriers can be used, such as iron and manganese oxides.

1.5.1 Chemical looping CO_2 splitting and H_2 production

Other CLR processes involve the oxidation of the OC with steam, CO_2 or both [142] instead of air. CO_2 oxidation can also produce gasification of possible carbon deposits and provide a CO concentrated stream at the reactor outlet [143]. However, steam and CO_2 oxidation suffers from thermodynamic limitations, that may hinder the complete regeneration of the metal oxide. Similarly, the formation of inert species towards H_2O/CO_2 oxidation such as $FeAl_2O_4$ (hercynite) can inhibit the chemical stability of the material [37]. A further oxidation step with air is thus necessary to achieve complete regeneration and close the cycle. In this

framework, one of the most important variants of CLR is represented by Chemical Looping Hydrogen Production (CLHP), where high purity H_2 production is achieved according to the three steps in Table 1.4. A simplified scheme of this process is reported in Figure 1.6-(b).

Table 1.4. Chemical looping hydrogen production reaction scheme

Reduction	$2M_xO_y + CH_4 \rightarrow 2M_xO_{y-2} + 2H_2O + CO_2$	(1.13)
Steam Oxidation	$M_xO_{y-2} + H_2O \rightarrow M_xO_{y-1} + H_2$	(1.14)
Air Oxidation	$2M_xO_{y-1} + 1/2O_2 \rightarrow 2M_xO_y$	(1.15)

In this case, the fully oxidized OC (M_xO_y) is first reduced by methane in the fuel reactor (FR) with CO_2 and steam production. Subsequently, partial oxidation of the OC to M_xO_{y-1} takes place in the steam reactor (SR) with high purity hydrogen production. Finally, the material is oxidized to the original chemical phase in the air reactor (AR) where ambient air is injected and a N_2 stream (depleted air) is produced. The process presents several advantages in terms of high purity H_2 production, no requirements of downstream H_2 purification steps and the inherent separation of the CO_2 content coming from the FR. The presence of a final step with air oxidation prevents the oxygen carrier deactivation by carbon deposition from methane cracking and the Boudouard reaction. These side reactions reduce the catalyst life and limit its catalytic activity. This process is generally coupled with further processing steps for the conversion of the gas species (CO_2, H_2O, H_2 and N_2) to chemicals such as methanol, dimethyl ether, ammonia etc [144], or can be used to produce high purity H_2 suitable for fuel cells applications [145].

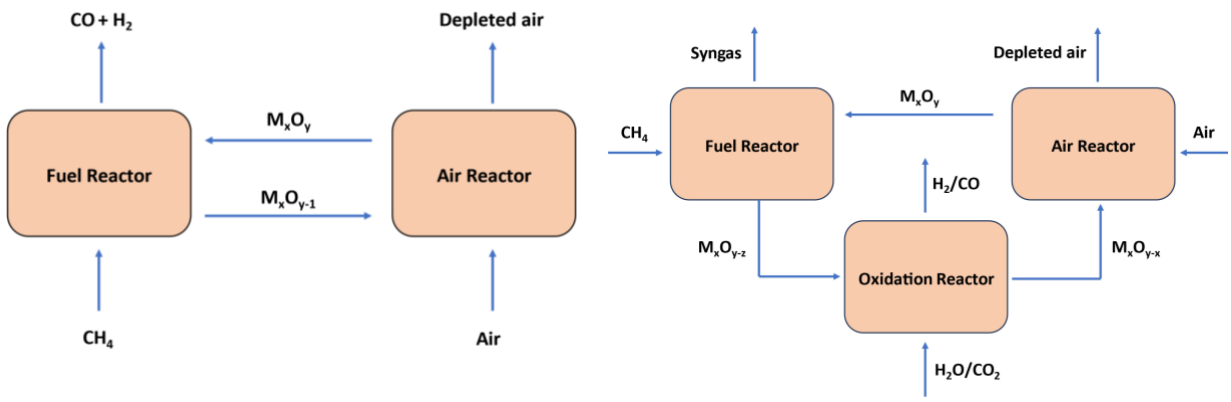

(a) (b)

Figure 1.6. Simplified scheme of CLR (a) and CLHP (b)

1.5.2 Advances in oxygen carriers research for CLR

To this date, nickel-based oxygen carriers have been extensively studied for CLR, but their toxicity and high cost is limiting their application [20,142,146]. Alternatives with a lower

toxicity level are high-cost materials, such as Ru and Pt [147]. For this reason, the addition of nickel to a pre-existing low cost and environmentally friendly material such as a natural ore can be a good compromise between cost and reactivity. For instance, in [148] Sun et al. compare pristine ilmenite and ilmenite with nickel addition, showing that the presence of nickel improves the catalytic activity towards reforming of CH_4/CO_2 blends. Similarly, in [46] Hu et al. show that calcite with the addition of nickel and iron has a better catalytic activity and cyclability compared to pristine calcite. Moreover, compared to other modified natural ores, higher CH_4 conversion and H_2 concentration in the syngas are detected. Mixed metal oxides provide increased reduction kinetics thanks to synergistic effect of the active phases. In [149] Huang et al. compare nickel oxides (NiO, mixed NiO and Fe_2O_3, NiFe) and iron oxides (Fe_2O_3) in a three-step process including reduction with methane, oxidation with CO_2 and then regeneration with air. From comparative analysis, it results that nickel ferrite is capable of dissociating CO_2 in the first oxidation step, while metallic nickel does not interact with CO_2. Similarly, in [150] Hu et al. show that the addition of Ni, Co and Cu as promoters of an iron-based oxygen carrier increases methane conversion in the process. Enhanced performance, such as 60% CH_4 conversion and 100% selectivity in multiple tests at 800 °C, have been observed by Li et al. for methane CLR with CO_2 splitting due to NiO addition to a CeO_2-MgO mixed metal oxide [151]. One drawback of mixed metal oxides is the difficult control of reaction selectivity to ensure syngas production [152]. In this sense, several alternatives can be identified. Metallic Fe shows catalytic activity towards high temperature water gas shift [153] and could be usefully integrated in a chemical looping reverse water gas shift process [154]. Copper-based oxygen carriers present catalytic activity in metallic form towards the reforming reaction, though a limited number of literature works have considered their utilization [137]. Both iron and copper oxides also present show better resistance to sulphur poisoning compared to nickel base OCs. La-Fe and La-Mn perovskites have demonstrated suitable characteristics for CLR applications [155,156]. In [157], Yin et al. test $LaMn_{1-x}B_xO_3$ (B = Co, Ni, Fe) perovskites as oxygen carriers in fixed bed configuration for chemical looping steam reforming. The addition of Co, Ni and Fe increases the oxygen release rate in the following order: Ni > Co > Fe. Fe 0.3 and Co 0.2 have provided the lowest carbon deposition, the highest syngas/hydrogen yield, and the highest oxygen release rate. Similarly, in [158] Valderrama et al. have demonstrated enhanced carbon deposition resistance by doping Ni into the B sites of a $LaCoO_3$ perovskite.

Combination of reforming catalyst with high temperature solid sorbents has been recently considered as a promising way to optimize H_2 production by removing CO_2 from the gas products and shifting the equilibrium. Calcium based sorbents are the most studied for several reasons: the carbonation reaction is exothermic, the reaction rate is moderately fast at 600 - 700 °C, the carbon deposition is minimized and the sorbent can be produced from a

variety of low-cost materials [158]. For instance, in [159] Fernandez et al. discuss a system of interconnected fluidized beds, illustrated in Figure 1.7, for a sorption enhanced chemical looping reforming process. The system is composed of the following sections: (1) a CLC section where Fe_2O_3 particles from the air reactor and $CaCO_3$ particles from the steam reforming section go through a fuel reactor and get reduced to Fe_3O_4 and CaO by interaction with the tail gases from PSA; (2) a reforming section where CaO and Ni (catalyst) particles are first separated from the iron oxides particles by density difference in a segregator and then perform steam methane reforming in a separate reformer; (3) an oxidation section with air to regenerate the separated iron oxide particles. A H_2 production efficiency of 88.4% with a CO_2 capture ratio of 98% have been obtained after sensitivity analyses on the main parameters. Li_2ZrO_3 sorbents are also promising candidates for capture at high CO_2 concentrations, as shown in [160] by Gao et al. for the CLR of glycerol.

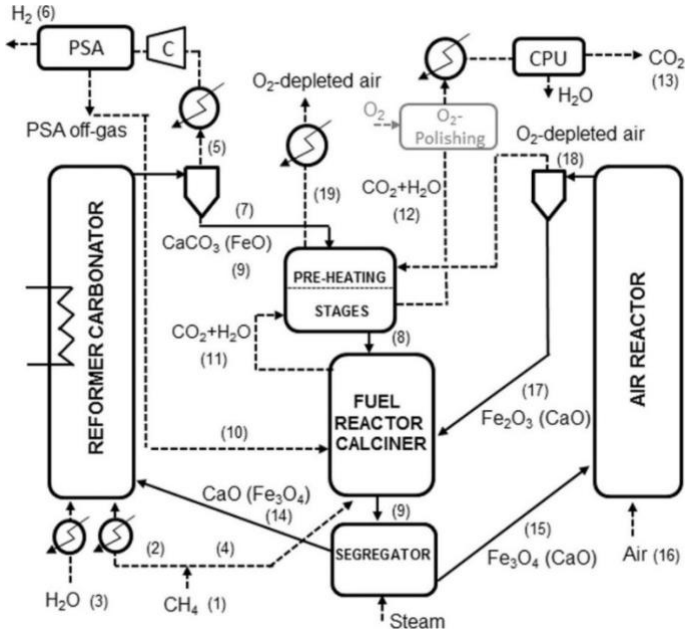

Figure 1.7. Process scheme combining sorption enhanced CLR with sorbent regeneration. Reproduced from [156].

1.5.3 Reactor configurations for CLR

As for CLC, in CLR the optimal reactor configuration is closely related to the material kinetics, conversion and mass/heat transfer rates. High-pressure operation facilitates the downstream processing of syngas to liquid fuels [161] as well as H_2 transportation and storage, which require very high pressures (500 bar and 900 bar, respectively) [162]. As for CLC, high pressures promote carbon accumulation on the catalyst surface. For CLR applications packed bed reactors, fluidized bed reactors and moving bed reactors have been considered [129]. As for CLC, high pressures promote carbon accumulation on the catalyst surface leading to its early deactivation. For CLR applications packed bed reactors, fluidized bed reactors and moving bed reactors have been considered [129]. Moving bed reactors have

been demonstrated for the chemical looping hydrogen production process at Ohio State University. The process involves reduction by syngas from coal gasification is used to reduce the fuel to Fe and FeO, then steam and air are used to oxidize it back. Pressurized operation has been demonstrated by Hsie et al. [163] in a 250 kWth unit at 10 bar reaching the thermodynamic limit. Specific reactor configurations are encountered in solar-driven chemical reforming to address conductive and radiative heat transfer across the material. Examples are represented by porous foams, textured plates, vertical pins, powder mixed with inerts (Al_2O_3) etc [164]. However, few works consider high-pressure operation in CLR and mainly involve packed and fluidized bed reactors, with gas switching reactors representing a promising pathway [165]. In [166] Zacharias et al. demonstrate hydrogen production up to 95 bar in a CLHP cycle with Fe_2O_3/Al_2O_3 oxygen carriers in packed bed configuration. The process involves reforming and reduction at atmospheric pressure to maximize conversion, and H_2 production by water splitting at high pressure. The pressurization is achieved by closing the outlet valve after the cooling section in the steam oxidation step while pressurizing the water injected into the system. In [167] Argyris et al. conduct high pressure CLR tests (oxidation, reduction, and dry reforming) in a packed bed reactor with $NiO/CaAl_2O_4$ (Figure 1.8-(a)). Fully continuous and stable operation has been demonstrated, with very high CH_4 conversion (> 99 %). Similarly, in [154] De Leeuwe et al. study an iron-based packed bed reactor for CL dry reforming and chemical looping reverse water gas shift (CLRWGS). Dry reforming achieves a total of 62.8% methane conversion, while by feeding H_2/CO_2 molar ratio of 2, a syngas with H_2:CO molar ratio of 2 is obtained in the CLRWGS. Coupling of membrane separation with fluidized bed CLR has also been proposed for high purity H_2 separation and experimentally demonstrated for the first time in [168,169] by Gallucci et al. A schematic of this configuration representation is reported in Figure 1.8-(b). The reactor has been operated over 100 hours test at lab-scale conditions by Medrano et al. [170]. Ultrapure H_2 has been separated through Pd membranes in the fuel reactor with a methane conversion higher than 90% at 600 °C and a Ni-based oxygen carrier.

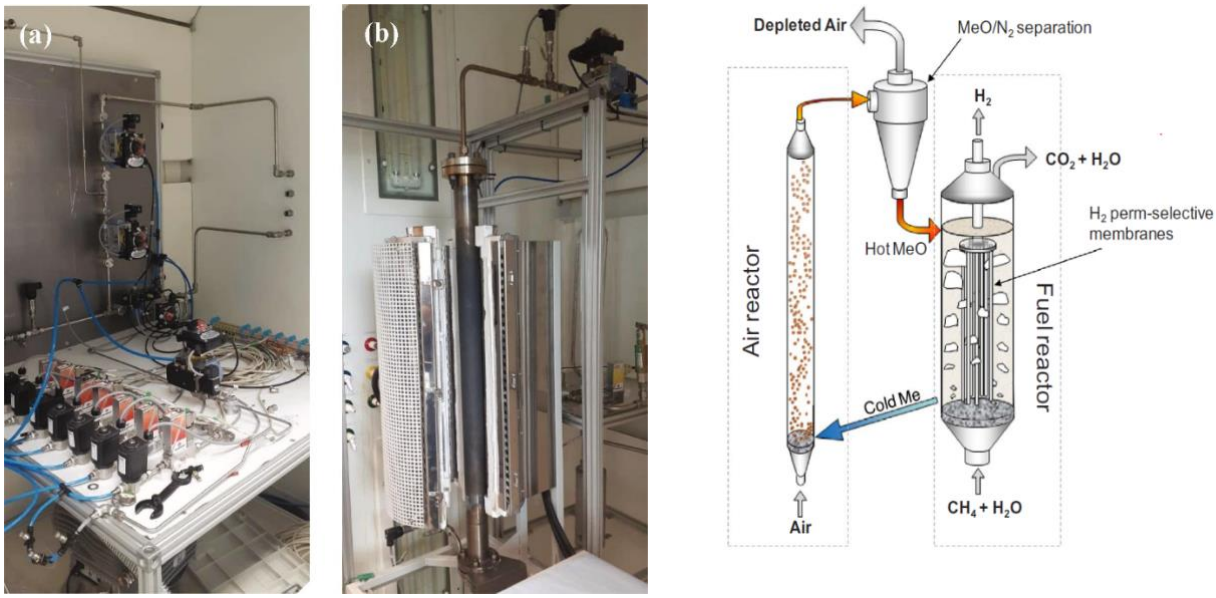

(a) (b)

Figure 1.8. Packed bed reactor for CLR (a), reproduced from [167]; membrane-assisted fluidized bed CLR (b), reproduced from [170].

1.6 Chemical looping gasification (CLG)

The main advantages of CLG over conventional gasification technologies are represented by: the production of high quality syngas without N_2 dilution, the internal heat supply for the reaction from the oxidation step, the inhibition of N_2 based contaminants, the absence of an air separation unit for concentrated O_2 supply. Moreover, a lower tar release from CLG has been observed in several works compared to other gasification technology [171]. A schematic representation of the process is provided in Figure 1.9. The process involves the following steps: in the fuel reactor, biomass or solid waste undergoes pyrolysis with the production of a gaseous fuel, liquid (tar) and solid (char). Subsequently, by both gas-solid reactions with the gasifying agent (steam or CO_2) and solid-solid reactions with the oxygen carrier additional gaseous fuel is produced. The reduced oxygen carrier is then sent to the air reactor, where it is regenerated to the initial phase by an exothermic reaction. The CLG process resembles CLC, therefore materials already developed for CLC have been considered for this scope. However, the development of this technology is at a much lower scale than CLC, with demonstrated continuous operating units in the thermal power range of 1.5 to 25 kW_{th} [172,173]. Chemical looping has also been proposed for converting the tar content of the syngas from gasification [174]. The process, called chemical looping tar reforming (CLTR), involves a catalytic bed mixed with the oxygen carrier for steam reforming, cracking, and partial oxidation by reaction with the lattice oxygen with the tars. Deposits of coke and sulphides are burnt in the air reactor where the oxygen carrier is also regenerated. Currently, this process is in an early stage of development and competitivity with conventional tar removal technologies needs to be assessed.

1.6.1 Oxygen carriers and biomass types for CLG

Iron based oxygen carriers represent the most promising solution for their competitive prices and environmental compatibility. They can be found in different forms: synthetic with ceramic support such as Fe_2O_3/Al_2O_3, naturally occurring such as ilmenite and waste materials such as steel slag and red mud. Bimetallic OCs based on Fe, Ni, Ba, Cu have also been analysed [175]. The addition of a sorbent material, such as CaO, has been considered also in biomass CLG to reduce the CO_2 concentration and upgrade the resulting syngas [176]. Different kinds of biomass that have been investigated for CLG include rice husk [177], crop straw [178], pine wood [171], lignite [175,179], polyethylene [180], high wet sludge [181], coal [182] etc.

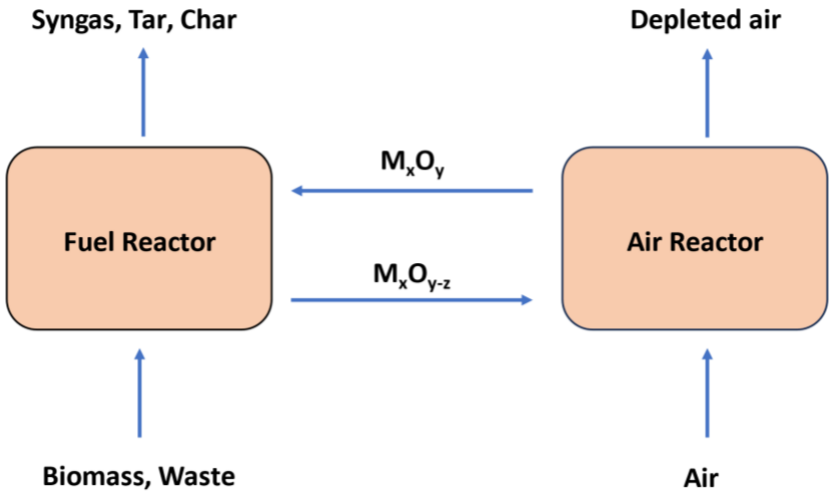

Figure 1.9. Schematic representation of the CLG of biomass [183]

1.7 Power production with CLC

CLC has been extensively studied for power production because it allows to obtain combustion off-gases composed of CO_2 and water. The high enthalpic content of these gases can be recovered by heat exchangers networks to produce thermal energy and in case of high-pressure operation they can be expanded for power production. For instance, CLC-based power production is integrated in [184] with a supercritical CO_2 cycle and with an Organic Rankine Cycle for low grade heat recovery. The process flowsheet of the plant is provided in Figure 1.10 and can be synthetically described as follows: the off-gases from the FR are sent to a cyclone for gas-solid separation and then to oxyfuel combustion with O_2 to complete the combustion of the remaining fuel gases. The outlet gases cross a first heat recovery unit supplying heat for successive reheating, superheating and economization of the supercritical CO_2. Subsequently, ashes are separated in an electrostatic precipitator and the gases are sent to exchange heat with the organic liquids in the bottoming ORC. The resulting low temperature gases are finally sent to a flue gas desulphurization unit for

sulphur removal and to an intercooled compression train with water removal for CO_2 storage. Similarly, the off-gases from the air reactor are first sent to a cyclone for gas-solid separation, then to heat exchange for reheating and economization of the supercritical CO_2, and to preheat the incoming air flow. Finally, after ashes separation in an electrostatic precipitator, they are sent to stack. However, in CLC plants the downstream power production block does not significantly affect the final investment cost, as shown in [185] by Tesio et al. where coupling of CLC with a supercritical CO_2 cycle can be more economically advantageous compared to a high temperature Organic or Steam Rankine cycle, though the former can present a capital cost up to three times more than the latter.

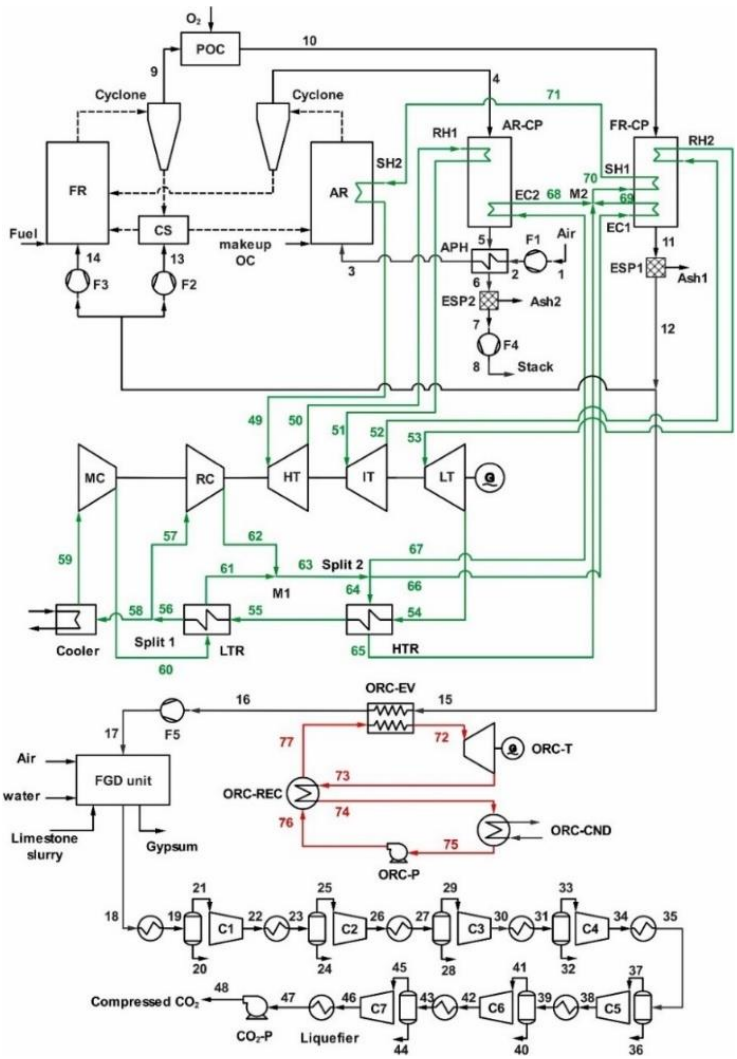

Figure 1.10. Process scheme of CLC integrated with supercities CO_2 cycle and Organic Rankine Cycle. Reproduced from [181].

1.7.1 Comparison with benchmark technologies

Compared to natural gas combined cycles (NGCC) and coal-fired power plants (CFPP) retrofitted with carbon capture and storage systems (CCS) or affected by carbon taxes,

plants that adopt CLC for power generation can obtain: (1) a lower levelized cost of electricity (LCOE), (2) a comparable or higher efficiency, (3) lower specific investment and energy costs, (4) acceptable CO_2 capture costs [131,186–188]. In [186] Zhao et al. propose and optimize a 600 MW coal-based CLC plant by pinch and exergy analysis methods. A final LCOE of 104 $/MWh is computed, which is lower than the 143 $/MWh of the CFPP plant retrofitted with MEA absorption. Sensitivity analyses demonstrate that with a 30% variation of the cost voices the CLC configuration remains economically competitive with respect to the benchmark plant. Similarly, in [187] a 300 MW_{th} CLC plant burning bituminous coal and producing electricity in a subcritical Rankine cycle provides a LCOE of 98.02 $/MWh and when more reactive fuels or a more efficient carbon stripper are employed, a slightly lower LCOE is computed compared with a CFPP with post-combustion CO_2 capture. In [189], glio et al. explore a 0.5 MW power plant configuration envisaging four adiabatic gas switching reactors for constant hot gas stream production integrated with a stationary power production section. The system achieves global energy efficiency of 51% and LCOE of 54 €/MW, which is more competitive than NGCC retrofitted with MEA solvents. The major contribution to the plant cost is for the high-temperature valves, whose lifetime can heavily affect the resulting LCOE. In [190], Mancuso et al. compare the economic performance of a packed bed CLC with an IGCC power block with other benchmarks. The proposed plant presents a LCOE and a cost of CO_2 avoided (CAC) of 104.2 €/MWh and 34 €/ton_{CO2} against 110.1 €/MWh and 47 €/ton_{CO2} of a conventional IGCC with pre-combustion capture. By including 140 €/ton_{CO2} tax the PB-CLC plant becomes much more competitive than both unabated IGCC and CFPP benchmarks. On the contrary, without CCS costs or the introduction of carbon taxes, the CLC plant thermal efficiency is lower and the LCOE higher than the benchmark technologies. For instance, in [191] a 550 MW_e CLC power plant fed by Victorian brown coal is compared with a CFPP plant without carbon capture and both lower thermal efficiency (32.1% vs 37.8%) and higher LCOE (145 $/MWh vs 105 $/MWh) are obtained for the CLC plant. Coupling with advanced steam cycles has also been considered by Saqline et al. in [192] and energy penalties of 5.1%, 5.0%, 5.2% and 13% have been computed for iG-CLC plants equipped with subcritical, supercritical, ultra supercritical and advanced ultra supercritical steam cycles, respectively, with respect to integrated gasification combined cycles.

The major drawback hindering CLC plants competitivity is the limit in the operating temperatures (800 - 1000 °C), that are significantly lower than traditional gas turbines inlet temperatures (around 1400 – 1600 °C). This temperature difference causes an energy penalty of about 13% compared to state-of-the-art NGCC when the air reactor outlet temperature is fixed at 1000 °C for the CLC plant [131]. In [193] Iloeje et al. design a rotary CLC plant integrated with a recuperative Brayton cycle by multiscale modelling approach.

Optimization of the thermodynamic efficiency and of the LCOE is carried out. Maximum efficiencies in the 54-56% range are reached with a 3-7 pressure ratio, while economic optimization can lead to 11% cost reduction compared to the efficiency optimization. However, due to the technology limited maturity and higher capital cost, an unabated recuperative Brayton benchmark presents about 27% lower LCOE. Over the years, technical measures have been designed to compensate for this limitation. In [131] Khan et al. study the insertion of a natural gas afterburner downstream of the CLC with an ICR reactor to increase the off-gases temperature and reach competitivity with traditional NGCCs in terms of LCOE and CO_2 avoidance cost (CAC, which indicates the CO_2 tax that would equalize the specific product cost of a plant without CCS systems with that of a plant with CCS systems). As illustrated in Figure 1.11, without an afterburner the CLC configuration provides a LCOE of about 100 €/MWh while the benchmark with and without CCS systems of 90.5 €/MWh and 62 €/MWh, respectively. This clearly shows the detrimental effect of low gas temperature at the reactors' outlet when a CLC plant is integrated in a combined cycle power plant. On the contrary, when a NG-fuelled afterburner is added downstream a LCOE and CAC of 73 €/MWh and 57 €/t_{CO2} are obtained, respectively, against 91 €/MWh and 88.5 €/t_{CO2} of the NGCC with post-combustion CO_2 capture (NGCC-PCC in Figure 1.11). The addition of a NG afterburner reduces the captured CO_2 to only the 52.4% and therefore a case with a H_2-based afterburner is also considered, providing a LCOE and CAC of 93.15 €/MWh and 90.84 €/t_{CO2} due to the high costs of green H_2. With a steam diluted H_2 combustor the LCOE and the CAC reduce slightly. Similarly, in [135] Arnaiz del Pozo et al. integrate a system of six gas switching reactors (1 for reduction and 5 for oxidation) in an IGCC configuration with a Shell gasifier: by introducing a post-combustion section downstream of the oxidation section and a heat exchanger for air preheating by the reduction off-gases, the efficiency can reach that of an unabated IGCC plant. Possible strategies to overcome the benchmark are represented by post-combustion gas cleanup and latent heat recovery from the CO_2 rich stream. H_2-post combustion firing is also discussed to compensate for the limited CO_2 avoidance in a high CO_2 prices futurescenario.

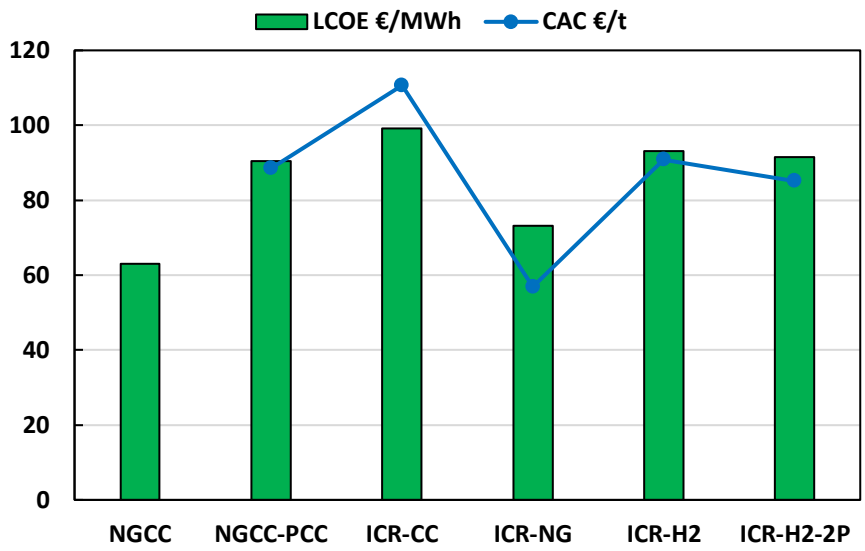

Figure 1.11. LCOE and CAC of: NGCC, NGCC-PCC, CLC of coal with ICR (ICR-CC), CLC and natural gas-powered-post-combustion (ICR-NG), CLC and hydrogen-powered post-combustion (ICR-H_2) and CLC and hydrogen-powered post-combustion with advanced heat integration.

On the contrary, CLOU-based power plants do not require any further technical modification because they already show comparable efficiency with NGCCs, even without CCS, and are more competitive than CCS-free solid fuelled benchmarks. For instance, in [194] Cormos et al. consider a CLOU plant with a copper-based oxygen carrier with a net power output of 100 MW with various fuels (natural gas, coal and lignite). They compute an LCOE between 85 €/MWh and 92 €/MWh and a carbon capture cost between 24 and 27 €/t_{CO_2}, which are lower than 90-110 €/MWh and 35-60 €/t_{CO_2} of the benchmark configurations retrieved from the literature (NGCC and super-critical power plants with and without CCS, oxyfuel combustion with CCS). In addition, an almost total carbon capture ratio of > 99% is computed. The optimal coupling of pressurized CLC plants with the downstream combined cycle block is of paramount importance to achieve competitivity with NGCC plants. In [195] Bartocci et al. review pressurized chemical looping layouts and reactor configurations for the efficient power production in combined cycle configurations. The coupling of pressurized chemical looping combustors with turboexpanders has not been yet demonstrated on a pilot scale, differently from CLC with steam cycles [195]. The importance of combining 0D models from TGA tests and CFD results is outlined for describing the behaviour of pressurized CL reactors in the absence of experimental data from pilot plants. Then guidelines for the optimal design of pressurized fluidised bed combustors coupled with turboexpanders are defined, starting from the design of turbine specifications in terms of capacity, inlet temperature and compression ratio, then moving to the CLC plant design

based on the identification of air mass flow, optimal quantity of fuel, oxygen carrier circulation rate and inventory.

1.7.2 Economic impact of waste materials

The recovery of waste materials for CLC allows in some cases to obtain a reduction in procurement costs with acceptable reaction performance [196]. In [197] the use of oxidized printed circuit boards (OPCB) in a CLC plant reduces the specific costs from 4374.60 €/kW with Fe_2O_3 to 3428.79 €/kW using OPCB, while the LCOE drops from 89.52 €/MWh to 81.03 €/MWh. However, despite being very influential for the thermodynamic performance of the plant, various economic analyses suggest that the oxygen carrier is not among the major parameters affecting the economics of a CLC plant [191,198,199]. Therefore, one of the most promising strategies to improve the economic competitivity of CLC is to study new types of OC with higher reactivity and lower oxygen demand. It is however to note that the OCs present other expenses that are not often considered, such as the storage cost and the power required to keep them in the desired fluidization conditions. For example, in [200] Zhu et al. compare ilmenite and a synthetic NiO-based oxygen carrier for the CLC of biogas, showing that the natural mineral presents a higher LCOE due to the higher energy expenditures required to achieve and maintain fluidization and the significant storage costs. A summary of the techno-economic analysis on fuel production from chemical looping is provided in Table 1.5. It can be observed that the CLC configurations are always competitive compared to benchmark plants retrofitted with carbon capture systems, irrespectively of the employed power block, while when the CCS system is not present economical competitivity is lost.

Table 1.5. Comparison of the LCOE for NGCC and CFPP from different references compared to CLC

Configuration	$LCOE_{CL} - LCOE_{trad}$	Reference
NGCC with CCS	-16,04 €/MWh	[131]
	-14,15 €/MWh	[188]
CFPP with CCS	-36,79 €/MWh	[186]
	-4,72 €/MWh	[187]
CFPP w/out CCS	+38,68 €/MWh	[191]

1.7.3 Chemical looping energy storage

Future electricity grid will be characterized by high shares of renewable-based supply and therefore, due to the intermittency of the sources, suitable energy storage solutions will be necessary to always ensure secure and reliable carbon-free-electricity supply. The ideal energy storage system should possess high energy densities and storage capacities (kW to

MW), long storage duration (hours to months), low capital cost (fornire esempio di costo) and impact on the environment. Currently, the most mature technologies are the pumped hydro and compressed air energy storage, which are affected by dependency on the geographical location, and the electrochemical batteries, which suffer from performance decay over time. High temperature chemical looping processes can overcome these drawbacks by providing carbon free electricity with long (ideally unlimited) transport and storage durations, high energy storage densities up to 15 and 6 times greater than the sensible and latent heat storage, respectively, high storage capacity and operation flexibility due to the large number of reversible reactions available, and limited storage costs when cheap materials are used. Few works present a system level analysis of chemical looping combustion as an energy storage system. In [201], Astolfi et al. perform a techno-economic analysis to evaluate the feasibility and the cost performance of a system involving the reactor system developed by Abanades et al. in [122]. Iron and nickel-based reactor systems are integrated with three blocks for power production: recuperative gas turbine, steam injected gas turbine, and combined cycle power plant. Constant power supply for 4 h is demonstrated with a multireactor configuration and the final LCOE associated with the processes amounts to around 125-200 €/MWh when biogas is used as a reducing agent. Negative CO_2 emissions can also be achieved when the CO_2 from biogas oxidation is stored, while the use of H_2 as a reducing agent increases the LCOE due to the high investment cost of the PEM electrolyzer. A similar configuration with a packed bed CL reactor replacing the combustion chamber of both conventional and recuperative Brayton cycles is introduced by Saghafifar et al. in [202]. The results indicate that the optimal material should possess a reaction enthalpy variation in the 170-200 MJ/kmol range and, among the typical oxygen carriers for CLC, the MnO_2/Mn_2O_3 couple are identified as the optimal candidates, because of the moderate reduction temperatures (< 900 °C) in a wide range of oxygen partial pressures. In [203], Cormos et al. present a conventional natural gas fuelled CLC power plant (250 MW) in two operation modes: baseload and time flexible. To achieve time flexibility part both reduced and oxidized iron oxides are stored in high temperature storage facilities. Benefits in terms of reduced CAPEX (3%), OPEX (2%), LCOE (2%) and CO_2 avoided cost (8%) are observed. However, the necessity of demonstrating CLC and high temperature solid storage at higher industrial capacities, i.e. hundreds of MW, is pointed out. On the industrial side, the RedoxBlox company is currently working on the development of thermochemical cycles based on Mn-Mg oxides for energy storage applications, as schematically shown in Figure 1.12-(a). In 2023, the 100 kWh_{th} energy storage module shown in Figure 1.12-(b) has been demonstrated under realistic operating conditions for more than 1000 h.

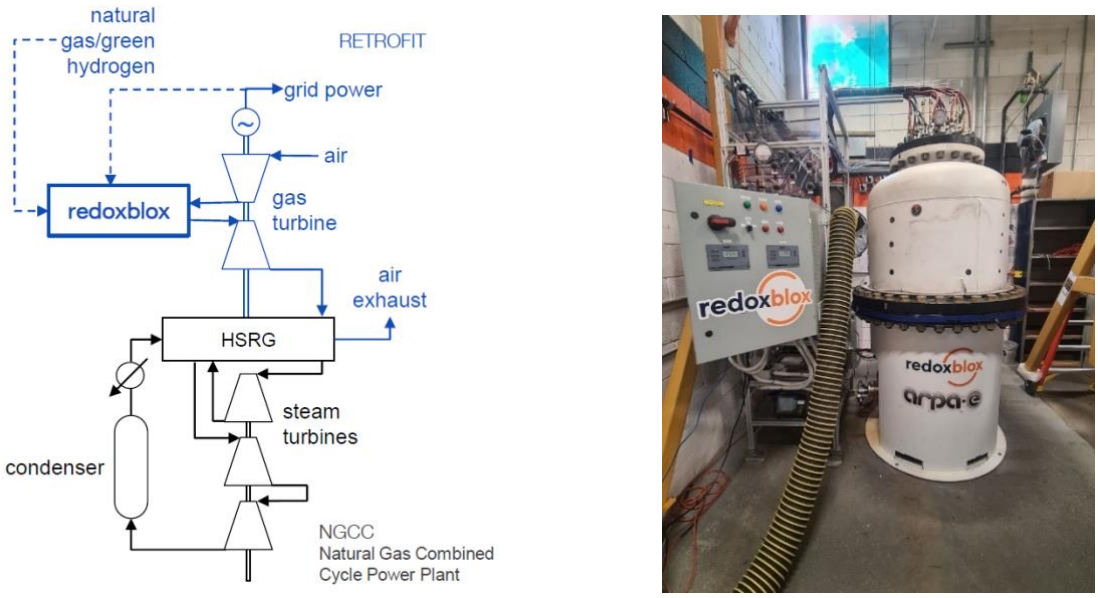

(a) (b)

Figure 1.12. Schematic representation of the RedoxBlox technology integration for energy storage (a), reproduced from [143]; prototype of the 100 kWhth thermochemical energy storage module by RedoxBlox, reproduced from [144].

1.8 Chemicals/fuel production with CLR

CLR presents a higher net reforming efficiency and lower hydrogen production costs compared to benchmark technologies with carbon capture systems [204], and this improvement is more evident in large-scale plants (10^5 Nm^3/h) than in very large-scale plants ($3.33 \cdot 10^5$ Nm^3/h) [204]. H_2 production from gas switching CLR reactors is investigated by Nazir et al. in [205] and in the optimal case (higher thermal mass in the GSR by insertion of steel rods, two phase evaporator exchanging with the reduction gases, and air preheating by the oxidation gases) 4.5% lower levelized cost of H_2 (1.83 $\$/kgH_2$) is achieved with respect to conventional SMR with a CO_2 tax of 15 $\$/t_{CO2}$. The authors underline the crucial role of the oxygen carrier lifetime for the economical competitivity and the need of long-term testing on the most promising materials at real plant conditions. Similarly, Khan and Shamin [206] perform a techno-economic analysis of a CLHP plant integrated with a double heat recovery steam generation and a gas turbine section expanding the N_2 stream from the air reactor. They report a levelized cost of H_2 from the CLHP plant of 1.679 €/kg which is much smaller than SMR with CO_2 capture. The integration of membranes in both gas switching and fluidized bed chemical looping reactors has been considered by Wassie et al. [207] and Spallina et al. [208], respectively. The presence of a H_2-selective membrane enables a higher H_2 production efficiency by 12-20% and lower specific product cost (0.274 €/Nm^3 and 0.19 €/Nm^3, respectively) compared to conventional SMR with CO_2 capture (around 0.28 €/Nm^3), though the process remains less competitive than the benchmark without CO_2 capture. Future decrease of the

cost/permeability ratio of membranes is expected to make the technology competitive. The application of CLR for liquid fuels production has been widely analysed in the literature by techno-economic analyses. In [209] Spallina et al. show that CH_3OH synthesis from natural gas CLR plant provides 17-20% lower production cost than the conventional process (without CO_2 capture), though the CH_3OH production efficiency is reduced by 4%. The plant, represented in the process flowsheet of Figure 1.13, is composed of the following sections: (1) a chemical looping reforming unit where the oxygen carrier is firstly oxidized by air, then is reduced by the incondensable gases from the CH_3OH purification section, and finally acts as a catalyst for steam methane reforming; (2) a power production section from N_2 expansion in an open cycle gas turbine and from recovered steam expansion in a Rankine cycle; (3) the methanol synthesis unit with downstream purification by a distillation column train; (4) a CO_2 compression and storage section. In [210], Xiang et al. propose a novel propylene production process where CLC is used for burning the tail gases from PSA separation of H_2 resulting from propane dehydrogenation and then the CO_2 content is sent to methanol production with H_2 and stored. In [211] Yang et al. combine CLHP with CH_3OH synthesis from coal and coke oven gases obtaining a reduction in the investment and production costs by 23.3% and 7.5%, respectively, compared to the conventional process, while the specific greenhouse emissions decrease from 2.86 to 0.78 $kg_{CO2equiv}/kg_{CH3OH}$. In [144] Pereira et al. propose a three-step CLR cycle, similar to the process in Figure 1.13, where the oxygen carrier is oxidized by air with high purity N_2 production, is reduced by the tail gases coming from PSA and finally catalyses methane reforming for syngas production. A water gas shift section is also added to enhance the H_2 content in the syngas. The H_2 and N_2 streams coming from the reforming and the air oxidation steps, respectively, are reacted in a conventional Haber-Bosch plant for ammonia synthesis. The process provides 19% lower capital costs and lower production cost compared to the conventional configuration and a negative CO_2 emissions avoidance cost of -5 $\$/t_{CO2}$. The process is more energy efficient than the benchmark but is characterized by higher capital costs. In [212], Edrisi et al. study urea production from chemical looping processes. An internal rate of return between 11% and 60% is computed for the plant according to the considered scenario, making it an interesting and economically valuable solution for further research.

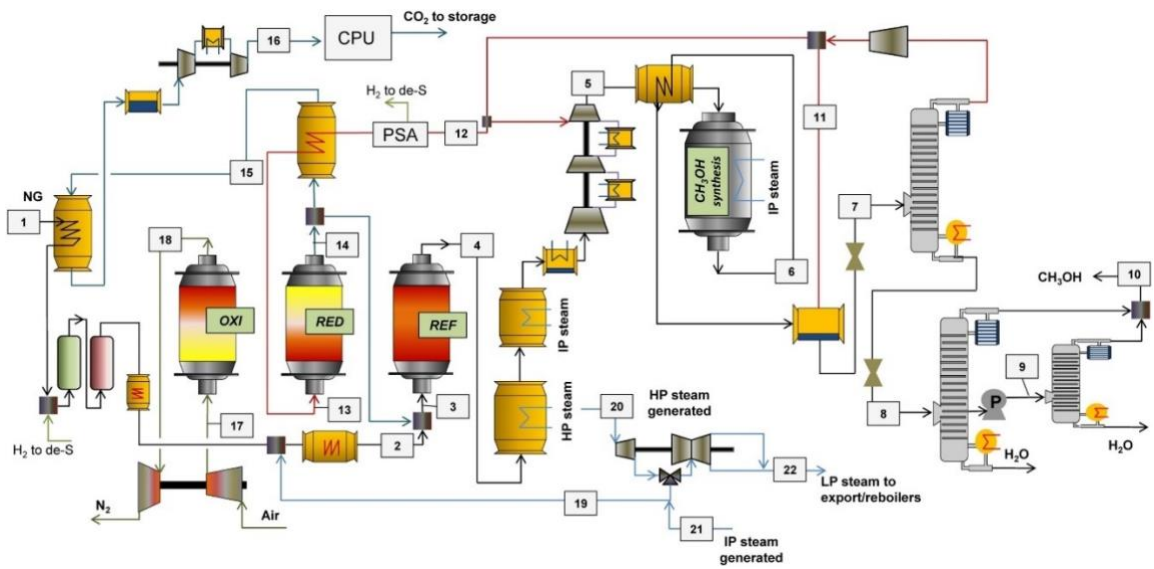

Figure 1.13. Process flowsheet of the NG-based CLR plant for CH3OH production, reproduced from [194].

To maximize the benefits of CLR and reach competitivity with traditional technologies, various alternative process designs have been proposed in the literature. An interesting configuration envisages CLR with heat supply from CLC, as a boiler for the reforming processes. This configuration allows to generate the necessary heat for the process with a very high carbon capture rate and to reuse the CO_2 itself in the reforming section, thus ensuring not only CO_2 removal but also its effective use [213]. In [214] Labbaf et al. present a methanol plant that uses CLC for heat supply with CO_2 conversion of 87% in natural gas reforming and specific emissions of 0.1 t_{CO2}/t_{Me}, which are significantly lower than those for conventional coal to methanol (1.67 t_{CO2}/t_{Me}) and natural gas to methanol (0.25 t_{CO2}/t_{Me}) pathways. However, the actual profitability of this process depends heavily on the demand for methanol, i.e. on its possible price increase, and on the cost of natural gas. CLC plants can also be coupled to other technologies for syngas or hydrogen production that are not CLR or CLHP. In [215] Ning Asih et al. study three configurations by changing the hydrogen production unit: first an SMR, then biomass gasification and finally photovoltaic electrolysis using a solid oxide electrolysis cell (PV-SOEC). The results show that currently the most convenient process is the CLC-SMR, since it obtains a levelized cost of methanol of 409.41 €/t, though the most promising technology is the PV-SOEC because it will become more economically competitive in the future by the reduction of equipment cost and because it is characterized by the lowest overall CO_2 emissions (0.013 kg_{CO2}/MJ_{MeOH}).

Alongside CLR, a promising technology to produce hydrogen and syngas from solid fuels is CLG, although it is still in the experimental state at small to medium scales [172,173]. As reported by Zhou et al. [216], in the production of synthetic natural gas (SNG) from coal, CLG presents several advantages over coal conventional gasification (with CCS) such as: reduced energy consumption for CO_2 capture by 25%, lower specific CO_2 emissions (by

15%), higher exergetic efficiency (by 21%), decreased cost per cubic meter of SNG (by 29%). Similarly, in [217] Li et al. compare butanol production costs from different biomass gasification technologies, confirming that CLG is among the most competitive ones. This comparison is collected in Table 1.6. In addition, a sensitivity analysis carried out by Zhou et al. on the final cost of ethanol from CLG of corn straw demonstrates that the main factor affecting the specific cost of the product is the feedstock cost [218].

Table 1.6. Comparison of levelized cost of butanol for different technologies

Process	Biomass	Specific cost of butanol
Fluidized bed gasification	Pine wood	0.87 €/kg
Fluidized bed gasification	Microalgae	2.05 €/kg
Biomass fermentation	Lignocellulosic biomass	1.47 €/kg
Acetone-Butanol-Ethanol fermentation	Switch grass	1.72 €/kg
Chemical looping gasification	Lignocellulosic biomass	1.30 €/kg

1.8.1 Economics of combined power and fuels production

An interesting feature of chemical looping is also the possibility of combined power and fuel production. Hydrogen production from CLR is generally performed in combination with WGS and PSA sections for H_2 purification. In [219] Nazir et al. investigate a pressurized CLR unit with nickel-based OC for hydrogen production and subsequent combustion in a combined cycle power block. Sensitivity analyses assess the impact of the air flow rate, the oxidation reactor outlet temperature, and the steam flow rate to the reducer on the LCOE, the electrical efficiency, the CH_4 conversion, and the CO_2 avoidance. Electrical efficiency in the 40-43.4% range is calculated and is lower than that of combined cycles with auto-thermal reforming and post-combustion capture. High sensitivity on the fuel price cost is detected for the LCOE. Similar results are shown by Nazir et al. for a gas switching reactor configuration performing CLR in [205]. Compared to standalone base hydrogen and power production, such as NGCC and SMR retrofitted with amine-based capture, both CLHP and CLC-SMR achieve savings in input energy (above 16%) and a clear reduction in CO_2 emissions (above 99%) [199]. CLHP guarantees an efficiency of 3.04% higher than CLC-SMR, greater environmental compatibility as it generates a lower global warming impact and lower hydrogen specific cost (31.01 €/MWh), though the hydrogen specific cost is very sensitive to the natural gas price and the electricity cost [199]. Moreover, Cormos et al. report that compared to combined power and hydrogen production from steam reforming of glycerol with MDEA scrubbing and heat recovery steam generation, CLHP achieves higher decarbonization rates (more than 93% vs 71%) and higher net power efficiencies (between 72.4% and 76% vs 68.5% without the capture). The major exergy losses for a case with CLHP-based power and ammonia production have been identified in the fuel reactor, amounting

to 28% of the total losses [120]. In comparison with other novel reforming technologies with carbon separation abilities such as calcium looping cycles, CLHP is characterized by higher carbon capture values (99% vs 95%), higher energy efficiencies (2.3% higher vs 2.5% lower than the benchmark with amine absorption), but also higher hydrogen production costs (37.14 €/MWh vs 42 €/MWh) when biogas is reformed [220]. In terms of power production, compared to a traditional coal fired power plants CLHP-based systems achieve a higher carbon capture efficiency but lower electric efficiency, while by including the energy output from hydrogen production the overall efficiency turns higher [221,222].

The versatility of the gas species produced by chemical looping processes enable the simultaneous production of power and two fuels, such as methanol and hydrogen [223], ammonia and hydrogen [224], propylene and methanol [225], light olefins and methanol [226]. For instance, in [15] Palone et al. propose and analyse a configuration for the simultaneous production of power, methanol and ammonia from CLHP. This system is basically composed of four sections: a CLHP plant fed by waste plastic; a heat recovery steam generator with turbine groups; a methanol synthesis unit fed by CO_2 and H_2 from the CLHP; an ammonia synthesis unit fed by N_2 from CLHP and H_2 from electrolysis. Levelized cost of the products are comparable with other sustainable technologies but not with benchmark plants for methanol and ammonia synthesis due to the presence of the electrolyser. Despite the high costs, the use of CLHP greatly simplifies the system, as air separation, water gas shift and CO_2 capture units are no longer required.

1.8.2 Nitrogen chemical looping for ammonia production

Ammonia is a potential renewable and carbon-free energy carrier due to its high energy density, its relatively easy liquefaction and transport and zero CO_2 emissions [85]–[88]. The most widely used process to produce of NH_3 is the Haber-Bosch (HB) process. However, this process requires very stringent operating conditions, in fact it is necessary to operate at a pressure of 100-200 bar, relatively high reaction temperature of about 400-500 °C and with high purity H_2 and N_2 as feedstock [227–229]. High pressure is the most critical aspect as compression to such high levels is very expensive and can affect up to 50% of the total cost of the system [230]. In addition, the HB process generates high amounts of CO_2 (about 1.9 t_{CO2}/t_{NH3}) using hydrogen from natural gas reforming and this value could increase considerably if hydrogen generated by coal gasification is used, reaching 6.1–7.8 t_{CO2}/t_{NH3} [231]. For these reasons, new methods are being sought to produce ammonia and one of the most promising processes is Nitrogen Chemical Looping, especially since its demonstration in [232]. The main difference between this process and other more established CL processes is the replacement of the oxygen carrier with a nitrogen carrier. Chemical looping ammonia production (CLAP) essentially consists of three separate steps:

- nitrogen carrier activation by formation of metal nitride or imide;
- ammonia production by reaction of the nitrogen carrier with water or hydrogen;
- regeneration of intermediaries and reuse in step one.

The nitrogen carriers used are mainly imides and metal nitrides based on aluminium and lithium [233]. Three technical routes have been identified for this scope: (1) ammonia production by the hydrolysis of metal nitrides [234]; (2) ammonia production with the hydrogenation of metal nitrides [235]; (3) ammonia production by the hydrogenation of alkaline earth metal imides [236]. The first process proceeds at low pressure, does not require catalyst and involves cheap feedstock, but the metal nitride regeneration occurs at high temperatures (above 1500 °C for the N_2 fixation step). On the contrary, the second process involves intermediate temperature conditions, but is affected by limited ammonia yield and costly feedstock (H_2). Finally, the third process involves low pressure and temperature conditions with low-cost reactants, configuring as a promising option for further development. Considering the recent proposal of this technology, research is currently undergoing to identify the optimal nitrogen carrier for the process and few systems level research work have been carried out. Wang et al. [237] have carried out process simulation and exergy analysis of the process illustrated in Figure 1.14, which is composed of the following sections: (1) air separation unit, where pure N_2 is separated from O_2 by cryogenic air separation; (2) two-steps CLAP system with the nitrogen fixation reactor and the hydrolysis reactor; (3) compression and purification unit for NH_3 separation from H_2, N_2, H_2O. The main exergy losses are identified in the heat exchangers, reactors, and pumps, with a final exergy efficiency of the system equal to 26%. If the high purity O_2 stream from the air separation unit and the syngas from N_2 fixation are instead considered as products, the exergy efficiency rises to 68%. Considering the high exergy losses and exergy cost computed, optimization of the heat exchangers network is expected to achieve a significant increase in the efficiency. In the systematic review by Lai et al. [233] future research efforts are outlined with respect to the current main limitations of the technology, which correspond to high reaction temperature, low lattice nitrogen reactivity, low selectivity towards ammonia and low stability of the N_2 carrier in long-term tests.

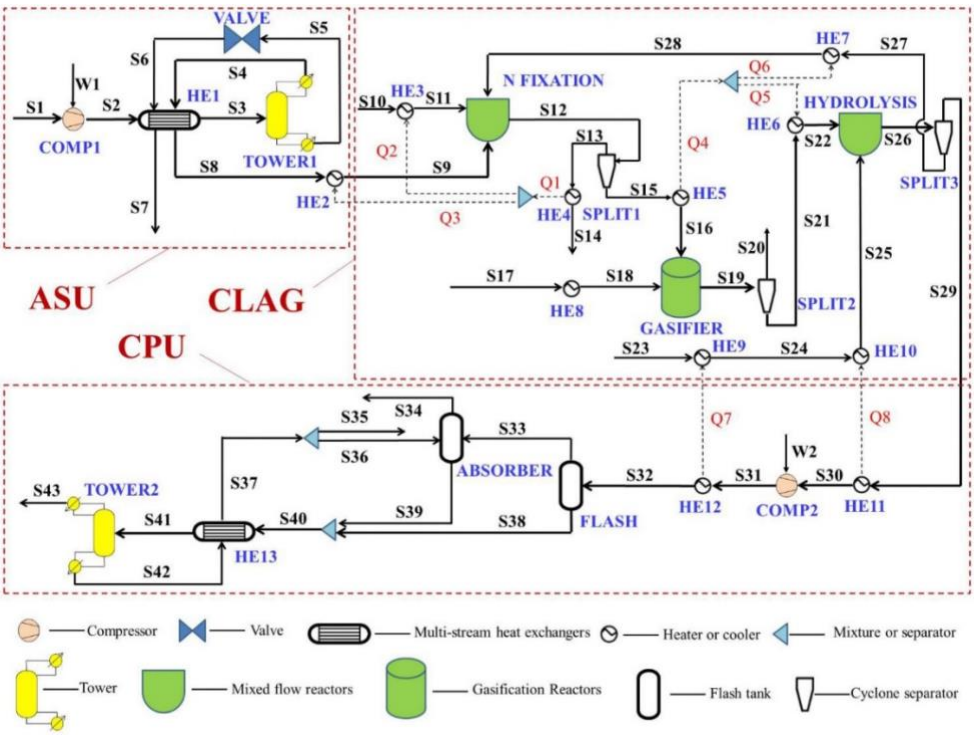

Figure 1.14. Process flowsheet of CLAP (CLAG) plant with the ASU and the CPU sections. Reproduced from [216].

1.9 Future perspectives

The presented recollection of the main scientific achievements on chemical looping processes paves the way for new research activities, such as:

1) Assessment of chemical looping reforming processes by experimental evaluations and process design activities, considering the promising performance of this technology compared to benchmark processes.
2) Assessment of the behaviour of new oxygen carriers based on natural ores or waste materials in different chemical looping applications, due to their low cost and limited environmental impact.
3) Increased operational time of chemical looping processes at industrially relevant operating conditions, especially high pressures and temperatures, to support the technology scale-up.

1.10 Thesis objective and outline

The main objective of this thesis is to analyse the potentials and drawbacks associated with the integration of chemical looping technology in a decarbonization scenario involving steel mills. This work is carried out by addressing the following challenges:

- **Potential of the latest technological solutions for achieving cleaner steel production**: Conventional steel production requires significant amounts of fossil

fuels (coal and natural gas) and electric energy. As a first step, currently available and more efficient technologies for steel production (direct reduction plant – electric arc furnace) are incorporated in a four-steps revamping methodology to define the long-term evolution of the sector towards a hydrogen-based steel production.

- **Pressurized syngas production with chemical looping technology from captured CO_2 and H_2O streams:** Current steel mills present several years of operation ahead and to address the climate targets immediate decarbonization strategies need to be put into place, such as plant retrofitting with downstream carbon capture and utilization technologies. The literature offers various process schemes for steel (or more generally industrial) decarbonization, though only few works consider chemical looping integration in this framework. Therefore, a preliminary feasibility study is carried out based on mass balances and computational fluid dynamic simulations on a chemical looping plant converting captured CO_2 and H_2O streams into a syngas with iron based oxygen carriers. Subsequently, experimental investigations on two aspects of chemical looping syngas production are carried out to support the technology scale up and its subsequent integration in the proposed process scheme: syngas production capability of chemical looping with an iron-based oxygen carrier; effect of high pressure operation on Fe/Ni oxygen carriers reactivity in chemical looping cycles. High pressure operation is in fact crucial for downstream processing of the thermochemical syngas to liquid fuels. The experimental campaigns allows to define the optimal syngas production from iron oxidation by CO_2 and H_2O and to assess the impact of high pressure conditions on the reduction of $NiFe/Al_2O_3$ oxygen carriers in terms of reactivity and long-term operation.
- **Industrial viability of chemical looping technology as a carbon capture and utilization pathway for liquid fuels production**: The final step is the conversion of the syngas from chemical looping to liquid fuels or chemicals. This aspect requires careful process design and optimization to reach the best economic performance and possibly competitivity with benchmark and/or alternative production technologies. Therefore, a techno-economic analysis is carried out on a process scheme that optimizes the thermochemical syngas utilization by combinedly producing methanol and ammonia.

This work begins with the assessment of a revamping methodology for a more efficient and cleaner steel production. In **Chapter 2**, starting from a conventional blast furnace-basic oxygen furnace process, the progressive introduction of direct reduction-electric arc furnace lines is analysed in terms of CO_2 emissions reduction and energy flows variation. After the complete retrofitting with the new and more efficient lines, the impact of H_2 blending with CH_4 is analysed. A final configuration with scrap iron reutilization and 100% H_2 is

considered. A milestone is thus put on future developments of steel production, encompassing H_2 utilization and a strong renewable power supply. However, to respond to the urgency of reducing CO_2 emissions from industrial activities, current plants require retrofitting with energy efficient carbon capture technologies. Therefore, **Chapter 3** considers the integration of a conventional steel mill with chemical looping syngas production for the reconversion of the CO_2 content of blast furnace gases. Preliminary mass balances are carried out on two types of oxygen carriers, namely iron oxides and nickel ferrites, while computational fluid dynamics simulations (with implemented reaction kinetics) are performed to assess the conversion efficiency of the syngas production step. **Chapters 4 and 5** focus on the experimental evaluation of this technology from two different perspectives considering iron-based oxygen carriers. In **Chapter 4** the producibility of an iron bed interacting at high temperatures with CO_2 and H_2O streams is investigated. The effect of several parameters is analysed and optimal conditions are drawn. Subsequently, in **Chapter 5** the effect of high-pressure operation of Ni and Fe aluminates over redox cycles is investigated. The effect of reactants flow rate, temperature, composition, total pressure and long-term cycling is assessed and compared with low pressure operation. Finally, in **Chapter 6** techno-economic analysis on a process scheme for the combined production of ammonia and methanol from a thermochemical syngas is carried out. The variety of gas species deriving from a typical chemical looping hydrogen production process with Fe_2O_3/FeO oxygen carrier couple is here optimally exploited for liquid fuels production. Comparison with benchmark processes and with alternative processes based on other carbon capture and utilization technologies is discussed in terms of economic and environmental performance. In **Chapter 7** the main conclusions from each chapter are collected and discussed.

1.11 Nomenclature

Air reactor	AR
Air separation unit	ASU
CO_2 avoidance cost	CAC
Carbon capture, utilization, and storage	CCUS
Chemical looping combustion	CLC
Chemical looping hydrogen production	CLHP
Chemical looping oxygen uncoupling	CLOU
Chemical looping reforming	CLR
Chemical looping tar reforming	CLTR
Circulating Fluidized Bed	CFB
Coal-fired power plants	CFPP

Compression and Purification Unit	CPU
European Union	EU
Fuel reactor	FR
Haber-Bosch	HB
Intergovernmental Panel on Climate Change	IPCC
Internally circulating reactor	ICR
Levelized cost of electricity	LCOE
Levelized cost of thermal energy	LCOTE
Natural gas combined cycles	NGCC
Oxygen carrier	OC
Oxygen carrier aided combustion	OCAC
Oxidized printed circuit boards	OPCB
Partially stabilized tetragonal zirconia	t-PSZ
Photovoltaic electrolysis using a solid oxide electrolysis cell	PV-SOEC

1.12 References

[1] IEA. World Energy Outlook 2022 2022. https://www.iea.org/reports/world-energy-outlook-2022 (accessed June 8, 2023).

[2] Babiker M, Reilly JM, Jacoby HD. The Kyoto Protocol and developing countries. Energy Policy 2000;28:525–36. https://doi.org/10.1016/S0301-4215(00)00033-1.

[3] UNFCC. Adoption of the Paris Agreement. Paris : 2015.

[4] Global Warming of 1.5 °C — n.d. https://www.ipcc.ch/sr15/ (accessed October 30, 2023).

[5] Commission E. The European green deal 2019.

[6] energy agency international. CO2 Emissions in 2022. 2022.

[7] Combined cycle n.d. https://www.ansaldoenergia.com/offering/simple-cycle/default-title (accessed November 21, 2023).

[8] Advanced Ultra-Supercritical Technology | GE Steam Power n.d. https://www.ge.com/steam-power/coal-power-plant/usc-ausc (accessed November 21, 2023).

[9] Romanelli F, Barabaschi P, Borba D, Federici G, Horton L, Neu R, et al. Fusion Electricity: A roadmap to the realization of fusion energy 2012.

[10] Mitali J, Dhinakaran S, Mohamad AA. Energy storage systems: a review. Energy Storage and Saving 2022;1:166–216. https://doi.org/10.1016/J.ENSS.2022.07.002.

[11] Chemicals - IEA n.d. https://www.iea.org/energy-system/industry/chemicals (accessed November 21, 2023).

[12] Gabrielli P, Rosa L, Gazzani M, Meys R, Bardow A, Mazzotti M, et al. Net-zero emissions chemical industry in a world of limited resources. One Earth 2023;6:682–704. https://doi.org/10.1016/J.ONEEAR.2023.05.006.

[13] Dubey A, Arora A. Advancements in carbon capture technologies: A review. J Clean Prod 2022;373:133932. https://doi.org/10.1016/J.JCLEPRO.2022.133932.

[14] Palone O, Hoxha A, Gagliardi GG, Di Gruttola F, Stendardo S, Borello D. Synthesis of Methanol From a Chemical Looping Syngas for the Decarbonization of the Power Sector. J Eng Gas Turbine Power 2023;145:21018.

[15] Palone O, Gagliardi GG, Mechelli M, Cedola L, Borello D. Techno-economic analysis of sustainable methanol and ammonia production by chemical looping hydrogen generation from waste plastic. Energy Convers Manag 2023;292:117389. https://doi.org/10.1016/J.ENCONMAN.2023.117389.

[16] Battaglia P, Buffo G, Ferrero D, Santarelli M, Lanzini A. Methanol synthesis through CO2 capture and hydrogenation: Thermal integration, energy performance and techno-economic assessment. Journal of CO2 Utilization 2021;44:101407.

[17] De Silvestri A, Stendardo S, Della Pietra M, Borello D. Decarbonizing cement plants via a fully integrated calcium looping-molten carbonate fuel cell process: Assessment of a model for fuel cell performance predictions under different operating conditions. Int J Hydrogen Energy 2021;46:14988–5007. https://doi.org/10.1016/J.IJHYDENE.2020.12.024.

[18] Cheng Y, Hou P, Wang X, Kang P. CO2 Electrolysis System under Industrially Relevant Conditions. Acc Chem Res 2022;55:231–40. https://doi.org/10.1021/acs.accounts.1c00614.

[19] Jiang Q, Chen Z, Tong J, Yang M, Jiang Z, Li C. Direct thermolysis of CO2 into CO and O2. Chemical Communications 2017;53:1188–91. https://doi.org/10.1039/c6cc08801e.

[20] Ramezani R, Di Felice L, Gallucci F. A review of chemical looping reforming technologies for hydrogen production: recent advances and future challenges. Journal of Physics: Energy 2023. https://doi.org/10.1088/2515-7655/acc4e8.

[21] Global Time Series | Climate at a Glance | National Centers for Environmental Information (NCEI) n.d. https://www.ncei.noaa.gov/access/monitoring/climate-at-a-glance/global/time-series/globe/land_ocean/12/1/1959-2023 (accessed October 26, 2023).

[22] Carbon Dioxide | Vital Signs – Climate Change: Vital Signs of the Planet n.d. https://climate.nasa.gov/vital-signs/carbon-dioxide/ (accessed October 26, 2023).

[23] Yu Z, Yang Y, Yang S, Zhang Q, Zhao J, Fang Y, et al. Iron-based oxygen carriers in chemical looping conversions: A review. Carbon Resources Conversion 2019;2:23–34. https://doi.org/10.1016/j.crcon.2018.11.004.

[24] Chiesa P, Lozza G, Malandrino A, Romano M, Piccolo V. Three-reactors chemical looping process for hydrogen production. Int J Hydrogen Energy 2008;33:2233–45.

[25] Hu J, Chen S, Xiang W. Sintering and agglomeration of Fe2O3-MgAl2O4 oxygen carriers with different Fe2O3 loadings in chemical looping processes. Fuel 2020;265. https://doi.org/10.1016/j.fuel.2019.116983.

[26] Evdou A, Zaspalis V, Nalbandian L. Ferrites as redox catalysts for chemical looping processes. Fuel 2016;165:367–78. https://doi.org/10.1016/j.fuel.2015.10.049.

[27] Wang X, Chen Z, Hu M, Tian Y, Jin X, Ma S, et al. Chemical looping combustion of biomass using metal ferrites as oxygen carriers. Chemical Engineering Journal 2017;312:252–62. https://doi.org/10.1016/j.cej.2016.11.143.

[28] Adnan MA, Al-Zahrani AA, Haque TI, Razzak SA, Hossain MM. In-situ reforming and combustion of liquid fuel using MnOx/Ce-γAl2O3 oxygen carrier in a chemical looping combustion process. Int J Hydrogen Energy 2021;46:25500–12. https://doi.org/10.1016/J.IJHYDENE.2021.05.104.

[29] Costa TR, Gayán P, Abad A, García-Labiano F, de Diego LF, Melo DMA, et al. Mn-based oxygen carriers prepared by impregnation for Chemical Looping Combustion with diverse fuels. Fuel Processing Technology 2018;178:236–50. https://doi.org/10.1016/J.FUPROC.2018.05.019.

[30] Donat F, Müller CR. CO2-free conversion of CH4 to syngas using chemical looping. Appl Catal B 2020;278. https://doi.org/10.1016/j.apcatb.2020.119328.

[31] Gu Z, Zhang L, Lu C, Qing S, Li K. Enhanced performance of copper ore oxygen carrier by red mud modification for chemical looping combustion. Appl Energy 2020;277. https://doi.org/10.1016/j.apenergy.2020.115590.

[32] Muhich CL, Ehrhart BD, Al-Shankiti I, Ward BJ, Musgrave CB, Weimer AW. A review and perspective of efficient hydrogen generation via solar thermal water splitting. Wiley Interdiscip Rev Energy Environ 2015;5:261–87. https://doi.org/10.1002/wene.174.

[33] Abdalla A, Mohamedali M, Mahinpey N. Recent Progress in the Development of Synthetic Oxygen Carriers for Chemical Looping Combustion Applications. Catal Today 2022.

[34] Vos Y De, Jacobs M, Voort P Van Der, Driessche I Van, Snijkers F, Verberckmoes A. Development of Stable Oxygen Carrier Materials for Chemical Looping Processes—A Review. Catalysts 2020, Vol 10, Page 926 2020;10:926. https://doi.org/10.3390/CATAL10080926.

[35] Gayán P, Luis F, Garc\'\ia-Labiano F, Adánez J, Abad A, Dueso C. Effect of support on reactivity and selectivity of Ni-based oxygen carriers for chemical-looping combustion. Fuel 2008;87:2641–50.

[36] San Pio MA, Gallucci F, Roghair I, van Sint Annaland M. On the mechanism controlling the redox kinetics of Cu-based oxygen carriers. Chemical Engineering Research and Design 2017;124:193–201. https://doi.org/10.1016/j.cherd.2017.06.019.

[37] Damizia M, Bracciale MP, Anania F, Tai L, De Filippis P, de Caprariis B. Efficient utilization of Al2O3 as structural promoter of Fe into 2 and 3 steps chemical looping hydrogen process: Pure H2 production from ethanol. Int J Hydrogen Energy 2023. https://doi.org/10.1016/j.ijhydene.2023.04.067.
[38] Hammache S, Means N, Burgess W, Howard B, Smith M. Investigation of low-cost oxygen carriers for chemical looping combustion at high temperature. Fuel 2020;273:117746.
[39] Wang Y, Tian X, Zhao H, Liu K. The use of a low-cost oxygen carrier prepared from red mud and copper ore for in situ gasification chemical looping combustion of coal. Fuel Processing Technology 2020;205:106460.
[40] Durmaz M, Dilmaç N, Dilmaç ÖF. Evaluation of performance of copper converter slag as oxygen carrier in chemical-looping combustion (CLC). Energy 2020;196:117055.
[41] Wang I, Ji G, Turap Y, Nie H, Li Z, Zhao M, et al. A short-cut chemical looping hydrogen generation system by using iron-based material from steel industry. Chemical Engineering Journal 2020;394:124882.
[42] Hedayati A, Soleimanisalim AH, Mattisson T, Lyngfelt A. Thermochemical conversion of biomass volatiles via chemical looping: Comparison of ilmenite and steel converter waste materials as oxygen carriers. Fuel 2022;313:122638.
[43] Cabello A, Mendiara T, Teresa Izquierdo M, García-Labiano F, Abad A. Energy use of biogas through chemical looping technologies with low-cost oxygen carriers. Fuel 2023;344. https://doi.org/10.1016/j.fuel.2023.128123.
[44] Yin K, Wang H, Veksha A, Dou X, Khairunnisa Binte Mohamed D, Heberlein S, et al. Oxygen carriers from incineration bottom ash for chemical looping combustion of syngas: Effect of composition on combustion efficiency. Chemical Engineering Journal 2021;405. https://doi.org/10.1016/j.cej.2020.127068.
[45] Palone O, Cava C, Paris E, Vincenti B, Migliarese Caputi M V., Gallucci F, et al. Experimental investigation of thermochemical syngas production in a scrap iron-based oxidizer reactor for industrial decarbonisation. Fuel 2023;347:128436. https://doi.org/10.1016/J.FUEL.2023.128436.
[46] Hu Z, Miao Z, Wu J, Jiang E. Nickel-iron modified natural ore oxygen carriers for chemical looping steam methane reforming to produce hydrogen. Int J Hydrogen Energy 2021;46:39700–18. https://doi.org/10.1016/j.ijhydene.2021.09.242.
[47] Lu X, Rahman RA, Lu DY, Ridha FN, Duchesne MA, Tan Y, et al. Pressurized chemical looping combustion with CO: Reduction reactivity and oxygen-transport capacity of ilmenite ore. Appl Energy 2016;184:132–9. https://doi.org/10.1016/j.apenergy.2016.09.107.
[48] Tan Y, Ridha FN, Duchesne MA, Lu DY, Hughes RW. Reduction Kinetics of Ilmenite Ore as an Oxygen Carrier for Pressurized Chemical Looping Combustion of Methane. Energy and Fuels 2017;31:7598–605. https://doi.org/10.1021/acs.energyfuels.7b01038.

[49] Linderholm C, Schmitz M, Knutsson P, Lyngfelt A. Chemical-looping combustion in a 100-kW unit using a mixture of ilmenite and manganese ore as oxygen carrier. Fuel 2016;166:533–42. https://doi.org/10.1016/J.FUEL.2015.11.015.

[50] Sun Z, Lu DY, Ridha FN, Hughes RW, Filippou D. Enhanced performance of ilmenite modified by CeO2, ZrO2, NiO, and Mn2O3 as oxygen carriers in chemical looping combustion. Appl Energy 2017;195:303–15. https://doi.org/10.1016/J.APENERGY.2017.03.014.

[51] Ishida M, Jin H. A Novel Combustor Based on Chemical-Looping Reactions and Its Reaction Kinetics. JOURNAL OF CHEMICAL ENGINEERING OF JAPAN 1994;27:296–301. https://doi.org/10.1252/JCEJ.27.296.

[52] Spallina V, Romano MC, Chiesa P, Gallucci F, van Sint Annaland M, Lozza G. Integration of coal gasification and packed bed CLC for high efficiency and near-zero emission power generation. International Journal of Greenhouse Gas Control 2014;27:28–41. https://doi.org/10.1016/J.IJGGC.2014.04.029.

[53] Erland N, Haugen L, Li Z, Gouraud V, Bertholin S, Li W, et al. Building the world's largest Chemical Looping Combustion (CLC) unit. International Journal of Greenhouse Gas Control 2023;129:1750–5836. https://doi.org/10.1016/j.ijggc.2023.103975.

[54] Lind F, Corcoran A, Thunman H. Validation of the oxygen buffering ability of bed materials used for OCAC in a large scale CFB boiler. Powder Technol 2017;316:462–8. https://doi.org/10.1016/J.POWTEC.2016.12.048.

[55] Ströhle J. Chemical Looping Combustion of Waste—Opportunities and Challenges. Energy and Fuels 2023;37:1465–71. https://doi.org/10.1021/acs.energyfuels.2c04297.

[56] Moldenhauer P, Rydén M, Mattisson T, Jamal A, Lyngfelt A. Chemical-looping combustion with heavy liquid fuels in a 10 kW pilot plant. Fuel Processing Technology 2017;156:124–37. https://doi.org/10.1016/J.FUPROC.2016.10.027.

[57] Kuang C, Wang S, Luo M, Cai J, Zhao J. Investigation of CuO-based oxygen carriers modified by three different ores in chemical looping combustion with solid fuels. Renew Energy 2020;154:937–48. https://doi.org/10.1016/j.renene.2020.03.027.

[58] Liu F, Wu X, Yang L, Bu H, Zhang X. Evaluation of a bauxite cement-bonded Fe-based oxygen carrier during a hundred of cycles under coal-fueled chemical looping combustion conditions. Fuel Processing Technology 2020;199. https://doi.org/10.1016/j.fuproc.2019.106267.

[59] Cuadrat A, Abad A, García-Labiano F, Gayán P, de Diego LF, Adánez J. Relevance of the coal rank on the performance of the in situ gasification chemical-looping combustion. Chemical Engineering Journal 2012;195–196:91–102. https://doi.org/10.1016/J.CEJ.2012.04.052.

[60] Shen L, Wu J, Xiao J, Song Q, Xiao R. Chemical-Looping Combustion of Biomass in a 10 kWth Reactor with Iron Oxide As an Oxygen Carrier. Energy & Fuels 2009;23:2498–505. https://doi.org/10.1021/ef900033n.

[61] Xiao R, Chen L, Saha C, Zhang S, Bhattacharya S. Pressurized chemical-looping combustion of coal using an iron ore as oxygen carrier in a pilot-scale unit. International Journal of Greenhouse Gas Control 2012;10:363–73. https://doi.org/10.1016/J.IJGGC.2012.07.008.

[62] Wang B, Guo C, Xu B, Li X, Ma J, Mei D, et al. Effects of pressure on the chemical looping combustion of coal with CuFe2O4 combined oxygen carrier. Journal of the Energy Institute 2022;100:22–32. https://doi.org/10.1016/j.joei.2021.10.009.

[63] Gayán P, Abad A, de Diego LF, García-Labiano F, Adánez J. Assessment of technological solutions for improving chemical looping combustion of solid fuels with CO2 capture. Chemical Engineering Journal 2013;233:56–69. https://doi.org/10.1016/J.CEJ.2013.08.004.

[64] Mattisson T, Lyngfelt A, Leion H. Chemical-looping with oxygen uncoupling for combustion of solid fuels. International Journal of Greenhouse Gas Control 2009;3:11–9. https://doi.org/10.1016/J.IJGGC.2008.06.002.

[65] Lyngfelt A, Brink A, Langørgen Ø, Mattisson T, Rydén M, Linderholm C. 11,000 h of chemical-looping combustion operation—Where are we and where do we want to go? International Journal of Greenhouse Gas Control 2019;88:38–56. https://doi.org/10.1016/J.IJGGC.2019.05.023.

[66] Cheng J, Zhou J, Liu J, Zhou Z, Huang Z, Cao X, et al. Sulfur removal at high temperature during coal combustion in furnaces: a review. Prog Energy Combust Sci 2003;29:381–405. https://doi.org/10.1016/S0360-1285(03)00030-3.

[67] Anthony EJ, Granatstein DL. Sulfation phenomena in fluidized bed combustion systems. Prog Energy Combust Sci 2001;27:215–36. https://doi.org/10.1016/S0360-1285(00)00021-6.

[68] Gu H, Shen L, Xiao J, Zhang S, Song T, Chen D. Evaluation of the effect of sulfur on iron-ore oxygen carrier in chemical-looping combustion. Ind Eng Chem Res 2013;52:1795–805. https://doi.org/10.1021/ie303023w.

[69] Mendiara T, Izquierdo MT, Abad A, de Diego LF, García-Labiano F, Gayán P, et al. Release of pollutant components in CLC of lignite. International Journal of Greenhouse Gas Control 2014;22:15–24. https://doi.org/10.1016/J.IJGGC.2013.12.013.

[70] Shen L, Wu J, Gao Z, Xiao J. Characterization of chemical looping combustion of coal in a 1 kWth reactor with a nickel-based oxygen carrier. Combust Flame 2010;157:934–42. https://doi.org/10.1016/J.COMBUSTFLAME.2009.10.009.

[71] Ma J, Wang C, Zhao H, Tian X. Sulfur Fate during the Lignite Pyrolysis Process in a Chemical Looping Combustion Environment. Energy & Fuels 2017;32:4493–501. https://doi.org/10.1021/acs.energyfuels.7b03149.

[72] Wang B, Yan R, Ho Lee D, Tee Liang D, Zheng Y, Zhao H, et al. Thermodynamic Investigation of Carbon Deposition and Sulfur Evolution in Chemical Looping Combustion with Syngas. Energy & Fuels 2008;22:1012–20. https://doi.org/10.1021/ef7005673.

[73] Mendiara T, Izquierdo MT, Abad A, Gayán P, García-Labiano F, De Diego LF, et al. Mercury release and speciation in chemical looping combustion of coal. Energy and Fuels 2014;28:2786–94. https://doi.org/10.1021/ef402377m.

[74] Xu K, Liu D, Feng L, Jin J, Xiong Z, Ni M, et al. Mercury removal by Co3O4@TiO2@Fe2O3 magnetic core-shell oxygen carrier in chemical-looping combustion. Fuel 2021;306. https://doi.org/10.1016/j.fuel.2021.121604.

[75] Zhang S, Xiao R, Zheng W. Comparative study between fluidized-bed and fixed-bed operation modes in pressurized chemical looping combustion of coal. Appl Energy 2014;130:181–9. https://doi.org/10.1016/j.apenergy.2014.05.049.

[76] Zhang Y, Jin B, Zou X, Zhao H. A clean coal utilization technology based on coal pyrolysis and chemical looping with oxygen uncoupling: Principle and experimental validation. Energy 2016;98:181–9. https://doi.org/10.1016/j.energy.2016.01.010.

[77] Mattisson T, Keller M, Linderholm C, Moldenhauer P, Rydén M, Leion H, et al. Chemical-looping technologies using circulating fluidized bed systems: Status of development. Fuel Processing Technology 2018;172:1–12. https://doi.org/10.1016/J.FUPROC.2017.11.016.

[78] Adánez J, Gayán P, Adánez-Rubio I, Cuadrat A, Mendiara T, Abad A, et al. Use of Chemical-Looping processes for coal combustion with CO2 capture. Energy Procedia 2013;37:540–9. https://doi.org/10.1016/J.EGYPRO.2013.05.140.

[79] André L, Abanades S. Investigation of metal oxides, mixed oxides, perovskites and alkaline earth carbonates/hydroxides as suitable candidate materials for high-temperature thermochemical energy storage using reversible solid-gas reactions. Mater Today Energy 2018;10:48–61. https://doi.org/10.1016/J.MTENER.2018.08.007.

[80] Cui H, Dong H, Zhou Z. A cadmium-magnesium looping for stable thermochemical energy storage and CO2 capture at intermediate temperatures. Chemical Engineering Journal 2021;425:131428. https://doi.org/10.1016/J.CEJ.2021.131428.

[81] Wu S, Zhou C, Doroodchi E, Nellore R, Moghtaderi B. A review on high-temperature thermochemical energy storage based on metal oxides redox cycle. Energy Convers Manag 2018;168:421–53. https://doi.org/10.1016/J.ENCONMAN.2018.05.017.

[82] Coppola A, Solimene R, Bareschino P, Salatino P. Mathematical modeling of a two-stage fuel reactor for chemical looping combustion with oxygen uncoupling of solid fuels. Appl Energy 2015;157:449–61. https://doi.org/10.1016/j.apenergy.2015.04.052.

[83] Carrillo AJ, Serrano DP, Pizarro P, Coronado JM. Improving the Thermochemical Energy Storage Performance of the Mn2O3/Mn3O4 Redox Couple by the Incorporation of Iron. ChemSusChem 2015;8:1947–54. https://doi.org/10.1002/CSSC.201500148.

[84] Mohammad Pour N, Leion H, Rydén M, Mattisson T. Combined Cu/Mn oxides as an oxygen carrier in chemical looping with oxygen uncoupling (CLOU). Energy and Fuels 2013;27:6031–9. https://doi.org/10.1021/EF401328U/ASSET/IMAGES/LARGE/EF-2013-01328U_0010.JPEG.

[85] Randhir K, King K, Rhodes N, Li L, Hahn D, Mei R, et al. Magnesium-manganese oxides for high temperature thermochemical energy storage. J Energy Storage 2019;21:599–610. https://doi.org/10.1016/J.EST.2018.11.024.

[86] Rahmatian N, Bo A, Randhir K, Klausner JF, Petrasch J. Bench-scale demonstration of thermochemical energy storage using the Magnesium-Manganese-Oxide redox system. J Energy Storage 2022;45:103682. https://doi.org/10.1016/J.EST.2021.103682.

[87] King K, Randhir K, Petrasch J, Klausner J. Enhancing thermochemical energy storage density of magnesium-manganese oxides. Energy Storage 2019;1. https://doi.org/10.1002/EST2.83.

[88] Källén M, Rydén M, Dueso C, Mattisson T, Lyngfelt A. CaMn0.9Mg0.1O3-δ as oxygen carrier in a gas-fired 10 kWthchemical-looping combustion unit. Ind Eng Chem Res 2013;52:6923–32. https://doi.org/10.1021/IE303070H/ASSET/IMAGES/LARGE/IE-2012-03070H_0014.JPEG.

[89] Babiniec SM, Coker EN, Miller JE, Ambrosini A. Investigation of LaxSr1−xCoyM1−yO3−δ (M = Mn, Fe) perovskite materials as thermochemical energy storage media. Solar Energy 2015;118:451–9. https://doi.org/10.1016/J.SOLENER.2015.05.040.

[90] Babiniec SM, Coker EN, Miller JE, Ambrosini A. Doped calcium manganites for advanced high-temperature thermochemical energy storage. Int J Energy Res 2016;40:280–4. https://doi.org/10.1002/ER.3467.

[91] Lee SH, Themelis NJ, Castaldi MJ. High-temperature corrosion in waste-to-energy boilers. Journal of Thermal Spray Technology 2007;16:104–10. https://doi.org/10.1007/s11666-006-9005-4.

[92] Liu G, Wang H, Deplazes S, Veksha A, Wirz-Töndury C, Giannis A, et al. Ba–Al-decorated iron ore as bifunctional oxygen carrier and HCl sorbent for chemical looping combustion of syngas. Combust Flame 2021;223:230–42. https://doi.org/10.1016/J.COMBUSTFLAME.2020.09.021.

[93] Wang J, Zhao H. Chemical looping dechlorination through adsorbent-decorated Fe2O3/Al2O3 oxygen carriers. Combust Flame 2015;162:3503–15. https://doi.org/10.1016/J.COMBUSTFLAME.2015.06.008.

[94] Liu G, Wang H, Veksha A, Giannis A, Lim TT, Lisak G. Chemical looping combustion-adsorption of HCl-containing syngas using alkaline-earth coated iron ore composites for simultaneous purification and combustion enhancement. Chemical Engineering Journal 2021;417. https://doi.org/10.1016/j.cej.2021.129226.

[95] García-Labiano F, F. de Diego L, Gayán P, Adánez J, Abad A, Dueso C. Effect of Fuel Gas Composition in Chemical-Looping Combustion with Ni-Based Oxygen Carriers. 1. Fate of Sulfur. Industrial & Engineering Chemistry Research 2009;48:2499–508. https://doi.org/10.1021/ie801332z.

[96] Forero CR, Gayán P, García-Labiano F, de Diego LF, Abad A, Adánez J. Effect of gas composition in Chemical-Looping Combustion with copper-based oxygen carriers: Fate of sulphur. International Journal of Greenhouse Gas Control 2010;4:762–70. https://doi.org/10.1016/J.IJGGC.2010.04.002.

[97] Wang H, Liu G, Veksha A, Giannis A, Lim TT, Lisak G. Effective H2S control during chemical looping combustion by iron ore modified with alkaline earth metal oxides. Energy 2021;218. https://doi.org/10.1016/j.energy.2020.119548.

[98] Izquierdo MT, García-Labiano F, Abad A, Cabello A, Gayán P, de Diego LF, et al. On the optimization of physical and chemical stability of a Cu/Al2O3 impregnated oxygen carrier for chemical looping combustion. Fuel Processing Technology 2021;215. https://doi.org/10.1016/j.fuproc.2021.106740.

[99] Rydén M, Jing D, Källén M, Leion H, Lyngfelt A, Mattisson T. CuO-Based Oxygen-Carrier Particles for Chemical-Looping with Oxygen Uncoupling – Experiments in Batch Reactor and in Continuous Operation. Industrial & Engineering Chemistry Research 2014;53:6255–67. https://doi.org/10.1021/ie4039983.

[100] Chen L, Zhang Y, Liu F, Liu K. Development of a Cost-Effective Oxygen Carrier from Red Mud for Coal-Fueled Chemical-Looping Combustion. Energy & Fuels 2015;29:305–13. https://doi.org/10.1021/ef501950w.

[101] Lin S, Gu Z, Zhu X, Wei Y, Long Y, Yang K, et al. Synergy of red mud oxygen carrier with MgO and NiO for enhanced chemical-looping combustion. Energy 2020;197. https://doi.org/10.1016/j.energy.2020.117202.

[102] Nordness O, Han L, Zhou Z, Bollas GM. High-Pressure Chemical-Looping of Methane and Synthesis Gas with Ni and Cu Oxygen Carriers. Energy and Fuels 2016;30:504–14. https://doi.org/10.1021/acs.energyfuels.5b01986.

[103] Hamers HP, Gallucci F, Williams G, Cobden PD, van Sint Annaland M. Reactivity of oxygen carriers for chemical-looping combustion in packed bed reactors under pressurized conditions. Energy & Fuels 2015;29:2656–63.
[104] García-Labiano F, Adánez J, de Diego LF, Gayán P, Abad A. Effect of pressure on the behavior of copper-, iron-, and nickel-based oxygen carriers for chemical-looping combustion. Energy and Fuels 2006;20:26–33. https://doi.org/10.1021/ef050238e.
[105] Palone O, Ramezani R, Navarro C, Di Felice L, Borello D, Grasa G, et al. On the reduction of NiFe/Al2O3 oxygen carrier in high-pressure chemical looping applications. Int J Hydrogen Energy 2023. https://doi.org/10.1016/J.IJHYDENE.2023.09.235.
[106] San Pio MA, Gallucci F, Roghair I, van Sint Annaland M. Gas-solids kinetics of CuO/Al2O3 as an oxygen carrier for high-pressure chemical looping processes: The influence of the total pressure. Int J Hydrogen Energy 2017;42:12111–21. https://doi.org/10.1016/j.ijhydene.2017.03.176.
[107] Garcia-Labiano F, Adánez J, de Diego LF, Gayán P, Abad A. Effect of pressure on the behavior of copper-, iron-, and nickel-based oxygen carriers for chemical-looping combustion. Energy & Fuels 2006;20:26–33.
[108] Rana S, Sun Z, Mehrani P, Hughes R, Macchi A. Ilmenite oxidation kinetics for pressurized chemical looping combustion of natural gas. Appl Energy 2019;238:747–59. https://doi.org/10.1016/J.APENERGY.2019.01.126.
[109] San Pio MA, Gallucci F, Roghair I, van Sint Annaland M. Gas-solids kinetics of CuO/Al2O3 as an oxygen carrier for high-pressure chemical looping processes: the influence of the total pressure. Int J Hydrogen Energy 2017;42:12111–21.
[110] Mishra A, Dudek R, Gaffney A, Ding D, Li F. Spinel oxides as coke-resistant supports for NiO-based oxygen carriers in chemical looping combustion of methane. Catal Today 2019. https://doi.org/10.1016/j.cattod.2019.09.010.
[111] Noorman S, Van Sint Annaland M, Kuipers H. Packed bed reactor technology for chemical-looping combustion. Ind Eng Chem Res 2007;46:4212–20. https://doi.org/10.1021/ie061178i.
[112] Wang X, Wang X, Kong Z, Shao Y, Jin B. Auto-thermal operation and optimization of coal-fueled separated gasification chemical looping combustion in a pilot-scale unit. Chemical Engineering Journal 2020;383. https://doi.org/10.1016/j.cej.2019.123159.
[113] Ohlemüller P, Ströhle J, Epple B. Chemical looping combustion of hard coal and torrefied biomass in a 1 MWth pilot plant. International Journal of Greenhouse Gas Control 2017;65:149–59. https://doi.org/10.1016/J.IJGGC.2017.08.013.
[114] Abad A, Pérez-Vega R, de Diego LF, García-Labiano F, Gayán P, Adánez J. Design and operation of a 50 kWth Chemical Looping Combustion (CLC) unit for solid fuels. Appl Energy 2015;157:295–303. https://doi.org/10.1016/J.APENERGY.2015.03.094.

[115] Haus J, Lyu K, Hartge E-U, Heinrich S, Werther J. Analysis of a Two-Stage Fuel Reactor System for the Chemical-Looping Combustion of Lignite and Bituminous Coal. Energy Technology 2016;4:1263–73. https://doi.org/https://doi.org/10.1002/ente.201600102.

[116] Li F, Zeng L, Velazquez-Vargas LG, Yoscovits Z, Fan LS. Syngas chemical looping gasification process: Bench-scale studies and reactor simulations. AIChE Journal 2010;56:2186–99. https://doi.org/10.1002/AIC.12093.

[117] Zhang Y, Wang D, Pottimurthy Y, Kong F, Hsieh TL, Sakadjian B, et al. Coal direct chemical looping process: 250 kW pilot-scale testing for power generation and carbon capture. Appl Energy 2021;282. https://doi.org/10.1016/j.apenergy.2020.116065.

[118] Sun Z, Aziz M. Comparative thermodynamic and techno-economic assessment of green methanol production from biomass through direct chemical looping processes. J Clean Prod 2021;321:129023.

[119] Miyahira K, Aziz M. Hydrogen and ammonia production from low-grade agricultural waste adopting chemical looping process. J Clean Prod 2022;372:133827.

[120] Sun Z, Wang S, Aziz M. Highly integrated system for ammonia and electricity production from biomass employing direct chemical looping: Exergy and exergoeconomic analyses. Energy Convers Manag 2022;251:115013. https://doi.org/10.1016/J.ENCONMAN.2021.115013.

[121] Hamers HP, Romano MC, Spallina V, Chiesa P, Gallucci F, Annaland MVS. Comparison on process efficiency for CLC of syngas operated in packed bed and fluidized bed reactors. International Journal of Greenhouse Gas Control 2014;28:65–78. https://doi.org/10.1016/J.IJGGC.2014.06.007.

[122] Abanades JC, Diego ME, Fernández JR. A novel air reactor concept for chemical looping combustion systems operated at high pressure. Chemical Engineering Journal 2020;390:124507. https://doi.org/10.1016/J.CEJ.2020.124507.

[123] Diego ME, Abanades JC. Experimental investigation of a diffusion-controlled chemical looping air reactor for energy storage applications. Chemical Engineering Journal 2022;428:132083. https://doi.org/10.1016/J.CEJ.2021.132083.

[124] Calvo LF, Grasa G, Alonso M, Diego ME. Investigation on the performance of fine iron ore particles for energy storage applications in a novel CLC reactor. Fuel Processing Technology 2023;245:107755. https://doi.org/10.1016/J.FUPROC.2023.107755.

[125] Luo M, Yi Y, Wang S, Wang Z, Du M, Pan J, et al. Review of hydrogen production using chemical-looping technology. Renewable and Sustainable Energy Reviews 2018;81:3186–214. https://doi.org/10.1016/j.rser.2017.07.007.

[126] Osman M, Khan MN, Zaabout A, Cloete S, Amini S. Review of pressurized chemical looping processes for power generation and chemical production with integrated CO2 capture. Fuel Processing Technology 2021;214. https://doi.org/10.1016/j.fuproc.2020.106684.

[127] Zaabout A, Cloete S, Johansen ST, van Sint Annaland M, Gallucci F, Amini S. Experimental Demonstration of a Novel Gas Switching Combustion Reactor for Power Production with Integrated CO2 Capture. Ind Eng Chem Res 2013;52:14241–50. https://doi.org/10.1021/ie401810n.
[128] Zhao Z, Chen T, Ghoniem AF. Rotary Bed Reactor for Chemical-Looping Combustion with Carbon Capture. Part 1: Reactor Design and Model Development. Energy & Fuels 2013;27:327–43. https://doi.org/10.1021/ef3014103.
[129] Osman M, Khan MN, Zaabout A, Cloete S, Amini S. Review of pressurized chemical looping processes for power generation and chemical production with integrated CO2 capture. Fuel Processing Technology 2021;214. https://doi.org/10.1016/j.fuproc.2020.106684.
[130] Kuramoto M, Furusawa T, Kunii D. Development of a new system for circulating fluidized particles within a single vessel. Powder Technol 1985;44:77–84. https://doi.org/https://doi.org/10.1016/0032-5910(85)85024-5.
[131] Khan MN, Chiesa P, Cloete S, Amini S. Integration of chemical looping combustion for cost-effective CO2 capture from state-of-the-art natural gas combined cycles. Energy Conversion and Management: X 2020;7. https://doi.org/10.1016/j.ecmx.2020.100044.
[132] Cloete S, Zaabout A, Amini S. The Internally Circulating Reactor (ICR) Concept Applied to Pressurized Chemical Looping Processes. Energy Procedia 2017;114:446–57. https://doi.org/https://doi.org/10.1016/j.egypro.2017.03.1187.
[133] Osman M, Zaabout A, Cloete S, Amini S. Experimental demonstration of pressurized chemical looping combustion in an internally circulating reactor for power production with integrated CO2 capture. Chemical Engineering Journal 2020;401:125974. https://doi.org/10.1016/J.CEJ.2020.125974.
[134] Dou B, Zhao L, Zhang H, Wu K, Zhang H. Renewable hydrogen production from chemical looping steam reforming of biodiesel byproduct glycerol by mesoporous oxygen carriers. Chemical Engineering Journal 2021;416. https://doi.org/10.1016/j.cej.2020.127612.
[135] Luo C, Dou B, Zhang H, Liu D, Zhao L, Chen H, et al. Co-production of hydrogen and syngas from chemical looping water splitting coupled with decomposition of glycerol using Fe-Ce-Ni based oxygen carriers. Energy Convers Manag 2021;238. https://doi.org/10.1016/j.enconman.2021.114166.
[136] Cormos AM, Dumbrava I, Cormos CC. Evaluation of techno-economic performance for decarbonized hydrogen and power generation based on glycerol thermo-chemical looping cycles. Appl Therm Eng 2020;179. https://doi.org/10.1016/j.applthermaleng.2020.115728.
[137] Cabello A, Mendiara T, Abad A, Izquierdo MT, García-Labiano F. Production of hydrogen by chemical looping reforming of methane and biogas using a reactive and durable Cu-based oxygen carrier. Fuel 2022;322. https://doi.org/10.1016/j.fuel.2022.124250.

[138] Stoppacher B, Sterniczky T, Bock S, Hacker V. On-site production of high-purity hydrogen from raw biogas with fixed-bed chemical looping. Energy Convers Manag 2022;268. https://doi.org/10.1016/j.enconman.2022.115971.
[139] Liu G, Lisak G. Inherently separated syngas production from plastic waste fast pyrolysis integrated with volatile chemical looping conversion with CO2 splitting. Chemical Engineering Journal 2023;465. https://doi.org/10.1016/j.cej.2023.142915.
[140] Wei G qiang, Feng J, Hou YL, Li FZ, Li WY, Huang Z, et al. Ca-enhanced hematite oxygen carriers for chemical looping reforming of biomass pyrolyzed gas coupled with CO2 splitting. Fuel 2021;285. https://doi.org/10.1016/j.fuel.2020.119125.
[141] Sun Z, Lu DY, Symonds RT, Hughes RW. Chemical looping reforming of CH4 in the presence of CO2 using ilmenite ore and NiO-modified ilmenite ore oxygen carriers. Chemical Engineering Journal 2020;401. https://doi.org/10.1016/j.cej.2019.123481.
[142] Hoxha A, Palone O, Cedola L, Stendardo S, Borello D. Development of a novel carbon capture and utilization approach for syngas production based on a chemical looping cycle. Fuel 2022;325:124760. https://doi.org/10.1016/j.fuel.2022.124760.
[143] Zheng Y, Sukma MS, Scott SA. The exploration of NiO/Ca2Fe2O5/CaO in chemical looping methane conversion for syngas and H2 production. Chemical Engineering Journal 2023;465. https://doi.org/10.1016/j.cej.2023.142779.
[144] Pereira RJL, Argyris PA, Spallina V. A comparative study on clean ammonia production using chemical looping based technology. Appl Energy 2020;280:115874.
[145] de Caprariis B, Damizia M, De Filippis P, Bracciale MP. The role of Al2O3, MgO and CeO2 addition on steam iron process stability to produce pure and renewable hydrogen. Int J Hydrogen Energy 2021;46:39067–78. https://doi.org/10.1016/j.ijhydene.2021.09.135.
[146] Ortiz M, Abad A, De Diego LF, García-Labiano F, Gayán P, Adánez J. Optimization of hydrogen production by Chemical-Looping auto-thermal Reforming working with Ni-based oxygen-carriers. Int J Hydrogen Energy 2011;36:9663–72. https://doi.org/10.1016/J.IJHYDENE.2011.05.025.
[147] Shanmugam V, Neuberg S, Zapf R, Pennemann H, Kolb G. Hydrogen production over highly active Pt based catalyst coatings by steam reforming of methanol: Effect of support and co-support. Int J Hydrogen Energy 2020;45:1658–70. https://doi.org/10.1016/J.IJHYDENE.2019.11.015.
[148] Sun Z, Lu DY, Symonds RT, Hughes RW. Chemical looping reforming of CH4 in the presence of CO2 using ilmenite ore and NiO-modified ilmenite ore oxygen carriers. Chemical Engineering Journal 2020;401:123481. https://doi.org/10.1016/J.CEJ.2019.123481.
[149] Huang Z, He F, Chen D, Zhao K, Wei G, Zheng A, et al. Investigation on reactivity of iron nickel oxides in chemical looping dry reforming. Energy 2016;116:53–63.

[150] Hu J, Chen S, Xiang W. Ni, Co and Cu-promoted iron-based oxygen carriers in methane-fueled chemical looping hydrogen generation process. Fuel Processing Technology 2021;221. https://doi.org/10.1016/j.fuproc.2021.106917.
[151] Li Z, Feng X, Gu Z, Lu C, Li D, Zhu X, et al. Enhanced performance of the CeO2[sbnd]MgO oxygen carrier by NiO for chemical looping CO2 splitting. Fuel Processing Technology 2022;225. https://doi.org/10.1016/j.fuproc.2021.107045.
[152] Baser DS, G. Nadgouda S, S. Joshi A, Fan L-S. 110th Anniversary: Indirect Partial Oxidation of Methane Using a Counter-Current Moving-Bed Chemical Looping Configuration for Enhanced Syngas Production. Industrial & Engineering Chemistry Research 2019;58:16407–16. https://doi.org/10.1021/acs.iecr.9b02520.
[153] Zhu M, E. Wachs I. Iron-Based Catalysts for the High-Temperature Water–Gas Shift (HT-WGS) Reaction: A Review. ACS Catal 2016;6:722–32. https://doi.org/10.1021/acscatal.5b02594.
[154] de Leeuwe C, Abbas SZ, Argyris PA, Zaidi A, Amiero A, Poultson S, et al. Thermochemical syngas generation via solid looping process: an experimental demonstration using Fe-based material. Chemical Engineering Journal 2023;453:139791.
[155] Iftikhar S, Martin W, Gao Y, Yu X, Wang I, Wu Z, et al. LaNixFe1−xO3 as flexible oxygen or carbon carriers for tunable syngas production and CO2 utilization. Catal Today 2023;416:113854. https://doi.org/10.1016/J.CATTOD.2022.07.022.
[156] Padula S, Tregambi C, Troiano M, Di Benedetto A, Salatino P, Landi G, et al. Chemical Looping Reforming with Perovskite-Based Catalysts for Thermochemical Energy Storage. Energies (Basel) 2022;15. https://doi.org/10.3390/en15228556.
[157] Yin X, Wang S, Wang B, Shen L. Perovskite-type LaMn1−xBxO3+δ (B = Fe, CO and Ni) as oxygen carriers for chemical looping steam methane reforming. Chemical Engineering Journal 2021;422. https://doi.org/10.1016/j.cej.2021.128751.
[158] Valderrama G, Kiennemann A, Goldwasser MR. Dry reforming of CH4 over solid solutions of LaNi1−xCoxO3. Catal Today 2008;133–135:142–8. https://doi.org/10.1016/J.CATTOD.2007.12.069.
[159] Fernández JR, Abanades JC. Sorption enhanced reforming of methane combined with an iron oxide chemical loop for the production of hydrogen with CO2 capture: Conceptual design and operation strategy. Appl Therm Eng 2017;125:811–22. https://doi.org/10.1016/j.applthermaleng.2017.07.063.
[160] Gao Z, Zeng D, Wu S, Ren S, Zhou F, Gao M, et al. High-purity hydrogen production from real biomass pyrolysis vapors via a chemical looping process. Sustain Energy Fuels 2023;7:2200–8. https://doi.org/10.1039/d2se01635d.
[161] Deshpande N, Majumder A, Qin L, Fan LS. High-pressure redox behavior of iron-oxide-based oxygen carriers for syngas generation from methane. Energy and Fuels 2015;29:1469–78. https://doi.org/10.1021/ef5025998.

[162] Voitic G, Nestl S, Lammer M, Wagner J, Hacker V. Pressurized hydrogen production by fixed-bed chemical looping. Appl Energy 2015;157:399–407. https://doi.org/10.1016/j.apenergy.2015.03.095.
[163] Hsieh TL, Xu D, Zhang Y, Nadgouda S, Wang D, Chung C, et al. 250 kWth high pressure pilot demonstration of the syngas chemical looping system for high purity H2 production with CO2 capture. Appl Energy 2018;230:1660–72. https://doi.org/10.1016/J.APENERGY.2018.09.104.
[164] Chuayboon S, Abanades S, Rodat S. Solar chemical looping reforming of methane combined with isothermal H2O/CO2 splitting using ceria oxygen carrier for syngas production. Journal of Energy Chemistry 2020;41:60–72. https://doi.org/10.1016/j.jechem.2019.05.004.
[165] Ugwu A, Arnaiz del Pozo C, Zaabout A, Nazir SM, Kalendar NU, Cloete S, et al. Gas switching technology: Economic attractiveness for chemical looping applications and scale up experience to 50 kWth. International Journal of Greenhouse Gas Control 2022;114:103593. https://doi.org/10.1016/J.IJGGC.2022.103593.
[166] Zacharias R, Visentin S, Bock S, Hacker V. High-pressure hydrogen production with inherent sequestration of a pure carbon dioxide stream via fixed bed chemical looping. Int J Hydrogen Energy 2019;44:7943–57. https://doi.org/10.1016/j.ijhydene.2019.01.257.
[167] Alexandros Argyris P, de Leeuwe C, Abbas SZ, Amieiro A, Poultson S, Wails D, et al. Chemical looping reforming for syngas generation at real process conditions in packed bed reactors: An experimental demonstration. Chemical Engineering Journal 2022;435. https://doi.org/10.1016/j.cej.2022.134883.
[168] Gallucci F, Van Sint Annaland M, Kuipers JAM. Autothermal reforming of methane with integrated CO2 capture in a novel fluidized bed membrane reactor. Part 1: Experimental demonstration. Top Catal 2008;51:133–45. https://doi.org/10.1007/s11244-008-9126-8.
[169] Gallucci F, Van Sint Annaland M, Kuipers JAM. Autothermal reforming of methane with integrated CO2 capture in a novel fluidized bed membrane reactor. Part 2 comparison of reactor configurations. Top Catal 2008;51:146–57. https://doi.org/10.1007/s11244-008-9127-7.
[170] Medrano JA, Potdar I, Melendez J, Spallina V, Pacheco-Tanaka DA, van Sint Annaland M, et al. The membrane-assisted chemical looping reforming concept for efficient H2 production with inherent CO2 capture: Experimental demonstration and model validation. Appl Energy 2018;215:75–86. https://doi.org/10.1016/J.APENERGY.2018.01.087.
[171] Samprón I, de Diego LF, García-Labiano F, Izquierdo MT, Abad A, Adánez J. Biomass Chemical Looping Gasification of pine wood using a synthetic Fe2O3/Al2O3 oxygen carrier

in a continuous unit. Bioresour Technol 2020;316. https://doi.org/10.1016/j.biortech.2020.123908.
[172] Condori O, García-Labiano F, de Diego LF, Izquierdo MT, Abad A, Adánez J. Biomass chemical looping gasification for syngas production using ilmenite as oxygen carrier in a 1.5 kWth unit. Chemical Engineering Journal 2021;405:126679. https://doi.org/10.1016/J.CEJ.2020.126679.
[173] Ge H, Guo W, Shen L, Song T, Xiao J. Biomass gasification using chemical looping in a 25 kWth reactor with natural hematite as oxygen carrier. Chemical Engineering Journal 2016;286:174–83. https://doi.org/10.1016/J.CEJ.2015.10.092.
[174] Bracciale MP, Damizia M, De Filippis P, de Caprariis B. Clean Syngas and Hydrogen Co-Production by Gasification and Chemical Looping Hydrogen Process Using MgO-Doped Fe2O3 as Redox Material. Catalysts 2022;12. https://doi.org/10.3390/catal12101273.
[175] Zhao K, Fang X, Huang Z, Wei G, Zheng A, Zhao Z. Hydrogen-rich syngas production from chemical looping gasification of lignite by using NiFe2O4 and CuFe2O4 as oxygen carriers. Fuel 2021;303. https://doi.org/10.1016/j.fuel.2021.121269.
[176] Huijun G, Laihong S, Fei F, Shouxi J. Experiments on biomass gasification using chemical looping with nickel-based oxygen carrier in a 25 kWth reactor. Appl Therm Eng 2015;85:52–60. https://doi.org/10.1016/j.applthermaleng.2015.03.082.
[177] Huang X, Wu J, Wang M, Ma X, Jiang E, Hu Z. Syngas production by chemical looping gasification of rice husk using Fe-based oxygen carrier. Journal of the Energy Institute 2020;93:1261–70. https://doi.org/10.1016/j.joei.2019.11.009.
[178] Shen X, Yan F, Zhang Z, Li C, Zhao S, Zhang Z. Enhanced and environment-friendly chemical looping gasification of crop straw using red mud as a sinter-resistant oxygen carrier. Waste Management 2021;121:354–64. https://doi.org/10.1016/j.wasman.2020.12.028.
[179] Pan Q, Ma L, Du W, Yang J, Ao R, Yin X, et al. Hydrogen-enriched syngas production by lignite chemical looping gasification with composite oxygen carriers of phosphogypsum and steel slag. Energy 2022;241. https://doi.org/10.1016/j.energy.2021.122927.
[180] Liu Q, Hu C, Peng B, Liu C, Li Z, Wu K, et al. High H2/CO ratio syngas production from chemical looping co-gasification of biomass and polyethylene with CaO/Fe2O3 oxygen carrier. Energy Convers Manag 2019;199:111951. https://doi.org/10.1016/J.ENCONMAN.2019.111951.
[181] Guozhen S, Wenzheng L, Kun W, Jialu L, Weiwei C, Laishun Y, et al. Investigation on hydrogen-rich syngas preparation from high wet sludge mixed with sawdust based on iron oxygen carrier. Fuel 2023;343. https://doi.org/10.1016/j.fuel.2023.127853.
[182] Zhu X, Zhang J, Yan J, Shen L. Characteristic Evaluation and Process Simulation of CuFe2O4 as Oxygen Carriers in Coal Chemical Looping Gasification. ACS Omega 2021;6:4783–92. https://doi.org/10.1021/acsomega.0c05691.

[183] Condori O, García-Labiano F, de Diego LF, Izquierdo MT, Abad A, Adánez J. Biomass chemical looping gasification for syngas production using LD Slag as oxygen carrier in a 1.5 kWth unit. Fuel Processing Technology 2021;222. https://doi.org/10.1016/j.fuproc.2021.106963.

[184] Farajollahi H, Hossainpour S. Techno-economic assessment of biomass and coal co-fueled chemical looping combustion unit integrated with supercritical CO2 cycle and Organic Rankine cycle. Energy 2023;274:127309. https://doi.org/10.1016/J.ENERGY.2023.127309.

[185] Tesio U, Guelpa E, Verda V. Integration of thermochemical energy storage in concentrated solar power. Part 1: Energy and economic analysis/optimization. Energy Conversion and Management: X 2020;6. https://doi.org/10.1016/j.ecmx.2020.100039.

[186] Zhao Y jie, Zhang Y ke, Cui Y, Duan Y yuan, Huang Y, Wei G qiang, et al. Pinch combined with exergy analysis for heat exchange network and techno-economic evaluation of coal chemical looping combustion power plant with CO2 capture. Energy 2022;238. https://doi.org/10.1016/j.energy.2021.121720.

[187] Farajollahi H, Hossainpour S. Macroscopic model-based design and techno-economic assessment of a 300 MWth in-situ gasification chemical looping combustion plant for power generation and CO2 capture. Fuel Processing Technology 2022;231. https://doi.org/10.1016/j.fuproc.2022.107244.

[188] Wang Y, Zhu L, He Y, Zhou Q, Hao Q. Tech-economic assessment of chemical looping combustion coupled with the combined supercritical CO2 Brayton cycle and ORC for power generation. J Taiwan Inst Chem Eng 2021;129:197–206. https://doi.org/10.1016/j.jtice.2021.09.010.

[189] Diglio G, Bareschino P, Mancusi E, Pepe F. Techno-Economic Evaluation of a Small-Scale Power Generation Unit Based on a Chemical Looping Combustion Process in Fixed Bed Reactor Network. Ind Eng Chem Res 2018;57:11299–311. https://doi.org/10.1021/acs.iecr.8b02378.

[190] Mancuso L, Cloete S, Chiesa P, Amini S. Economic assessment of packed bed chemical looping combustion and suitable benchmarks. International Journal of Greenhouse Gas Control 2017;64:223–33. https://doi.org/10.1016/j.ijggc.2017.07.015.

[191] Sayeed I, Kibria MA, Bhattacharya S. Process modelling and techno-economic analysis of a 550MWe chemical looping power plant with victorian brown coal. International Journal of Greenhouse Gas Control 2022;113. https://doi.org/10.1016/j.ijggc.2021.103547.

[192] Saqline S, Chua ZY, Liu W. Coupling chemical looping combustion of solid fuels with advanced steam cycles for CO2 capture: A process modelling study. Energy Convers Manag 2021;244:114455. https://doi.org/10.1016/J.ENCONMAN.2021.114455.

[193] Iloeje CO, Zhao Z, Ghoniem AF. Design and techno-economic optimization of a rotary chemical looping combustion power plant with CO2 capture. Appl Energy 2018;231:1179–90. https://doi.org/10.1016/j.apenergy.2018.09.058.
[194] Cormos CC. Chemical Looping with Oxygen Uncoupling (CLOU) concepts for high energy efficient power generation with near total fuel decarbonisation. Appl Therm Eng 2017;112:924–31. https://doi.org/10.1016/j.applthermaleng.2016.10.156.
[195] Bartocci P, Abad A, Mattisson T, Cabello A, Loscertales M de las O, Negredo TM, et al. Bioenergy with Carbon Capture and Storage (BECCS) developed by coupling a Pressurised Chemical Looping combustor with a turbo expander: How to optimize plant efficiency. Renewable and Sustainable Energy Reviews 2022;169. https://doi.org/10.1016/j.rser.2022.112851.
[196] Cabello A, Mendiara T, Teresa Izquierdo M, García-Labiano F, Abad A. Energy use of biogas through chemical looping technologies with low-cost oxygen carriers. Fuel 2023;344. https://doi.org/10.1016/j.fuel.2023.128123.
[197] Bhui B, Prabu V. Techno-economic evaluation of electronic waste based oxygen carriers for co-chemical looping combustion of coal and biomass integrated combined cycle power generating systems. Energy Convers Manag 2021;236. https://doi.org/10.1016/j.enconman.2021.114075.
[198] Li G, Chang Y, Liu T, Yu Z, Liu Z, Liu F, et al. Hydrogen element flow and economic analyses of a coal direct chemical looping hydrogen generation process. Energy 2020;206. https://doi.org/10.1016/j.energy.2020.118243.
[199] He Y, Zhu L, Li L, Liu G. Hydrogen and Power Cogeneration Based on Chemical Looping Combustion: Is It Capable of Reducing Carbon Emissions and the Cost of Production? Energy and Fuels 2020;34:3501–12. https://doi.org/10.1021/acs.energyfuels.9b04157.
[200] Zhu L, He Y, Li L, Wu P. Tech-economic assessment of second-generation CCS: Chemical looping combustion. Energy 2018;144:915–27. https://doi.org/10.1016/j.energy.2017.12.047.
[201] Astolfi M, Diego ME, Romano M, Abanades JC. Integration of a novel Chemical Looping Combustion reactor into a thermochemical energy storage system. Energy Convers Manag 2023;291:116985. https://doi.org/10.1016/J.ENCONMAN.2023.116985.
[202] Saghafifar M, Schnellmann MA, Scott SA. Chemical looping electricity storage. Appl Energy 2020;279:115553. https://doi.org/10.1016/J.APENERGY.2020.115553.
[203] Cormos AM, Petrescu L, Cormos CC. Techno-economic implications of time-flexible operation for iron-based chemical looping combustion cycle with energy storage capability. Energy 2023;278:127746. https://doi.org/10.1016/J.ENERGY.2023.127746.

[204] Argyris PA, Wong J, Wright A, Pereira LMC, Spallina V. Reducing the cost of low-carbon hydrogen production via emerging chemical looping process. Energy Convers Manag 2023;277. https://doi.org/10.1016/j.enconman.2022.116581.
[205] Nazir SM, Cloete JH, Cloete S, Amini S. Pathways to low-cost clean hydrogen production with gas switching reforming. Int J Hydrogen Energy 2021;46:20142–58. https://doi.org/10.1016/j.ijhydene.2020.01.234.
[206] Khan MN, Shamim T. Techno-economic assessment of a plant based on a three reactor chemical looping reforming system. Int J Hydrogen Energy 2016;41:22677–88.
[207] Wassie SA, Cloete S, Spallina V, Gallucci F, Amini S, van Sint Annaland M. Techno-economic assessment of membrane-assisted gas switching reforming for pure H2 production with CO2 capture. International Journal of Greenhouse Gas Control 2018;72:163–74. https://doi.org/10.1016/j.ijggc.2018.03.021.
[208] Spallina V, Pandolfo D, Battistella A, Romano MC, Van Sint Annaland M, Gallucci F. Techno-economic assessment of membrane assisted fluidized bed reactors for pure H2 production with CO2 capture. Energy Convers Manag 2016;120:257–73. https://doi.org/10.1016/J.ENCONMAN.2016.04.073.
[209] Spallina V, Motamedi G, Gallucci F, van Sint Annaland M. Techno-economic assessment of an integrated high pressure chemical-looping process with packed-bed reactors in large scale hydrogen and methanol production. International Journal of Greenhouse Gas Control 2019;88:71–84.
[210] Xiang D, Li P, Xia Y. Conceptual design and techno-economic analysis of a novel propane dehydrogenation process integrated with chemical looping combustion and CO2 hydrogenation. Energy Convers Manag 2023;281:116820. https://doi.org/10.1016/J.ENCONMAN.2023.116820.
[211] Yang Q, Li X, Yang Q, Huang W, Yu P, Zhang D. Opportunities for CO2 utilization in coal to green fuel process: optimal design and performance evaluation. ACS Sustain Chem Eng 2019;8:1329–42.
[212] Edrisi A, Mansoori Z, Dabir B. Urea synthesis using chemical looping process–Techno-economic evaluation of a novel plant configuration for a green production. International Journal of Greenhouse Gas Control 2016;44:42–51.
[213] Xiang D, Li P, Yuan X. System optimization and performance evaluation of shale gas chemical looping reforming process for efficient and clean production of methanol and hydrogen. Energy Convers Manag 2020;220:113099. https://doi.org/10.1016/J.ENCONMAN.2020.113099.
[214] Labbaf B, Tabatabaei M, Mostafavi E, Tijani M, Mahinpey N. Methanol production via integrated methane reforming and chemical looping combustion: Process simulation

and techno-economic assessment. Process Safety and Environmental Protection 2021;148:1346–56. https://doi.org/10.1016/j.psep.2021.03.008.
[215] Ning Asih SA, Syauqi A, Purwanto WW. Techno-enviro-economic analysis of integrated direct chemical looping coal-based power generation and methanol synthesis using renewable hydrogen. Journal of CO2 Utilization 2021;54. https://doi.org/10.1016/j.jcou.2021.101768.
[216] Zhou H, Meng W, Wang D, Li G, Li H, Liu Z, et al. A novel coal chemical looping gasification scheme for synthetic natural gas with low energy consumption for CO2 capture: Modelling, parameters optimization, and performance analysis. Energy 2021;225. https://doi.org/10.1016/j.energy.2021.120249.
[217] Li G, Chang Y, Chen L, Liu F, Ma S, Wang F, et al. Process design and economic assessment of butanol production from lignocellulosic biomass via chemical looping gasification. Bioresour Technol 2020;316. https://doi.org/10.1016/j.biortech.2020.123906.
[218] Zhou X, Li G, Liu F, Li N. Production of ethanol from corn straw based on chemical looping gasification: Economic analysis. Bioresour Technol 2022;360:127568. https://doi.org/10.1016/J.BIORTECH.2022.127568.
[219] Nazir SM, Morgado JF, Bolland O, Quinta-Ferreira R, Amini S. Techno-economic assessment of chemical looping reforming of natural gas for hydrogen production and power generation with integrated CO2 capture. International Journal of Greenhouse Gas Control 2018;78:7–20. https://doi.org/10.1016/j.ijggc.2018.07.022.
[220] Dumbrava ID, Cormos CC. Techno-economical evaluations of decarbonized hydrogen production based on direct biogas conversion using thermo-chemical looping cycles. Int J Hydrogen Energy 2021;46:23149–63. https://doi.org/10.1016/J.IJHYDENE.2021.04.142.
[221] Surywanshi GD, Patnaikuni VS, Vooradi R, Anne SB. 4-E and life cycle analyses of a supercritical coal direct chemical looping combustion power plant with hydrogen and power co-generation. Energy 2021;217. https://doi.org/10.1016/j.energy.2020.119418.
[222] Norouzi N;, Talebi, Saeed. Exergy, Economical and Environmental Analysis of a Natural Gas Direct Chemical Looping Carbon Capture and Formic Acid-Based Hydrogen Storage System. vol. 41. 2022.
[223] Xiang D, Li P, Yuan X. System optimization and performance evaluation of shale gas chemical looping reforming process for efficient and clean production of methanol and hydrogen. Energy Convers Manag 2020;220. https://doi.org/10.1016/j.enconman.2020.113099.
[224] Pan X, Ma J, Hu X, Guo Q. Energy and economic analysis of a hydrogen and ammonia co-generation system based on double chemical looping. Chin J Chem Eng 2021;36:190–8. https://doi.org/10.1016/j.cjche.2020.10.007.

[225] Xiang D, Li P, Xia Y. Conceptual design and techno-economic analysis of a novel propane dehydrogenation process integrated with chemical looping combustion and CO2 hydrogenation. Energy Convers Manag 2023;281. https://doi.org/10.1016/j.enconman.2023.116820.

[226] Khani L, Tabriz ZH, Mohammadpourfard M, Gökçen Akkurt G. Energy and exergy analysis of combined power, methanol, and light olefin generation system fed with shale gas. Sustain Cities Soc 2022;87:104214. https://doi.org/10.1016/J.SCS.2022.104214.

[227] Chen JG, Crooks RM, Seefeldt LC, Bren KL, Morris Bullock R, Darensbourg MY, et al. Beyond fossil fuel–driven nitrogen transformations. Science (1979) 2018;360. https://doi.org/10.1126/science.aar6611.

[228] Ye TN, Park SW, Lu Y, Li J, Sasase M, Kitano M, et al. Vacancy-enabled N2 activation for ammonia synthesis on an Ni-loaded catalyst. Nature 2020;583:391–5. https://doi.org/10.1038/s41586-020-2464-9.

[229] Iriawan H, Andersen SZ, Zhang X, Comer BM, Barrio J, Chen P, et al. Methods for nitrogen activation by reduction and oxidation. Nature Reviews Methods Primers 2021;1:56. https://doi.org/10.1038/s43586-021-00053-y.

[230] Wang L, Xia M, Wang H, Huang K, Qian C, Maravelias CT, et al. Greening Ammonia toward the Solar Ammonia Refinery. Joule 2018;2:1055–74. https://doi.org/10.1016/j.joule.2018.04.017.

[231] Liu X, Elgowainy A, Wang M. Life cycle energy use and greenhouse gas emissions of ammonia production from renewable resources and industrial by-products. Green Chemistry 2020;22:5751–61. https://doi.org/10.1039/d0gc02301a.

[232] Zhu X, Imtiaz Q, Donat F, Müller CR, Li F. Chemical looping beyond combustion-a perspective. Energy Environ Sci 2020;13:772–804. https://doi.org/10.1039/c9ee03793d.

[233] Lai Q, Cai T, Tsang SCE, Chen X, Ye R, Xu Z, et al. Chemical looping based ammonia production—A promising pathway for production of the noncarbon fuel. Sci Bull (Beijing) 2022;67:2124–38. https://doi.org/10.1016/j.scib.2022.09.013.

[234] E. Gálvez M, Halmann M, Steinfeld A. Ammonia Production via a Two-Step Al2O3/AlN Thermochemical Cycle. 1. Thermodynamic, Environmental, and Economic Analyses. Industrial & Engineering Chemistry Research 2007;46:2042–6. https://doi.org/10.1021/ie061550u.

[235] Laassiri S, Zeinalipour-Yazdi CD, Catlow CRA, Hargreaves JSJ. The potential of manganese nitride based materials as nitrogen transfer reagents for nitrogen chemical looping. Appl Catal B 2018;223:60–6. https://doi.org/10.1016/J.APCATB.2017.04.073.

[236] Gao W, Guo J, Wang P, Wang Q, Chang F, Pei Q, et al. Production of ammonia via a chemical looping process based on metal imides as nitrogen carriers. Nature Energy 2018 3:12 2018;3:1067–75. https://doi.org/10.1038/s41560-018-0268-z.

[237] Wang X, Su M, Zhao H. Process design and exergy cost analysis of a chemical looping ammonia generation system using AlN/Al2O3 as a nitrogen carrier. Energy 2021;230:120767. https://doi.org/10.1016/J.ENERGY.2021.120767.

Chapter 2

Assessment of a multistep revamping methodology for cleaner steel production

This chapter is based on the following paper

Palone, O., Barberi, G., Di Gruttola, F., Gagliardi, G. G., Cedola, L., & Borello, D. (2022). Assessment of a multistep revamping methodology for cleaner steel production. Journal of Cleaner Production, 381, 135146

Abstract

In this chapter a novel revamping methodology is proposed to achieve a deep decarbonization of integrated steel mills without reducing steel production levels. Such a method encompasses four successive steps involving cleaner and more energy efficient technologies: step 1, partial replacement of coke with recycled plastic in a conventional Blast Furnace – Basic Oxygen Furnace (BF-BOF) plant; step 2, implementation of a Direct Reduction-Electric Arc Furnace (DR-EAF) line combined with the BF-BOF plant; step 3, complete shut-down of the BF-BOF line and full operation of two DR-EAF lines fed by CH_4; step 4, installation of an alkaline electrolyzer and use of 100% green H_2 as a reducing agent in the DR plants. The gradual replacement of the integrated steel mill with DR-EAF lines causes a progressive drop in CO_2 emissions, ranging from 8.5 Mt/y at step 0 to a minimum of 0.68 Mt/y at step 4 (92% decrease). Coke replacement with recycled plastic in the blast furnace of step 1 leads to a slight decrease in CO_2 emissions without altering the structural layout of the plant. In step 2, the combined operation of BF-BOF and DR-EAF lines causes a 39% decrease in CO_2 emission compared to the initial configuration, while keeping total steel production constant. Step 3 involves two DR-EAF lines fed by CH_4 and reduces the CO_2 emissions by 75% compared to the initial configuration. The operation of two DR-EAF lines increases the electricity consumption, especially when 100% green H_2 is involved as a reducing agent in step 4. By increasing the scrap mass fraction in the EAFs of step 4, both electricity and H_2 demands of the DR plant decrease, while the CO_2 emission levels remain almost unchanged. By assuming an initial 10% scrap mass fraction at the EAFs inlet of step 4, the demand of green hydrogen is significant, thus requiring the installation of a 1.42 GW electrolyzer. The capital expenditure estimated upon completion of the revamping methodology amounts to approximately 2.97 B€. The transition towards a full decarbonization of steel production technologies is demonstrated to be technically feasible and at the same time strictly dependent upon the large availability of low-emissions electric power, scrap material and H_2 sources. Therefore, alternative pathways for an earlier decarbonization of hard-to-abate industries and for large scale syngas/H_2 production need to be considered.

2.1 Introduction

The iron and steel industry represents the second largest industry sector worldwide in terms of production volumes after the cement industry and the first in terms of CO_2 emissions. Due to economic growth of developing countries, the production of steel and iron has been continuously increasing over the years [1]. In 2019, the steel sector globally consumed about 35.6 EJ of energy (20% of the total industrial consumption) and emitted 2.6 Gt of CO_2 (30% of the total CO_2 industrial emission) [2]. Currently, the two most widespread steel production routes are represented by the Blast Furnace – Basic Oxygen Furnace (BF-BOF), also known as integrated steel mill, and the Direct Reduction – Electric Arc Furnace (DR-EAF) plants. The BF-BOF pathway covers around 70% of world steel production [3] and it is heavily reliant on fossil fuels, such as coking coal and pulverized coal, making it a hard-to-abate route. In particular, blast furnaces are responsible for 70% of the total energy consumption in the steel industry [4] and their optimization is of utmost importance to address climate change. The Ultra-Low CO_2 Steelmaking (ULCOS) project launched in 2004 gathered all major European Union steel plants, universities, research institutes and engineering partners with the aim of achieving 50% CO_2 emissions reduction in steel production [5], [6]. Four promising technologies were identified for this purpose:

a) the Top Gas Recycling Blast Furnace (TGR-BF) integrated with Carbon Capture and Storage (CCS);

b) the Hisarna smelting technology integrated with CCS;

c) the Direct-Reduced Iron (DRI) technology;

d) iron ore electrolysis.

In TGR-BF technology, oxygen is used in place of air in the blast furnace, so that N_2 is not present in the off gases, and then vacuum pressure swing adsorption is employed for CO_2 permanent sequestration or conversion to liquid fuels. However, some drawbacks related to CO_2 transport and storage have to be overcome [7] as well as public criticism regarding the destructive potential of this technology [8]. At the present moment only one steel plant retrofitted with CCS technology is operational in the world (located in Abu Dhabi). Hisarna technology combines the Cyclone Converting Furnace (CCF) of the Isarna process with the Hismelt Smelting Reduction Vessel [9]. This process does not require iron ore pretreatment in a sinter plant and coke production, thus increasing the energy efficiency of the steelmaking process and reducing the corresponding CO_2 emissions by at least 20% [10]. In the DRI technology (ULCORED Ultra Low CO_2 iron ores REDuction), coke is replaced by natural gas or syngas from biomass and then solid iron is melted in an electric arc furnace

(EAF) [11]. The investigation of this technology aimed at optimizing natural gas consumption for direct reduced iron production and a carbon capture and storage unit was also integrated. Iron ore electrolysis uses electricity to perform the reduction process [12]. This technology is still immature and far from commercial feasibility. Within the ULCOWIN and ULCOLYSIS (Ultra Low CO_2 iron ores electroWINning and electroLYSIS, respectively) technologies, the reduction process is performed at low temperatures (110 °C) in an alkaline (NaOH) electrolytic solution and high temperatures (1600 °C) in a molten oxide solution, respectively [3].

2.1.1 Hydrogen in steel production

In light of current climate objectives and with the reduction in renewable energy cost, process electrification and hydrogen utilization in steelmaking are attracting growing interest as new pathways for steelmaking decarbonization. Industrialized water electrolysis technologies for hydrogen production include alkaline water electrolysis and polymeric electrolyte membrane (PEM) electrolysis. The structure of the PEM electrolyzer is similar to that of the alkaline electrolyzer. The main difference is in the use of a different electrolyte: a polymeric perfluoro sulfonic membrane, Nafion, for the PEM and a 30% wt. KOH solution or 25%wt. NaOH solution as electrolyte for an alkaline device [13]. Two main routes can be identified for hydrogen utilization in the steel sector: the conversion to liquid fuels with captured CO_2 from exhaust gases, the direct utilization of H_2 as a reducing agent. In carbon capture and utilization (CCU) techniques, CO_2 is separated from off-gases and reacts with hydrogen from electrolysis to produce marketable hydrocarbons (e.g. methanol and dimethyl ether). Thyssenkrupp AG has carried out the development and technical implementation of such technology in the Carbon2Chem project [14]. The objective is to convert 20 Mt of CO_2 from German steel industry into chemicals and subsequently to reach large scale implementation. On the contrary, in H_2-based steel production hydrogen is the reducing agent for iron ore reduction either in BF units (alternative reducing agent) or in DR plants. Iron ore reduction by hydrogen was demonstrated to be technically feasible for the first time in 1999 in Trinidad using a fluidized bed reactor [15]. More recently, various projects around the world (especially in Europe) have addressed steel production by hydrogen. In 2016, SSAB, LKAB and Vattenfall launched the Hybrit project [4,5,16], with the aim of investigating green hydrogen application across the steel production phases such as iron ore sintering, iron ore pellets production, pellets reduction in a shaft furnace and subsequent steelmaking in an electric arc furnace. The H2FUTURE project was launched in 2017 and currently achieved the construction of the largest pilot plant based on hydrogen reduction in Linz, integrated with a 6 MW PEM electrolyzers [17]. Electrolyzer testing under rapid changing electric power load represents one of the main objectives of the project along with investigation of hydrogen application in the different steel manufacturing stages. The

GrInHy 2.0 project was signed by Salzgitter in 2019 for the realization of the world's most powerful high temperature electrolyzer. The main scope was to increase hydrogen production efficiency and contribute to the development of 100% H_2-based direct reduction of iron and subsequent steelmaking [18].

2.1.2 Literature review

Current academic research efforts are directed to assess the environmental impact of novel or hybrid concepts of steel mills, as well as proposing predictions relating to selected pathways to achieve "green" steel production [19]. In this section, a strong focus is given on modelling works relating to hydrogen application in steel production, which represents the ending point of the proposed methodology, and to the long-term impact of cleaner steel production routes on CO_2 emissions, material and energy consumption.

Hydrogen application in steel production has been investigated both in conventional blast furnaces and in more efficient direct reduction plants. In [20], Yilmaz et al. assess green hydrogen as an alternative reducing agent (ARA) in conventional blast furnaces, providing a maximum 21.4% CO_2 emissions reduction compared to pulverized coal injection. In [21], the same authors conduct Aspen Plus simulations on the injection of different kinds of direct reduced iron in a state-of-the-art blast furnace and demonstrate a maximum CO_2 emissions reduction of 26.7%. In [22] Hamadeh et al. develop a detailed model of the direct reduction shaft and validate it against two existing shaft furnaces of different scale. Subsequently, a model is developed in [23] by Patisson et al. to study direct reduction with H_2, showing that the reduction kinetics is faster and thus high metallization can be achieved in smaller shaft furnaces compared to H_2-CO blendings. Vogl et al. [24] have developed a model performing mass and energy balances of direct reduction with 100% hydrogen from water electrolysis. Cost competitiveness with the conventional BF-BOF route is demonstrated at a carbon price of 34 - 68 EUR/t_{CO2} and electricity costs of 40 EUR/MWh. In [25], alkaline electrolysis (AEL), polymer electrolyte membrane electrolysis (PEMEL) and solid oxide electrolysis (SOEL) are compared by Jacobash et al. for green steel production. While AEL technology is indicated as the best option, the expected equipment cost reduction in the SOEL can make it an interesting alternative in the future. Co-feed of H_2 and CH_4 is often proposed as a bridging technology in the next years. In [26], Muller et al. provide a comprehensive model of the Energiron/HYL direct reduction process coupled with hydrogen production by either SOEL or PEMEL. CO_2 emissions reduction by (maximum) 97.8% is demonstrated compared with the conventional route. A comparison between the two electrolysis technologies is also carried out, showing that a reduction of primary energy demand by 12.4% can be achieved by heat integration with SOEL. The flexibility in the inlet gas composition is finally highlighted when mixtures of CH_4 and H_2 are considered.

The comprehensive analysis of different pathways for a cleaner steel production is crucial to identify the optimal technology for governmental investments planning in the near and far future. Zhang et al. [27] explore different scenarios for China steel industry up to 2100, involving: the current and new policies introduced by the government; high electrification of production using EAF; coal-based and H_2-based DRI production. Despite of a dramatic reduction in CO_2 emissions in all cases, it is demonstrated that the electrification pathway requires 25-220 % more scrap and 25-40 % less iron ore than the national policies and DRI scenario. The deep electrification scenario also shows a reduction in energy consumption compared to the other scenarios. On the same line, in [28] Shen et al. develop an optimization model that illustrates the best pathways for realizing the decarbonization of the steel sector. Three main ways are identified: development of breakthrough technologies (hydrogen steelmaking and CCS); transition towards renewable electricity generation; change in the production structure by increasing the scrap fraction. Similarly, in [29] Flores-Grenoble et al. compare eight scenarios involving CCUS (methanol production from all the captured H_2 and part of the captured CO_2 with storage of the remaining CO_2), CCU (methanol production from all the captured CO_2 and H_2 with additional H_2 production from electrolysis), H_2 steelmaking and conventional steel production. They showed that before a large availability of renewable energy is established, CCUS can achieve 55% CO_2 emissions reduction with a mixed grid carbon intensity. In [30], a model based on material flow analysis is presented for CO_2 emissions computation and subsequently applied to two case studies in China to assess possible optimization routes. The use of scrap dramatically reduces CO_2 emissions and decreases the power generation by the thermal power plant of the steel mill. Multi-objective optimization of cost, energy, CO_2 emissions, particulate matter intensity, SO_2 and NO_x are carried out in [31] by Huang et al. By taking out interrelated parameters (SO_2 and NO_X) from the calculation, the total variables number can be reduced and it results that byproduct reutilization and cleaner steel production are the most indicated strategies for optimization purposes, due to the high cost of upgrading equipment. Industrial symbiosis represents a promising opportunity for CO_2 and waste reduction/management as well as for process optimization. In [32], symbiotic measures for process optimization in an integrated steel mill are analyzed. The analysis concludes that off-gases (blast furnace gases BFG and coke oven gases COG) reutilization and selling off-site as fuel, along with deep sensible heat recovery of gaseous/solid flows represent more effective solutions than symbiotic measures with other enterprises. For more details on energy and material optimization in steel mills, a complete review work is available in [33]. The scope of this work is to propose and assess a multistep methodology aimed at achieving a gradual and deep decarbonization (as well as an energy optimization) of conventional steel production. Differently from the presented works, the analysis is entirely carried out through detailed simulations in Aspen Plus. Each step introduces promising solutions and

models that are retrieved from the literature. The most emitting units of the integrated steel mill (lime kiln, sinter plant, coke ovens, blast furnace, hot stoves, desulphurization, basic oxygen furnace, ladle metallurgy, continuous casting and hot rolling mills) and of the DR-EAF plants (direct reduction plant, electric arc furnace) are modelled. The model validation is performed by comparison with data reported in [34] by Santos et al. regarding an existing BF-BOF steel mill located in the coastal area of Western Europe and with technical reports by Tenova and Danieli for the DR-EAF steel mill. Material and energy balance results are discussed with emphasis on CO_2 emissions and energy consumption, including the electricity demands. Preliminary capital cost analysis is finally presented for the whole revamping methodology. In this way, the main benefits and drawbacks associated with the transition towards a fully decarbonized steel production are assessed, thus providing useful data for both public and private investments allocation in the forthcoming years.

2.2 Description of the revamping methodology

Achieving net-zero emissions in steel production requires a radical transformation in the process. For this purpose, a revamping methodology for steel plants is proposed and investigated, comprising four successive process steps. Each step must be considered with reference to the previous one and is described in the following paragraphs. In the first step, recycled plastic (polystyrene PS is taken as a reference) is injected into the blast furnace, thus partially substituting coke (Figure 2.1). Due to PS higher hydrogen content compared to coke or pulverized coal, it is expected to realize a deeper reduction of the iron ore as well as to decrease CO_2 emissions from the blast furnace [35]. Plastic injection is currently performed in a few steel plants in Europe and Japan, e.g. Voestalpine still mill in Linz.
Waste plastic coming from mechanical recycling (collection, washing, crushing and storage) [36] is stored and then sent towards the BFs where it is injected in the tuyeres as a reducing agent and as a fuel [37]. No plant variation is expected, though mass flow rates through the coke oven arrays are reduced compared to the initial configuration, since lower coke flow rates are required. In step 2, the implementation of a new DR-EAF line, composed of one direct reduction plant and two electric arc furnaces, is carried out (as illustrated in red in Figure 2.2). The choice of two electric arc furnaces instead of a single larger one is justified by a better flexibility of the whole plant. However, the integrated process with the BF-BOF line persists, since the new DR-EAF line cannot ensure the adequate production volumes by itself.

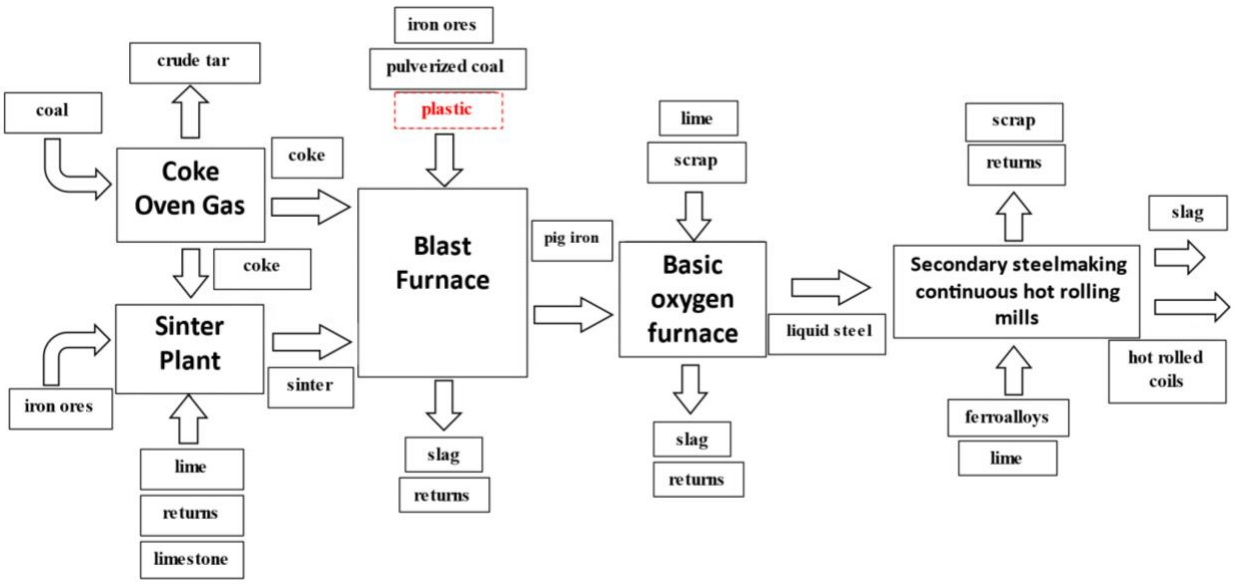

Figure 2.1. Simplified flowsheet of plant 1 configuration

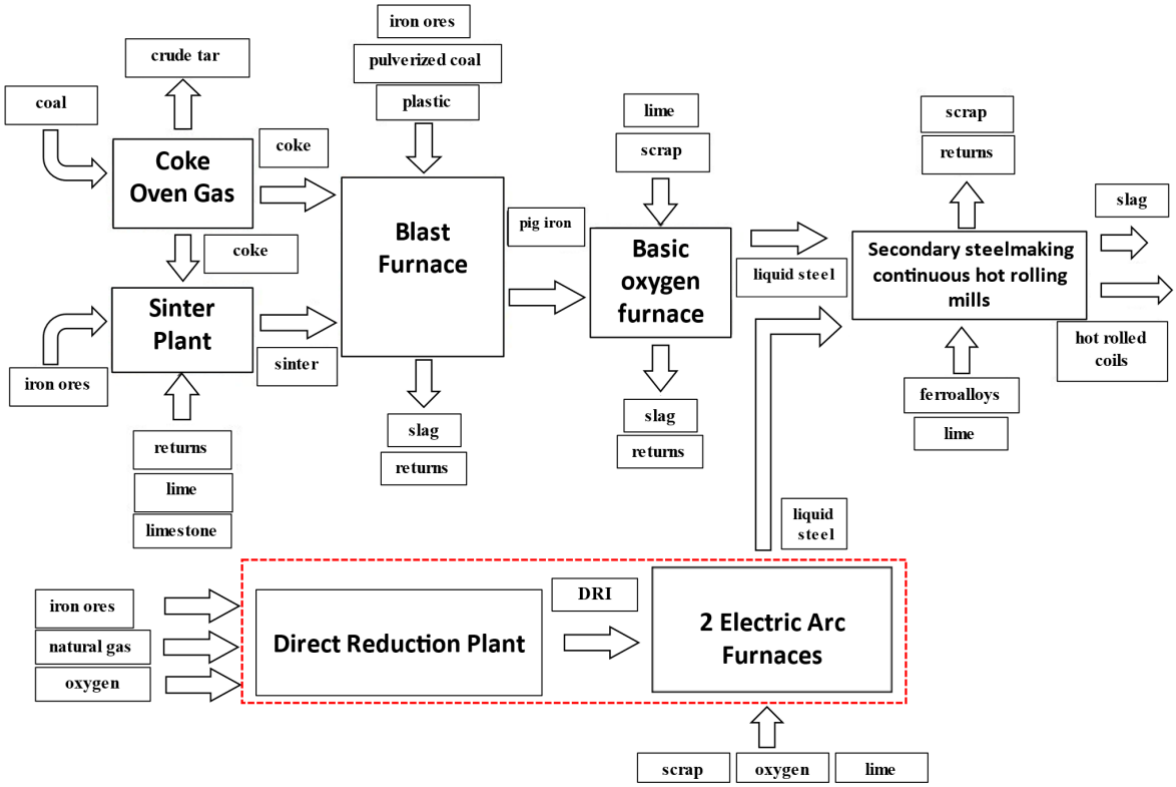

Figure 2.2. Simplified plant flowsheet of step 2 configuration

In step 3 (Figure 2.3), the shut-down of the BF-BOF line and the installation of an additional DR-EAF line are envisaged. The effects of blending hydrogen with methane as reducing agents are investigated in terms of CO_2 emissions reduction potential and energy consumption.

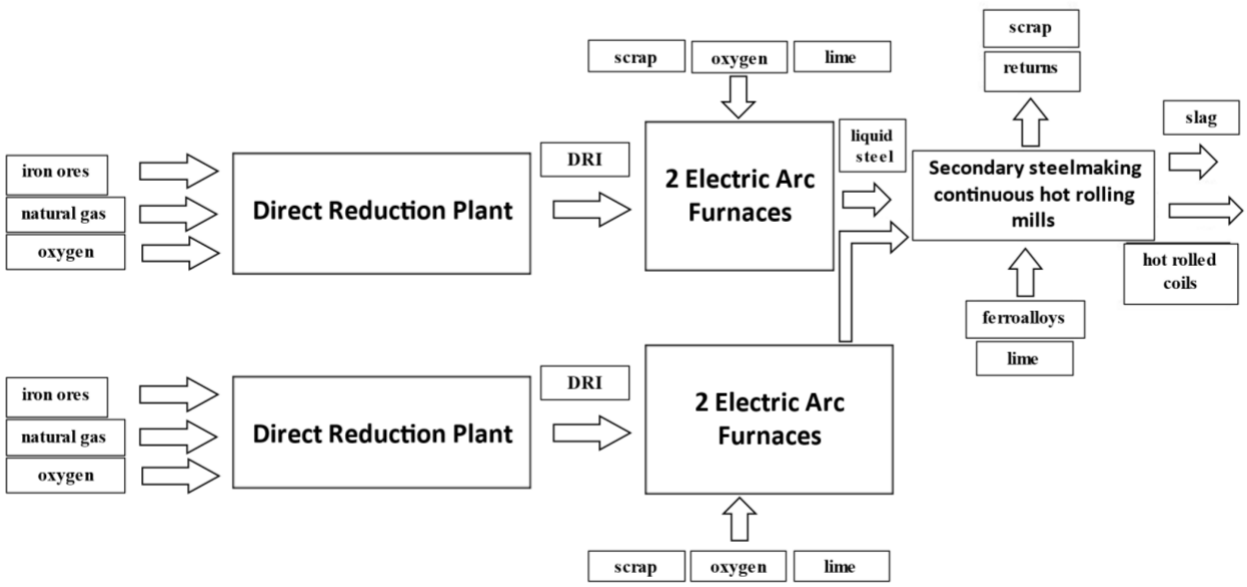

Figure 2.3. Simplified plant flowsheet of step 3 configuration

The last step (step 4) involves hydrogen as a reducing agent in place of natural gas in the two DR plants (Figure 2.3). Here, the DRI produced by the DR plant has no carbon content, so a certain amount of coal (or biochar) is injected in the EAFs to provide the required carbon content of steel.

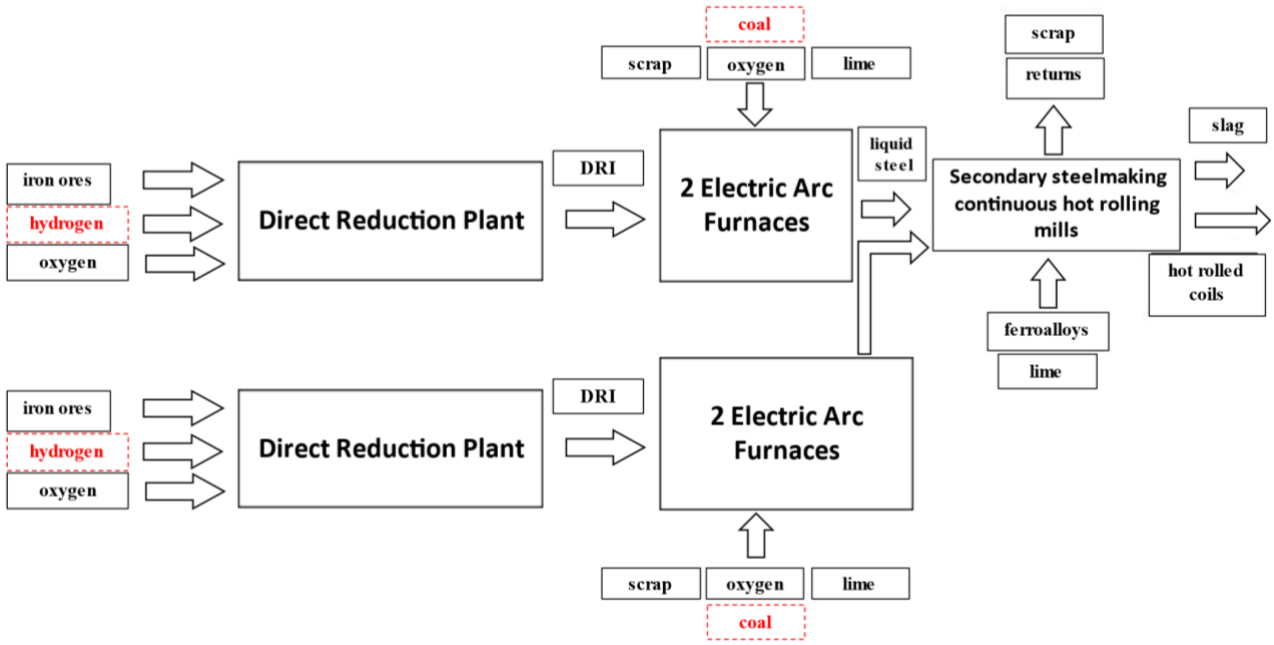

Figure 2.4. Simplified plant flowsheet of step 4 configuration

2.3 Method

2.3.1 Sinter plant and coke oven modelling

In the sinter plant, iron ores (mostly Fe_2O_3) are mixed with coke breeze, limestone, lime, olivine, quartzite, slag and returns from other units in order to produce a homogeneous solid mixture, i.e. the sinter. Figure 2.5 shows the simplified flowsheet of the sinter plant.

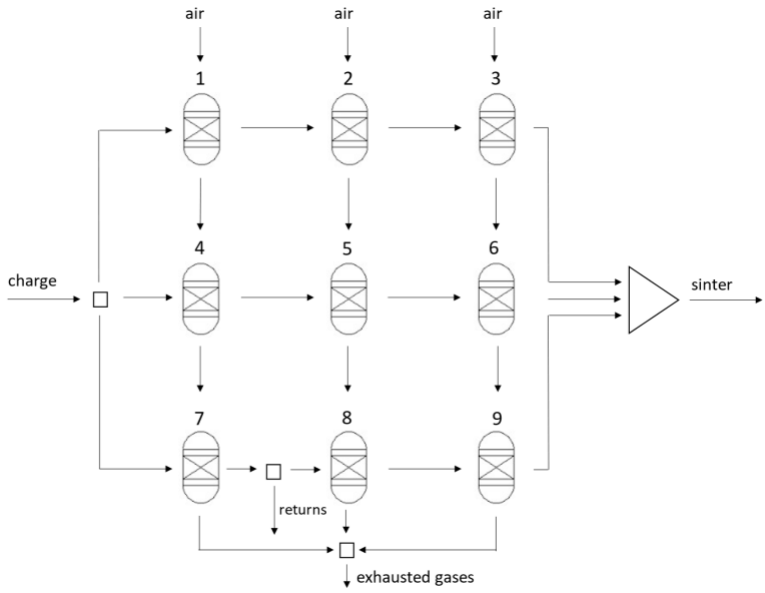

Figure 2.5. Simplified plant flowsheet of the sinter plant

In the model, the sintering bed is modelled with three successive columns of three Gibbs reactors each, where every Gibbs reactor represents either the sintered zone, the combustion zone or the raw material bed according to the position. Hence, a 3x3 Gibbs reactors matrix with four temperature levels was built (Table 2.1), where the diagonal represents the progression of the sintering zone, the region above the diagonal represents the sinter cooling by fresh air and finally the region below the diagonal accounts for the preheating and drying of fresh materials. The thermodynamic basis of this model is derived from the work in [38] by Schultmann et al. Air injection occurs from the top, while the exhausted gases are collected in the lower part of the bed by a line of wind boxes, which are modelled by a mixer.

Table 2.1. Thermodynamic conditions of the sintering unit [38]

Components	Operating conditions
4, 7, 8 – Gibbs reactor	P=1 bar; T=150 °C
1, 5, 9 – Gibbs reactor	P=1 bar; T=1200 °C
2, 6 – Gibbs reactor	P=1 bar; T=900 °C
3 – Gibbs reactor	P=1 bar; T=700 °C

In coke ovens, coal undergoes high temperature pyrolysis (1000 °C−1100 °C), thus producing coke and a gas mixture (Figure 2.6) [39]. The coke stream is sent to the blast furnace and to the sinter plant as a feedstock, while the coke oven gas first undergoes a cleaning process for the abatement of sulphur, ammonia, tar and aromatic hydrocarbons, and then is sent to other units (e.g. hot stoves, hot rolling mills) of the integrated steel mill, due to its high share of fuel gases (hydrogen, methane and carbon monoxide). A part of the coke oven gas along with part of the BFG is employed for thermal power supply to the coking process itself. The process is modelled by a Yield reactor operating at 1100 °C and implements the following experimental correlations in an external Fortran calculator [40]:

$$y_{coke} = 103.19 - 0.75VM_{coal} - 0.0067T_{coking} \tag{2.1}$$

$$y_{COG} = k \cdot \sqrt{VM_{coal} - y_{coke}VM_{coke}} \tag{2.2}$$

$$y_{tar} = -18.36 + 1.53VM_{daf,coal} - 0.026\left(VM_{daf,coal}\right)^2 \tag{2.3}$$

$$y_{benz} = -1.61 + 0.144VM_{daf,coal} - 0.0016\left(VM_{daf,coal}\right)^2 \tag{2.4}$$

$$y_{H_2O} = \frac{18}{16}aO_{daf} \tag{2.5}$$

$$y_{ammonia} = \frac{17}{14}bN \tag{2.7}$$

$$y_S = cS_{daf} \tag{2.8}$$

Where y_i is the mass yield of product i; VM_{coal} and VM_{coke} are the volatile matter content of coal and coke (wt%, dry); $VM_{daf,coal}$, O_{daf} and S_{daf} represent the volatile matter, oxygen and sulphur content of coal in absence of ashes (wt%, dry), respectively; N is the nitrogen content of coal (wt%, dry); T_{coking} is the coking temperature of coal; k, a, b and c are coefficients of the experimental model, whose values are reported in Table 2.2.

Table 2.2. Coefficients of the experimental coking yield model [40]

Coefficients	k	a	b	c
Values	3.3	0.42	0.15	0.17

Coal and coke are modelled in Aspen Plus as non-conventional solids, implementing proximate and ultimate analysis compositions as reported in Table 2.3. Since the gases are expected to exit the coke ovens at 750 °C, a heat exchanger (MHX) is located before the gas treatment unit to preheat the entering coal stream and cool down the gas stream from 1100 °C to the desired temperature. The coke oven gas treatment section is modelled as a

series of coolers and separators, so that the clean gas exits at 29 °C (AGR hierarchy block in Figure 2.6). In the CC hierarchy block, a part of the blast furnace gases and of the coke oven gases also undergo combustion in an adiabatic Gibbs reactor with ambient air.

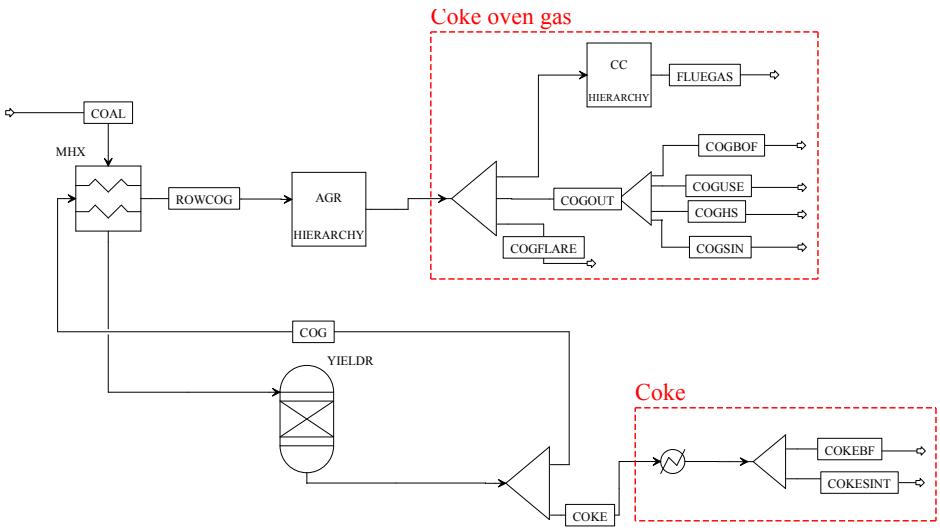

Figure 2.6. Aspen Plus flowsheet of the coke ovens

Table 2.3. Proximate and ultimate analysis of coal and coke

Proximate (wt%)	**Coal [41]**	**Coke [34]**
Moisture	8	4
Fixed Carbon	68.78	88
Volatile Matter	16.48	2
Ash	14.74	10
Ultimate (wt%)		
Ash	14.74	10
Carbon	79.02	88.05
Hydrogen	0.6	0.1
Nitrogen	1.28	1.1
Chlorine	0	0
Sulfur	1.14	0.6
Oxygen	3.22	0.15

2.3.2 Blast furnace modelling

In the blast furnace (Figure 2.7) coke, iron ores and other low-melting materials are alternatively charged from the top of the blast furnace and descend, while in the lower part of the furnace hot air (hot blast) and an alternative reducing agent, such as pulverized coal (PC), are injected from the tuyeres and ascend in the form of reducing gases. The combined

effect of carbon combustion and gasification in the raceway zone produces carbon monoxide and hydrogen, which in turn are responsible for iron ores reduction. From iron ores reduction and melting, pig iron and slag (containing SiO_2, Al_2O_3, CaO and MgO) are produced and collected in the hearth, where they are easily separated by density differences. To properly model all chemical processes occurring in a blast furnace, it is common practice [42] to discretize it with a number of regions characterized by proper temperature and pressure conditions: the heating zone, the upper furnace, the central furnace, the lower furnace, the raceway and the hearth (red boxes in Figure 2.7). Every portion is modelled by the combination of a RStoic reactor and a Gibbs reactor, both operating at the same temperature and pressure conditions: in the first one, the solid charge is converted according to literature, while in the second one the gas composition is adjusted. A heat exchanger is located at the top of the blast furnace to simulate the heat exchange between the charge and the outgoing BFGs, which are cooled down to 140 °C. The temperature and pressure conditions are derived from [43]. In the BF1 reactor ($T = 500\,°C$ and $p = 2.41$ bar), hematite (Fe_2O_3) is mainly reduced to magnetite (Fe_3O_4) by the carbon monoxide stream, while the moisture content of the charge undergoes the water gas shift reaction, which is also catalyzed by the presence of Fe_2O_3. This reaction is responsible for the presence of hydrogen in the blast furnace gases and its conversion degree is adjusted by a design-spec to match literature data. At this temperature level, the Boudouard reaction also takes place in BF1. In the BF2 reactor ($T = 850°C$ and $p = 2$ bar), Fe_3O_4 is almost completely reduced to FeO (wustite) by carbon monoxide and hydrogen. At this point, the calcination of the $CaCO_3$ content occurs. In the BF3 reactor ($T = 1100°C$ and $p = 1.03$ bar), the FeO content is almost completely converted to Fe by interaction with carbon monoxide and hydrogen, while part of the SiO_2 is reduced to Si by solid carbon. The Si content in pig iron reported in the literature is obtained by a design-spec. For simplicity, the content of other metals (Mn, Mg etc.) in pig iron is neglected. Finally, in the raceway zone (RACEWAY) an adiabatic Gibbs reactor models the reactions occurring between the hot blast, the pulverized carbon and the descending solid charge. At this point, the reduction to iron is complete and the charge is melted.

In step 1, the addition of 230 kt/y of PS as an alternative reducing agent (ARA) is considered. Proximate and ultimate analysis values of PS are reported in Table 2.4. In this case, due to the limited amount of plastic injected in the blast furnace from the tuyeres, the thermal balance of the blast furnace is assumed to be preserved. In [44], a maximum allowed plastic injection to the blast furnace of 70 $kg_{plastic}/t_{pig\ iron}$ is set according to thermochemical and kinetic conditions, which is lower than 61.6 $kg_{plastic}/t_{pig\ iron}$ resulting from step 1 simulation. The coke replacement ratio (CPR), representing the ratio between the quantity of plastic necessary to substitute a unitary amount of coke, was computed by iterative calculations so that the resulting carbon fraction in pig iron is equal to 4.7% wt [34]. The hot blast is obtained

by heating ambient air (compressed up to 3.8 bar and added with steam and oxygen) in the hot stoves (Figure A2.1 in Appendix A), where parts of the COG and of the BFG are burnt in an adiabatic Gibbs reactor at 3.8 bar.

Table 2.4. Proximate and ultimate analysis of PS

Proximate (wt%)	**PS [45]**
Moisture	0.20
Fixed Carbon	0
Volatile Matter	99.30
Ash	0.50
Ultimate (wt%)	
Ash	0.50
Carbon	90.40
Hydrogen	8.56
Nitrogen	0.07
Chlorine	0
Sulphur	0.08
Oxygen	0.18

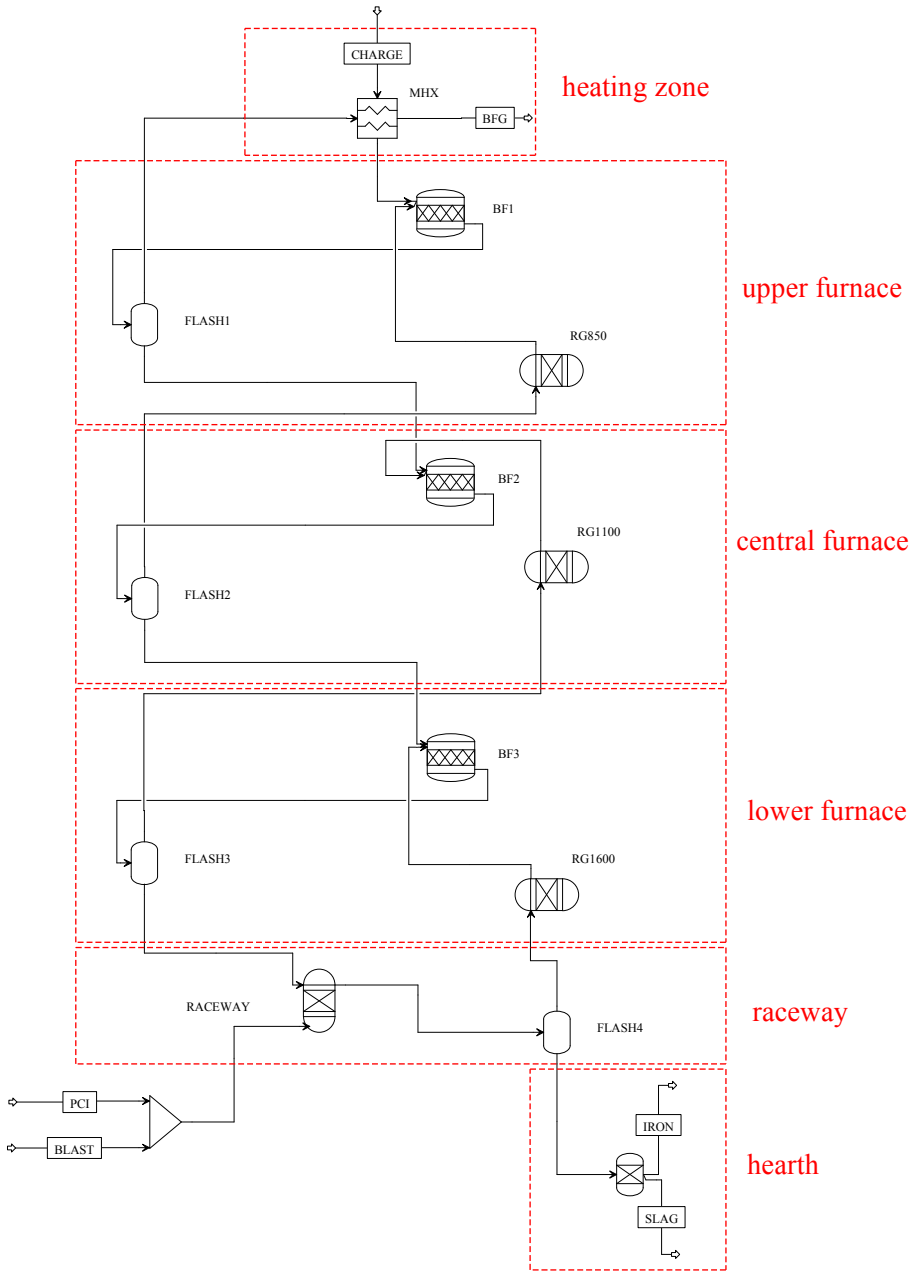

Figure 2.7 Simplified flowsheet of the blast furnace divided according to the main reaction regions

2.3.3 Basic oxygen furnace and secondary steelmaking

The Aspen flowsheet of the desulphurization unit, BOF, ladle metallurgy, continuous casting and hot rolling mills is reported in Figure A2.2 of Appendix A. The hot metal from the blast furnace is sent to desulphurization and then to the basic oxygen furnace. The desulphurization unit is modelled with a Gibbs reactor (DESULF) operating at 1360 °C and 1 bar. After slag separation, the hot metal is sent to the basic oxygen furnace (BOF), where a stream of pure oxygen (with the addition of lime, dolomite, scrap and iron ore for temperature control) reduces the carbon content of the hot metal in a Gibbs reactor

operating at 1672 °C and 1 bar. In this reactor, the thermal dissociation of the added iron ore and the Si and C content oxidation take place. After dust separation, the basic oxygen furnace gas (BOFG) is sent to the power plant, while liquid steel is sent to ladle metallurgy (LM), continuous casting (CC) and finally hot rolling (HRM). In the hot rolling mills, the heat produced by the adiabatic combustion of part of the COG is employed to process the steel.

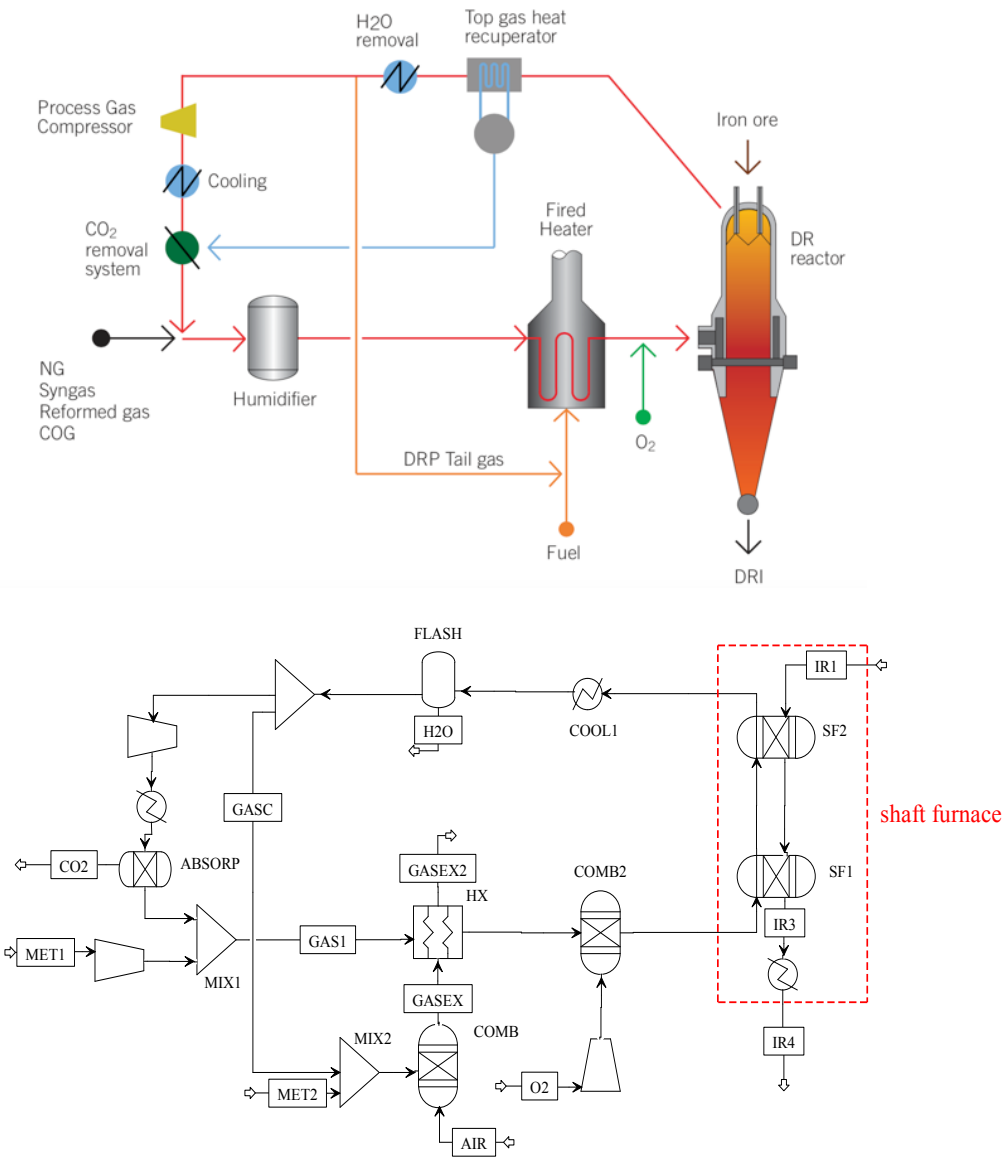

Figure 2.8. HYL/Energiron direct reduction plant scheme by Tenova and Danieli (top); Aspen Plus flowsheet of the HYL/Energiron direct reduction plant (bottom)

2.3.4 Direct reduction plant modelling

The HYL/Energiron direct reduction plant (DRP) developed by Tenova and Danieli is taken as reference (Figure 2.8-top). In the direct reduction reactor, iron ores are injected from the top and interact in counter-current flow with reducing gases deriving from methane

reforming (Eqs. (2.9) and (2.10)), carrying out reduction and carburization of the iron oxide content according to Eqs. (2.11) to (2.13):

$$CH_4 + H_2O \rightleftharpoons CO + 3H_2 \tag{2.9}$$

$$CH_4 + CO_2 \rightleftharpoons 2CO + 2H_2 \tag{2.10}$$

$$Fe_2O_3 + 3H_2 \rightarrow 2Fe + 3H_2O \tag{2.11}$$

$$Fe_2O_3 + 3CO \rightarrow 2Fe + 3CO_2 \tag{2.12}$$

$$3Fe + CH_4 \rightarrow Fe_3C + 2H_2 \tag{2.13}$$

The reaction product is a solid mixture, the direct reduced iron (DRI), mostly consisting of iron and a percentage of carbon between 2% and 4.5%, corresponding to low-carbon DRI and high-carbon DRI [46], respectively. The exhausted gases leaving the reactor are conveyed to water separation by condensation and then, after compression, carbon dioxide absorption by amines. On the contrary, the unreacted fuel gases are mixed with the inlet feed of methane and then heated by burning natural gas. Oxygen injection before the shaft furnace is used to adjust composition and temperature of the reactant stream. In steps 2 and 3, the DR plant employs methane as the reducing agent. Methane/hydrogen blendings are also assessed in step 3. In step 4, 100% green hydrogen is employed as a reducing agent.

2.3.5 Methane/hydrogen blending as a reducing agent (step 2 and step 3)

In Figure 2.8-bottom, the shaft furnace is modelled as indicated by Muller et al. in [47]. The series of two Gibbs reactors (SF1 and SF2) represent two temperature levels (T_1 = 1050 °C below and T_2 = 550 °C top) occurring along the height of a typical shaft furnace operating at an average of 7 bar [48]. The gases from MIX1 are employed as reducing agent in the DR unit, while the gases from MIX2 are burnt in an adiabatic Gibbs reactor in order to provide the thermal power to preheat the reducing gases. A Gibbs reactor (COMB2) is located before the shaft furnace, where temperature and composition of the reducing gas mixture are adjusted to the optimal values by a design-spec varying the oxygen injection. Input mass flow rates of methane and iron ores (reported in Table 2.5) are computed by linear interpolation from the flow rates reported by Tenova and Danieli in [48], assuming a hot DRI output of 2500 kt_{DRI}/y for the single DR plant [46].

Table 2.5. Inlet streams characterization in the single DR plant of steps 2 and 3

Inlet Streams	Mole Fraction	Input Values
MET1		
	100% CH_4	80.8 Nm^3/h

MET2		
IR1	2% FeO; 95% Fe_2O_3; 2% SiO_2; 1% Al_2O_3	$3.375 \cdot 10^3$ kt/y

In step 3, the inlet flow rates are all doubled because two DR-EAF lines are operating and methane/hydrogen blending are investigated in terms of CO_2 emissions and energy flows for a fixed molar flow rate entering the plant. The outlet streams are represented by:

a) liquid water separated by condensation from the gases exiting the reactor;
b) CO_2 at the exit of the separator modelling amine absorption;
c) combustion gases, whose heat content is exchanged with the reducing gases directed to the shaft furnace;
d) hot DRI (IR3) coming from the shaft reactor.

This last stream represents the input stream to the EAFs units. Due to the assumption of CO_2 absorption by ammines, the only source of emissions is represented by the exhausted gas from natural gas combustion. In order to evaluate the quality of the DRI, the metallization M is calculated according to Eq. (2.14):

$$M = \frac{n_{Fe,out}}{\left(3 \cdot n_{Fe_3O_4} + 2 \cdot n_{Fe_2O_3} + n_{FeO}\right)_{in}} \tag{2.14}$$

Where $n_{Fe,out}$ stands for the mole flow rates (mol/h) of iron in the outlet stream, while $n_{Fe_3O_4}$, $n_{Fe_2O_3}$ and n_{FeO} represents the mole flow rates of Fe_3O_4, Fe_2O_3 and FeO in the initial iron ore stream. The metallization is a measure of the reduction extent of DRI, i.e. how many moles of iron bounded as iron oxides (Fe_2O_3, Fe_3O_4, FeO) in the initial iron ore are reduced to Fe. Current direct reduction plants by Tenova and Danieli achieve 96% metallization of the initial charge [49] when natural gas is employed as reducing agent.

2.3.6 Green hydrogen as reducing agent (step 4)

This section focuses on the calculation of the hydrogen flow rate involved in the DR plants during the last step of the industrial plan. A DR plant entirely based on hydrogen is slightly different from that based on natural gas, since it works with carbon-free compounds. Hence, some departments such as the CO_2 absorption unit are not required. The Aspen Flowsheet of the DRP is represented in Figure 2.9 and reproduces the configuration presented in [24]. The shaft furnace modelling is identical to the previous case, with a series of two Gibbs reactors (SF1 and SF2) operating at 7 bar and at two temperature levels ($T_1 = 570$ °C below and $T_2 = 780$ °C top), according to the values obtained by Patisson et al. in [23]. In this case, the series of a heat exchanger and a flash separator is employed to simulate the condenser for water separation in the exhaust gases. The non-reacted hydrogen gas stream, once

compressed and cooled, is recycled back and mixed with fresh hydrogen. In this case, the reducing gas stream is assumed to be electrically heated (HEATER) before being injected into the shaft furnace. Three moles of hydrogen per mole of Fe_2O_3 are involved in the reduction process, according to the reaction equation in Eq. (2.15). Hence, the stochiometric flow rate of hydrogen introduced into the DR reactor is computed as:

$$\dot{m}_{H_2st} = 3 \cdot PM_{H_2} \cdot \frac{\dot{m}_{Fe_2O_3}}{PM_{Fe_2O_3}} \tag{2.15}$$

Where:

- PM_{H2}= 2.015 g/mol is the molecular weight of H_2
- $PM_{Fe_2O_3}$= 159.69 g/mol is the molecular weight of Fe_2O_3
- $\dot{m}_{Fe_2O_3}$= 6750 kt/y is the mass flow rate of Fe_2O_3 in the iron ore stream (it is assumed the same iron ore flow rate of step 3)

However, the quantity of hydrogen supplied to the shaft must be higher than the stoichiometric value to reach reaction completion. Therefore, the parameter λ can be defined as in [24]:

$$\lambda = \frac{n_{H_2,shaft}}{n_{H_2,st}} \tag{2.16}$$

Where $n_{H_2,shaft}$ represents the moles of H_2 fed to the shaft reactor, while $n_{H_2,st}$represents the stoichiometric moles of H_2 required to fully reduce the Fe_2O_3 content in the initial iron ore stream.

In this case, $\lambda = 1.8$ is assumed to guarantee the reduction reaction completion (since 2% wt FeO is also present in the initial stream). For lower values of λ it was not possible to guarantee a metallization M equal to 90%. In this case 100% green hydrogen is involved in the process together with iron ores, whose composition and flow rate are unvaried from step 3. A summary of the operating conditions and calculation options of step 4 DRP is reported in Table 2.6.

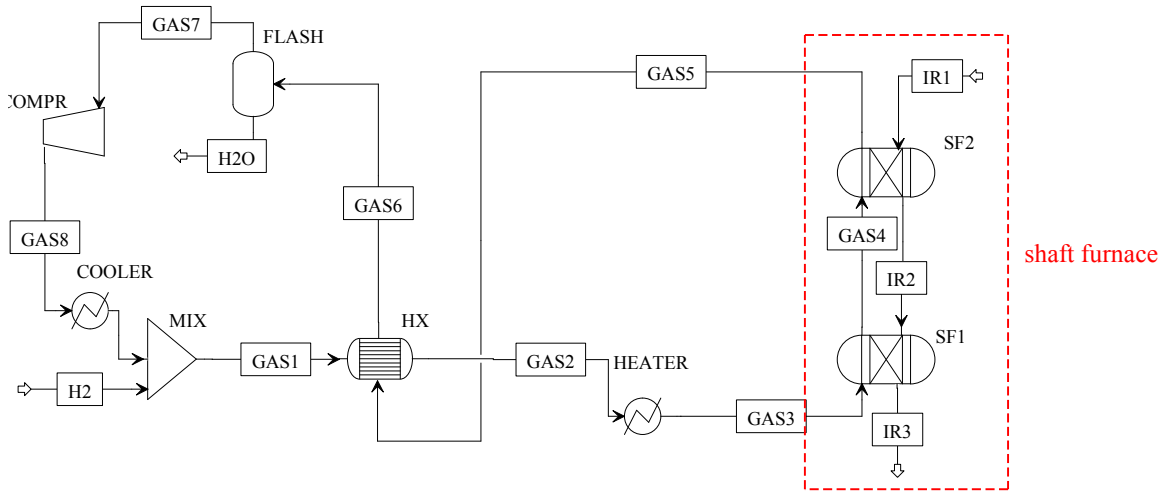

Figure 2.9. Aspen flowsheet of DR plant in the step 4

Table 2.6. Summary of the main components in the DR plant of step 4 implemented in Aspen Plus

Components	Operating conditions	Calculation options
SF1 – Gibbs Reactor	P = 7 bar; T = 780 °C	Phase and chemical equilibrium
SF2 – Gibbs Reactor	P = 7 bar; T = 570 °C	Phase and chemical equilibrium
HX – Heat exchanger	$T_{hot,out}$ = 90 °C, 11 bar	Shortcut, Countercurrent
FLASH – Flash separator	T = 70 °C, p = 7 bar	

2.3.7 Electric arc furnace modelling

DRI produced by the DR plant is conveyed to the EAFs where it is blended with lime and scrap. Here, solid charge is melted by the electric arc produced between two or three graphite electrodes and chemically refined through oxygen injection. The EAF units produce liquid steel which can be treated in continuous casting and hot rolling mills units for the production of hot rolled coils. A part of the electric arc furnace gas (EAFG) is employed for thermal power supply to the subsequent hot rolling process. In step 2, a mixture of 72.65 kt/y COG and 72.65 kt/y EAFG is used for the hot rolling, while in steps 3 and 4 a mixture of 80 kt/y methane and 100 kt/y EAFG. In Figure A.3 of Appendix A, the Aspen Plus flowsheet of the EAF is represented. An adiabatic Gibbs reactor simulates the reactions occurring in the EAF at 1600 °C. Coal is injected to compensate for the required carbon content when hydrogen is the reducing gas. In step 4, about 11.5 $kg_C/t_{liquidsteel}$ and 10% wt scrap (calculated based on the inlet solid mass flow rate) are injected into the basic oxygen furnace in order to meet the prescriptions by Tenova and Danieli, which suggest a range between 12 $kg_C/ t_{liquidsteel}$ and 15 $kg_C/ t_{liquidsteel}$ for carbon injection in the EAF when hydrogen-based DRI (i.e. 0% wt C) is produced [50]. As for the graphite electrodes' consumption, which is responsible for additional CO_2 emissions, a specific consumption of

4 kg_C/t_{LS} (about 15 kg_{CO2}/t_{LS}) is considered according to the data reported by Rainer et al. in [44]. The inlet streams compositions and flow rates are summarized in Table 2.7.

Table 2.7. Inlet stream characterization in the EAF

Inlet streams	Mass fraction	Flow rates
SCRAP	98.8% Fe; 1.2% C	10 % wt of the initial solid mass flow
LIME	64% CaO; 36% $CaCO_3$	40 kg/t_{DRI}

2.3.8 Energy flows modelling

Steel mills consume fossil fuels (coal, pulverized coal, coke, plastic) and gaseous fuels (natural gas, blast furnace gas, coke oven gas, basic oxygen furnace gas and EAF gas. The enthalpy rates of each fuel in input, assuming ambient conditions, are obtained by multiplying the flow rates of the solid and gaseous fuels $\dot{m}_i$ by the lower calorific values:

$$\dot{h}_i = \dot{m}_i \cdot LHV_i \qquad [PJ/y] \qquad (2.17)$$

The steel mill electric consumption is calculated by multiplying the specific electric consumption s_i (SEC) of each department (retrieved from the literature) by the mass flow rate of the main product $\dot{m}_{prd,i}$:

$$Ec_i = s_i \cdot \dot{m}_{prd,i} \qquad [PJ/y] \qquad (2.18)$$

The specific electric consumption values of each unit are reported in Table 2.8. The specific electric consumption for the DRP is determined as the arithmetic average of the values reported in Tenova and Danieli (2013), while the specific values reported by Hydrogenics are considered for the electrolyzer [51]. An alkaline electrolyzer is adopted for hydrogen production due to its higher technological maturity, lower costs and longer lifetime. Nowadays, several commercial devices are available for H_2 production with an efficiency up to 85% when operating at low pressure and up to 78% when operating at high pressure [52]. By assuming a proper use, current stacks work for $6 \cdot 10^4 - 9 \cdot 10^4$ hours, ensuring $7 - 10$ years of stack lifetime [53,54]. However, the degradation of nickel-based catalysts must be regularly checked. Depending on the model of the electrolyzer, replacement of the electrodes must occur at least after 5 years, considering 10 years as total running time. Along with the maintenance of the electrodes, it can be expected a simultaneous renewal of the diaphragms [55].

Table 2.8. Specific electric consumption (SEC) of the units

Department	SEC (kWh/t_{prd})	Reference	Product
Sinter plant	32	[34]	Sinter

Coke oven	35	[34]	Coke
Air separation	385.2	[34]	Oxygen
Lime kiln	30	[34]	Lime
Blast furnaces	98.8	[34]	Pig iron
BOF	20	[34]	Liquid steel
Hot rolling mills	143.4	[34]	Hot rolled coils
DR plant	67.5	[34]	DRI
EAF	380	[56]	Liquid steel (from hot DRI)
Electrolyzer	4.85[1]	[51]	Hydrogen

2.4 Results and discussion

2.4.1 Model validation

For the integrated steel mill, the input values to each unit are set according to the data in [34] and subsequently compared in terms of mass flow rates and compositions with the same reference document. The elaborated model encompasses all the units in a single simulation file, so that the outputs of a certain unit represents (when it is the case) the input to the following one, e.g. coke from coke ovens is an input to the blast furnace and to the sinter plant. Tables 2.9 and 2.10 show the model validation regarding the main products of the blast furnace and basic oxygen furnace. Other comparisons were carried out for the sinter plant, hot stoves, ladle metallurgy, continuous casting, hot rolling mills and are reported in Tables A2.1 to A2.4 of Appendix A. The results related to the main products of each unit show an accuracy within 5% of literature values. As for the DRP validation (Table A2.5 of Appendix A), comparison was carried out for the case with 100% natural gas injection from data provided in technical reports by Tenova and Danieli, assuming high-carbon hot DRI production. The results fall within 6% of literature values.

Table 2.9. Blast furnace validation[2]

BFG	Composition			Flow rates (kt/y)			**Pig iron**	Composition			Flow rates (kt/y)		
Element	Simulation	Ref.	Error	Sim.	Ref.	Error (%)	Element	Sim.	Ref.	Error (%)	Sim.	Ref.	Error (%)
H_2	3.59	3.75	**4.09%**	8810.91	8724.52	**-0.99%**	Fe	94.73%	94.15%	**-0.62%**	3975.85	3968.76	**-0.18%**
N_2	48.80	50.32	**3.02%**				C	4.77%	4.70%	**-1.42%**			
CO_2	23.75	22.81	**-4.08%**				Si	0.50%	0.50%	**0.00%**			
CO	23.74	23.07	**-2.90%**										

Table 2.10. Basic oxygen furnace validation

[1] kWh/Nm^3 of hydrogen

[2] Tables 2.9 and 2.10 are also reported in Appendix A for better readability

BOFG	Composition			Flow rates (kt/y)			**Liq.steel**	Composition			Flow rates (kt/y)		
Element	Simulation	Reference	Error(%)	Simulation	Reference	Error(%)	Element	Simulation	Reference	Error(%)	Simulation	Reference	Error(%)
H_2	2.64%	2.64%	**0.00%**	453.752	448	**1.27%**	Fe	99.96%	99.90%	**-0.06%**	4432.72	4323	**-2.67%**
CO_2	14.44%	14.44%	**-0.28%**				C	0.04%	0.042%	**-5.00%**			
CO	56.90%	56.92%	**-0.04%**										
N_2	13.83%	13.83%	**0.00%**										
H_2O	12.18%	12.16%	**0.55%**										

2.4.2 CO_2 emissions

The total and specific CO_2 emissions throughout the four steps are shown in Figure 2.10-top. Literature data on specific CO_2 emissions confirm the result for the initial step, ranging between 1.8 t/t_{hrc} and 2 t/t_{hrc} according to [34] and [57], respectively. The total and specific CO_2 emissions (normalized with respect to the hot rolls production) follow similar trends since steel production is about constant through the steps of the methodology. In step 1, although a certain reduction in CO_2 emissions is expected, the limited coke replacement by PS leads to a slight decrease in CO_2 emissions (Figure 2.10-top). Steel production is unvaried from step 0 and amounts to 4.44 Mt/y of liquid steel from the BOF. The change in other pollutant emissions due to plastic introduction, such as mercury, cadmium, zinc and lead, was neglected according to the work in [58], where experimental analysis on a full-scale blast furnace demonstrated that the emission of heavy metals to the atmosphere and hydrosphere are completely independent from their input into the blast furnace itself. Moreover, dioxins formation is excluded by the high temperatures in the raceway zone. As for the material consumption related to plastic mechanical recycling, the raw material consumption involves water washing (2 $L_{H_2O}/kg_{plastic}$), wastewater treatment by chemicals (polyaluminum chloride-coagulant 8.1 $g/kg_{plastic}$, caustic soda 50%wt 24 $g/kg_{plastic}$, polyacrylamide-flocculant 0.27 $g/kg_{plastic}$), deionized water (126.6 $g_{H_2O}/kg_{plastic}$) and diesel for the bale holder (1.65 $g/kg_{plastic}$) [59]. In comparison, material consumption for energetic coal production involves water (4.34 L_{H_2O}/kg_{coal}), explosives (1.38 g/kg_{coal}), diesel (1.19 $g/kg_{plastic}$) and limestone (3.5 g/kg_{coal}) and causes pollution of the pumped groundwater [60]. In step 2, liquid steel production from the BF-BOF line is reduced to 2.39 Mt/y and the first DR-EAF line is introduced, producing other 2.59 Mt/y of liquid steel with 0.12% wt carbon content. In this case, the introduction of a more efficient DR-EAF line fed by CH_4 reduces the CO_2 emissions from 8.20 Mt/y of step 1 to 5.16 Mt/y, i.e. 39% decrease in CO_2 emissions. The CO_2 captured the DR plant by amine absorption is assumed to be stored and is not included in the computation of total CO_2 emissions. In step 3, the CO_2 emissions level refers to the full CH_4 case and reach 2.09 Mt/y CO_2 while the liquid steel production increases to 5.17 Mt/y. In Figure 2.10-bottom, the effect of various CH_4/H_2 blendings on CO_2 emissions associated with step 3 is analyzed. The CH_4 mole fractions range between 0.6 and 1, since for lower ratios the carbon content in the liquid steel from the EAF gets below 0.12% wt and a carbon injection in the EAF results necessary. For CH_4

mole fractions higher than 0.8, a maximum reduction of only 7.45% is achieved compared to the full CH_4 case. On the contrary, for lower CH_4 mole fraction a steep and almost linear reduction in CO_2 emissions is observed, reaching a maximum 36.3% reduction for CH_4 mole fraction of 0.6. However, beyond certain hydrogen mole fractions, Fe_2O_3 is reduced to Fe_3O_4 rather than Fe, thus impacting on DRI metallization. For the investigated range of methane mole fractions, metallization is constant and equal to 96%, as illustrated in Figure 2.10-bottom. Finally, in step 4 green hydrogen is the reducing agent, leading to 92% CO_2 emissions drop (0.682 Mt/y) compared to step 0 and 67.3% drop compared to the full CH_4 case of step 3. The CO_2 emissions from step 4 are due to the injection of 56.5 kt/y of C_s in the EAF and to the combustion of 80 kt/y methane and 100 kt/y EAFG in the hot rolling mills section. For the considered hydrogen flow rate, the resulting DRI metallization (not shown) decreases to 92% due to the formation of Fe_3O_4 in the DRI, which is all collected in the slag at the EAF outlet. For this reason, the liquid steel production from the EAF of step 4 decreases to 4.91 Mt/y. In Figure 2.11, the effect of increasing scrap mass fractions in the total solid mass flow rate at the EAF inlet is shown in terms of total and specific CO_2 emissions. Carbon injection is carried out according to the DRI mass flow rate at the EAF inlet (Table 2.10).

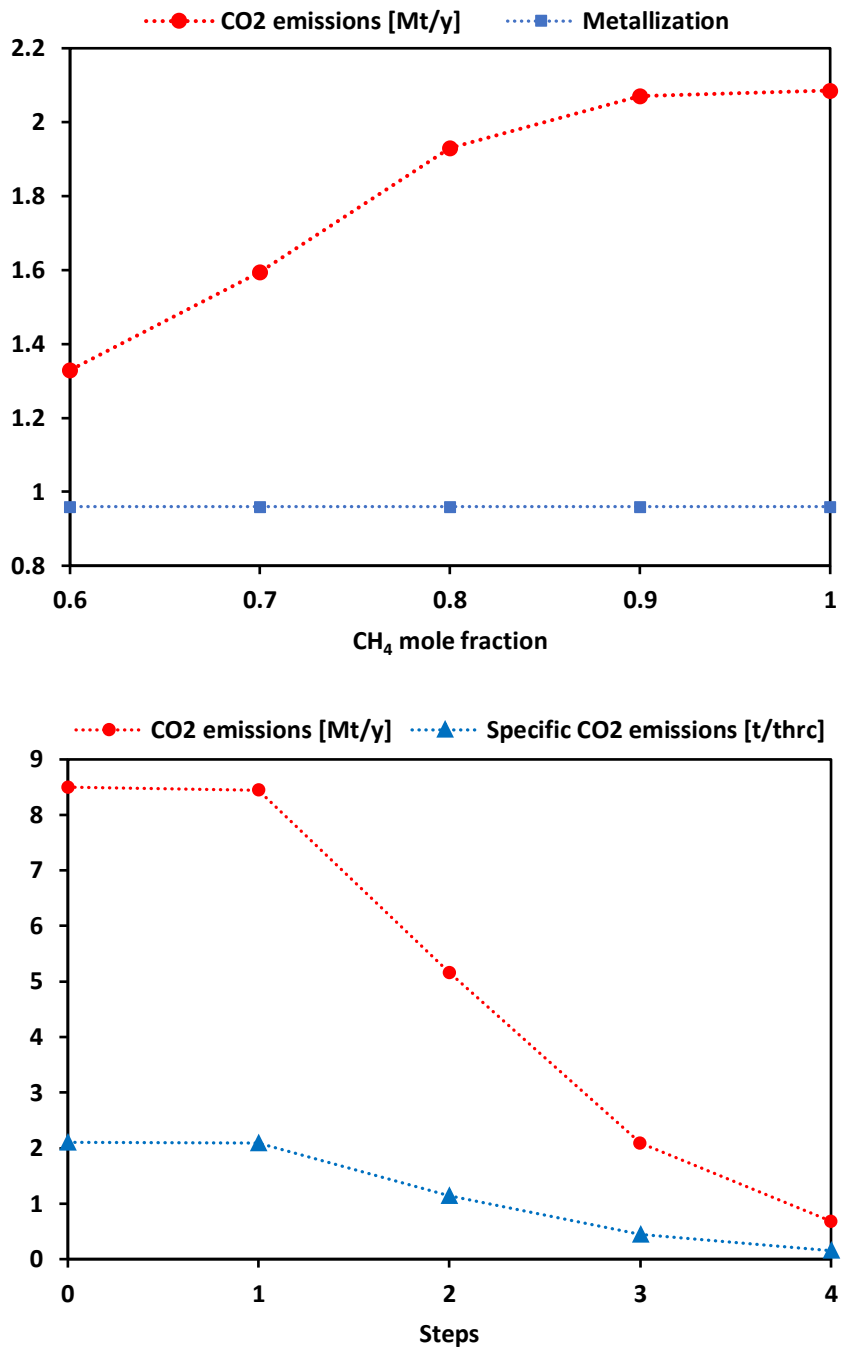

Figure 2.10. Annual and specific CO_2 emissions throughout the steps (top); CO_2 emissions and DRI metallization for various CH_4/H_2 blendings in step 3 (bottom)

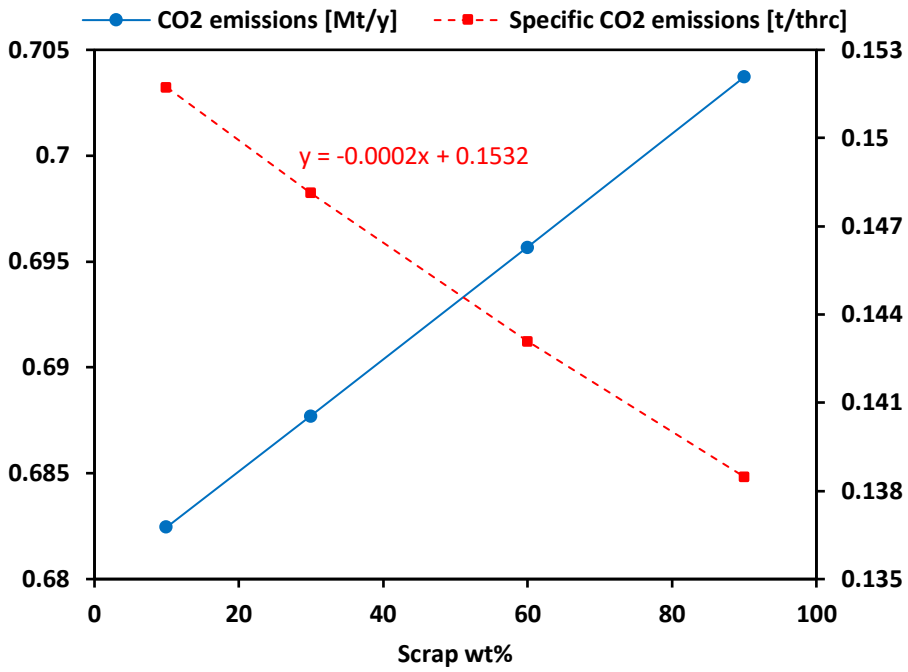

Figure 2.11. Total CO_2 emissions and specific CO_2 emissions for step 4 with changing scrap fraction at EAF inlet

Table 2.11. Carbon and DRI mass flow rates at EAF inlet

		C_s [kt/y]	DRI [kt/y]
Scrap wt%	10%	56.5	5063
	30%	43.6	3904
	60%	23.9	2144
	90%	4.3	385

The results indicate that total CO_2 emissions increase with the scrap mass fraction, though the relative increment between the two extremes (10% − 90%) is of only 3.11%. On the contrary, the specific CO_2 emissions decrease with the scrap mass fraction, since a higher steel production (hot rolled coils) is achieved due to the reduced injection of DRI, whose Fe_3O_4 content is separated with the slag and does not contribute to liquid steel flow rate. By linear interpolating the simulation results on specific CO_2 emissions, it was possible to develop the correlation of Eq. (2.18):

$$CO_{2,sp} = -2 \cdot 10^{-4} \cdot M_{scrap} + 1.532 \cdot 10^{-1} \quad (2.18)$$

Where:

- M_{scrap} represents the scrap mass fraction (%) in weight;

- $CO_{2,sp}$ represents the specific CO_2 emissions in $[t_{CO_2}/t_{hrc}]$ from a DR-EAF steel mill including the secondary steelmaking section (continuous casting and hot rolling mill);

The error analysis is presented in Table A2.4 of Appendix A. The correlation is valid for a DR-EAF plant including the continuous casting and hot rolling mills sections, where the DRP is fed by 100% H_2 (thus producing 0% C DRI), the scrap carbon content is 1.2 wt% and solid carbon injection is carried out in the EAF.

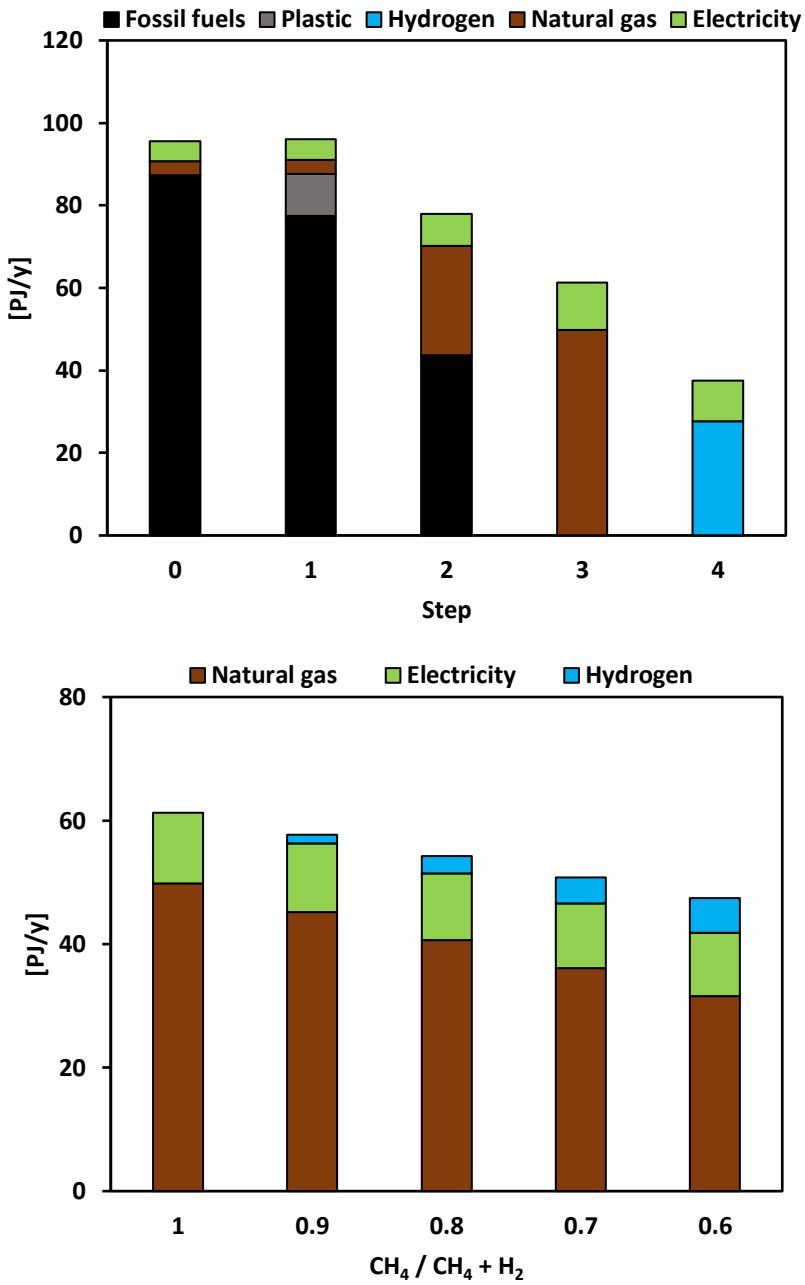

Figure 2.12. Annual energy consumption (TJ) as a function of the revamping methodology step (top); annual energy consumption (TJ) for various CH_4/H_2 blendings in step 3 (bottom)

2.4.3 Energy balance results

Figure 2.12-top illustrates the total energy consumption for each proposed configuration. The trend indicates that from the initial step to step 4, fossil fuel consumption (coal, pulverized coal, coke, plastic, natural gas) decreases while electric consumption increases. Zerp emissions electricity is assumed and thus the CO_2 emissions derive exclusively from the solid and gaseous fossil fuels involved in the processes. The electricity demand of step 0 and 1 configurations is locally produced by the internal thermal power plant, while from step 2 electricity is supplied externally from low or zero CO_2 energy sources such as renewable power plants or nuclear power plants. In step 1 (Figure 2.12-top), PS injection in the blast furnace slightly affects the total energy consumption, since the CPR resulting from iterative calculation amounts to 1.06. In step 2, a new DR-EAF line fed by 100% CH_4 is introduced and the integrated steel mill production levels are halved compared to the previous step. Natural gas becomes an important term in fossil fuels consumptions, amounting to 26.6 PJ/y. However, a 15.2% energy consumption reduction is achieved compared to step 0 configuration. In step 3, the energy consumption is mainly due to natural gas and electricity, since two DR-EAF lines are present. Electricity consumption increases by 74.8% from step 2, while 33.5% total energy consumption reduction is achieved compared to the initial step.

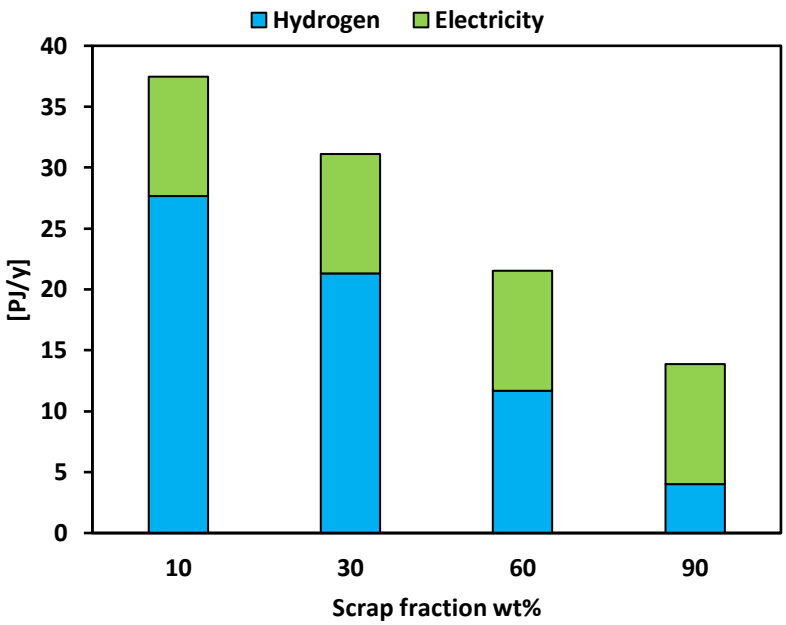

Figure 2.13. Energy consumption for varying scrap fractions at EAF inlet in step 4

In step 4 (10% wt scrap in the EAF), the total annual energy consumption is associated with hydrogen and electricity, achieving 59.4 % reduction (37.4 PJ/y) compared to the initial configuration. The effect of different CH_4/H_2 blendings in step 3 steel mill is analysed in Figure 2.12-bottom. The introduction of an increasing hydrogen mole fraction leads to a decrease in the total energy flows, while electricity consumption is constant for all the

investigated blendings since a constant solid mass flow rate is obtained at the outlet of both DRP and EAF.

The impact of varying scrap mass fractions on the energy consumption of step 4 is assessed in Figure 2.13. Since the DRI mass flow rate is progressively reduced with increasing scrap mass fractions at the EAF inlet, the energy flows of the DRP are reduced from 37.5 PJ/y to 13.9 PJ/y (63%). The H_2 flow rate required by the shaft reactor of the DRP drops by one order of magnitude for 90% wt scrap ($4.26 \cdot 10^4$ Nm^3/h) compared to the 10% wt scrap case ($5.60 \cdot 10^5$ Nm^3/h).

The electricity consumption increases with the steps, as shown in Figure 2.14. An annual electricity consumption of 40.3 PJ/y (1.42 GW assuming 90% availability) is required by the electrolyzer for the 10% wt scrap case, representing the main contribution to the total electricity consumption of step 4 and more than nine times that of step 0. The electrolyzer was sized according to the H_2 flow rate at the DRP inlet provided by Aspen, which is lower than that of the shaft reactor due to recirculation. On the contrary, with 90% scrap mass fraction the electric power consumption of the electrolyzer drops to 0.202 GW, since the DRI production is substantially reduced.

These results highlight the complexity of realizing this last step, which requires large availability of low CO_2 electric power supply from the grid. It is thus evident that one of the greatest challenges for the transition towards a low CO_2 steel production is represented by the capacity to stably provide large quantities of low carbon electricity at a competitive cost compared to the conventional pathways of energy generation.

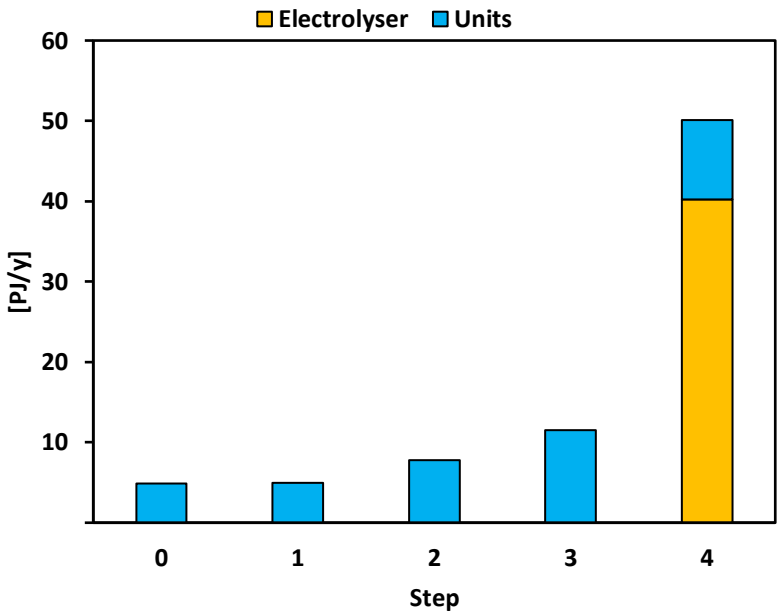

Figure 2.14. Annual electricity consumption (TJ) as a function of the revamping methodology step

2.4.4 Exhaust gas energy flows

The exhaust gas energy content represents an important resource in current steel mills. The BFG and COG are involved in process heating, such as in coke ovens, continuous casting units and hot stoves, while the BOFG and part of the BFG are directed to power production (generally by a steam cycle) along with an external stream of natural gas. In step 1, since coke oven operation is reduced due to plastic injection, the BFG flow rate to the coke ovens is reduced and a slightly larger fraction is directed to the power plant, as illustrated in Figure 2.15-top. In the subsequent steps, the progressive decommissioning of the integrated steel mill negatively affects power production since lower exhaust gases flow rates can be usefully employed for the scope. In step 4, since the DRI carbon content is zero because no carbon source is present, carbon injection in the EAF is required for compensation and thus an EAFG is produced. The EAFG produced in steps 2, 3 and 4 is split between hot rolling and power production sections.

The process gas (COG, BFG and EAG) energy flows to users (i.e. hot rolling mills, coke ovens, hot stoves) are represented in Figure 2.15-bottom. In steps 0 to 2, the COG and the BFG are used for thermal supply to coke ovens and hot rolling mills/hot stoves, respectively. A 50% reduction in process gas energy flows to users is observed between steps 0 and 2, since half of the steel mill steel production derives from the DR-EAF line. Specifically, in step 2 the total gas flow rate directed to the hot rolling mills is composed of both COG and EAFG (72.65 kt/y each), since coke oven production provides not enough COG flow rate for the full operation of the hot rolling mills (which receives steel from both the BF-BOF and DR-EAF lines). In steps 3 and 4, only the EAFG contributes to the exhaust gases energy flows to users, which are thus significantly reduced. In order to ensure the hot rolling mills full operation, 80 kt/y of CH_4 are injected (not reported in Figure 2.15-bottom) in the reheating furnace of the hot rolling mills both in steps 3 and 4.

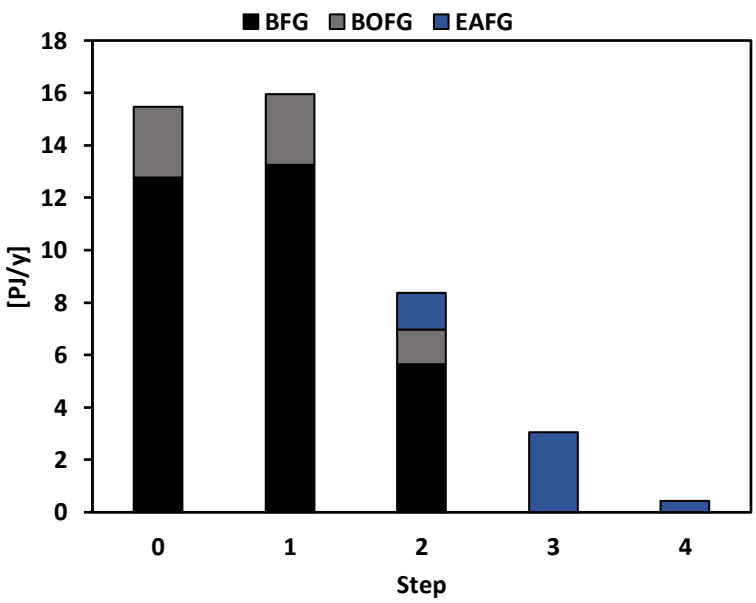

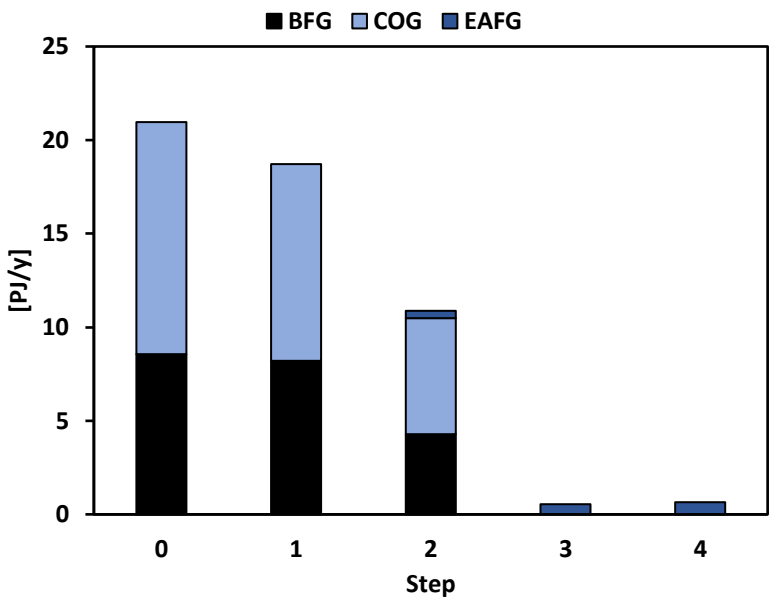

Figure 2.15. Process gases energy flow rates to power plant (top), to users (bottom) as a function of the revamping methodology step

2.4.5 Capital cost analysis

In addition to an in-depth technical analysis, the project requires an economic analysis, which aims at defining the capital expenditure (CAPEX) associated to the methodology. For the first step, interventions are necessary to the tuyeres of the BF to allow for plastic injection. Furthermore, a handling system capable of transporting 230 kt/y of plastic from the parks to the BFs must be installed. The costs incurred for these operations are assumed equal to 20 M€, which is the cost for an injection capacity of 220 kt/y reported in [44]. In step 2, the installation of a DR plant and two EAFs of nominal 2500 kt/y DRI production is estimated to cost respectively 515 M€ (230 €/t_{CS}/y) and 412 M€ (184 €/t_{CS}/y) [61]. By retrofitting the DR-EAF line with an amine-based (MEA) CO_2 capture unit, additional 29.5 M€ are included in the CAPEX considering a specific cost of 0.882 M€/kg_{CO_2}/s [62]. This cost includes the high-purity CO_2 compression section. In step 3, the installation cost of a second DR-EAF line amounts to 961 M€, according to the values estimated for the first DR-EAF line retrofitted with the CO_2 capture unit. Other interventions to be realized for this step are the complete demolition of the integrated steel mill plant. The reference value is obtained from the estimated demolition costs [63] of the Redcar plant in the United Kingdom (150 M£ for a nominal capacity of 3.4 Mt/y pig iron [64]). By linear interpolation, the demolition cost for an integrated steel mill with nominal 3.98 Mt/y pig iron production is equal to about 202 M€, assuming 1.15 £/€ conversion. In step 4, the electrolyzer installation is expected for green H_2 production. Assuming a specific cost equal to 0.585 €/W [65], the capital cost of the 1.42 GW alkaline electrolyzer amounts to about

830 M€. The total capital cost involved by the revamping methodology is equal to 2.97 B€, as reported in Table 2.12.

Table 2.12. CAPEX for each step

# Step		Cost (M€)
Step 1		**20**
Interventions to tuyeres	20	
Step 2		**956.5**
Installation of one DR plant	515	
Installation of two EAFs	412	
Installation of CO_2 capture	29.5	
Step 3		**1158.5**
Installation of one DR plant	515	
Installation of two EAFs	412	
Installation of CO_2 capture	29.5	
Demolition of BF-BOF line	202	
Step 4		**830**
Electrolyzer	830	
Total		**2.974**

2.5 Chapter summary and conclusions

This chapter presents a new industrial revamping methodology to decarbonise the steel mills sector by a gradual transition from the integrated steel mill (step 0), characterized by blast furnace - basic oxygen furnace lines, to a more efficient configuration based on direct reduced-electric arc furnace plants with green hydrogen as a final reducing agent (step 4). The methodology envisages four subsequent and strategical steps. In the first step, the coke flow rate destined to the BF is partly replaced by injecting 230 kt/y of recycled plastic. The substitution of fossil coal with a circular carbon-based source, like recycled plastic, is not only a step towards the green transition, but it also represents a solution to dispose such material, otherwise harmful if improperly released to the environment. However, since the resulting reduction of CO_2 emissions is very low (0.65%) compared with the integrated steel mill and the energy consumption is slightly increased due to polystyrene higher calorific value, this solution is deemed to be useful only from a carbon circularity standpoint.
In step 2, liquid steel from the BF-BOF lines is reduced to 2.40 Mt/y and a new DR-EAF line with a design capacity of 2.59 Mt/y is added. In this case, CO_2 emissions and energy flows decrease by 39% and 15.3% respectively, compared to the conventional plant. Step 3 involves the complete shut-down of the hot area and the installation of two DR-EAF lines.

When 100% natural gas is involved, the total energy consumption decreases by 33.5% compared to the initial configuration and liquid steel production increases to 5.17 Mt/y. Methane and hydrogen blending is also considered for this step. In direct reduction plants, hydrogen mole fractions, between 0.2 and 0.4, are demonstrated to be effective in both decreasing CO_2 emissions and ensuring the same DRI quality. Lower exhaust gases flow rates are produced from the DR-EAF lines, leading to a significant reduction in process gases energy flows to users and power plants. The configuration proposed in step 3 with the introduction of 100% of CH_4 represents an interesting option to achieve the revamping methodology goals with currently available technology, while posing the basis for hydrogen-based steel production. The plant configuration in step 4 is characterized by 92% less total CO_2 emissions compared to the initial step and 59.4% reduction in energy consumption. However, the most challenging point in this step is the large amount of green hydrogen demanded by the DR plants and the installation of 1.42 GW alkaline electrolyzere. By increasing the scrap mass fraction in the EAFs of step 4, both electricity (assumed emissions free) and H_2 demands of the DR plant decrease while the CO_2 emission levels remain almost unchanged. A linear correlation was also developed to predict the specific CO_2 emissions for step 4 steel mill as a function of the scrap mass fraction in the EAF. The estimated CAPEX for the whole revamping plan would be of 2.97 B€, including the following voices of cost: interventions to tuyeres to allow plastic injection, demolition of the BF-BOF lines, installation of two DRPs and four EAFs, installation of 1.42 GW alkaline electrolyzer. The methodology hereby presented establishes a line for guiding future governmental investments towards cleaner steel production and clarifies the main drawbacks associated within each step.

2.6 Nomenclature

AEL	Alkaline electrolysis
ARA	Alternative reducing agent
BF	Blast furnace
BFG	Blast furnace gas
BOF	Basic oxygen furnace
BOFG	Basic oxygen furnace gas
CC	Continuous casting
CCF	Cyclone converting furnace
CCS	Carbon capture and storage
COG	Coke oven gas
CPR	Coke replacement ratio
DRI	Direct reduced iron

DR-EAF	Direct reduction – Electric arc furnace
DRP	Direct reduction plant
EAF	Electric arc furnace
EAFG	Electric arc furnace gas
LM	Ladle metallurgy
MEA	Mono-ethanol amine
PC	Pulverized coal
PEM	Polymeric electrolyte membrane
PEMEL	Polymer electrolyte membrane electrolysis
PS	Polystyrene
SEC	Specific electric consumption
SOEL	Solide oxide electrolyte membrane
t_{hrc}	Tonne of hot rolled coils
$t_{pig\ iron}$	Tonne of pig iron
t_{prd}	Tonne of product

2.7 References

[1] Pauliuk S, Milford RL, Müller DB, Allwood JM. The steel scrap age. Environ Sci Technol 2013;47:3448–54.

[2] Zhongming Z, Linong L, Xiaona Y, Wangqiang Z, Wei L, others. Iron and Steel Technology Roadmap 2020.

[3] Ren L, Zhou S, Peng T, Ou X. A review of CO2 emissions reduction technologies and low-carbon development in the iron and steel industry focusing on China. Renewable and Sustainable Energy Reviews 2021;143:110846.

[4] Zhang X, Jiao K, Zhang J, Guo Z. A review on low carbon emissions projects of steel industry in the World. J Clean Prod 2021;306:127259.

[5] Ramirez-Santos ÁA, Castel C, Favre E. A review of gas separation technologies within emission reduction programs in the iron and steel sector: Current application and development perspectives. Sep Purif Technol 2018;194:425–42.

[6] Quader MA, Ahmed S, Ghazilla RAR, Ahmed S, Dahari M. A comprehensive review on energy efficient CO2 breakthrough technologies for sustainable green iron and steel manufacturing. Renewable and Sustainable Energy Reviews 2015;50:594–614.

[7] Lu H, Ma X, Huang K, Fu L, Azimi M. Carbon dioxide transport via pipelines: A systematic review. J Clean Prod 2020;266:121994.

[8] Braun C. Not in my backyard: CCS sites and public perception of CCS. Risk Analysis 2017;37:2264–75.

[9] Meijer K, Guenther C, Dry RJ, others. HIsarna pilot plant project. Proc. 1st Int. Conf. on Energy Efficiency and CO2 Reduction in the Steel Industry, 2011.

[10] TATA steel. HISARNA Building a sustainable steel industry. 2020.
[11] Rieger J, Colla V, Matino I, Branca TA, Stubbe G, Panizza A, et al. Residue Valorization in the Iron and Steel Industries: Sustainable Solutions for a Cleaner and More Competitive Future Europe. Metals (Basel) 2021;11:1202.
[12] Liu W, Zuo H, Wang J, Xue Q, Ren B, Yang F. The production and application of hydrogen in steel industry. Int J Hydrogen Energy 2021;46:10548–69.
[13] Gagliardi GG, Ibrahim A, Borello D, El-Kharouf A. Composite polymers development and application for polymer electrolyte membrane technologies—A review. Molecules 2020;25:1712.
[14] Deerberg G, Oles M, Schlögl R. The Project Carbon2Chem®. Chemie Ingenieur Technik 2018;90:1365–8.
[15] Nuber D, Eichberger H, Rollinger B. Circored fine ore direct reduction. Millen Steel 2006;2006:37–40.
[16] Åhman M, Olsson O, Vogl V, Nyqvist B, Maltais A, Nilsson LJ, et al. Hydrogen steelmaking for a low-carbon economy A joint LU-SEI working paper for the HYBRIT project. 2018.
[17] GreenHydrogen. H2FUTURE green hydrogen, 2020 2020. https://www.h2futureproject.eu/. (accessed June 9, 2022).
[18] GrInHy 2.0. GrInHy 2.0, 2019 2019. https://www.green-industrial-hydrogen.com/ (accessed June 9, 2022).
[19] Muslemani H, Liang X, Kaesehage K, Ascui F, Wilson J. Opportunities and challenges for decarbonizing steel production by creating markets for `green steel'products. J Clean Prod 2021;315:128127.
[20] Yilmaz C, Wendelstorf J, Turek T. Modeling and simulation of hydrogen injection into a blast furnace to reduce carbon dioxide emissions. J Clean Prod 2017;154:488–501. https://doi.org/10.1016/j.jclepro.2017.03.162.
[21] Yilmaz C, Turek T. Modeling and simulation of the use of direct reduced iron in a blast furnace to reduce carbon dioxide emissions. J Clean Prod 2017;164:1519–30. https://doi.org/10.1016/j.jclepro.2017.07.043.
[22] Hamadeh H, Mirgaux O, Patisson F. Detailed modeling of the direct reduction of iron ore in a shaft furnace. Materials 2018;11. https://doi.org/10.3390/ma11101865.
[23] Patisson F, Mirgaux O. Hydrogen ironmaking: How it works. Metals (Basel) 2020;10:1–15. https://doi.org/10.3390/met10070922.
[24] Vogl V, Åhman M, Nilsson LJ. Assessment of hydrogen direct reduction for fossil-free steelmaking. J Clean Prod 2018;203:736–45. https://doi.org/10.1016/j.jclepro.2018.08.279.
[25] Jacobasch E, Herz G, Rix C, Müller N, Reichelt E, Jahn M, et al. Economic evaluation of low-carbon steelmaking via coupling of electrolysis and direct reduction. J Clean Prod 2021;328:129502.

[26] Müller N, Herz G, Reichelt E, Jahn M, Michaelis A. Assessment of fossil-free steelmaking based on direct reduction applying high-temperature electrolysis. Clean Eng Technol 2021;4:100158.

[27] Zhang S, Yi B, Guo F, Zhu P. Exploring selected pathways to low and zero CO2 emissions in China's iron and steel industry and their impacts on resources and energy. J Clean Prod 2022;340:130813.

[28] Shen J, Zhang Q, Xu L, Tian S, Wang P. Future CO2 emission trends and radical decarbonization path of iron and steel industry in China. J Clean Prod 2021;326:129354.

[29] Flores-Granobles M, Saeys M. Minimizing CO 2 emissions with renewable energy: a comparative study of emerging technologies in the steel industry. Energy Environ Sci 2020;13:1923–32.

[30] Zhang Q, Li Y, Xu J, Jia G. Carbon element flow analysis and CO2 emission reduction in iron and steel works. J Clean Prod 2018;172:709–23.

[31] Huang D, Dinga CD, Tao Y, Wen Z, Wang Y. Multi-objective optimization of energy conservation and emission reduction in China's iron and steel industry based on dimensionality reduction. J Clean Prod 2022;368:133131.

[32] Yu B, Li X, Shi L, Qian Y. Quantifying CO2 emission reduction from industrial symbiosis in integrated steel mills in China. J Clean Prod 2015;103:801–10.

[33] Wang RQ, Jiang L, Wang YD, Roskilly AP. Energy saving technologies and mass-thermal network optimization for decarbonized iron and steel industry: A review. J Clean Prod 2020;274:122997.

[34] Santos S. Iron and steel CCS study (techno-economics integrated steel mill). IEAGHG, Cheltenham 2013;1.

[35] Murai R, Sato M, Ariyama T. Design of innovative blast furnace for minimizing CO2 emission based on optimization of solid fuel injection and top gas recycling. ISIJ International 2004;44:2168–77.

[36] Ogaki Y, Tomioka K, Watanabe A, Arita K, Kuriyama I, Sugayoshi T. Recycling of waste plastic packaging in a blast furnace system. NKK Technical Review 2001;84:1–7.

[37] Awasthi AK, Cheela VRS, D'Adamo I, Iacovidou E, Islam MR, Johnson M, et al. Zero waste approach towards a sustainable waste management. Resources, Environment and Sustainability 2021;3:100014.

[38] Schultmann F, Engels B, Rentz O. Flowsheeting-based simulation of recycling concepts in the metal industry. J Clean Prod 2004;12:737–51.

[39] Liu X, Yuan Z. Life cycle environmental performance of by-product coke production in China. J Clean Prod 2016;112:1292–301.

[40] Qin S, Chang S. Modeling, thermodynamic and techno-economic analysis of coke production process with waste heat recovery. Energy 2017;141:435–50.

[41] Wang R. Energy saving technologies and optimisation of energy use for decarbonised iron and steel industry. 2022.
[42] Suzuki K, Hayashi K, Kuribara K, Nakagaki T, Kasahara S. Quantitative evaluation of CO2 emission reduction of active carbon recycling energy system for ironmaking by modeling with aspen plus. Isij International 2015;55:340–7.
[43] Petullà M. Analisi energetica di un'acciaieria a ciclo integrale con cattura della CO2. Master's thesis. Politecnico di Milano , 2017.
[44] Rainer R, Miguel AM, Serge R, Luis DS. Best Available Techniques (BAT) Reference Document: for: Iron and Steel Production: Industrial Emissions Directive 2010/75/EU:(Integrated Pollution Prevention and Control) 2012.
[45] Yao D, Yang H, Chen H, Williams PT. Co-precipitation, impregnation and so-gel preparation of Ni catalysts for pyrolysis-catalytic steam reforming of waste plastics. Appl Catal B 2018;239:565–77. https://doi.org/10.1016/j.apcatb.2018.07.075.
[46] Morales J. Energiron - The innovative direct reduction technology 2015. https://docplayer.net/94981109-Joel-morales-marketing-manager-tenova-hyl-kish-island-the-innovative-direct-reduction-technology.html (accessed July 5, 2022).
[47] Müller N, Herz G, Reichelt E, Jahn M. CO2 emission reduction potential in the steel industry by integration of a direct reduction process into existing steel mills. Challenges for Petrochemicals and Fuels: Integration of Value Chains and Energy Transition, Berlin: 2018.
[48] Tenova and Danieli. Energiron DRI technology brochure 2020. https://www.energiron.com/wp-content/uploads/2020/01/Energiron_Brochure-2020.pdf (accessed June 10, 2022).
[49] Tenova and Danieli. Energiron DRI plants - Flexibility for any steelmaking. Dubai: 2013.
[50] Dorndorf M. Hydrogen use in Direct Reduction (DR) Plant – Potentials for CO2 mitigation in steel works 2019. https://salcos.salzgitter-ag.com/fileadmin/footage/MEDIA/SZAG_microsites/salcos/2022/grinhy-20/downloads/deliverables/D5.4_Hydrogen_use_in_Direct_Reduction__DR__Plant_-_potentials_for_CO2_mitigation_in_steel_works.pdf (accessed June 9, 2022).
[51] Navarro RM, Guil R, Fierro JLG. Introduction to hydrogen production. Compendium of Hydrogen Energy, Elsevier; 2015, p. 21–61.
[52] Wang L, Düll J, Maréchal F, others. Trade-off designs and comparative exergy evaluation of solid-oxide electrolyzer based power-to-methane plants. Int J Hydrogen Energy 2019;44:9529–43.
[53] Luo Y, Shi Y, Cai N. Bridging a bi-directional connection between electricity and fuels in hybrid multienergy systems. Hybrid Systems and Multi-Energy Networks for the Future Energy Internet Elsevier 2021:41e84.

[54] Bhandari R, Trudewind CA, Zapp P. Life cycle assessment of hydrogen production via electrolysis–a review. J Clean Prod 2014;85:151–63.

[55] Smolinka T, Günther M, Garche J. Stand und Entwicklungspotenzial der Wasserelektrolyse zur Herstellung von Wasserstoff aus regenerativen Energien. Fraunhofer ISE 2011.

[56] Duarte PE, Becerra J, Lizcano C, Martinis A. ENERGIRON direct reduction technology-economical, flexible, environmentally friendly. vol. 6. 2008.

[57] Muscolino F, Martinis A, Ghiglione M, Duarte P. Introduction to direct reduction technology and outlook for its use. Metallurgia Italiana 2016;4:25–31.

[58] Trinkel V, Kieberger N, Bürgler T, Rechberger H, Fellner J. Influence of waste plastic utilisation in blast furnace on heavy metal emissions. J Clean Prod 2015;94:312–20. https://doi.org/10.1016/j.jclepro.2015.02.018.

[59] Mart\'\in-Lara MA, Moreno JA, Garcia-Garcia G, Arjandas S, Calero M. Life cycle assessment of mechanical recycling of post-consumer polyethylene flexible films based on a real case in Spain. J Clean Prod 2022;365:132625.

[60] Restrepo Á, Bazzo E, Miyake R. A life cycle assessment of the Brazilian coal used for electric power generation. J Clean Prod 2015;92:179–86.

[61] Wörtler M, Schuler F, Voigt N, Schmidt T, Dahlmann P, Lüngen HB, et al. Steel's contribution to a low-carbon Europe 2050: Technical and economic analysis of the sector's CO2 abatement potential. London: BCG Retrieved April 2013;20:2015.

[62] Chung W, Roh K, Lee JH. Design and evaluation of CO2 capture plants for the steelmaking industry by means of amine scrubbing and membrane separation. International Journal of Greenhouse Gas Control 2018;74:259–70.

[63] Morby A. Bidding opens for £150m Redcar steelworks demolition 2020. https://www.constructionenquirer.com/2020/08/17/bidding-opens-for-150m-redcar-steelworks-demolition/ (accessed October 22, 2022).

[64] Hugill S. SSI UK, in Redcar, reveals increase in iron, steel and coke production 2013. https://www.thenorthernecho.co.uk/business/10603119.ssi-uk-redcar-reveals-increase-iron-steel-coke-production/ (accessed October 22, 2022).

[65] Mergel J, Carmo M, Fritz D. Status on technologies for hydrogen production by water electrolysis. Transition to Renewable Energy Systems 2013:425–50.

Chapter 3

A novel CCU approach from blast furnace gases based on a chemical looping cycle

This chapter is based on the following paper:
Hoxha, A., Palone, O., Cedola, L., Stendardo, S., & Borello, D. (2022). Development of a novel carbon capture and utilization approach for syngas production based on a chemical looping cycle. Fuel, 325, 124760.

Abstract

In this chapter a novel process scheme encompassing the separation and reconversion of the CO_2 content of blast furnace gases is proposed and assessed by mass balances and computational fluid dynamics simulations. The system is composed of a calcium looping cycle for the separation of the CO_2 content, a chemical looping cycle for syngas production from CO_2 and H_2O_v, and a post-treatment section for liquid fuels production. The feasibility of the process is assessed by focusing on the chemical looping cycle, which is composed of three reactors: the reducer reactor, where the oxygen carrier is reduced by a solid fuel; the oxidizer reactor, where the reduced oxygen carrier is partially oxidized by a stream of CO_2 and H_2O_s producing CO and H_2; the air reactor, where the oxidation is completed by interaction with air. A MATLAB model is developed to determine the mass flow rate of each component flowing through the chemical looping cycle. The analyses are carried out focusing on the treatment of 1 t/h of CO_2, resulting in 7.1 t/h of $NiFe_2O_4$ or 12.1 t/h of Fe_2O_3. The syngas at the outlet of the oxidizer reactor is composed of H_2 and CO in equimolar content (mass flow rates of 0.05 t/h and 0.64 t/h, respectively). Subsequently, a separate MATLAB model is developed to identify the fluidization conditions for a fluidized bed reactor composed of a FeO particle bed. CFD simulations are carried out to evaluate the reactor hydrodynamics above minimum fluidization conditions and the associated reaction kinetics. For an inlet gas velocity higher (2.6 times) than the minimum fluidization velocity, large bubbles with low frequency are observed, while full consumption of the reactant gases is achieved during the first 15 s of simulation. The results of the CFD simulation allow to validate the assumptions on the FeO particles conversion in the oxidizer and confirm the feasibility and potentials of the process.

3.1 Introduction

Currently, the blast furnace – basic oxygen furnace (BF-BOF) and the direct reduction – electric arc furnace (DR-EAF) are the main steel production technologies [1]. In particular, the majority of steel mills adopts the BF-BOF pathway, where the blast furnace is responsible for an average of 1.14 – 1.40 t_{CO2} per tonne of liquid steel [2]. Carbon capture and utilization strategies can contribute to the mitigation of the carbon footprint associated with steel production, while providing a way to employ power excesses from renewable energy sources such as wind and solar [3]. Originally, direct splitting of CO_2 is proposed as a way to produce CO, but the extremely high temperatures required (T > 2000°C) to reach a significant conversion constituted a drawback. Today this is more feasible by combining CO_2/H_2O solar splitting with ceria membranes separation [4]. However, chemical looping cycles can directly avoid this issue by dividing the process in two or more steps that involve lower temperature levels in the 800 - 1100 °C range [5,6]. In this chapter, a novel process scheme encompassing CO_2 separation from blast furnace gases and its subsequent reconversion by chemical looping processes is proposed and assessed. Mass balances are carried out on the chemical looping plant for syngas production. To support the assumptions on the oxygen carrier conversion in the mass balances, computational fluid dynamics (CFD) simulations of a lab-scale fluidized bed reactor (with implemented reaction kinetics) are also carried out.

3.1.1 Computational fluid dynamics in multiphase flows

Computational fluid dynamics has become a very useful and increasingly reliable tool to understand the complex hydrodynamics of multiphase flows [7,8]. Currently, the most widespread CFD approaches used for simulating multiphase flows are the Eulerian-Lagrangian and the Eulerian-Eulerian approaches [9]. In the Eulerian-Lagrangian approach, Newton's second law is solved for each particle (discrete element model, DEM) or group of particles, as in the dense discrete phase model (DDPM) and in the multiphase particle-in-cell-model (MP-PIC), and the trajectory is determined for each of them. For a dense fluidized bed, the large number of particles to track determines a high computational cost, while the cell size must be large enough to contain the largest particle or group of particles in the distribution, depending on the model. On the contrary, the Eulerian-Eulerian approach, also known as Two Fluids Model (TFM), does not have limitations on mesh refinement, since it considers both the phases as interpenetrating continua (fluids) and solves the averaged conservation equation of momentum, mass and energy for each phase. Constitutive relations are required to close the system of partial differential equations and the kinetic theory of granular flow (KTGF) is commonly used for this purpose [10]. The number of equations to solve is thus drastically reduced with respect to the Eulerian-Lagrangian approach. To the author's best knowledge, a limited number of works presents CFD

simulation of chemical looping cycles, especially when CO_2 splitting is involved [11]. The hydrodynamics of a lab-scale fluidized bed reactor for CO_2 and H_2O splitting is therefore simulated with Ansys/FLUENT 2020 R2 [12] and a proper reaction kinetics implemented to assess the syngas composition and solid conversion variation over time.

3.2 Materials and method

Figure 3.1 presents the industrial integration of a chemical looping cycle in an energy-intensive process with high CO_2 emissions, such as the steel industry. The process addresses the regeneration of the gaseous and solid streams coming from a blast furnace (BF) and is composed of several interrelated units:

- The blast furnace, where iron oxides react with coke and $CaCO_3$ under a mixed gas stream (air, iron ore, pulverised coal, coke) for pig iron production (see Chapter 2).
- A calcium looping cycle (CaL) for the separation of the CO_2 content. The cycle is composed of two reactor units. In the first unit, the BF exhaust gases interact with CaO inside a carbonator reactor operating at approximately $650 - 750\ °C$ [13]. The result is the production of $CaCO_3$ and a gas stream with very low CO_2 content. The produced $CaCO_3$ is subsequently processed in a calcinator, where it thermal decomposes in CaO and CO_2 at approximately $850 - 900\ °C$ [13]. Thus, a stream of pure CO_2 is obtained at the outlet.
- The $CaCO_3$ production unit, where the BF slag and part of the CO_2 from the calcinator are converted into $CaCO_3$. This latter can be subsequently used, for example, as an input for the CaL cycle or for bricks production.
- The chemical looping syngas production cycle, where the CO_2 coming from the calcium looping cycle and an external stream of H_2O react inside an oxidizer reactor with metal oxides. In this way, a syngas composed of H_2, CO and unreacted CO_2 and H_2O is generated. The metal oxides are then sent to an air reactor, where compressed air completes the oxidation of the oxygen carrier. A N_2 treatment unit is located downstream of the air reactor for further separation of N_2 and O_2 [14]. In the reducer, the metal oxides are reduced by means of an endothermic reaction occurring at high temperatures, generally higher than $1400\ °C$ depending on the metal oxide [15]. In the presence of a reducing agent, such as biomass or gaseous fuels, the reaction temperature can be reduced. In this work, biogenic carbon (biomass powder) is employed to promote reduction. Other systems present in the literature involve solar heating by solar concentrators without any reducing agent [16]. The resulting CO_2 stream from the reducer can be stored or added to the CO_2 stream from the calcinator at the oxidizer inlet. After reduction, the metal oxides are sent back to the oxidizer reactor, repeating the cycle.

- The liquid fuel synthesis unit, where the syngas from the oxidizer reactor undergoes a catalytic reaction producing liquid fuels or chemicals.

In this process, syngas production is carried out in the oxidizer reactor, where the oxygen carrier is introduced in its reduced form and is then oxidized by the incoming gases through an exothermic process described by the following general reaction:

$$\alpha MO_{red} + \beta CO_2 + (1-\beta)H_2O_g \rightarrow ZMO_{ox} + \beta CO + (1-\beta)H_2 \qquad (3.1)$$

Where $MO_{ox/red}$ represents the metal oxide in the oxidized or reduced phase, α is the stoichiometric number of the oxygen carrier, β is the molar fraction of CO_2 in the initial stream of CO_2 and H_2O. By capturing oxygen atoms from the gas streams, this process develops the conversion of CO_2 into CO and H_2O into H_2. A model has been developed in MATLAB to analyse the chemical looping cycle through simple mass balances (red dotted rectangle in Figure 3.1). The model is flexible and evaluates syngas production depending on the oxygen carrier of choice: minor adjustments are included to the input parameters to switch from one oxygen carrier to the other. Split-fraction coefficients have been used to define the set of simultaneous equations for the mass balances. Details on the mass balances implementation are reported in Appendix B section B.1. Then, a second MATLAB model has been developed to preliminary design a fluidized bed oxizider reactor with FeO particles. The results of the design have been used as boundary conditions for the computational fluid dynamics simulation. It is important to note that the implementation of preliminary mass balances in Chapter 3, although with simplifying assumptions, has been crucial to underline the potentials and the drawbacks of chemical looping integration in a novel decarbonization scenario. From the insights provided by this Chapter, the research pathway leading to the following part of the work has been established.

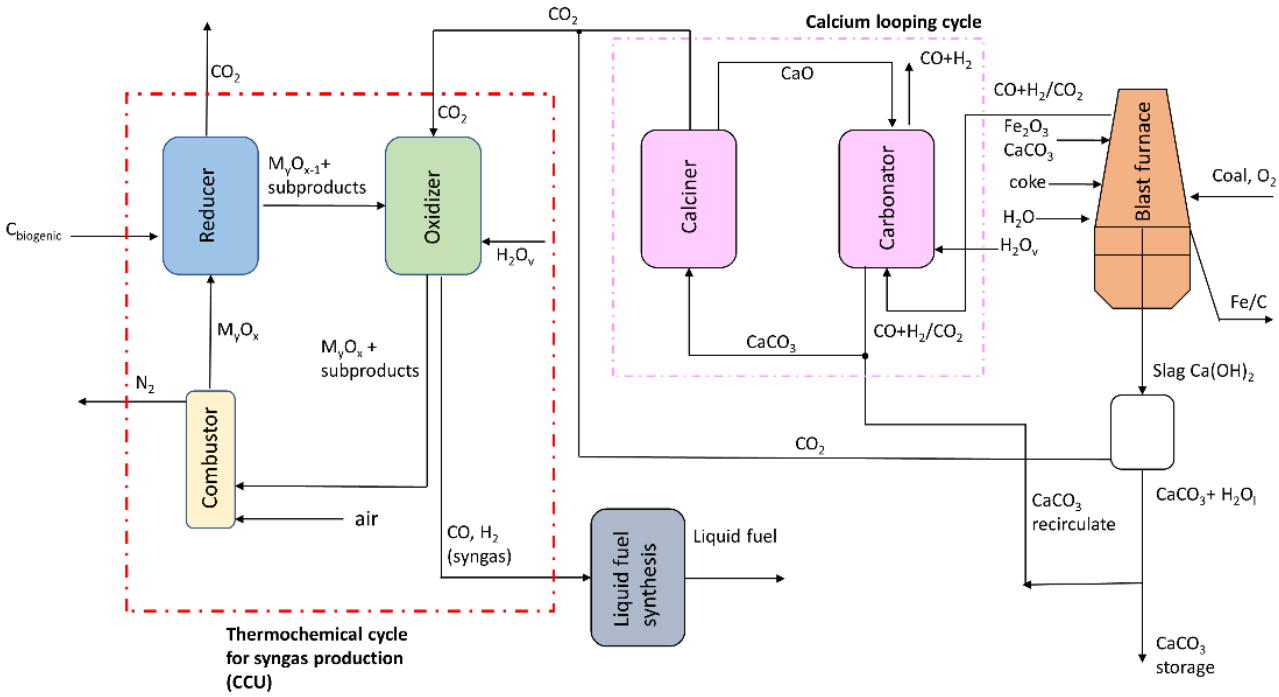

Figure 3.1. Process flowsheet of the industrial integration strategy with a chemical looping cycle

3.2.1 Nickel ferrite ($NiFe_2O_4$)

In the first scenario, $NiFe_2O_4$ is the oxygen carrier flowing through the three reactors of the cycle. In the reducer, the following reduction reaction is modelled:

$$NiFe_2O_4 + C_{biogenic} \rightarrow (1-\eta_1)NiFe_2O_4 + (\eta_1)Ni + 2(\eta_1)FeO + (1-\eta_1)C_{biogenic} + (\eta_1)CO_2 \quad (3.3)$$

The conversion degree (η_1) in the reducer reactor is determined by simulation with Aspen Plus software at equilibrium conditions imposing T = 1100°C and atmospheric pressure. The results indicate that conversion of the oxygen carrier is almost complete at T = 1100°C. Therefore, assuming that equilibrium conditions are met in the reducer, the conversion degree of $NiFe_2O_4$ is set equal to 1. The oxygen released in the reduction step is employed to burn biogenic carbon and provide thermal power to the reactor. The inlet molar flow rate of $C_{biogenic}$ is obtained by assuming a stoichiometric ratio with O_2, accounting for the maximum thermal power produced by the combustion. The CO_2 content in the off-gas from the reducer reactor is assumed to be compressed and stored in a separate unit. The outgoing flow of oxygen carrier from the reducer is subsequently split between the oxidizer and a bypass to the air reactor (90% - 10% in this work), which is introduced to assess the effect

on syngas composition and on plant thermal balance. The reactions occurring in the oxidizer are reported in Eqs. (3.4) and (3.5):

$$2(x \cdot \eta_1)Ni + (x \cdot \eta_1)CO_2 + (x \cdot \eta_1)H_2O_g \rightarrow 2(x \cdot \eta_1)NiO + (x \cdot \eta_1)CO + (x \cdot \eta_1)H_2 \quad (3.4)$$

$$6(x \cdot \eta_1)FeO + (x \cdot \eta_1)CO_2 + (x \cdot \eta_1)H_2O_g \rightarrow 2(x \cdot \eta_1)Fe_3O_4 + (x \cdot \eta_1)CO + (x \cdot \eta_1)H_2 \quad (3.5)$$

Where:

- η_1 is the molar conversion in the reducer;
- x is the percentage of the reducer's products going into the oxidizer.

The degree of conversion in the oxidizer reactor is assumed equal to 1, with the inlet CO_2 stream from the calcinator at 850°C and H_2O at 200°C. In the air reactor, the reactions in Eqs. (3.6) to (3.8) take place:

$$3(1-x) \cdot \eta_1 FeO + (1-x) \cdot \eta_1 Ni + (1-x) \cdot \eta_1 O_2 \rightarrow (1-x) \cdot \eta_1 Fe_3O_4 + (1-x) \cdot \eta_1 NiO \quad (3.6)$$

$$4\eta_1 Fe_3O_4 + \eta_1 O_2 \rightarrow 6\,\eta_1 Fe_2O_3 \quad (3.7)$$

$$\eta_1 Fe_2O_3 + \eta_1 NiO \rightarrow \eta_1 NiFe_2O_4 \quad (3.8)$$

In the first reaction, the stream from the reducer undergoes oxidization by the molecular oxygen content of the air stream to Fe_3O_4. In the last two reactions, $NiFe_2O_4$ is regenerated. Therefore, three streams are directed to the air reactor section: the oxygen carrier in the oxidized state, external air (T = 25°C) and a part of the oxygen carrier in the reduced state from the reducer bypass. Similarly to the oxidizer reactor, the conversion degree of all the reactions is assumed unitary at T = 1200°C and ambient pressure conditions. It is beyond the scope of the work to consider the effects of high temperatures on the oxygen carrier due to prolonged residence time in the reactor, e.g. sintering/agglomeration. A summary of the operating conditions in the three reactors is reported in Table 3.1

Table 3.1. Operating conditions in each unit of the system

Unit	Temperature (°C)	Pressure (atm)
Reducer	1100	1
Oxidizer	1100	1
Air reactor	1200	1
External streams		

H_2O	200	1
CO_2	850	1
Air	25	1

3.2.2 Iron oxide (Fe_2O_3)

The second scenario considers Fe_2O_3 as an oxygen carrier. The following reduction reaction is taken into account:

$$Fe_2O_3 + \frac{1}{2}C_{biogenic} \rightarrow (1-\eta_2)Fe_2O_3 + 2\eta_2 FeO + \frac{1}{2}(1-\eta_2)C_{biogenic} + \frac{1}{2}\eta_2 CO_2 \quad (3.9)$$

The conversion degree (η_2) in the reducer reactor is determined by simulation with Aspen Plus software under equilibrium conditions. The results indicate that conversion to FeO of Fe_2O_3 is almost complete (95%) at $T = 1100°C$ and atmospheric pressure. Therefore, assuming that equilibrium conditions are met in the reducer, the conversion degree of Fe_2O_3 is set to 1. In the oxidizer reactor, FeO is oxidized according to the following reaction:

$$6x \cdot \eta_2 FeO + x \cdot \eta_2 CO_2 + x \cdot \eta_2 H_2O_g \rightarrow 2x \cdot \eta_2 Fe_3O_4 + x \cdot \eta_2 CO + x \cdot \eta_2 H_2 \quad (3.10)$$

The degree of conversion in the oxidizer is assumed equal to 1. Lastly, in the air reactor, the reactions in Eqs. (3.11) and (3.12) take place:

$$3(1-x) \cdot \eta_2 FeO + \frac{1}{2}(1-x) \cdot \eta_2 O_2 \rightarrow (1-x) \cdot \eta_2 Fe_3O_4 \quad (3.11)$$

$$4\eta_2 Fe_3O_4 + \eta_2 O_2 \rightarrow 6\eta_2 Fe_2O_3 \quad (3.12)$$

The FeO bypassed from the reducer to the air reactor is completely oxidized by the oxygen content of the air stream to form Fe_3O_4. Subsequently, the Fe_3O_4 deriving from the oxidation of FeO and from the oxidizer reacts with oxygen to regenerate Fe_2O_3.

3.2.3 Lab-scale oxidizer reactor design

A lab-scale oxidizer reactor is designed in terms of the operating conditions to achieve fluidization. The operating conditions are imposed in accordance with the mass balances. The selected temperature promotes the desired oxidation reaction, remaining below the melting temperature of FeO. The diameter of the bed, the average diameter of the FeO particles and the sphericity factor are fixed to 82.9 mm, 450 μm and 0.85, respectively. The diameter of the particles is calibrated according to the density value, in order to correspond to class B of Geldart classification which is optimal for achieving fluidization [17]. Assuming an initial inventory of 0.8 kg of FeO in the lab-scale reactor, by increasing the surface velocity

of the gas passing through the solid particulate bed different modes of interaction between the two phases are encountered: bubbly flow, slug flow, turbulent flow and pneumatic transport. For each flow pattern, experimental correlations are employed to determine the characteristic velocity values, i.e. slug flow velocity u_{sl} [18], turbulent regime starting transition velocity u_c, ending transition velocity u_k [19], pneumatic drag velocity u_t [20]. The minimum fluidization velocity is estimated by taking the arithmetic average of six correlations available in the literature, reported in generic form in Eq. (3.13), while the pressure drop across the bed is calculated according to Eq. (3.14). The coefficients of the correlations are reported in Table 3.2.

$$u_{mf} = (\nu_g/\rho_g \Delta p_{bed}) \cdot (\sqrt{(A^2 + B \cdot Ar)} - C) \tag{3.13}$$

$$\Delta p_{bed} = h_{bed} \cdot (1 - \epsilon_{mf}) \cdot (\rho_{bed} - \rho_g) \cdot 9.81 \tag{3.14}$$

Where:

- Δp_{bed} is the pressure drop throughout the bed;
- h_{bed} is the height of the bed, obtained by dividing V_{bed} by A_{bed};
- ρ_g is the gas mixture density;
- $\nu_g$is the gas mixture viscosity;
- ρ_{bed} is the density of the powder in the bed;
- ϵ_{mf} is the bed porosity at minimum fluidization conditions;
- Ar is the Archimedes number

Table 3.2. Coefficients of the u_{mf} correlations

A, C	B	Ref.
33.7	0.0408	[21]
25.7	0.0365	[22]
25.3	0.0571	[23]
25.3	0.0651	[24]
27.2	0.0408	[25]
28.7	0.0494	[26]

A more detailed discussion on the procedure for the preliminary bed design is reported in Appendix B section B.3.

3.2.4 CFD simulation method

A CFD model has been developed on the lab-scale oxidizer reactor to investigate the time variation of FeO conversion to Fe_3O_4 along the bed and the hydrodynamic behaviour of the particles. The Eulerian-Eulerian approach is employed due to the characteristics of a dense

two-phases flow and the reduced computational load required compared to the Eulerian-Lagrangian approach. The conservation equations of mass and momentum are both solved for each phase (fluid g and solid S). To have a closed system of partial differential equations several constitutive relations are employed. A detailed discussion of simulation set-up is reported in Appendix B section B.4.

3.2.5 Reaction kinetics

The implemented reaction rate expression follows a Langmuir-Hinshelwood model and is derived from the work of Stamatiou et al. [27] assuming that the interfacial area density $\frac{\alpha_S}{d_s}$ does not change with time:

$$R_r = k_3 \cdot \frac{k_1 y_{CO_2} + k_2 y_{H_2O}}{k_3 + k_1 y_{CO_2} + k_2 y_{H_2O}} \cdot 6 \frac{\alpha_S}{d_s} \qquad \left[\frac{kmol}{m^3 s}\right] \tag{3.15}$$

The reaction constant k_i follows the Arrhenius law:

$$k_i = k_{0i} \cdot \exp\left(-\frac{E_i}{RT}\right) \qquad \left[\frac{kmol}{m^2 s}\right] \tag{3.16}$$

Where:

- k_i is the reaction constant for each of the three elementary reactions in which the heterogeneous reaction is divided in [27] [kmol $m^{-2}s^{-1}$];
- k_{0i} is the frequency factor of the Arrhenius law;
- R is the universal constant of ideal gases [kJ $mol^{-1}K^{-1}$];
- E_i is the activation energy for each elementary reaction [J $kmol^{-1}$];
- y_i the molar fraction of all the gas species in the bed;
- $6 \cdot \alpha_S/d_S$ the interfacial area density, i.e. the ratio of particle surface to cell volume [m^{-1}].

The values selected for k_{0i} and E_i are reported in Table 3.3. This reaction rate expression ha been implemented in Ansys Fluent by writing a user-defined function (UDF). It is important to point out that the implemented kinetics addresses only the initial interface-controlled regime of particles oxidation, where the particle surface resistance is the controlling one. Experimentally it is observed that after a certain time the interface-controlled regime is replaced by the much slower diffusion-controlled regime, where the dominating resistance is represented by that of the oxide layer around the particle.

Table 3.3. Fitted parameters for FeO reaction with H_2O/CO_2 [27]

Parameter	H_2O_s-CO_2/FeO
k_{01} [kmol $m^{-2}s^{-1}$]	$0.129 \cdot 10^{-2}$
k_{02} [kmol $m^{-2}s^{-1}$]	6.26
k_{03} [kmol $m^{-2}s^{-1}$]	$0.427 \cdot 10^{-3}$
E_1 [kJ $mol^{-1}K^{-1}$]	30.4
E_2 [kJ $mol^{-1}K^{-1}$]	80.0
E_3 [kJ $mol^{-1}K^{-1}$]	0
R [kJ $mol^{-1}K^{-1}$]	$3.1445 \cdot 10^{-3}$

3.2.6 Models and boundary conditions

The simulation is conducted under transient conditions to take into account the non-stationarity of the heterogeneous reaction (gas-solid) and of the flow field. Laminar flow conditions are selected, due to the limited gas velocities through the bed. Several works in the literature confirm that a laminar model is consistent with experimental data on fluidized beds as much as a turbulence flow model [28]. The Phase-Coupled SIMPLE algorithm is adopted for the resolution of the Navier-Stokes equations. First-order spatial and temporal implicit discretization is set, except for pressure, where the second order is used to increase the accuracy of the simulation. The first-order discretization is selected to enforce stability and convergence. In fact, the interaction of several models implemented in the simulation (momentum, energy, multiphase and UDF with reaction kinetics) has lead to high instability in the calculations. The advancing time-step is set to $\Delta T = 10^{-4}$ to further ensure computational stability. The adopted mesh is block-structured with $5 \cdot 10^5$ hexahedral cells, which are denser in proximity of the walls and of the central core, as shown in Figure 3.2. A mesh sensitivity analysis is not necessary the since dimension of the FeO particles are 10 times greater than the average grid scale, thus demonstrating the grid discretization quality as indicated in [29]. The mixture of CO_2 and H_2O_s is injected with a uniform velocity of 0.423 m/s, which is higher than the calculated minimum fluidization velocity, and with a uniform temperature of 515 °C, assuming that CO_2 coming the calcium looping cycle (850°C) mixes with H_2O at 200°C in a heated mixing chamber (T_{wall} = 400°C) located underneath the reactor. The imposed temperature values aim at reproducing lab-scale conditions. For equimolar concentration of CO_2 and H_2O in the gas mixture, the inlet gases mass fractions are set to 0.709 and 0.291, respectively. On the reactor walls, a temperature of 1100 °C and a partial slip condition (Johnson and Jackson wall boundary condition [30]) with specularity coefficient of 0.6 is imposed for the solid phase. At the outlet, a gauge pressure of $\Delta P = 0$ is fixed for the gas-solid mixture. The imposed boundary conditions derive from the lab-scale oxidizer reactor design. A summary of the employed multiphase models is presented in Table 3.4.

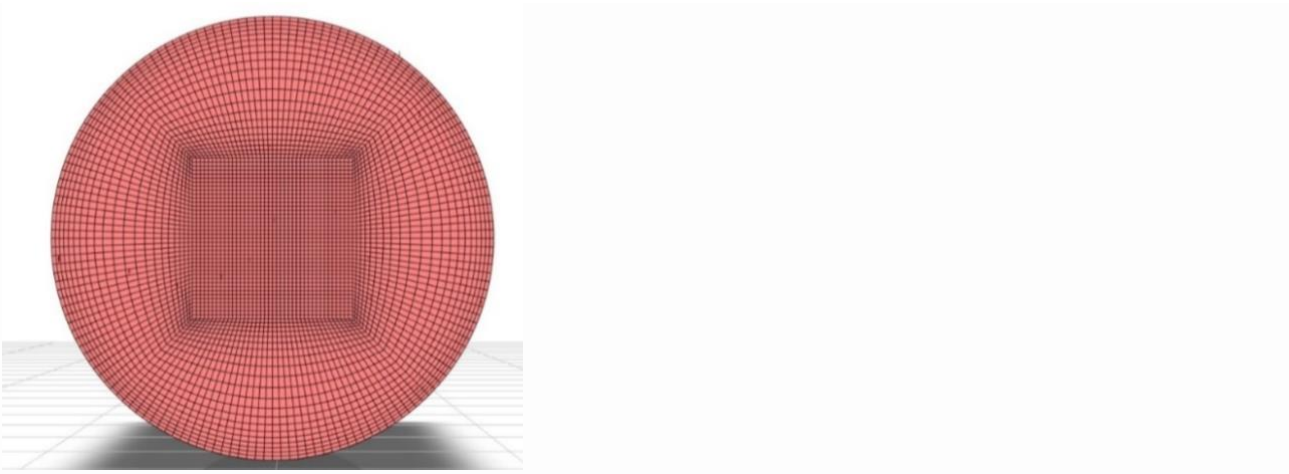

Figure 3.2. Hexaedral mesh

Table 3.4. Constitutive relations for the multiphase model

Parameter	Model
Granular viscosity	Gidaspow [31]
Bulk viscosity.	Lun et al. [32]
Frictional viscosity	Schaeffer [33], Johnson-Jackson [30]
Granular temperature	Algebraic approach
Solids pressure	Lun et al. [32]
Radial distribution function	Lun et al. [32]
Drag coefficient	Gidaspow [31]
Heat exchange coefficient	Gunn [34]

3.3 Results and discussion

3.3.1 Mass balance results

The quantities related to the compounds flowing in the cycle are evaluated assuming to treat 1 t_{CO_2}/h. The results of the mass balances for both oxygen carriers are reported in Tables 3.5 and 3.6.

Table 3.5. Mass flow rates (t/h) at the inlet of each system unit with $NiFe_2O_4$

	$NiFe_2O_4$	Ni	FeO	$C_{biogenic}$	CO_2	H_2O	CO	H_2	NiO	Fe_3O_4	O_2	N_2
Red.	7.10	0	0	0.36	0	0	0	0	0	0	0	0
Oxi.	0	1.60	3.92	0	**1.00**	0.41	0	0	0	0	0	0
Com.	0	0.18	0.44	0	0	0	0	0	2.04	4.21	0.24	0.80
Liq Fuel	0	0	0	0	0	0	0.64	0.05	0	0	0	0

CO_2-st.	0	0	0	0	1.33	0	0	0	0	0	0	0
N_2-tr.	0	0	0	0	0	0	0	0	0	0	0	0.80

Table 3.6. Mass flow rate (t/h) at the inlet of each system unit with Fe_2O_3

	Fe_2O_3	**FeO**	**$C_{biogenic}$**	**CO_2**	**H_2O**	**CO**	**H_2**	**Fe_3O_4**	**O_2**	**N_2**
Red.	12.09	0	0.45	0	0	0	0	0	0	0
Oxi.	0	9.79	0	**1.00**	0.41	0	0	0	0	0
Com.	0	1.09	0	0	0	0	0	10.52	0.48	1.60
Liq Fuel.	0	0	0	0	0	0.64	0.05	0	0	0
CO_2-st.	0	0	0	1.67	0	0	0	0	0	0
N_2-tr.	0	0	0	0	0	0	0	0	0	1.60

In the $NiFe_2O_4$ scenario, 7.10 t/h of oxygen carrier are reduced in the reducer reactor with 0.36 t/h of $C_{biogenic}$. The resulting CO_2 stream (1.33 t/h) is sent to storage while the Ni/FeO stream is sent to the oxidizer reactor (1.60 t/h and 3.92 t/h) and to the air reactor (0.18 t/h and 0.44 t/h). In the oxidizer reactor, CO_2 and H_2O in equimolar concentration (1.00 t/h and 0.41 t/h) react with the oxygen carrier in the reduced phase and generate a syngas (0.64 t/h of CO and 0.05 t/h H_2). In the air reactor, 10% of the Ni-FeO stream from the reducer and the NiO-Fe_3O_4 stream from the oxidizer interact with ambient air and regenerate the oxygen carrier. Depleted air at the air reactor outlet (0.80 t/h) is then sent to treatment, such as cryogenic N_2 separation . Similarly, in the Fe_2O_3 scenario, 12.09 t/h of oxygen carrier are sent to the inlet of the reducer and are completely converted to 10.88 t/h of FeO and 1.67 t/h of CO_2 by interaction with $C_{biogenic}$. Subsequently, 9.79 t/h of FeO are sent to the oxidizer reactor and 1.09 t/h to the air reactor. In the oxidizer reactor, the same syngas flow rate as in the $NiFe_2O_4$ scenario is produced. In the air reactor, FeO is converted to Fe_3O_4 and then Fe_2O_3, while 1.60 t/h of N_2 are sent to treatment. Therefore, for the same CO_2 mass flow rate injected into the oxidizer reactor, $NiFe_2O_4$ is a more convenient choice since it requires a lower oxygen carrier mass flow rate (7.10 t/h). As discussed in Chapter 1, the addition of nickel to iron oxides is beneficial because it provides increased reaction kinetics towards methane conversion and H_2 generation, as well as increased melting temperature of the reduced phase which in turn allows for increased stability over multiple cycles [35]. However, the well-known Ni toxicity [36] and high-cost [37] have led to extensive studies on alternatives. In this framework, iron oxides represent promising candidates due to their availability, low-cost, and the environmentally friendly nature [38]. Furthermore, thermal stability of iron oxides in the $1000 - 1400°C$ temperature range can be enhanced by support on inert ceramic materials, such as Al_2O_3 [15] (see Chapter 5).

3.3.2 Lab-scale oxidizer fluidization conditions

The preliminary design results and the characteristic velocities values for each hydrodynamic regime are reported in Tables 3.7 and 3.8. The estimated minimum fluidization velocity, considering the gas mixture at 1100°C and atmospheric pressure, is equal to 0.162 m/s. The bed porosity estimated at minimum fluidization conditions is $\epsilon_{mf} = 0.45$. An initial bed porosity of 0.4 in fixed bed conditions can thus be assumed for the subsequent CFD simulations, as in minimum fluidization conditions it tends to increase with respect to fixed bed conditions. Table 3.9 collects the results from bed design calculations, which are used as boundary conditions for the CFD simulation.

Table 3.7. Bed parameters

D_{bed}	D_p	ε_{mf}	φ	m_{FeO}	V_{bed}	h_{bed}	c	Δp_{bed}
[mm]	[μm]	[-]	[-]	[kg]	[cm³]	[mm]	[-]	[Pa]
82.9	450	0.45	0.85	0.8	253	47	1	1455

Table 3.8. Hydrodynamic regimes [m/s]

u_{mf}	u_{mb}	u_{slug}	u_c	u_k	u_g
0.162	0.162	0.225	7.15	11.15	0.334

Table 3.9. Boundary conditions for CFD simulation

Parameter	Value
Gas inlet velocity	0.423 m/s
Reactor internal diameter	82.90 mm
Fixed bed height	47 mm
Granular phase diameter	450 μm
FeO density	5745 kg/m^3
Fe_3O_4 density	5200 kg/m^3
Initial bed porosity	0.4
Simulated total reactor height	250 mm

3.3.3 CFD results

The CFD simulation is conducted over 15 seconds, during which a steady-state fluidization condition is reached. The oxidation reaction rate along the centerline at $t = 15$ s is plotted in Figure 3.3, showing a highly reactive region concentrated 1.5 cm above the inlet (over a total fixed bed height of 4.7 cm) and with the gas-solid reaction rate reaching a maximum value of 2.6 kmol/s · m^3. The mean operating temperature in the whole domain is equal to 1393 K, therefore slightly greater than the imposed wall temperature of 1373 K due to

reaction exothermicity. In Figure 3.3, the experimental conversion extent of FeO particles (T = 973 K and d = 131 μm) under an equimolar flow of CO_2 and H_2O_s is compared with the simulation results for d = 450 μm particles under the same reactants molar ratio at T = 973 K and 1373 K [27]. For the same temperature conditions of 973 K, the simulation results reproduce correctly the experimental data trend, while at 1373 K increased reaction kinetics and thus increased FeO conversion takes place. Figure 3.4 shows the H_2O (a) and CO_2 (b) mole fractions trend along the centreline at the end of the simulation (t = 15 s). The gas conversion behavior is similar to that experimentally observed in the literature [39] for the catalytic decomposition of ozone in a fluidized bed reactor, where the asymptotic value of conversion is reached at about 1/3 of the total reactor height. At the outlet, the gas mixture is composed of CO and H_2 in nearly equimolar concentration (Figure 3.4 (c) and (d)), thus validating the results provided by the MATLAB model. These results demonstrate that: the assumption of high (complete in this case) conversion to Fe_3O_4 in the oxidizer is appropriate if the full reaction conversion time is ensured; the reaction kinetics is fast enough to allow for the complete consumption of the gaseous reactants. Finally, Figure 3.6 shows the solid volume fraction variation with time on plane x = 0. Assuming a condition of $\alpha_S \leq 0.2$ [40] for bubble determination, the adopted Gidaspow et al. model [31] for drag predicts bubble formation and rising, thus confirming that the selection of flow conditions is able to guarantee bed fluidization. Since the minimum fluidization velocity and the slug flow starting velocity are equal to 0.162 m/s and 0.225 m/s (Table 3.8), respectively, with a superficial gas velocity of 0.423 m/s, the slug flow regime takes place. The low frequency of bubble formation and the significant bubble sizes (often comparable with reactor's diameter) typical of this hydrodynamic regime are clearly visible in the profiles of Figure 3.6.

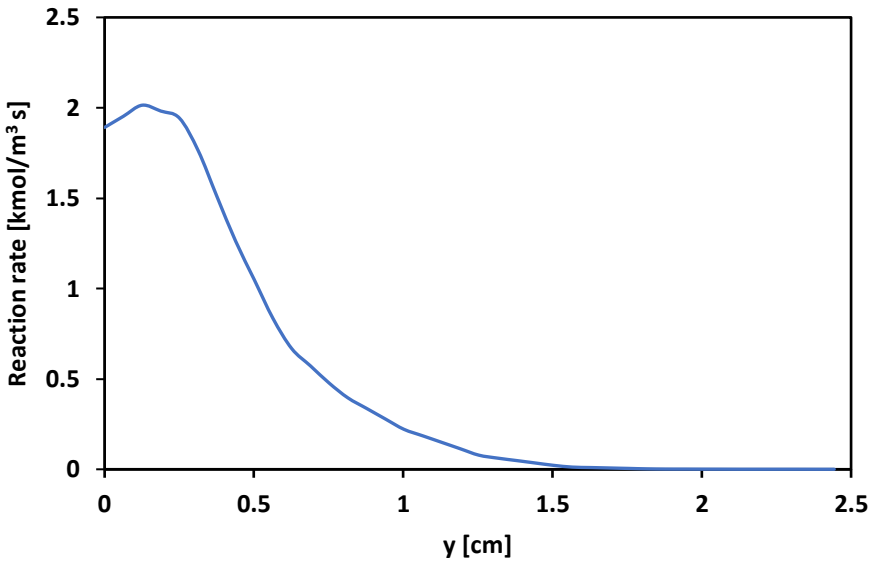

Figure 3.3. Heterogeneous reaction rate for t = 15 s along the centerline

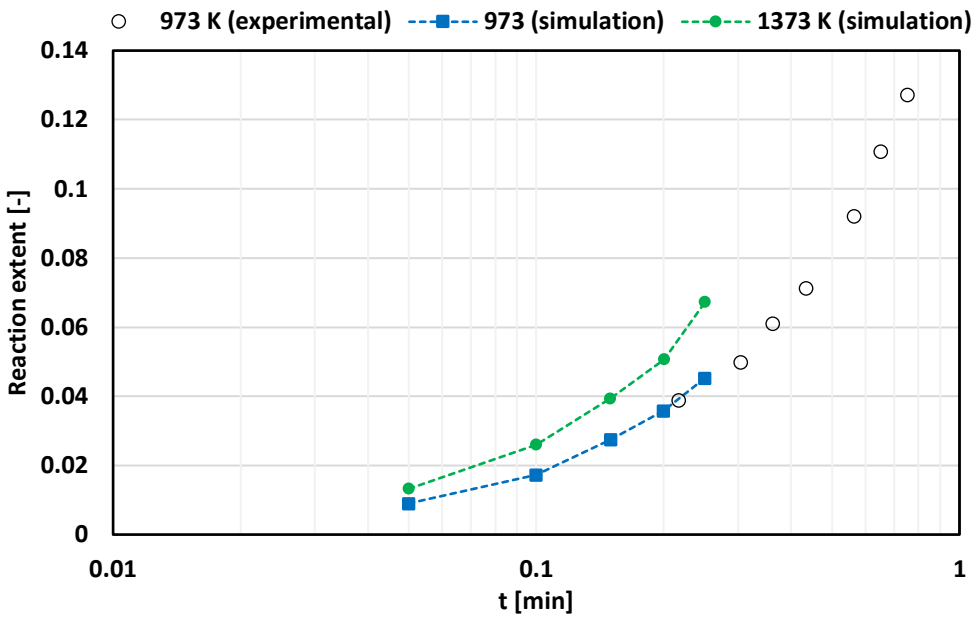

Figure 3.4. Reaction extent comparison between experimental values and simulation results

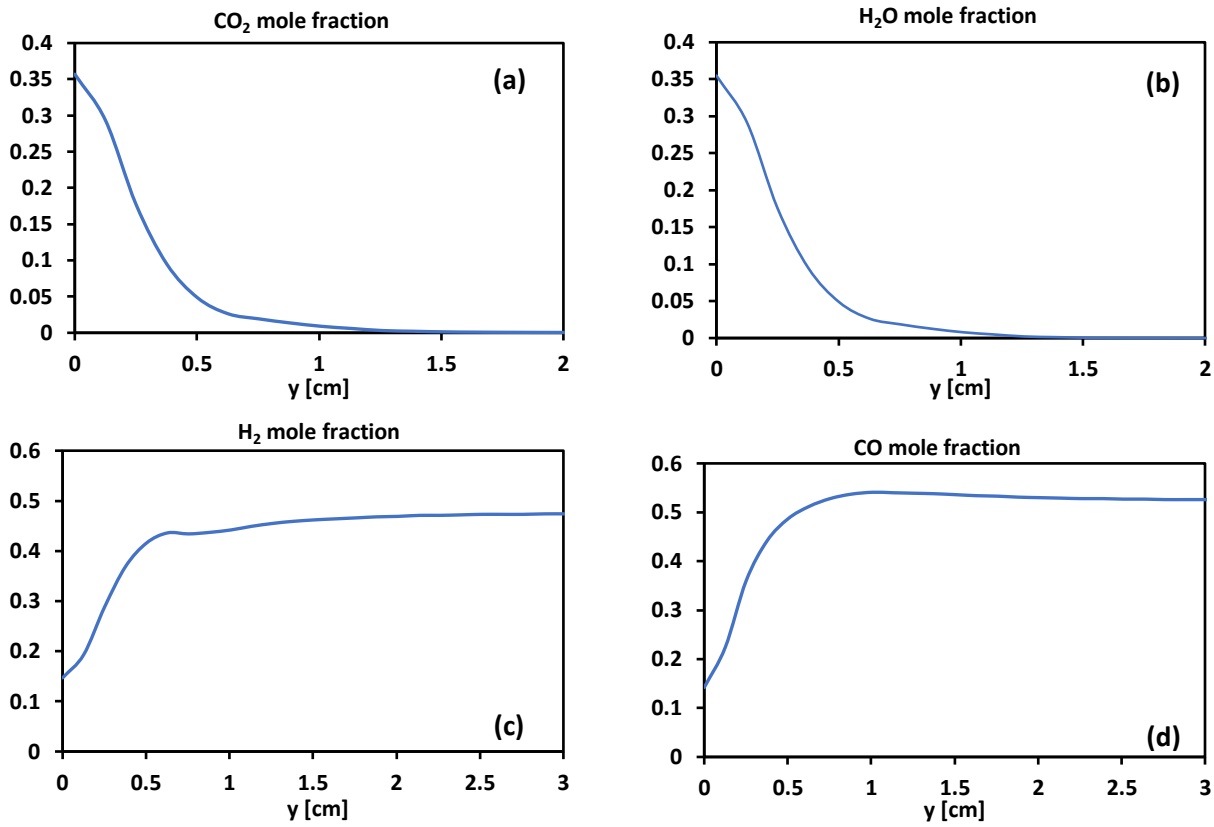

Figure 3.5. Gases mole fractions of H_2O (a), CO_2 (b), H_2 (c), CO (d) at t = 15 s along oxidizer's centreline

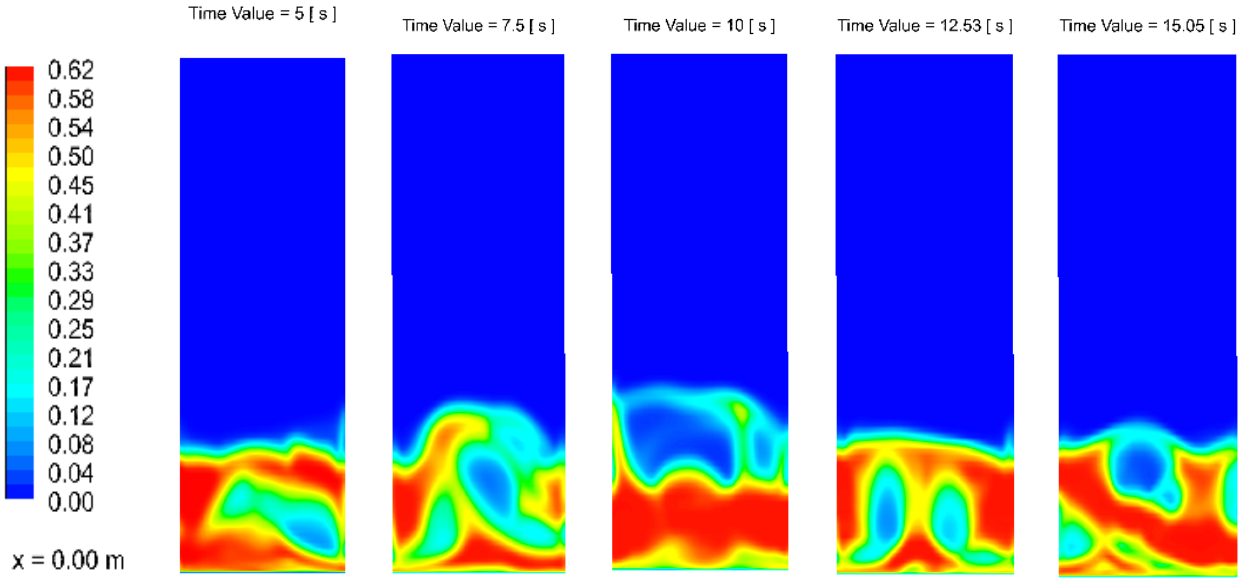

Figure 3.6. Solids (FeO and Fe_3O_4) volume fraction for t = 5 s,7.5 s,10 s,12.53 s and 15.05 s in the x = 0 plane

3.4 Chapter summary and conclusions

In this chapter, a novel process scheme for the reutilization of the CO_2 content from blast furnace gases is proposed. The process encompasses the following units: a calcium looping cycle for the separation of the CO_2 separation in blast furnace gases, a chemical looping cycle for CO_2 and H_2O splitting, a syngas post-treatment section for liquid fuels production and a CO_2 carbonation section for $CaCO_3$ production. A preliminary feasibility study on the chemical looping cycle is carried out by mass balances and computational fluid dynamics simulations. Two different oxygen carriers, $NiFe_2O_4$ and Fe_2O_3, are considered for comparative analysis. For a fixed syngas molar flow rate (22.72 kmol/h), lower oxygen carrier mass flow rates are computed in the $NiFe_2O_4$ scenario. However, further analyses are carried out for the Fe_2O_3 case, due to highest availability of this material, especially in proximity of a steel mill, and due to its low toxicity. Considering a lab-scale fluidized bed reactor, fluidization conditions are determined for FeO particles and subsequently employed as boundary conditions for the CFD simulation. The Eulerian-Eulerian multiphase approach is used to simulate the hydrodynamics of the fluidized bed reactor. Literature kinetics of FeO reaction with H_2O and CO_2 is implemented in the simulation by a UDF. An interface-controlled limited regime is assumed for the whole duration of the simulation, considering the limited simulation time of 15 s. In the results, the gaseous reactants are almost fully consumed at about 40% of total bed height and confirm the gas compositions at the oxidizer outlet from the MATLAB model. From the 15 s of operation it is possible to predict that high conversion of FeO into Fe_3O_4 can be achieved if the solids residence time is long enough inside the reactor. From the hydrodynamics side, low

frequency and large bubble formation are observed throughout the 15 s of simulation, indicating that a slug flow is fully established accordingly with the estimations in the preliminary design of the lab-scale oxidizer reactor.

ACKOWLEDGEMENT

This research is funded by the Italian Ministry of Economic Development, under the project SFERO (Systems for Flexible Energy Reusing carbOn) within the Italian research programme 2019-2021:"Ricerca di Sistema" (Grant number I34I19005780001).

3.5 Nomenclature

BF	Blast furnace
BF-BOF	Blast furnace-Basic Oxygen Furnace
CaL	CaL Calcium Looping
CFD	Computational Fluid Dynamics
DDPM	Dense Discrete Phase Model
DR-EAF	Direct Reduction – Electric Arc Furnace
GHG	Greenhouse Gas
MPIC	Multiphase Particle-in-Cell-model
NIST	National Institute of Standards and Technology
TFM	Two Fluids Model
UDF	User Defined Function

3.6 References

[1] Energy Agency I. Iron and Steel Technology Roadmap Towards more sustainable steelmaking Part of the Energy Technology Perspectives series. n.d.

[2] Ramírez-Santos ÁA, Castel C, Favre E. A review of gas separation technologies within emission reduction programs in the iron and steel sector: Current application and development perspectives. Sep Purif Technol 2018;194:425–42. https://doi.org/10.1016/j.seppur.2017.11.063.

[3] Ince AC, Colpan CO, Hagen A, Serincan MF. Modeling and simulation of Power-to-X systems: A review. Fuel 2021;304:121354. https://doi.org/10.1016/j.fuel.2021.121354.

[4] Tou M, Michalsky R, Steinfeld A. Solar-Driven Thermochemical Splitting of CO2 and In Situ Separation of CO and O2 across a Ceria Redox Membrane Reactor. Joule 2017;1:146–54. https://doi.org/10.1016/J.JOULE.2017.07.015.

[5] de Klerk A. Engineering evaluation of direct methane to methanol conversion. Energy Sci Eng 2015;3:60–70. https://doi.org/10.1002/ese3.51.

[6] Oruc O, Dincer I. Assessing the potential of thermo-chemical water splitting cycles: A bridge towards clean and sustainable hydrogen generation. Fuel 2021;286:119325. https://doi.org/10.1016/j.fuel.2020.119325.

[7] Venturini P, Andreoli M, Borello D, Rispoli F, Gabriele S. Modeling of Water Droplets Erosion on a Subsonic Compressor Cascade. Flow Turbul Combust 2019;103:1109–25. https://doi.org/10.1007/s10494-019-00086-0.

[8] Borello D, Rispoli F, Venturini P. An Integrated Particle-Tracking Impact/Adhesion Model for the Prediction of Fouling in a Subsonic Compressor. J Eng Gas Turbine Power 2012;134. https://doi.org/10.1115/1.4006840.

[9] Ranade V V. Computational flow modeling for chemical reactor engineering. Academic Press; 2002.

[10] Fan L-S. Multiphase flow and fluidization: Continuum and kinetic theory descriptions. By Dimitri Gidaspow, Academic Press, New York, 1994, 467 pp.,$69.50. AIChE Journal 1996;42:1197–8. https://doi.org/10.1002/aic.690420438.

[11] Nguyen VN, Blum L. Syngas and Synfuels from H_2O and CO_2: Current Status. Chemie Ingenieur Technik 2015;87:354–75. https://doi.org/10.1002/cite.201400090.

[12] Fluent A. Ansys Fluent: Theory guide. 2021.

[13] Blamey J, Anthony EJ, Wang J, Fennell PS. The calcium looping cycle for large-scale CO2 capture. Prog Energy Combust Sci 2010;36:260–79. https://doi.org/10.1016/j.pecs.2009.10.001.

[14] Jiang Q, Chen Z, Tong J, Yang M, Jiang Z, Li C. Direct thermolysis of CO2 into CO and O2. Chemical Communications 2017;53:1188–91. https://doi.org/10.1039/c6cc08801e.

[15] ABANADES. Metal Oxides Applied to Thermochemical Water-Splitting for Hydrogen Production Using Concentrated Solar Energy. ChemEngineering 2019;3:63. https://doi.org/10.3390/chemengineering3030063.

[16] Lyngfelt A, Linderholm C. Chemical-Looping Combustion of Solid Fuels – Status and Recent Progress. Energy Procedia 2017;114:371–86. https://doi.org/10.1016/j.egypro.2017.03.1179.

[17] Geldart D. The effect of particle size and size distribution on the behaviour of gas-fluidised beds. Powder Technol 1972;6:201–15. https://doi.org/10.1016/0032-5910(72)83014-6.

[18] Stewart PSB, Davidson JF. Slug flow in fluidised beds. Powder Technol 1967;1:61–80. https://doi.org/10.1016/0032-5910(67)80014-7.

[19] Horio M, Morishita K. FLOW REGIMES OF HIGH VELOCITY FLUIDIZATION. JAPANESE JOURNAL OF MULTIPHASE FLOW 1988;2:117–36. https://doi.org/10.3811/jjmf.2.117.

[20] Turton R, Clark NN. An explicit relationship to predict spherical particle terminal velocity. Powder Technol 1987;53:127–9. https://doi.org/10.1016/0032-5910(87)85007-6.

[21] Wen CY, Yu YH. A generalized method for predicting the minimum fluidization velocity. AIChE Journal 1966;12:610–2. https://doi.org/10.1002/aic.690120343.

[22] Author F, Harrison D. Fluidization. vol. 61. 1933.

[23] Saxena SC, Vogel GJ. Segregation and fluidization characteristics of a dolomite bed with a range of particle sizes and shapes. The Chemical Engineering Journal 1977;14:59–63. https://doi.org/10.1016/0300-9467(77)80023-3.

[24] Babu, Shah, Talwalkar. Fluidization correlation for coal gasification materials—minimum fluidization velocity and fluidized bed expansion ratio. AIChE Symposium Series 1978.

[25] Grace JR. Handbook of Multiphase Systems. vol. 8. Hemisphere Publishing Corp; 1982.

[26] Chitester DC, Kornosky RM, Fan L-S, Danko JP. Characteristics of fluidization at high pressure. Chem Eng Sci 1984;39:253–61. https://doi.org/10.1016/0009-2509(84)80025-1.

[27] Stamatiou A, Loutzenhiser PG, Steinfeld A. Solar Syngas Production From H2O and CO2 via Two Step Thermochemical Cycles Based on FeO/Fe3O4 Redox Reactions: Kinetic Analysis. ASME 2010 4th International Conference on Energy Sustainability, Volume 2, ASMEDC; 2010. https://doi.org/10.1115/es2010-90009.

[28] Gao X, Wu C, Cheng Y, Wang L, Li X. Experimental and numerical investigation of solid behavior in a gas–solid turbulent fluidized bed. Powder Technol 2012;228:1–13. https://doi.org/10.1016/j.powtec.2012.04.025.

[29] Andrews, Loezos PN, Sundaresan S. Coarse-Grid Simulation of Gas-Particle Flows in Vertical Risers. Industrial & Engineering Chemistry Research 2005;44:6022–37. https://doi.org/10.1021/ie0492193.

[30] Johnson PC, Jackson R. Frictional–collisional constitutive relations for granular materials, with application to plane shearing. J Fluid Mech 1987;176:67. https://doi.org/10.1017/s0022112087000570.

[31] Gidaspow D, Bezburuah R, Ding J. Hydrodynamics of circulating fluidized beds: kinetic theory approach. 7th Fluidization Conference, 1992.

[32] Lun CKK, Savage SB, Jeffrey DJ, Chepurniy N. Kinetic theories for granular flow: inelastic particles in Couette flow and slightly inelastic particles in a general flowfield. J Fluid Mech 1984;140:223–56. https://doi.org/10.1017/s0022112084000586.

[33] Schaeffer DG. Instability in the evolution equations describing incompressible granular flow. J Differ Equ 1987;66:19–50. https://doi.org/10.1016/0022-0396(87)90038-6.

[34] Gunn DJ. Transfer of heat or mass to particles in fixed and fluidised beds. Int J Heat Mass Transf 1978;21:467–76. https://doi.org/10.1016/0017-9310(78)90080-7.

[35] Sun Z, Lu DY, Symonds RT, Hughes RW. Chemical looping reforming of CH4 in the presence of CO2 using ilmenite ore and NiO-modified ilmenite ore oxygen carriers. Chemical Engineering Journal 2020;401:123481. https://doi.org/10.1016/J.CEJ.2019.123481.

[36] De Filippis P, D'Alvia L, Damizia M, Caprariis B, Del Prete Z. Pure hydrogen production by steam-iron process: The synergic effect of MnO and Fe_2O_3. Int J Energy Res 2020;45:4479–94. https://doi.org/10.1002/er.6117.

[37] Samprón I, de Diego LF, García-Labiano F, Izquierdo MT. Effect of the Fe content on the behavior of synthetic oxygen carriers in a 1.5 kW biomass chemical looping gasification unit. Fuel 2022;309:122193. https://doi.org/10.1016/j.fuel.2021.122193.

[38] Yu Z, Yang Y, Yang S, Zhang Q, Zhao J, Fang Y, et al. Iron-based oxygen carriers in chemical looping conversions: A review. Carbon Resources Conversion 2019;2:23–34. https://doi.org/10.1016/j.crcon.2018.11.004.

[39] Zimmermann S, Taghipour F. CFD Modeling of the Hydrodynamics and Reaction Kinetics of FCC Fluidized-Bed Reactors. Industrial & Engineering Chemistry Research 2005;44:9818–27. https://doi.org/10.1021/ie050490+.

[40] van Wachem BGM, Schouten JC, Krishna R, van den Bleek CM. Eulerian simulations of bubbling behaviour in gas-solid fluidised beds. Computers & Chemical Engineering 1998;22:S299–306. https://doi.org/10.1016/s0098-1354(98)00068-4.

Chapter 4

Thermochemical syngas production in an iron-based oxidizer reactor

This chapter is based on the following paper:
Palone, O., Cava, C., Paris, E., Vincenti, B., Caputi, M. V. M., Gallucci, F., & Borello, D. (2023). Experimental investigation of thermochemical syngas production in a scrap iron-based oxidizer reactor for industrial decarbonisation. Fuel, 347, 128436.

Abstract

In this chapter the syngas production performance of scrap iron reacting with CO2 and water steam is assessed under different operating conditions in a fixed bed oxidizer reactor. At 1050 °C, a maximum volume percentage of 37% CO in the product gases is detected with the injection of 1 nl/min CO_2. The CO_2 conversion is confirmed to be significantly promoted by temperature. Subsequently, combined tests with CO_2 and water steam are carried out by varying the reactants total flow rate, the iron bed mass and the reactants molar ratio. The objective is to optimize syngas yield and composition in terms of H_2 and CO. By decreasing the total reactants flow rate, the splitting process is promoted and below a certain flow rate, CO_2 splitting is greater than that of H_2O. On the contrary, by increasing the H_2O/CO_2 molar ratio, the splitting is enhanced for both species. In particular, for the tested flow rate H_2O splitting increases by 10% when the H_2O/CO_2 molar ratio goes from 1 to 3, with respect to the 3.5% increase of CO_2 splitting. Finally, with H_2O/CO_2 = 6 and low total flow rate, the optimal thermochemical syngas composition is achieved, including 41% H_2 and 12.1% CO, with the rest constituted by CO_2 when computed on a dry basis.

4.1 Introduction

The most important chemicals in the chemical industry such as ammonia, methanol and high hydrocarbons, are conventionally produced by gas to liquid processes involving carbon gasification or steam methane reforming processes aiming at syngas production, with significant CO_2 emissions. Currently, efforts are made to reduce both the cost of these processes as well as the associated greenhouse gas emissions. In the future, the increasing availability of high purity CO_2 from hard-to-abate industrial sectors, such as steel mills and cement plants [1], is expected to trigger the development of CO_2 valorization processes. CO_2 can be separated or captured by absorption (chemical or physical) techniques, adsorption techniques [2], membranes separation [3] and calcium looping cycles [4]. Chemical looping configures as a promising technology for the efficient separation and utilization of CO_2 streams. As discussed in Chapter 1, in chemical looping hydrogen generation H_2O is used in the first oxidation step for high purity H_2 production with inherent CO_2 separation. However, the oxidation step can also be performed with CO_2 coming from capture processes or with both CO_2 and H_2O, thus producing an outlet syngas (H_2 and CO) stream. Iron-based materials are attractive oxygen carriers for chemical looping applications due to iron large availability, high melting temperatures in the 1650-1870 K range [5], oxygen transport capacities of 0.10 and 0.30 for Fe_2O_3/FeO and Fe_2O_3/Fe redox pairs, respectively [6], low cost and low toxicity. Furthermore, iron oxides are very abundant and they are extracted within a highly developed and mature mining industry or from recycling processes. The main drawback of these oxygen carriers is their limited cyclability, since they suffer from agglomeration and sintering during the reduction and oxidation steps, both of which are commonly performed at temperatures above 800 °C [7]. The thermal resistance of iron oxides can be enhanced by support with ceramic materials such as Al_2O_3 [8], monoclinic ZrO_2 [9], partially stabilized tetragonal zirconia (t-PSZ) and yttria-stabilized cubic zirconia (c-YSZ) [10]. From a thermodynamic standpoint, CO_2 splitting with iron oxides is characterized by high conversion values, i.e. > 50% for Fe and > 30% for FeO between 200 °C and 1000 °C, and 100% selectivity towards CO above 700 °C [11]. On the other hand, H_2O splitting by iron is thermodynamically favoured below 900 °C, according to the variation of the Gibbs free energy [12]. Thermodynamic analyses have demonstrated that the conversion efficiency for the combined CO_2/H_2O splitting is higher than that of pure H_2O splitting but lower than the pure CO_2 splitting [13].

4.1.1 Combined CO_2/H_2O splitting with iron oxides

A limited number of experimental works has investigated syngas production from CO_2 and H_2O splitting involving iron oxides as oxygen carriers. In [14], Abanades et al. investigate syngas production by both separate and combined CO_2/H_2O splitting over a FeO bed. The conversion variation with time for the separate oxidation with CO_2 and H_2O at 700 °C

presents an inflection point in the first 5 minutes of test and reaches maximum conversions of 70% and 80% after 40 minutes, respectively. Previous studies have also tested FeO oxidation with H_2O at 575 °C over a FeO powder and have achieved conversion values limited to 54% [15]. In the combined splitting case, a gas flow with H_2O:CO_2 molar ratio of 6 is injected with Ar as the inert gas. At 700 °C, CO production is much lower than H_2 production, though the water gas shift reaction between the gas products could be partly responsible for the results. On the same line, in [16] Stamatiou et al. perform thermodynamic analyses and experimental evaluations on syngas production from CO_2/H_2O with Zn/ZnO and FeO/Fe_3O_4 redox pairs. Regarding FeO oxidation, during the initial interface controlled regime H_2O is more reactive with FeO compared to CO_2, as also observed by Abanades et al. A linear behaviour of the products molar ratio with respect to the reactants molar ratio is observed for both metal oxides [16,17].

4.1.2 Potentials of iron-based waste materials

Recently, the potential of natural ores or industrial waste material (e.g. red mud, copper slag) as oxygen carriers has received increasing attentions. Especially waste materials with high iron content show promising behavior for CL applications. In [18], Hammache et al. compare red mud and iron impregnated spent fluid cracking catalyst for high temperature chemical looping (1100 °C). Better sintering and attrition resistance are observed for the iron modified catalyst compared to red mud. Another comparison between ores (ilmenite, iron-titanium ore) and waste materials (steel converter slag) is carried out in [19] by Hedayati et al. on chemical looping combustion and gasification processes. Ilmenite has proved to be the best candidate in terms of fuel conversion and syngas fraction at the outlet of the fuel reactor for a similar effective air ratio, i.e. ratio of the moles of oxygen transferred from the air reactor to the moles of oxygen required to completely burn the fuel. In [20], Wang et al. test cement bonded fine particles of copper ore and red mud for in situ gasification chemical looping combustion of coal. The presence of copper ore determines a higher CO_2 yield and a higher oxygen transport capability compared to pure red mud, also when lignite is used in place of coal char. In [21] Durmaz et al. test copper converter slag in a bench-scale fluidized bed reactor operating at 850 °C during reduction over 50 cycles. High conversions are achieved for all the tested mixtures, with almost complete conversion (97%) under 50% H_2 mixture. The increase of porosity and the formation of a highly reactive copper ferrite contribute to the observed increase in reactivity along the cycles. A similar behaviour is also detected in the experimental evaluations discussed in Chapter 5. Similarly, in [22] Condori et al. analyse the suitability of converter slag in a continuous 1.5 kWth biomass chemical looping gasification unit. Biomass and carbon conversions above 90% and syngas yields of 0.66 $Nm^3/kg_{drybiomass}$ are achieved under autothermal operating conditions. In [23], Zornoza et al. test different low cost iron-based oxygen carriers demonstrating that iron ore deriving

from spray roasting (also known as Ruthner process) in steel mills has high reactivity with methane at 950 °C and high stability when reduced to FeO or Fe. Finally, in [24] Wang et al. propose a short-cut chemical looping hydrogen production process from steel iron dust to avoid the reactivity reduction due to iron ores sintering in chemical looping processes. The iron dust from electric arc furnaces is oxidized by water steam and then regenerated by an electric arc furnace rather than a conventional reduction reactor, which is affected by a number of issues, such as source of energy, intermittency of the source, necessity of a reducing agent. In this chapter, the process proposed in [24] by Wang et al. is taken as a reference and retrofitted for thermochemical syngas production from scrap iron (Figure 4.1). The reduction step is represented by either the blast furnace – basic oxygen furnace line or the direct reduction line of a steel mill, where the solid material coming from the oxidizer is sent for efficient reduction. The main scope of this work is the experimental assessment of the optimal conditions for enhancing H_2 and CO production from scrap iron oxidation by H_2O and CO_2, in order to make the syngas a valid building block for processing into a liquid fuel, such as methanol.

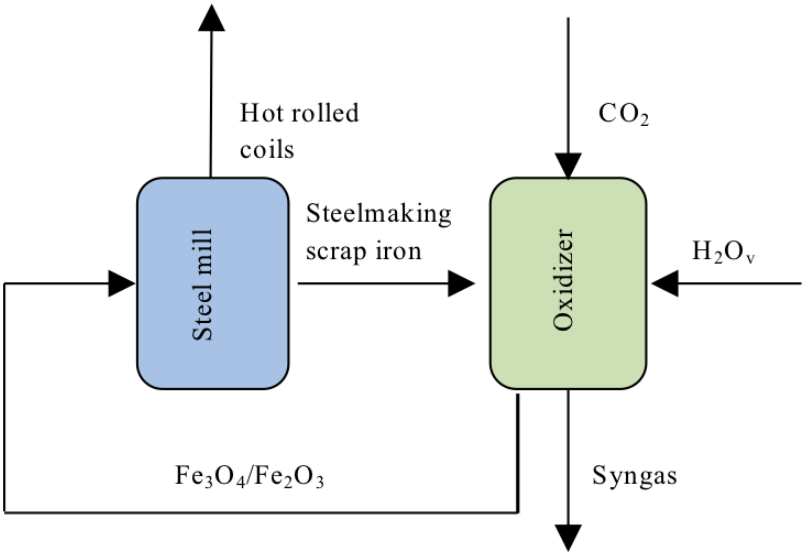

Figure 4.1. Simplified layout of the proposed chemical looping cycle involving scrap iron and captured CO_2

4.2 Materials and method

4.2.1 Material

The preparation of oxygen carriers for chemical looping applications may represent an important voice of cost. To overcome this drawback, the utilization of abundant materials on earth, such as iron ores, or iron-based waste materials from industry is often suggested, though their applicability could be limited due to their low reactivity. In this work, experimental tests are carried out to investigate the interaction between a scrap iron powder

provided by Alquera and different CO_2 and H_2O streams in a fixed bed reactor. In this context, the employed scrap iron powder is representative of secondary steelmaking scrap. More details on the material properties are provided in Appendix C.

4.2.2 Experimental set-up

The scheme of the experimental apparatus is synthetically presented in Figure 4.2-left. The reactor is composed of a steel pipe located inside an electric furnace manufactured by Carbolite Gero (Figure 4.2-right) . The central part of the furnace is equipped with a type N thermocouple for temperature monitoring and regulation. The reactants enter the reactor through two different pipes assembled to a flange that closes the inlet. The scrap iron powder is located inside a cylindrical steel container, held by a steel threaded rod screwed to the flange at the base of the reactor. The base of the cylindrical container consists of a steel orifice plate covered by an Inconel mesh manufactured by Fratelli Mariani (250 μm mesh size), suitable to support the iron particles bed. The orifice plate is located 2 cm above the flange so that the injected gases can mix and reach a homogeneous temperature just before interacting with the iron bed. The CO_2 flow rate is obtained from the expansion of liquefied CO_2 contained in a bottle provided by Sapio at saturation conditions and its flow rate is controlled by a mass flow controller (MFC, El Flow Select F 201 by Bronkhorst). H_2O is injected at overheated conditions (150 °C) by an electric steam generator (Cast-X 500 by Watlow) and its flow rate is set by a circulation pump (BT4B by Prominent) coupled with a mass flow controller (Mini Cori-Flow M14 by Bronkhorst). Below the exhaust gas pipe, a capillary tube is positioned for sampling the outflow gas composition by a micro gas chromatograph analyser (Micro GC Inficon 3000) or bags. The water content in the product gas is condensed in a water trap before the GC injection. In each test, the iron powder is charged in the reactor after reaching the desired temperature conditions, to avoid early particle agglomeration and air oxidation before the beginning of the experimental run. Once the test is completed, the gas flows are stopped and the entire reactor is cooled back to room temperature. The characterization of the fresh and reacted iron bed is performed by XRD (X-Ray Powder Diffraction, Philips X'Pert device by PANalytical B.V., The Netherlands), SEM (Scanning Electron Microscopy, Zeiss EVO MA 10) and Energy Dispersive Spectroscopy (EDS, Bruker Quantax). XRD measurements are carried out at 40 kV and 40 mA, CuKα radiation ($\lambda K\alpha_1 = 1.540598$ A and $\lambda K\alpha_2 = 1.540598$ A), scan range 5°-90° (2θ), step size 0.02° and acquisition time of 2 s/step. SEM analysis is carried out with 20 kV acceleration voltage, beam current between 6 and 14 pA, gain +3.

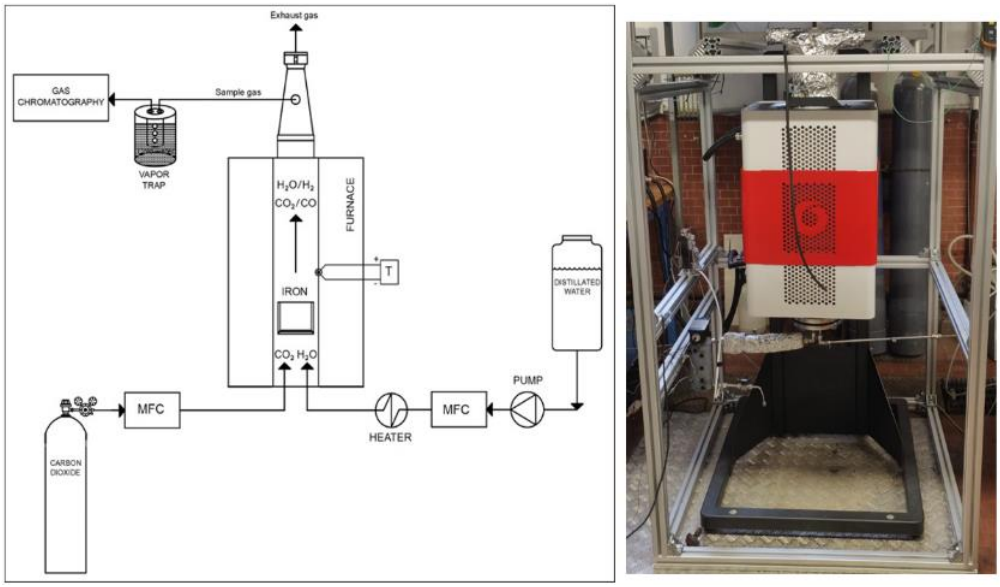

Figure 4.2. Simplified scheme of the experimental set-up (left); front picture of the set-up (right)

4.2.3 Calculation method

The reactions considered for iron oxidation are reported in Eqs. (4.1) and (4.2).

$$2Fe + CO_2 + H_2O \rightarrow 2FeO + CO + H_2 \tag{4.1}$$

$$3Fe + 2CO_2 + 2H_2O \rightarrow Fe_3O_4 + 2CO + 2H_2 \tag{4.2}$$

The reactants dissociation $X_{CO_2}$and X_{H_2O} are computed as:

$$X_{CO_2} = \frac{v_{CO}}{v_{CO_2} + v_{CO}} \tag{4.3}$$

$$X_{H_2O} = \frac{v_{H_2}}{v_{H_2} + v_{H_2O}} \tag{4.4}$$

Where v_i represents the time averaged volume percentage of the gas species detected from gas chromatography. The time average is performed over a total of 12 ~14 points equally distributed throughout the test. Since water is separated before analysis, v_{H_2O} is computed from the H_2 volume percentages and the inlet flow rates of the reactants. The dissolution of gases (CO_2, CO and H_2) in the water trap is neglected in the calculations. Since the temperatures in the mass flow controllers and in the reactor are different, the volumetric flow rates in the reactor are computed according to Eq. (4.6):

$$Q_{reactor,i} = Q_{MFC,i} \cdot \frac{\rho_i(T_{MFC})}{\rho_i(T_{reactor})} \qquad [l/min] \tag{4.5}$$

Where $Q_{reactor,i}$ stands for the volumetric flow rate of each gaseous species in the reactor; $Q_{MFC,i}$ is the volumetric flow rate measured by the mass flow controllers (MFC); $\rho_i(T)$ is the density of the gaseous species at the different temperature conditions, either T_{MFC} or $T_{reactor}$. This value is important for the determination of the real reactants molar ratio at the inlet of the reactor, which allows to properly calibrate the injection of liquid water and CO_2 for syngas production optimization. In the subsequent results discussion on the combined CO_2/H_2O case, the total gas flow rate will be considered under the reactor operating conditions in L/min, while the single reactants flow rates (CO_2, H_2O_l) will be addressed with the standard flow rates (in nl/min or ml/min) provided by the instrumentation. For the combined tests, the molar fractions of gaseous reactants α and products γ are computed as:

$$\alpha = \frac{Y_{CO_2}}{Y_{CO_2} + Y_{H_2O_g}} \tag{4.6}$$

$$\gamma = \frac{Y_{CO}}{Y_{CO} + Y_{H_2}} \tag{4.7}$$

Finally, the reactor is characterized by the Weight Hourly Space Velocity (WHSV), expressed as in Eq. (4.9).

$$WHSV = \frac{\dot{m}_{r,std}}{m_{Fe}} \qquad [h^{-1}] \tag{4.8}$$

Where $\dot{m}_{r,std}$ is the mass flow rate of the reactants at standard conditions, m_{Fe} is the iron loading in mass. This parameter is representative of the average residence time of the reactants in the iron bed, which is critical for conversion optimization.

4.2.4 Experimental campaign

The first set of runs analyse the interaction of the scrap iron powder with pure CO_2 for system optimization and to assesl the decarbonization potential of the process. The following tests are carried out:

- Preliminary runs (not shown) with 10 nl/min CO_2 flow rate and N_2 dilution.
- Dynamic test with two subsequent CO_2 flow rates (1 nl/min and 4 nl/min) and fixed temperature conditions. A total of four samples is collected in 1 hour with 450 g of iron.

- Constant CO_2 flow rate (1 nl/min) and different temperatures ranging from 850 °C to 1050 °C with 450 g of iron.

Subsequently, a complete analysis with CO_2 and H_2O is carried out to define the optimal combination of parameters for a successive use in methanol synthesis. To this aim, the tests are carried out by investigating:

- The effect of total gas volume flow rate. Four tests are carried out with decreasing reactor flow rates, total temperature of 1025 °C, and bed mass of 200 g.
- The effect of the inlet H_2O/CO_2 molar ratio for a fixed total flow rate (37 L/min), bed mass (450 g), and temperature (1025 °C).
- The effect of the increase in bed mass. The aim is to understand if there is a conversion plateau above a certain amount of oxygen carrier. Tests are performed in two opposite conditions: low flow rate and high reactants molar ratio (23 L/min and H_2O/CO_2 = 4), high flow rate and low reactants molar ratio (37 L/min and H_2O/CO_2 = 1). These conditions are compared to confirm the behaviour described in the previous tests.

Finally, the reactants molar ratio and composition are chosen for maximizing dissociation and thus achieving a H_2/CO ratio of 3 - 3.5, which is optimal for methanol synthesis.

4.3 Results and discussion

4.3.1 CO_2 splitting

Figure 4.3 shows the volumetric percentages of CO and CO_2 in the outlet gas for a dynamic run with two consecutive CO_2 flow rates, i.e. 1 nl/min and 4 nl/min at 1050 °C. This test aims at establishing the optimal flow rate condition for the subsequent experimental campaign with both CO_2 and CO_2/H_2O streams. The minimum of 1 nl/min CO_2 flow rate is imposed by the instrumentation lower limit of reliability. Two samplings are carried out at 15 and 30 min after temperature and flow rates stabilization in the reactor. As shown in Figure 4.3, the CO volume percentage at 1 nl/min is equal to 30% and 35% at 15 and 30 min, respectively. At 4 nl/min a significant drop in CO production occurs, providing 18% and 15% volume concentration, respectively. Therefore, with a fourfold increase of the reactants flow rate, the conversion decreases by about 50%. This drop in reactivity can be attributed to the combined effect of the reduced residence time of the reactants in the active zone as well as to iron bed sintering. The effect of temperature on CO production is then assessed at 1 nl/min CO_2. The investigated temperature range extends from 850 °C to 1050 °C. As shown in Figure 4.2, at 1050 °C CO production increases in the first 30 minutes and then remains stable, while below 1000 °C it increases during the first 30 minutes and then undergoes a

linear decay over time. Only at 950 °C no peak is detected in the sampling at 30 minutes but a continuous reduction. The observed decay in CO production with time can be attributed to the progressive conversion of Fe to Fe_xO_y and to the decrease of available reaction sites due to progressive sintering. From a thermodynamic point of view, lower temperatures promote iron oxidation to higher oxidized states such as Fe_3O_4. At the detected CO volume fractions, thermodynamics predicts FeO formation for the tests at 1000 °C and 1050 °C, while below 1000 °C Fe_3O_4 formation is expected. On average, the results indicate that CO_2 splitting kinetics is significantly promoted by high temperatures and low flow rates, since a 200 °C increase in the 850 °C – 1050 °C range account for an average conversion gain of 180%. The maximum CO production occurs in the third sampling of the 1050 °C test (36.8%), while the minimum conversion occurs in the first sampling of the 850 °C test (9.6%). After cooling, the material is found completely agglomerated due to the high temperatures and the prolonged times in the reactor. However, according to the proposed scheme of Figure 4.1, the exhaust material should be crushed and then injected into a blast furnace or an electric arc furnace of a steel mill for reduction and melting.

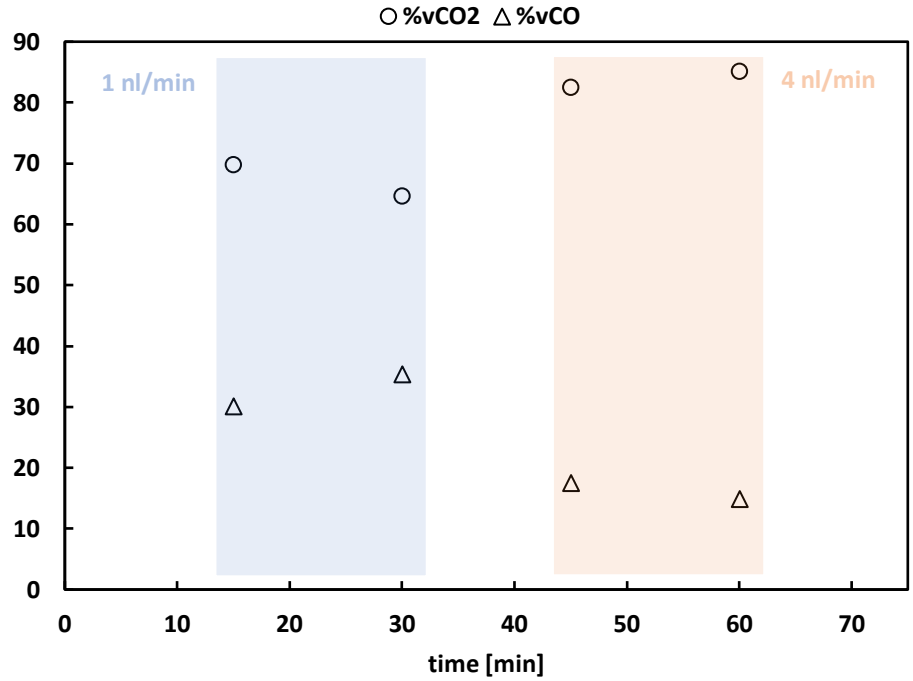

Figure 4.3. CO and CO_2 %vol variation with time for a dynamic run with 1 nl/min and 4 nl/min CO_2 at 1050°C

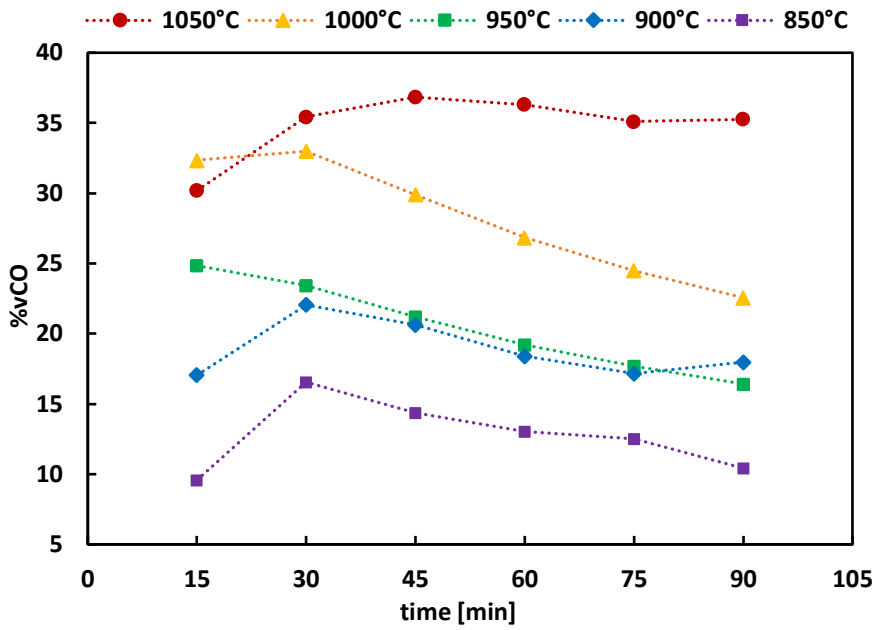

Figure 4.4. CO production as a function of time for different temperatures and 1 nl/min CO_2

4.3.2 Combined CO_2 and H_2O splitting: effect of the total flow rate

In the combined CO_2/H_2O tests, the temperature is kept constant at 1025 °C to maximize CO_2 splitting. All the tests investigating the effect of the total flow rate are carried out with a 200 g iron powder bed and a constant H_2O/CO_2 molar ratio of 3. As shown in Figure 4.5, a decrease in the total reactor flow rate correspond to an increase in both CO_2 and H_2O dissociation rates. This behaviour can be justified with the increase in residence time of both gaseous reactants. The dissociation trends intersect at about 30 L/min and for lower values CO_2 dissociation is higher than that of H_2O. In particular, when the total flow rate in the reactor is reduced from 68 L/min to 37 L/min, X_{CO2} and X_{H2O} increase from 3.6% to 7.3% and from 5.1% to 10.1%, respectively. On the contrary, when the flow rate is reduced to 24 L/min, a little change in X_{H2O} (of about 1%) occurs while X_{CO2} continues increasing up to about 13%. For flow rates larger than about 30 L/min, H_2O dissociation prevails on CO_2, though the conversion is globally decreasing with the flow rate. A relatively low flow rate is thus a better option for maximizing dissociation, especially for CO_2.

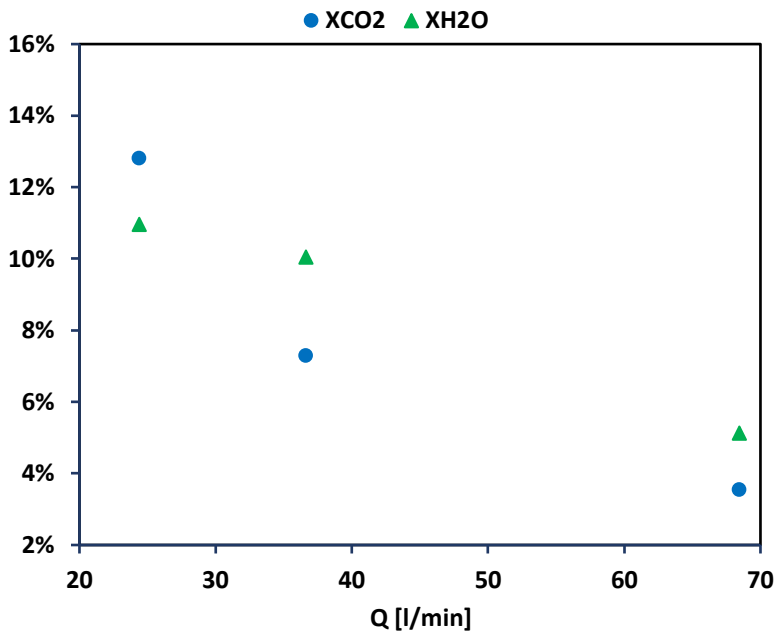

Figure 4.5. Effect of the total volumetric flow rate [L/min] on CO_2 and H_2O_v dissociation at 1025 °C

4.3.3 Effect of reactants molar ratio

The effect of the gaseous reactants molar ratio on syngas production is investigated by comparing three tests carried out at 37 L/min flow rate in the reactor, 1025 °C and 450 g iron bed. The CO_2 and H_2O flow rates are reported in Table 4.1.

Table 4.1 Operating conditions for the tests on the effect of H_2O_v/CO_2 molar ratio

Q_{CO2} [nl/min]	Q_{H2O} [ml/min]	n_{H2O}/n_{CO2}
4	3	1
2.7	4	2
2	4.5	3

In Figure 4.6, X_{CO2} and X_{H2O} are plotted as a function of the H_2O/CO_2 molar ratio of the reactants stream.

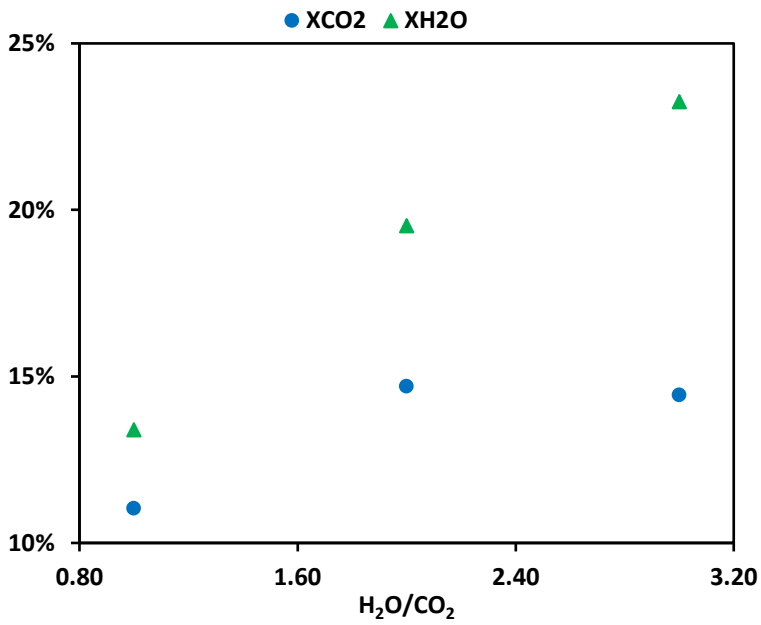

Figure 4.6. Average CO_2 and H_2O_v dissociations for different reactants molar ratio at 37 L/min and 1025 °C and with 450 g iron bed.

According to Figure 4.6, at 37 L/min flow rate water dissociation is larger than that of CO_2 for each tested molar ratio. The CO_2 dissociation rate initially increases and then reaches a plateau. On the contrary, water splitting shows a linear increase along the investigated range. This indicates that below a certain CO_2 flow rate dissociation reaches stability, while higher steam flow rates are able to promote dissociation. A gain of 10% in water dissociation is observed going from H_2O/CO_2 of 1 to 3. However, this trend could be enhanced by the water gas shift reaction taking place among the product gas (and not a real splitting process) at high molar fractions, which increases the content of H_2 and correspondingly decreases the volume fraction of CO in the products. Lower values of the H_2O/CO molar ratio are not investigated since the target is the optimal syngas composition for methanol synthesis, thus requiring around 75% H_2 in the feedstock. In Figure 4.7, the gaseous products molar ratio α is plotted against that of the reactants γ and compared with literature data for a FeO bed [16].

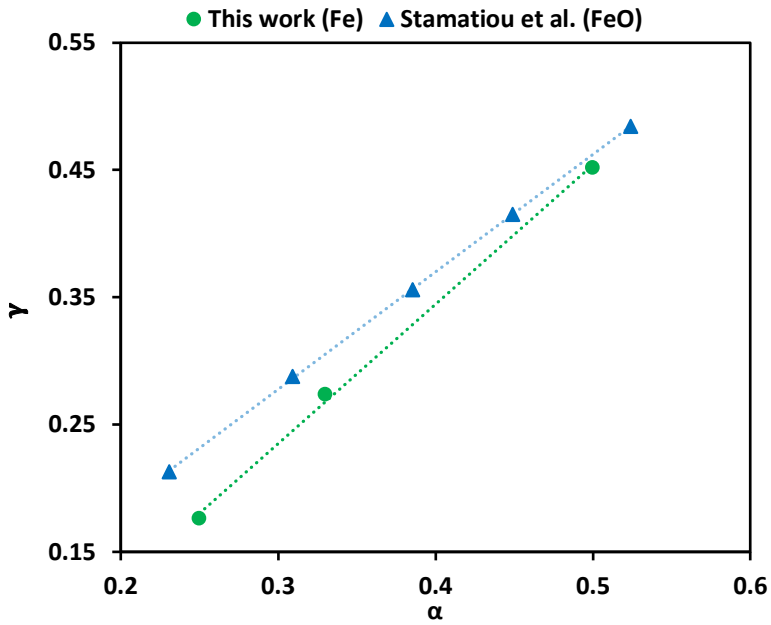

Figure 4.7. Products molar ratio variation with the reactants molar ratio and comparison with experimental results on FeO oxidation

The results exhibit a linear variation of γ with α, as observed in the experiments carried out by Stamatiou et al. over a FeO bed [16]. These indicates that the CO content in the outgoing syngas is influenced by the reactant composition and that a higher CO_2 content leads to a higher CO fraction in the products. Moreover, with respect to literature results on a FeO bed Fe shows a lower CO content in the products for $\alpha < 0.5$, though exhibiting a steeper trend over the whole investigated range of α.

4.3.4 Effect of the bed mass

The effect of the increase in bed mass is investigated by comparing the results under the same operating conditions and different bed weights, namely:

- Total flow rate in the reactor of 37 L/min and H_2O/CO_2 molar ratio equal to 1;
- Total flow rate in the reactor of 23 L/min and H_2O/CO_2 molar ratio equal to 4.

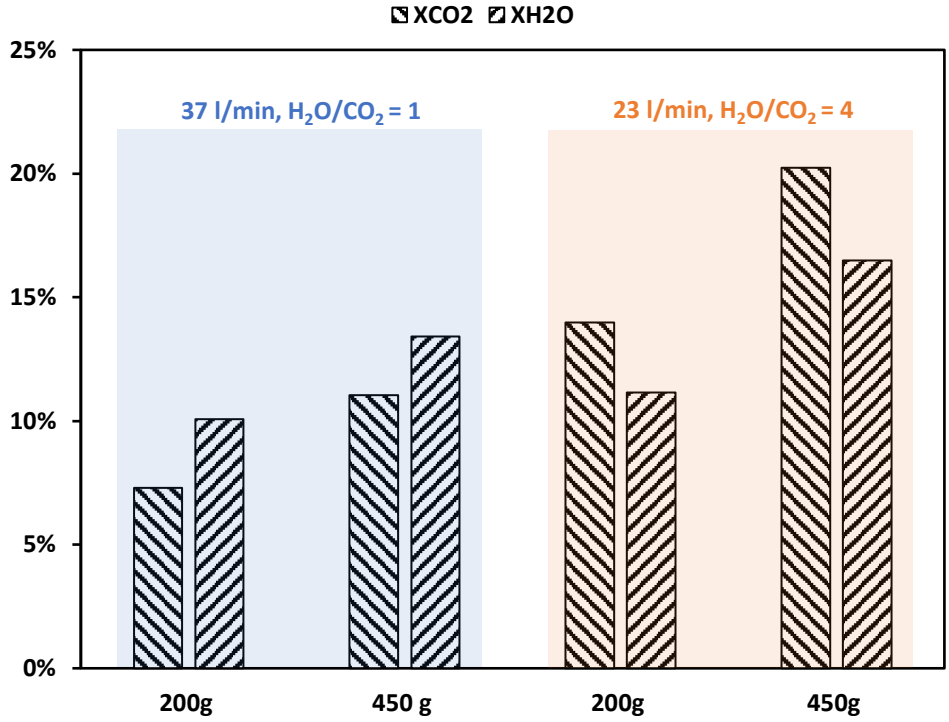

Figure 4.8. Average dissociation values for different iron bed masses and fixed total flow rates at 1025 °C

The results are displayed in Figure 4.8. As expected, the increase in bed mass enhances both CO_2 and H_2O dissociation. At 37 L/min total flow and unitary molar ratio water dissociation is larger than that of CO_2. By increasing the bed mass to 450 g, an average gain of about 3.6% in dissociation of both species is observed. Differently, at 23 L/min total flow the conversion gain is larger, i.e. 6.3% for CO_2 dissociation and 4.9% for water dissociation, though the total increase is less than expected considering the bed mass is 2.25 times higher. The relatively high values of X_{CO2} (20%) and X_{H2O} (16%) at 23 L/min and 450 g iron bed confirm that high molar ratios enhance syngas production. However, the effect of the flow rate on conversion has demonstrated to be more significant than that of reactants composition, since even for a molar ratio of 4, at 23 L/min CO_2 splitting is higher than that of H_2O for both bed masses, while the opposite holds at 37 L/min and H_2O/CO_2 = 1. This last result is important for achieving the optimal syngas composition since the unreacted water could be easily separated by condensation, while unreacted CO_2 removal would require additional processing. Hence, it can be concluded that within the investigated bed weights and for the considered reaction conditions, a bed mass of 450 g increases the reactants dissociation and this effect can be further enhanced by optimally calibrating the other reaction parameters (flow rate, molar ratio, temperature).

4.3.5 Analysis of syngas compositions

Finally, in Figure 4.9 the results of all the combined tests with 450 g iron bed, namely tests 1 to 5, are reported in terms of CO_2, CO and H_2 average volume percentages in the product gases. A summary of the operating conditions for each test is reported in Table 4.2.

Table 4.2. Operating conditions for all tests with CO_2/H_2O_v performed with 450 g of iron powder

Test nr.	Q_{CO2} [nl/min]	Q_{H2OL} [ml/min]	n_{H2O}/n_{CO2}
1	4	3	1
2	2.7	4	2
3	2	4.5	3
4	1	3	4
5	1	4.5	6

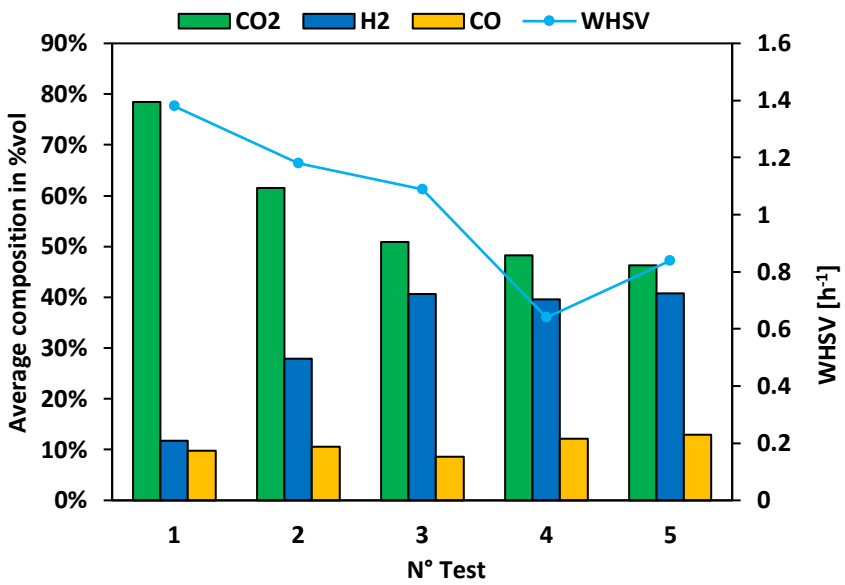

Figure 4.9. Time averaged outlet syngas compositions from gas chromatography for each test with 450 g bed and WSHV values

The syngas compositions vary according to the reactants H_2O/CO_2 molar ratio and flow rate. On test 1, the unitary H_2O/CO_2 molar ratio and the high space velocity cause low syngas quality, with 79% CO_2, 9.7% CO and 12% H_2 on a dry basis. On the contrary, all the subsequent tests performed with H_2O/CO_2 molar ratios greater or equal than 2 and lower space velocities report good syngas compositions, characterized by H_2 and CO volume percentages in the 28% - 40.6% and 8.6 - 12.9% range, respectively. Test 5 is carried out by adopting the optimal values of CO_2 and H_2O flow rates for maximizing dissociation, i.e. 1 nl/min of CO_2 and 4.5 ml/min of liquid water. The optimal value for CO_2 splitting is derived

from the first experimental campaign with CO_2 and subsequently confirmed by test 4 in combined conditions, while the optimal liquid water flow rate for maximizing dissociation is determined from Figure 4.6. The H_2O/CO_2 molar ratio is equal to 6 and the resulting average product gases composition is: 41% H_2, 12.1% CO and 46% CO_2. This composition is the best achieved throughout all the experimental campaign, providing an average H_2/CO ratio equal to 3.17 (though the CO/CO_2 ratio is lower 1). The average value of CO_2 dissociation is the highest of all the experimental runs (21%), while that of H_2O amount to 11.7%. This behavior has also been observed in Figure 4.8, where water dissociation is lower than that of CO_2, and it could be related to the optimal value of CO_2 flow rate which enhances its splitting and thus reduces the available active sites for water. However, the high H_2 content in the product gases is obtained due to unreacted water separation. With respect to the CO_2 only case, X_{CO2} is reduced for the co-splitting since a maximum dissociation of 36.8% is achieved in the first campaign compared to the 21.4% for test 5. This confirms thermodynamic analyses in the literature, indicating that the conversion efficiency of the co-splitting is lower than that of the pure CO_2 splitting [13].

4.3.6 Material characterization

XRD analyses are carried out on three representative material samples (Figure 4.10 from bottom to top):

a) Iron powder before test (Fe0);

b) Exhausted iron powder at 1050 °C, 1 nl/min CO_2, 450 g bed (Fe1C);

c) Exhausted iron powder at 1025 °C, 3 ml/min H_2O and 1 nl/min CO_2, 450 g bed (Fe1C3H);

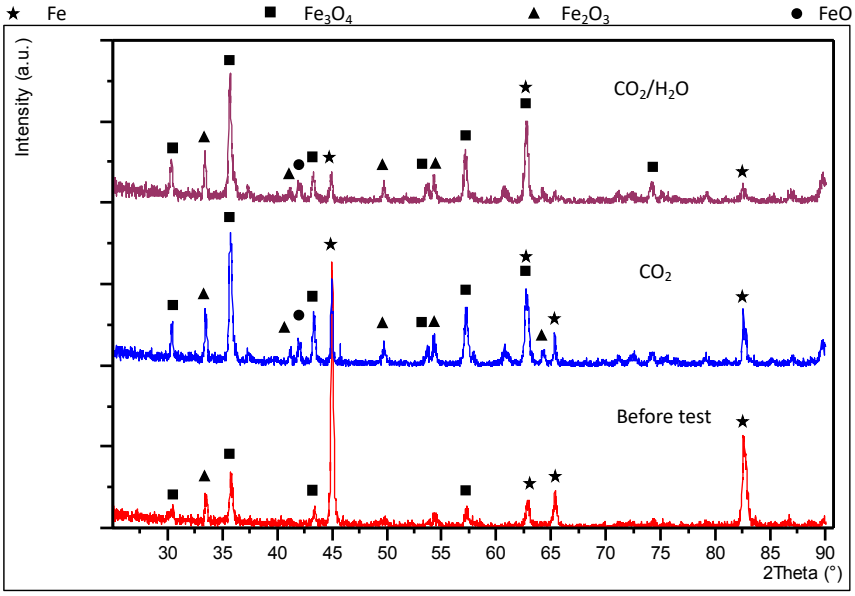

Figure 4.10. XRD patterns of the initial (red) powder, the oxidized iron powder with 1 nl/min CO_2 (blue) and with 1 nl/min CO_2 and 3 ml/min H_2O_v (magenta)

The fresh material diffraction pattern confirms that Fe^0 is largely present in the initial powder, as inferred from the two peaks at $2\theta = 45°$ and 82.5°. However, both Fe_2O_3 and Fe_3O_4 are also detected. The diffraction patterns for the two considered exhausted powders are similar, showing a reduction in the Fe^0 phase and the formation of iron oxides phases, mainly Fe_3O_4. The pattern for Fe1C powder still shows the two Fe^0 peaks at 45° and 82.5°, while in the Fe1C3H pattern these peaks are negligible, confirming that a deeper oxidation occurred in the combined CO_2/H_2O test compared to the CO_2 only test. Accordingly, the increase in the peak counts at $2\theta \approx 36°$ and $2\theta \approx 63°$ indicates the progression of oxidation in both the exhausted powders. The almost complete absence of Fe_2O_3 peaks in both exhausted powders diffraction patterns is in line with expectations, since due to thermodynamic limitations it is not possible to form Fe_2O_3 from H_2O and/or CO_2 oxidation of the iron oxides.

The SEM pictures provide insight into the morphological changes of the iron powder throughout the experimental activity. In the presence of oxidation of the iron particles, the

SEM images should present the formation of a superficial iron oxide layer. SEM images of the initial iron powder and of the exhausted powder after the test at 1050 °C with 1 nl/min CO_2 are reported in Figure 4.11 for comparative analysis. The fresh scrap iron particles in Figure 4.11-A appear smooth and spherical on the outside, while on the inside they are characterized by a moderately rough surface probably associated with previous mechanical attrition. On the contrary, Figure 4.11-B shows the formation of a layer on the surface with edged uprisings and irregularities that is probably associated with iron oxide production.

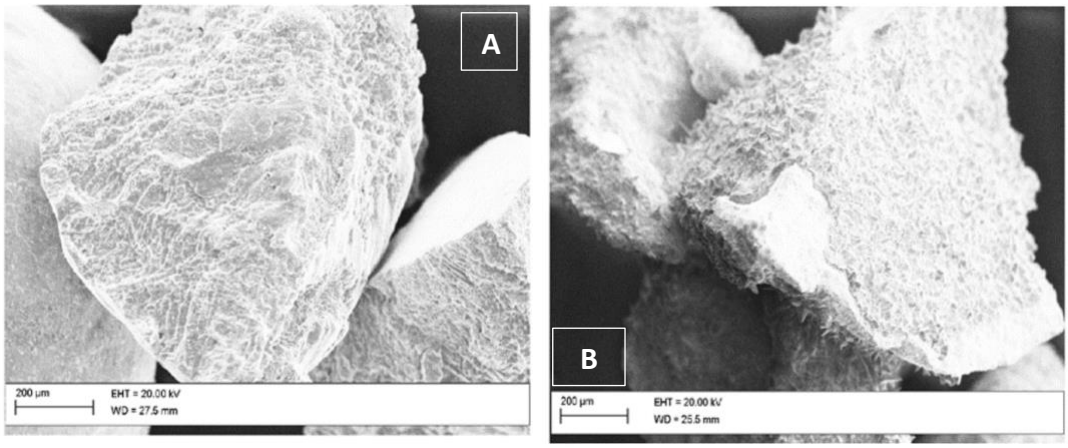

Figure 4.11. SEM images of the powder before (a) and after the test at 1050 °C with 1-4 nl/min CO_2 flow rate (b)

4.4 Chapter summary and conclusions

In this chapter experimental evidence on the use of a scrap iron-based oxidizer reactor to produce a thermochemical syngas has been reported. The syngas generation step is part of a novel process scheme encompassing the reutilization of secondary steelmaking iron scrap and the conversion of CO_2 and H_2O into a syngas. An experimental set up is built, composed of a tubular reactor heated by an electric furnace. This system aims at optimizing the production of a thermochemical syngas formed by H_2, CO and CO_2. A first experimental campaign regards CO_2 splitting. The results confirm that temperature promotes CO_2 splitting, with a maximum CO percentage in the product gases of 37% at 1050 °C and 1 nl/min CO_2. Subsequently, the oxidation of iron by CO_2/H_2O is analysed and the effect of total flow rate, bed mass and reactants molar ratio on syngas productivity is assessed. By reducing the injected flow rate in the combined gases case, the reactants dissociation increases for both species and below a certain threshold CO_2 dissociation (13%) is higher than that of H_2O (11%). At 37 L/min total flow rate, by increasing the H_2O/CO_2 molar ratio in the 1-3 range, H_2 production is enhanced with respect to CO. The products molar ratio $CO/CO+H_2$ shows a linear dependency on reactants molar ratio CO_2/CO_2+H_2O, in agreement with experimental data on FeO oxidation reported in the literature. For H_2O/CO_2

molar ratios above 2 and low reactor space velocity, H_2 and CO volume percentages in the syngas range from 28% to 41% and from 8.6 to 12.9%, respectively. Hence, high H_2O/CO_2 molar ratios and low space velocities are confirmed as the best combination of parameters for enhancing syngas production. Finally, in the last test the optimal thermochemical syngas composition is achieved, including 41% H_2 and 12.1% CO, with the rest constituted by CO_2.

ACKOWLEDGEMENT

This research is funded by the Italian Ministry of Economic Development, under the project SFERO (Systems for Flexible Energy via capture and Reuse of carbOn) within the Italian research program 2019-2021: "Ricerca di Sistema" (Grant number I34I19005780001).

4.5 Nomenclature

EDS	Energy Dispersive Spectroscopy
MFC	Mass flow controller
OC	Oxygen Carrier
SEM	Scanning electron microscopy
WHSV	Weight Hourly Space Velocity
XRD	X-ray Diffraction

4.6 References

[1] Bayham SC, Tong A, Kathe M, Fan L-S. Chemical looping technology for energy and chemical production. Wiley Interdiscip Rev Energy Environ 2015;5:216–41. https://doi.org/10.1002/wene.173.

[2] Ramírez-Santos ÁA, Castel C, Favre E. A review of gas separation technologies within emission reduction programs in the iron and steel sector: Current application and development perspectives. Sep Purif Technol 2018;194:425–42. https://doi.org/10.1016/j.seppur.2017.11.063.

[3] Wu H, Li Q, Sheng M, Wang Z, Zhao S, Wang J, et al. Membrane technology for CO2 capture: From pilot-scale investigation of two-stage plant to actual system design. J Memb Sci 2021;624:119137. https://doi.org/10.1016/J.MEMSCI.2021.119137.

[4] Blamey J, Anthony EJ, Wang J, Fennell PS. The calcium looping cycle for large-scale CO2 capture. Prog Energy Combust Sci 2010;36:260–79. https://doi.org/10.1016/j.pecs.2009.10.001.

[5] Abuelgasim S, Wang W, Abdalazeez A. A brief review for chemical looping combustion as a promising CO2 capture technology: Fundamentals and progress. Science of The Total Environment 2021;764:142892. https://doi.org/10.1016/j.scitotenv.2020.142892.

[6] Yu Z, Yang Y, Yang S, Zhang Q, Zhao J, Fang Y, et al. Iron-based oxygen carriers in chemical looping conversions: A review. Carbon Resources Conversion 2019;2:23–34. https://doi.org/10.1016/j.crcon.2018.11.004.

[7] Ramezani R, Di Felice L, Gallucci F. A review of chemical looping reforming technologies for hydrogen production: recent advances and future challenges. Journal of Physics: Energy 2023. https://doi.org/10.1088/2515-7655/acc4e8.

[8] Tijani MM, Aqsha A, Mahinpey N. Synthesis and study of metal-based oxygen carriers (Cu, Co, Fe, Ni) and their interaction with supported metal oxides (Al2O3, CeO2, TiO2, ZrO2) in a chemical looping combustion system. Energy 2017;138:873–82. https://doi.org/10.1016/j.energy.2017.07.100.

[9] Gokon N, Murayama H, Nagasaki A, Kodama T. Thermochemical two-step water splitting cycles by monoclinic ZrO2-supported NiFe2O4 and Fe3O4 powders and ceramic foam devices. Solar Energy 2009;83:527–37. https://doi.org/10.1016/j.solener.2008.10.003.

[10] Ishihara H, Kaneko H, Hasegawa N, Tamaura Y. Two-step water-splitting at 12731623K using yttria-stabilized zirconia-iron oxide solid solution via co-precipitation and solid-state reaction. Energy 2008;33:1788–93. https://doi.org/10.1016/j.energy.2008.08.005.

[11] Najera M, Solunke R, Gardner T, Veser G. Carbon capture and utilization via chemical looping dry reforming. Chemical Engineering Research and Design 2011;89:1533–43. https://doi.org/10.1016/j.cherd.2010.12.017.

[12] Stehle RC, Bobek MM, Hahn DW. Iron oxidation kinetics for H2 and CO production via chemical looping. Int J Hydrogen Energy 2015;40:1675–89. https://doi.org/10.1016/j.ijhydene.2014.11.035.

[13] Hao Y, Jin J, Jin H. Thermodynamic analysis of isothermal CO2 splitting and CO2-H2O co-splitting for solar fuel production. Appl Therm Eng 2020;166:113600. https://doi.org/10.1016/j.applthermaleng.2019.04.010.

[14] Abanades S, Villafan-Vidales HI. CO2 and H2O conversion to solar fuels via two-step solar thermochemical looping using iron oxide redox pair. Chemical Engineering Journal 2011;175:368–75. https://doi.org/10.1016/j.cej.2011.09.124.

[15] Charvin P, Abanades S, Flamant G, Lemort F. Two-step water splitting thermochemical cycle based on iron oxide redox pair for solar hydrogen production. Energy 2007;32:1124–33. https://doi.org/10.1016/J.ENERGY.2006.07.023.

[16] Stamatiou A, Loutzenhiser PG, Steinfeld A. Solar Syngas Production via Hsub2/subO/COsub2/sub-Splitting Thermochemical Cycles with Zn/ZnO and FeO/Fesub3/subOsub4/sub Redox Reactions. Chemistry of Materials 2009;22:851–9. https://doi.org/10.1021/cm9016529.

[17] Stamatiou A, Loutzenhiser PG, Steinfeld A. Solar Syngas Production From H2O and CO2 via Two Step Thermochemical Cycles Based on FeO/Fe3O4 Redox Reactions: Kinetic

Analysis. ASME 2010 4th International Conference on Energy Sustainability, Volume 2, ASMEDC; 2010. https://doi.org/10.1115/es2010-90009.

[18] Hammache S, Means N, Burgess W, Howard B, Smith M. Investigation of low-cost oxygen carriers for chemical looping combustion at high temperature. Fuel 2020;273:117746.

[19] Hedayati A, Soleimanisalim AH, Mattisson T, Lyngfelt A. Thermochemical conversion of biomass volatiles via chemical looping: Comparison of ilmenite and steel converter waste materials as oxygen carriers. Fuel 2022;313:122638.

[20] Wang Y, Tian X, Zhao H, Liu K. The use of a low-cost oxygen carrier prepared from red mud and copper ore for in situ gasification chemical looping combustion of coal. Fuel Processing Technology 2020;205:106460.

[21] Durmaz M, Dilmaç N, Dilmaç ÖF. Evaluation of performance of copper converter slag as oxygen carrier in chemical-looping combustion (CLC). Energy 2020;196:117055.

[22] Condori O, Garc\'\ia-Labiano F, Luis F, Izquierdo MT, Abad A, Adánez J. Biomass chemical looping gasification for syngas production using LD Slag as oxygen carrier in a 1.5 kWth unit. Fuel Processing Technology 2021;222:106963.

[23] Zornoza B, Abad A, Mendiara T, Izquierdo MT. Iron-based oxygen carrier particles produced from micronized size minerals or industrial wastes. Powder Technol 2022;396:637–47.

[24] Wang I, Ji G, Turap Y, Nie H, Li Z, Zhao M, et al. A short-cut chemical looping hydrogen generation system by using iron-based material from steel industry. Chemical Engineering Journal 2020;394:124882.

Chapter 5

On the reduction of $NiFe/Al_2O_3$ oxygen carrier in high-pressure chemical looping applications

This chapter is based on the following paper

Palone, O., Ramezani, R., Navarro, C., Di Felice, L., Borello, D., Grasa, G., Gallucci, F. (2023). On the reduction of $NiFe/Al_2O_3$ oxygen carrier in high-pressure chemical looping applications. International Journal of Hydrogen Energy (2023)

Abstract

In this chapter two NiFe aluminates with different Ni loadings (4.3% wt. and 12% wt.) and similar Fe loadings (9.9% wt. and 8.5% wt.) are synthesized through a co-precipitation/impregnation route and tested in two thermogravimetric analysers. The effect of temperature (700 – 900 °C) on the oxygen transport capacity and reduction conversion of both the NiFe aluminates is assessed at ambient pressure (0.5 nl/min with 20% H_2/N_2). The influence of material loading is also studied, and it is shown that higher Ni loadings provide a significant improvement in material activity. Complete reduction conversion is achieved at 900 °C and ambient pressure. At high pressure (10 – 20 bar), tests are carried out in a temperature range of 700 – 850 °C. The effect of flow rate (2 nl/min to 6 nl/min with 50% H_2/N_2) is first assessed to prevent external mass transfer limitations. Higher total pressures have a negative effect on reduction kinetics, while higher Ni loadings demonstrate increased final reduction conversion also at high pressure, reaching about 75% conversion after 20 minutes. The long-term cyclability of the material is also investigated both at low (100 cycles) and high pressure (80 cycles) conditions and a conversion gain is observed throughout the cycles. No changes in the material microstructure are observed after 80 high pressure cycles.

5.1 Introduction

As explained in previous chapters, a key issue for the development of the chemical looping technology is the selection of an oxygen carrier with suitable properties. The oxygen carrier must accomplish several characteristics such as sufficient oxygen transport capacity, high reactivity for reduction and oxidation reactions, minimum solids inventory in the reactors, stability over many successive redox cycles, negligible carbon deposition (that would release CO_2 in the air reactor reducing the CO_2 capture efficiency), environmentally friendly characteristics, low cost and large availability [1,2]. There are more than 900 different materials based on iron, nickel, copper, manganese, as well as other mixed oxides and low-cost materials that have been investigated as potential oxygen carrier materials for chemical looping applications [3]. Nickel-based oxygen carriers have been the most extensively analysed in the literature [4], due to their very high reactivity, good performance working at high temperatures and low attrition rates. Iron-based oxygen carriers are another attractive option for chemical looping due to their low cost, large availability and environmental compatibility [5]. Moreover, different oxidation states can be found when Fe_2O_3 is reduced (Fe_3O_4, FeO or Fe) and thus flexibility for different chemical looping applications (combustion reforming, CLR and hydrogen production) is ensured. However, iron oxides suffer from agglomeration and sintering when operated at high temperatures and require support with other materials to be competitive for chemical looping applications [6].

5.1.1 Support materials for CL applications

The most common support materials are Al_2O_3 [7,8], monoclinic ZrO_2, partially stabilized tetragonal zirconia (t-PSZ), yttria-stabilized cubic zirconia (c-YSZ), titanium dioxide (TiO_2), manganese oxide, bentonite, and their mixtures [9]. In [10] Adanez et al. analyse 240 samples of Cu, Fe, Mn and Ni oxides under reduction and oxidation cycles to assess the optimal active phase content, sintering temperature during material preparation and support material among Al_2O_3, sepiolite, SiO_2, TiO_2 and ZrO_2. The use of alumina-based compounds as support material has been extensively investigated in the literature, due to their benefits for the long-term stability of the oxygen carrier. Most of the oxygen carriers supported on Al_2O_3 compounds show very high reactivity with all fuel gases, no agglomeration problems, low attrition rates during operation in fluidized beds and avoidance of carbon deposition at CLC conditions [11]. Nevertheless, Al_2O_3 can interact with the active phase of the oxygen carrier, such as Fe_2O_3, and form spinel structures that change the particle reactivity. In chemical looping hydrogen production, the formation of $FeAl_2O_4$ (hercynite) is the reason for oxygen carrier deactivation over many cycles, because it is inert to the steam iron-reaction. A third step with air oxidation or a low mass loading (few percentage) of Al_2O_3 are suggested as possible solutions for the regeneration of Fe_2O_3 and Al_2O_3 from the hercynite

structure [12–15]. On the contrary, Ni/Al_2O_3 and $NiO/NiAl_2O_4$ oxygen carriers have proved high reactivity in chemical looping combustion of gas fuels (CH_4, CO and H_2), as well as good chemical, mechanical and reactive stability [16]. The formation of $NiAl_2O_4$ by the interaction of free NiO with the Al_2O_3 support is however responsible for a decrease in the oxygen carrier reactivity. Dueso et al. [17] have shown that irrespective of the final solid conversion in the reduction of NiO/Al_2O_3, 80% of the reacted oxygen carrier is regenerated after oxidation to free NiO and the rest to less reactive $NiAl_2O_4$.

5.1.2 Mixed metal oxides for CL applications

An increasing number of studies is currently focusing on combined or mixed-metal oxides to enhance performance of each single species. In [18], Bhavsar et al. compare bimetallic Fe-Ni compounds with Al_2O_3 and CeO_2 supports with iron and nickel oxides. Increased stability and higher selectivity towards fuel oxidation are observed for the bimetallic compound compared to a simple supported iron oxide, similar to the observations by Kuo et al. [19]. Increased reactivity when a reactive support (CeO_2) is present are also highlighted. In [20] Evdou et al., compare the performance of different ferrites incorporating Mn, Ni, Zn, Co and Cu. Cu ferrite shows the highest reactivity towards methane and good stability, Ni and Zn present high reactivity but fast deactivation after few cycles due to sintering (Ni/Fe) or phase decomposition (Zn/Fe), while Co presents the best stability configurating as a promising active support. In [21,22], due to the catalytic effect of metallic Ni, the bimetallic Fe-Ni oxygen carrier provides improved gasification efficiency compared to Fe_2O_3/Al_2O_3. On the same line, Wei et al. [23] compare four different ferrites (Ba, Ni, Cu and Co ferrites) for chemical looping gasification of biomass in a fixed-bed reactor. Though all four ferrites show improved gasification performance with respect to an inert bed, Ba ferrite has provided the highest syngas yield and H_2 content from biomass gasification as well as good tar cracking performance. Finally, Wang et al. [24] compare Ni, Cu and Co ferrite for chemical looping combustion of pine sawdust. All three ferrites provide high values of carbon conversion and carbon capture efficiency (around 95%), though after five cycles only Cu and Co ferrites show stable values. On the contrary, Ni ferrite provides higher catalytic activity for tar cracking and reforming at every tested temperature.

5.1.3 Nickel-based oxygen carriers for CLR

Iron and nickel-based oxygen carriers have also been extensively studied in the literature for chemical looping reforming processes [25–27]. Compared to the traditional reforming processes, the most immediate advantages of CLR are the absence of the air separation unit for pure oxygen production (necessary for the autothermal reforming) and the intrinsic CO_2 separation. In [28] Ortiz et al. investigate the catalytic activity of two Ni-based oxygen carriers for both the steam methane reforming and the water gas shift reactions, showing

that the activity increases with the reduction conversion of the oxygen carrier. Comparison with conventional catalysts indicate a lower catalytic activity of the oxygen carriers. Huang et al. [29] have compared nickel oxides (NiO, mixed NiO and Fe_2O_3, NiFe) and iron oxides (Fe_2O_3) for chemical looping dry reforming applications. The process encompasses three steps: reduction with methane and oxidation with CO_2 and then air. Nickel ferrites dissociate CO_2 in the first oxidation step due to the spinel structure, while metallic nickel does not show any oxidizability with CO_2. Antzara et al. [30] have analysed the effect of different supports (ZrO_2, TiO_2, SiO_2, Al_2O_3) on NiO in terms of CH_4 conversion and long-term stability both as conventional catalysts and in CLR. SiO_2 and TiO_2 supports lead to poor performances (low activity and fast deactivation) as conventional catalysts. The other supported materials (Al_2O_3 and ZrO_2) have been tested for chemical looping reforming and ZrO_2 has shown the best stability after 20 cycles (less than 2% decrease in the activity) as well as a competitive methane conversion.

5.1.4 High-pressure chemical looping

As explained in Chapter 1, high-pressure operation represents an important condition for industrial scale-up of chemical looping [31]: in chemical looping combustion high-pressures are mandatory to better exploit the enthalpic content of the off-gases for power generation in a combined cycle power plant. In chemical looping reforming, high-pressure facilitates the downstream processing of syngas to liquid fuels [32], such as methanol [33], ammonia [34], kerosene [35] etc., thus reducing the total equipment cost and the carbon footprint of the process. High pressure operation also impacts the process design of the reactors; e.g. in fluidized bed reactors high pressure leads to smaller and more frequent bubble formation, lower minimum fluidization velocities and terminal velocities (easier elutriation) [36]. Furthermore, a change in kinetics at high pressure influences the choice of the optimal thermodynamic conditions and of reactor geometry to achieve the desired solid conversion and products composition. Several works in the literature present data on high-pressure chemical looping cycles. In [37], a comparative analysis between chemical looping coal combustion in fixed bed and fluidized bed configurations is carried out by Zhang et al. The results indicate that up to 0.5 MPa total pressure has a beneficial impact on gasification while the opposite holds for higher values. Gallucci et al. [38] have tested ilmenite in a pressurized 10 kW packed bed reactor for the chemical looping combustion of syngas. The effect of syngas composition and total pressure (maximum 6 bar) is discussed and full autothermal operation is demonstrated after 3 cycles. A model is developed and validated with the experimental results. Argyris et al. [25] have investigated methane chemical looping reforming with $NiO/CaAl_2O_4$ as the oxygen carrier in a lab scale reactor under different temperatures (400 – 900 °C), pressures (1 – 5 bar) and flowrates (10 – 40 nl/min). Full autothermal operation has been demonstrated as well as > 99 % CH_4 conversion.

Hamers et al. [39] have reported experimental evidence on the reactivity of CuO/Al_2O_3 and $NiO/CaAl_2O_4$ for chemical looping combustion under high pressure conditions. The effect of pressure is detrimental for reaction kinetics, while different reducing gas molar fractions provided different reduction behaviours, likely due to a competitive adsorption mechanism. Garcia-Labiano [40] have tested the reactivity of Cu, Fe and Ni-based oxygen carriers for chemical looping at 450 - 900 °C and 1 – 30 bar and have provided an expression for the reaction kinetics at high pressure. The negative effect on reaction kinetics from pressurized operation is confirmed also in this work. In [41] Lu et al. investigate the reactivity of ilmenite ore during high pressure chemical looping combustion cycles with CO as fuel. Increasing temperature and CO partial pressure has a positive impact on the reduction rate, while increasing total pressure has the reverse effect. Similar results for methane fuelled chemical looping combustion of ilmenite ore are reported by Tan et al. in [42]. On the oxidation side, Rana et al. have analysed the high pressure oxidation kinetics (with O_2) of ilmenite ore and confirm the negative effect of total pressure, while constant O_2 volume fractions have shown a positive impact on kinetics up to a certain threshold. However, cracks have been detected at high O_2 partial pressures. Finally, chemical looping combustion of methane and synthesis gas has been investigated on Ni and Cu oxygen carriers at high pressure conditions (1 - 10 bar) by Nordness et al. [43]. High pressure has led to increased carbon deposition and lower reduction rate. In contrast with the presented works, in [44] San Pio et al. carry out high pressure chemical looping cycles of CuO/Al_2O_3 and demonstrate that total pressure does not impact conversion kinetics nor the morphological and chemical structure of the oxygen carrier. The previous results are thus justified by the presence of mass transfer limitations in the setups.

In this chapter, a set of tests is carried out over a chemical looping process at ambient pressure to analyse NiFe oxygen carriers properties regarding oxygen transport ability and how parameters such as nickel content or temperature can affect them. This is an interesting aspect of the applications that these materials can have in different processes, such as reforming and H_2 production. Subsequently, the materials are extensively tested in high pressure chemical looping cycles to provide useful data (currently missing in the literature) on the effect of high pressure operation on reactivity and possibly support future scale-up of the technology to the industrial level. The effect of different operating conditions, such as temperature, reducing gas composition, total pressure, and oxygen carrier material loading, is studied and discussed in detail. Finally, long-term stability tests are carried out to assess the activity change over many cycles. The materials have been characterized by several techniques (Inductively Coupled Plasma Spectrometry, X-Ray Diffraction, Temperature Programmed Reduction, Scanning Electron Microscopy, Energy Dispersive X-Ray Analysis) and comparisons made between the fresh and spent material samples.

5.2 Materials and method

5.2.1 Material synthesis and characterization

Materials with approximately 10%wt. Fe and with two different Ni loadings of 5%wt. and 12%wt. are synthesized through a co-precipitation/impregnation route. The co-precipitation protocol started by preparing a solution combining 0.3 M aluminium nitrate and 1.5 M iron nitrate stocks to the desired proportion. Under vigorous stirring a 2 M sodium carbonate solution is added dropwise in a 30% volume excess over stoichiometric value to ensure proper precipitation. The pH is adjusted to 9 followed by a two-hour ageing period at room temperature. After the incubation period, the solution is filtered and washed to remove sodium traces. The material is then dried overnight and grounded (100 - 200 μm). The next step is calcination in a furnace to obtain oxides (at 1000 °C for four hours with a 10 °C/min heating ramp). For the impregnation method, the co-precipitated materials are used as a support and loaded with nickel. 5 g of support is mixed with a nickel nitrate solution and stirred at room temperature until it turned into slurry, then dried and finally calcined at 875 °C for two hours with a 10 °C/min ramp. Before and after testing, the materials are characterized through diverse techniques to determine the quality of the synthesis and their functionality. Inductively Coupled Plasma (ICP-OES, with an ICP-OES Xpectroblue-EOP FMT 26 spectrophotometer) served to corroborate the amount of Fe and Ni present in them. Characterization results are compiled in Table 5.1, which contains the amount of Ni, Fe and Al in the materials. X-Ray diffraction (XRD) analysis is performed on both the oxidized and reduced material states to assess the material phases evolution over the chemical looping cycles. The oxidized materials are 'as produced', while the other ones have been reduced in a H_2/N_2 atmosphere in the two setups. Material reducibility is assessed through Temperature Programmed Reduction tests (TPR, AutoChem II 2920 from Micromeritics) that consist in heating up the sample with a relatively low heating ramp (10 °C/min) in a 10 % vol. H_2 in an Ar stream from room temperature up to 950 °C while measuring H_2 consumption. Finally, the morphology evolution and the fresh material homogeneity are investigated through Scanning Electron Microscopy (SEM) and Energy Dispersive X-Ray (EDX) scans.

Table 5.1. Composition of the two synthesized NiFe aluminates from ICP-OES

Batch	Ni	Fe	Al
1	4.3%	9.9%	41%
2	12%	8.5%	36%

5.2.2 Calculation method

The reaction performance of the materials is assessed by calculating the oxygen transport capacity (OTC) and the reduction conversion X(t) from the observed mass change in the two thermogravimetric analyser (TGA) setups. The oxygen transport capacity represents the fraction of oxygen in the fresh material that is extracted by the gases and it is calculated according to Eq. (5.1).

$$\mathrm{OTC} = \frac{m_{O_2}}{m_{ox}} = \frac{m_{ox} - m(t)}{m_{ox}} \tag{5.1}$$

Where:

- m(t) is the net sample mass at time t;
- m_{ox} is the net sample mass at the end of the oxidation step.

All data are corrected by the blank test before performing any calculations. The instantaneous oxygen carrier reduction conversion is computed according to Eq. (5.2).

$$X(t) = \frac{m_{ox} - m(t)}{m_{ox} - m_{red}} \tag{5.2}$$

Where:

- m_{red} is the completely reduced sample mass (calculated with stoichiometry from m_{ox}).

5.2.3 Ambient pressure TGA setup

For ambient pressure tests, a thermogravimetric analyser (TGA-CI Electronics Ltd.) is used to determine the materials chemical and mechanical stability under oxidizing and reducing conditions. This equipment consists of two concentrically arranged quartz tubes located inside a furnace. Each sample is introduced in a platinum basket placed at the bottom of this device. The apparatus is equipped with gas mass flow controllers that allow feeding H_2, CO, CH_4, O_2 and N_2. A thermocouple is located at the bottom of the setup for optimal temperature regulation. More details on the setup geometry can be found in [45]. In this TGA, 25 mg of material are manually loaded in a platinum crucible. The chemical looping cycles consisted of a 7 minutes reduction stage in a 20% H_2/N_2 atmosphere and a 5 minutes oxidation stage in 20% O_2/N_2. Intermediate purge of 1 min with N_2 is carried out to prevent reactive gases mixing, while continuous flushing with N_2 is provided in the balance head to prevent the gases from entering it.

5.2.4 High-pressure TGA setup

For high-pressure chemical looping tests, a high-pressure thermogravimetric analyser (HP-TGA) is used. A schematic layout of the setup is provided in Figure 5.1. It consists of mass

flow controllers for the reacting gases, a water vaporizer, a backpressure controller, pressure and temperature sensors and a microbalance (model MK2-5 M from CI-Precision). The microbalance has a sensitivity of 0.1 μg, a maximum capacity of 5 g and +/- 500 mg operating range. The setup can operate at pressures and temperatures up to 30 bar and 1100 °C, respectively. Air, CO, CO_2, CH_4, H_2O, H_2, N_2 are the available gases for testing. The balance is connected to a porous basket made of alumina (40 μm pores) through an Ir wire. A robotic lift is used to bring the basket outside the reactor to load it with the sample. The temperature in the reactor is controlled using a thermocouple positioned close to the sample to ensure stable conditions, while the temperature of the balance head is kept constant and is continuously purged with N_2 as a protection measure.

Prior to the test, the oxygen carrier is loaded into the basket. The sample weight used for the experiments is about 30 mg. After loading the sample, the basket is inserted in the reactor by the robotic lift and then the desired temperature and pressure conditions are imposed. Before testing the material at the desired conditions, preliminary activation cycles with reduction and oxidation steps are carried out. The reduction step (20 minutes) involves a 50% H_2/N_2 mixture, while the oxidation step (20 minutes) is carried out with 100% air. Between each reaction segment 100% N_2 is purged for 2 minutes to avoid reactant mixing. To ensure the reliability of the results, each chemical looping cycle is repeated at least 3 times and the data from the last cycle are used for post processing. In both TGAs only H_2 is used as a reducing agent because the focus is more on the redox properties and on the different kinetics of the NiFe aluminates at ambient and high-pressure conditions, rather than on the effect of different reducing gas species. Moreover, the presence of CO in the reducing gas mixture has caused carbon deposition in preliminary testing, especially at high-pressure. The tests are mainly performed at 20 bar, which is typical for chemical looping applications [46]. Blank tests are performed under the same operating conditions to remove the effect of buoyancy on the basket due to the changes in the feed gases and reactor temperature [47].

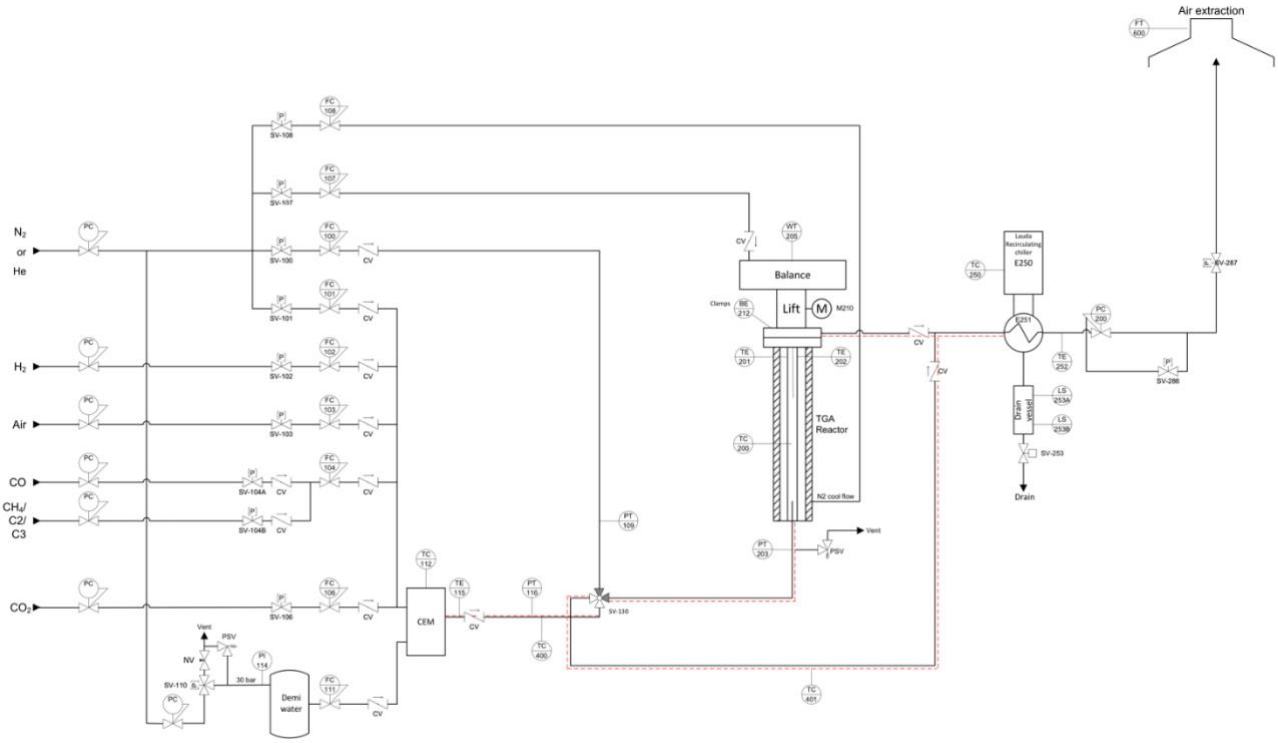

Figure 5.1. P&ID of the experimental apparatus for HP-TGA

5.3 Results and discussion

5.3.1 Ambient pressure chemical looping tests

The two NiFe aluminates are subjected to reduction/oxidation cycles under isothermal conditions to determine their oxygen transport capacity and reduction conversion along multiple reaction cycles in a range of temperatures between 700 and 900 °C with 0.5 nl/min total flow rate. This set of experiments carried out at ambient pressure is focused on the effect of temperature along the redox cycles. Up to 20 cycles are performed for each temperature to assess how oxygen transport capacity evolves in each material. As shown in Figure 5.2 (a) and (b), the OTC behaviour along the cycles is dependent on the temperature. At 720 °C the OTC decreases with the cycles and after the 5th cycle reaches stability. Similarly, at 820 °C the OTC increases and then from the 10th cycle it presents a plateau. On the contrary, for higher temperature values the OTC shows an increasing trend with the cycles. As expected, batch 2 (which has a higher amount of Ni) presents higher OTC values compared to batch 1. For example, at 900 °C the OTC of batch 2 NiFe aluminate is about twice the value of batch 1. In Figure 5.2 (c) and (d), the evolution of reduction conversion with time is represented and compared at different temperature levels. Only the results for cycle 20 are displayed since the materials present a more stable OTC at that point. For batch 1 material, reduction conversion is around 19% at 720 °C increasing up to 67% at the highest temperature tested. In batch 2, temperature is still crucial in the reduction phase and

conversion values range from 35% at 700 °C to full (100%) conversion at 900 °C. In this last case, full conversion is achieved in less than 200 seconds. The effect of temperature is thus more significant on batch 2 material compared to batch 1. The stronger interaction of Ni and Fe with the Al_2O_3 support for the material with lower Ni content could be responsible of this behaviour. The absence of NiO species shown in XRD and TPR (see the material characterization section) corroborate the TGA results.

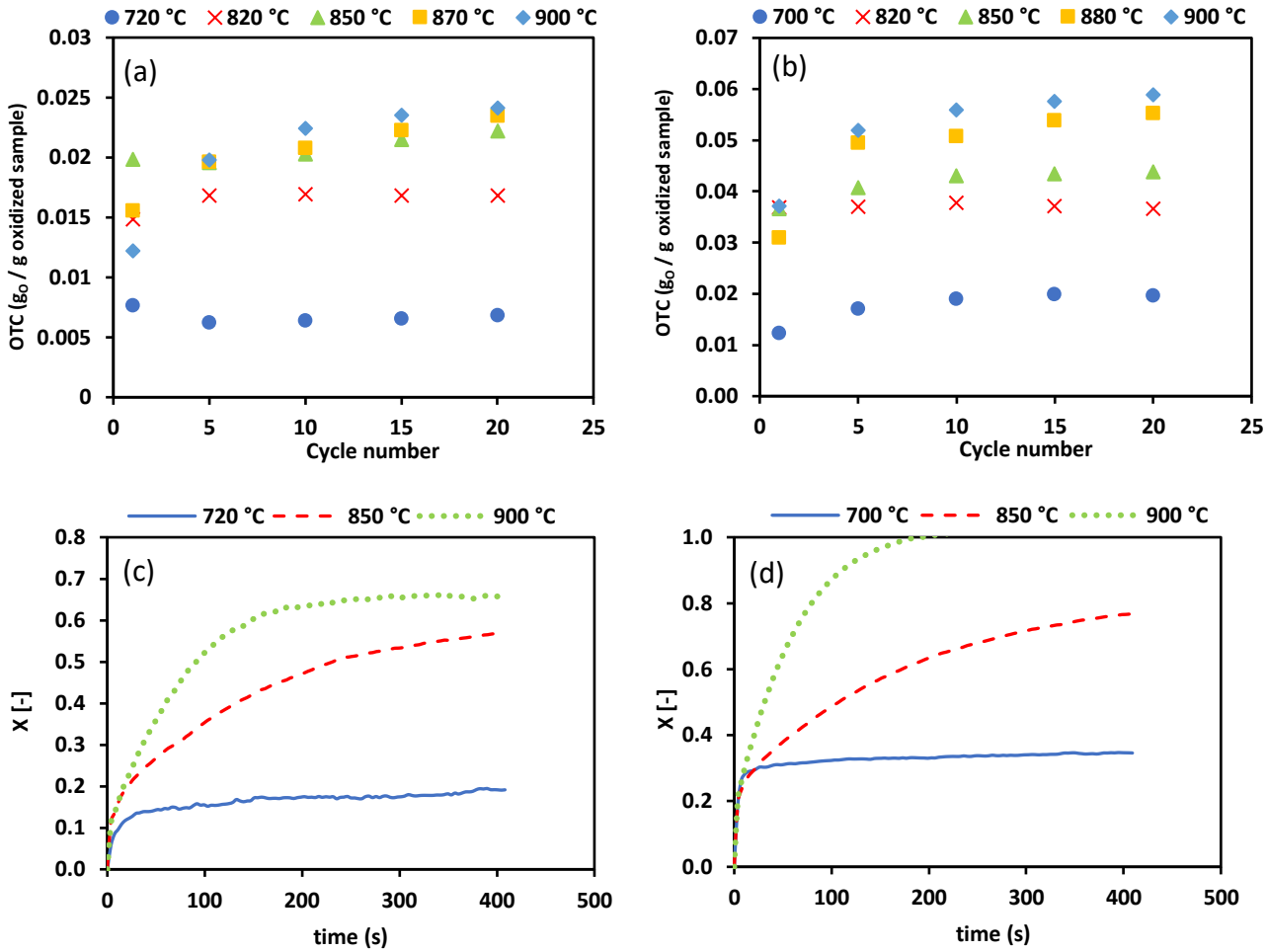

Figure 5.2. Oxygen transport capacity along reduction-oxidation cycles and reduction conversion at cycle 20 at different temperatures from batch 1 (a and c) and batch 2 (b and d)

5.3.2 HPTGA validation

Before investigating the high-pressure redox behaviour of the NiFe aluminates, the HP-TGA setup is tested with a 12.5 wt% CuO/Al_2O_3 powder (1.1 mm diameter provided by Sigma Aldrich) at 800 °C and the results are compared with literature data [44]. Two tests are carried out at 6 bar, 3 nl/min and 4 nl/min total flow rate and 50% H_2/N_2 mixture. The plots of Figures D1 and D2 of Appendix D show a good agreement and ensure the safe and good operation of the HP-TGA.

5.3.3 High pressure reactivity of the NiFe aluminates

In the high-pressure experimental campaign, batch 1 NiFe aluminate is tested under different operating conditions, such as flow rate, temperature, gas composition, and pressure, to assess the influence of these parameters on reduction conversion. A comparison with batch 2 material conversion under specific conditions is also carried out. Subsequently, the long-term stability of batch 2 NiFe aluminate is investigated over 80 high pressure cycles and compared with the results for 100 cycles at ambient pressure conditions.

Firstly, measurements are carried out at 800 °C, 20 bar and four flow rates under 50% H_2/N_2 atmosphere. The results on reduction conversion are plotted in Figure 5.3. At 2 nl/min, the system presents mass transfer limitations causing a slower reaction rate during the first seconds and a slightly lower total conversion at the end of the test. On the contrary, almost the same initial reaction rate is observed for all flow rates above 4 nl/min with similar final conversions of about 67%. This indicates that from 4 nl/min the system is not mass transfer limited. The 8 nl/min case presents a different behaviour which is ascribed to a certain degree of instability of the setup due to the very high flow rates in the reactor.

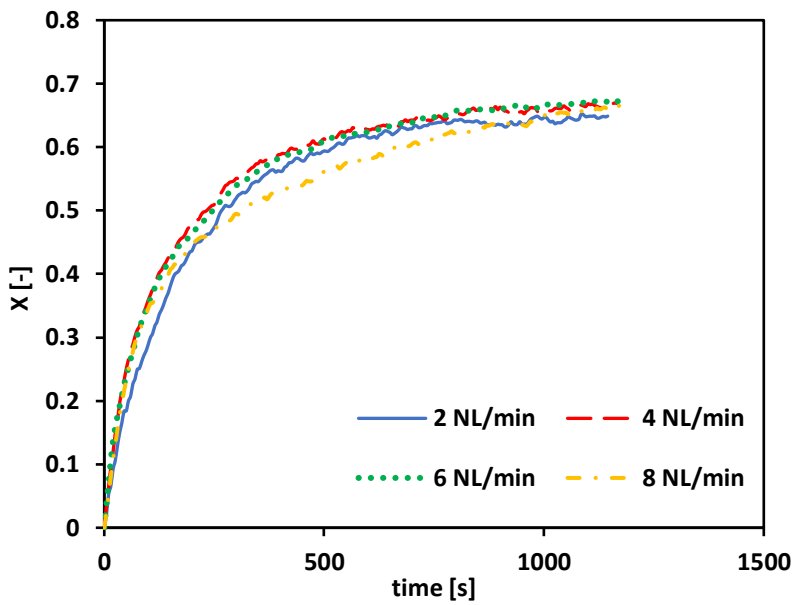

Figure 5.3. Reduction conversion of batch 1 NiFe aluminate at 20 bar, 800 °C and different flow rates

The influence of temperature on batch 1 material reduction is then assessed in Figure 5.4. Tests are carried out at 6 nl/min, 20 bar and four temperature levels. with a 50% H_2/N_2 atmosphere. As it is described for material testing at atmospheric pressure, reducing temperature impacts in a significant way on final conversion. The final conversion at 700 °C amounts to about 38% and is significantly lower compared to the other temperatures. At 750 °C, the reaction rate increases and a final conversion of about 61% is achieved. Above

800 °C, a similar final reduction conversion of about 67% is reached, and an increase of the initial linear behaviour is observed.

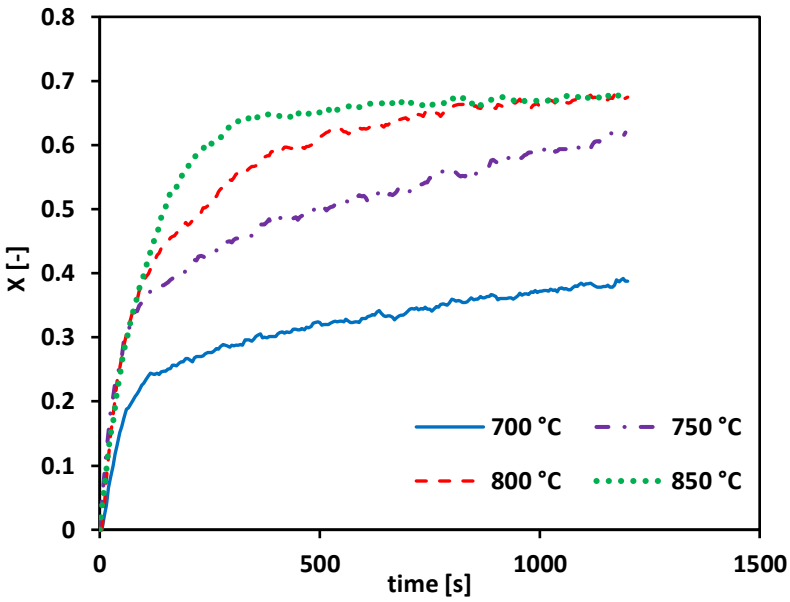

Figure 5.4. Reduction conversion of batch 1 NiFe aluminate at 20 bar, 800°C, 6 nl/min and different temperature levels

The effect of the reducing gas composition on batch 1 reduction is assessed by using different mixtures of N_2 and H_2. Tests are carried out at 20 bar, 800 °C, 6 nl/min and three H_2/N_2 mixtures containing 25%, 50% and 75% H_2. The results are plotted in Figure 5.5. Since a constant total pressure of 20 bar is imposed, different H_2 percentages in the mixtures correspond to different H_2 partial pressures in the reactor. For this reason, when the H_2 content is 25% H_2, slower reaction rate and lower final conversions are achieved. An increasing trend is observed at the end of the 25% H_2 test, meaning that the conversion is still proceeding. For the other compositions, a similar final conversion is achieved but with a faster kinetics for higher H_2 contents, as expected.

The effect of total pressure is investigated by fixing the hydrogen partial pressure at p_{H2}=10 bar while changing the total pressure in the system. The reduction conversion trends at 10, 15 and 20 bar are plotted in Figure 5.6. The presence of a certain noise level in the 10 bar trend is associated with the backpressure controller trying to establish a stable pressure level in the reactor during the utilization of pure H_2 (p_{H2} = 10 bar). By comparing the plots, lower total pressure levels enhance the reaction rate, while approximately the same final conversion is achieved for the three cases. This confirms the negative effect of pressure on reduction kinetics, as detected in other literature works [39–43]. Several explanations have been provided to justify this phenomenon. The most widespread focuses on the slower products diffusion when the gases leave the particle surface, which then makes it more difficult for the fresh reactants to reach the active sites.

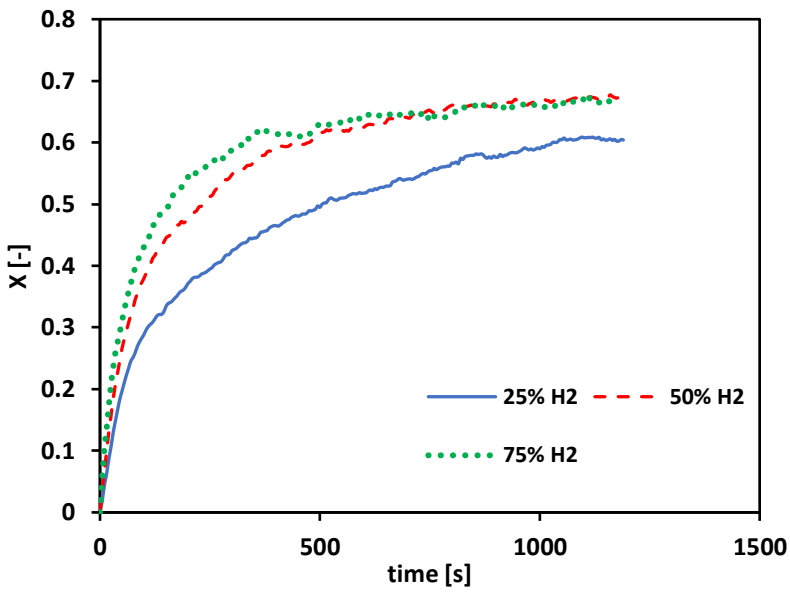

Figure 5.5. Reduction conversion of batch 1 NiFe aluminate at 20 bar, 800 °C, 6 nl/min and different H_2/N_2 mixtures

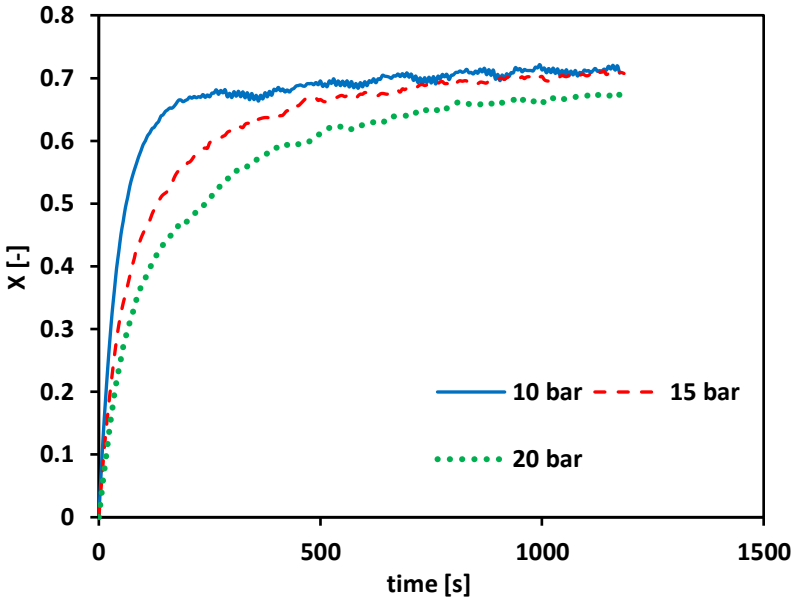

Figure 5.6. Reduction conversion of batch 1 NiFe aluminate at 800 °C, 6 nl/min, p_{H2} = 10 bar and different total pressures

To further corroborate this observation, another test is carried out at 6 nl/min, 800 °C and 50% H_2/N_2 mixture with different total pressures in the system, corresponding to different H_2 partial pressures in the reactor. The results are plotted in Figure 5.7. In these conditions, the negative effect of the total pressure is counterbalanced by the positive effect of higher partial pressures in the system. Hence, at 25 bar a slower initial reaction kinetics is observed compared to the 15 bar case, while comparable final conversions are achieved at the end of the test. The 20 bar plot shows a slightly better reduction rate along the whole 20 minutes reduction.

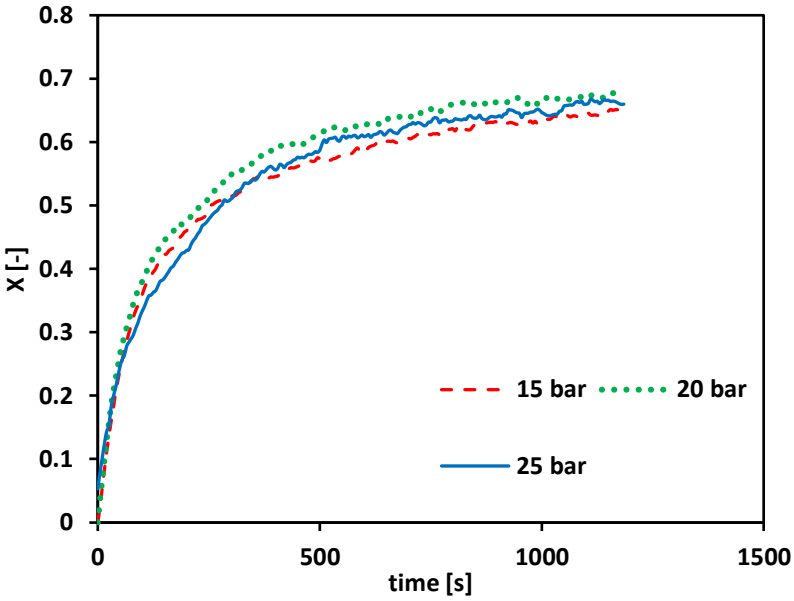

Figure 5.7. Reduction conversion of batch 1 NiFe aluminate at three total pressures, 800 °C, 6 nl/min and 50% H_2/N_2

Finally, a comparison with batch 2 NiFe aluminate is carried out to assess the effect of higher Ni loadings on reduction conversion. As can be seen in Figure 5.8, the material shows a similar reduction behaviour to that of batch 1 NiFe aluminate, which is represented in the detail of Figure 5.8 for comparison. By increasing the H_2 content in the mixture, the reaction kinetics is enhanced. About the same final conversion (75%) is achieved for the 50% and 75% H_2 mixtures, while for the 25% H_2 case the conversion trend is always below during the test and still increasing at the end of it. As already observed in Figure 5.2 at ambient pressure, also at 20 bar a larger Ni content improves reduction kinetics.

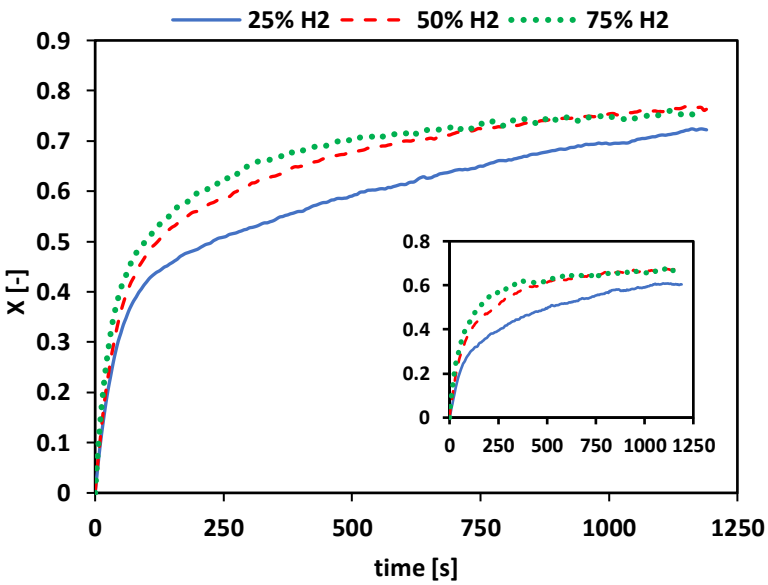

Figure 5.8. Reduction conversion of batch 2 NiFe aluminate at 20 bar, 800 °C, 6 nl/min and different H_2/N_2 mixtures

5.3.4 Long-term stability

The long-terms stability of the materials is an important aspect to be considered for scale up of chemical looping processes. Two sets of runs are performed for ambient and high-pressure conditions on batch 2 NiFe aluminate, which has proved better reaction performance. At ambient pressure, the long-term stability is assessed by performing approximately 100 redox cycles at 900 °C following the same conditions previously described. Figure 5.9 shows that reduction conversion is not complete in the first cycles, but it tends to improve until it reaches (after cycle n. 40) a stable level. These results are consistent with the increase of OTC shown in Figure 5.2 when the material is submitted to consecutive cycles. This "activation" phenomenon is also observed in other works on chemical looping with perovskites [48,49] and could be associated with an increase in specific surface area/porosity of the oxygen carrier as well as a change in the active phase after each oxidation step i.e. the aluminates are not fully regenerated. However, the effect of many cycles on reduction conversion curve in the early moments of reaction (see 20 sec detail in Figure 5.9) is the opposite, i.e. the reaction is slightly slower in later cycles

compared with the first ones, but the decrease is quite low between cycle 40 and 70 and stable after that point.

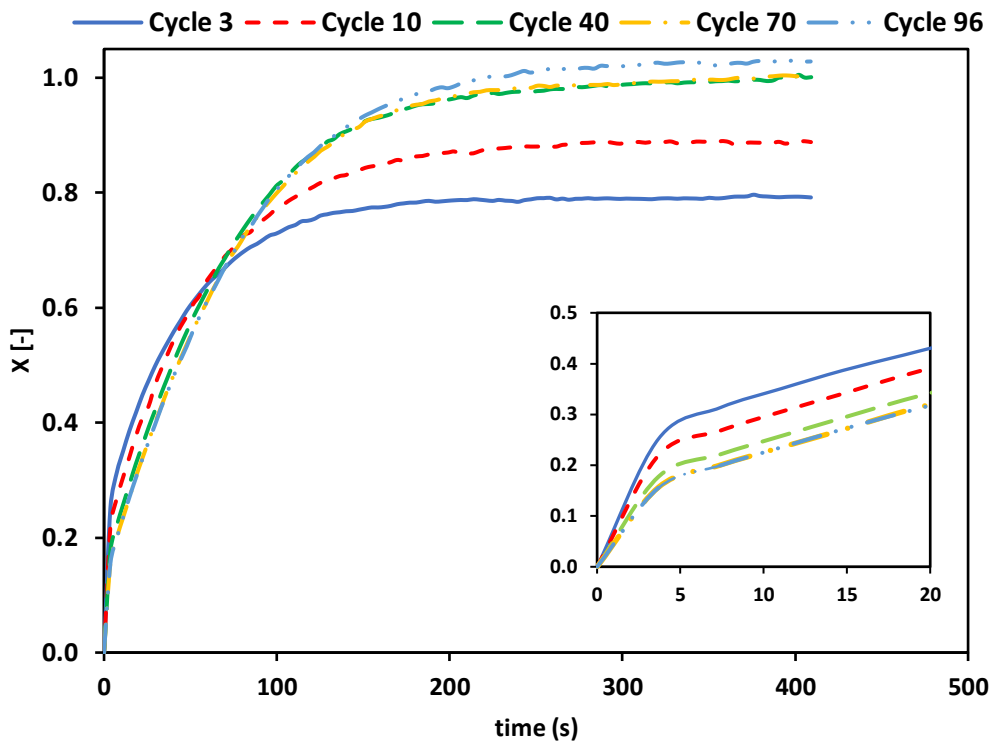

Figure 5.9. Reduction conversion of batch 2 NiFe aluminate at 900 °C and ambient pressure along multiple redox cycles

The reduction conversion trend throughout 80 chemical looping cycles at 20 bar is plotted in Figure 5.10. The detail in Figure 5.10 shows that after the first redox, the initial slope of

the reduction curve decreases along the cycles. On the contrary, the reduction conversion increases steadily until the 60th cycle.

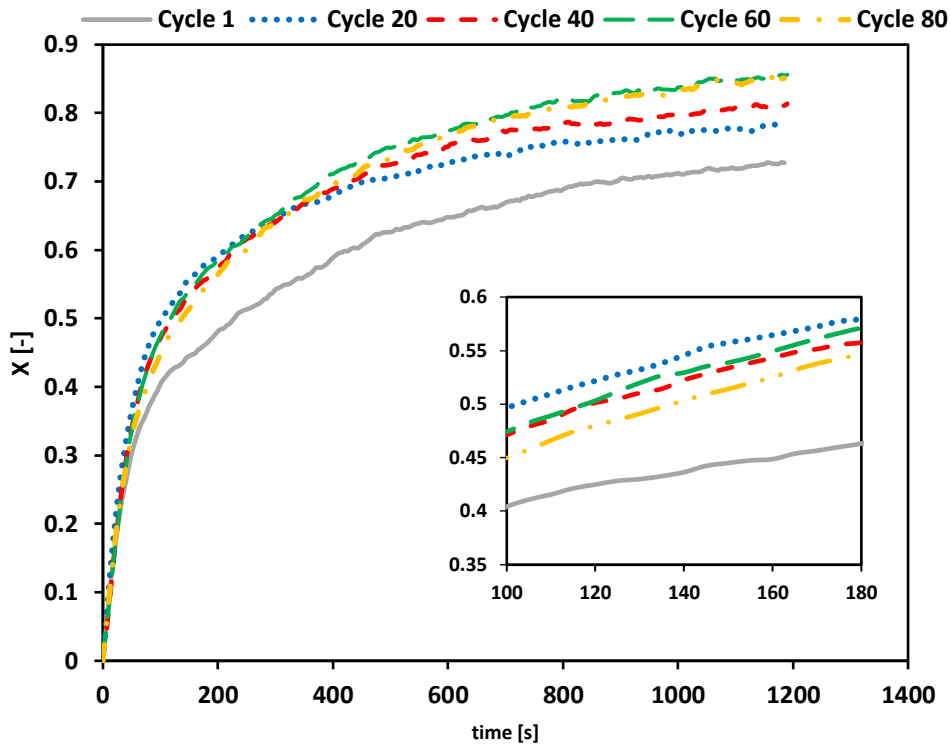

Figure 5.10. Reduction conversion of batch 2 NiFe aluminate at 20 bar along multiple redox cycles

5.3.5 Material characterization

Fresh materials reducibility is assessed through TPR tests. As shown in Figure 5.11, the materials present an important consumption peak between 730 °C and 830 °C. There is also a H_2 consumption peak at lower temperatures (around 400 °C) that is more evident for the material with higher Ni loadings. This consumption peak is typical for the reduction of NiO with low interaction with the support [50]. In general, it has been observed that materials with lower Ni loading present a higher interaction with the support or higher presence of $NiAl_2O_4$ that reduces at higher temperatures. This observation is confirmed by TPR and XRD tests.

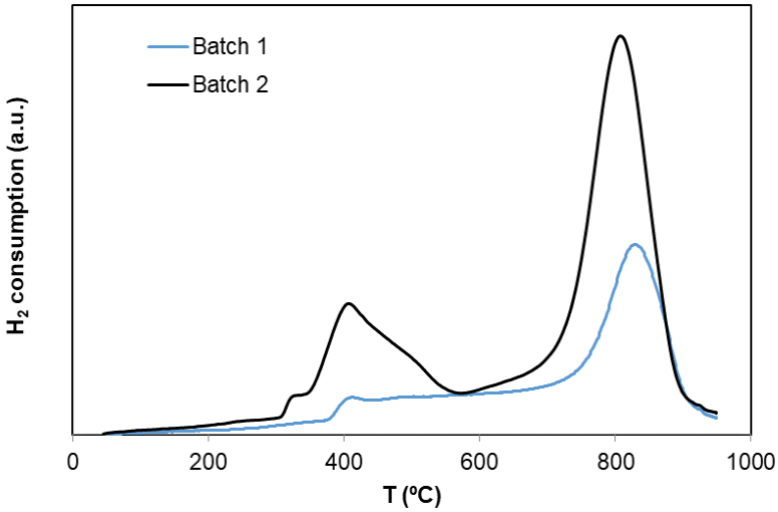

Figure 5.11. TPR data showing H_2 consumption up to 950 °C for materials from batch 1 and 2

The fresh materials from batch 1 and 2 have been characterised through SEM-EDX (Hitachi S-3400-N) at crosscut to assess the dispersion of Fe and Ni within the particles. The results, including the EDX line-scan data, are shown in Figure 5.12. For batch 1 material, the Fe content is about twice the Ni content, as corroborated by ICP results shown in Table 5.1. On the contrary, for batch 2 the Fe and Ni loadings are similar. All elements show homogeneous distribution within the particle, indicating that the support impregnation is successfully achieved.

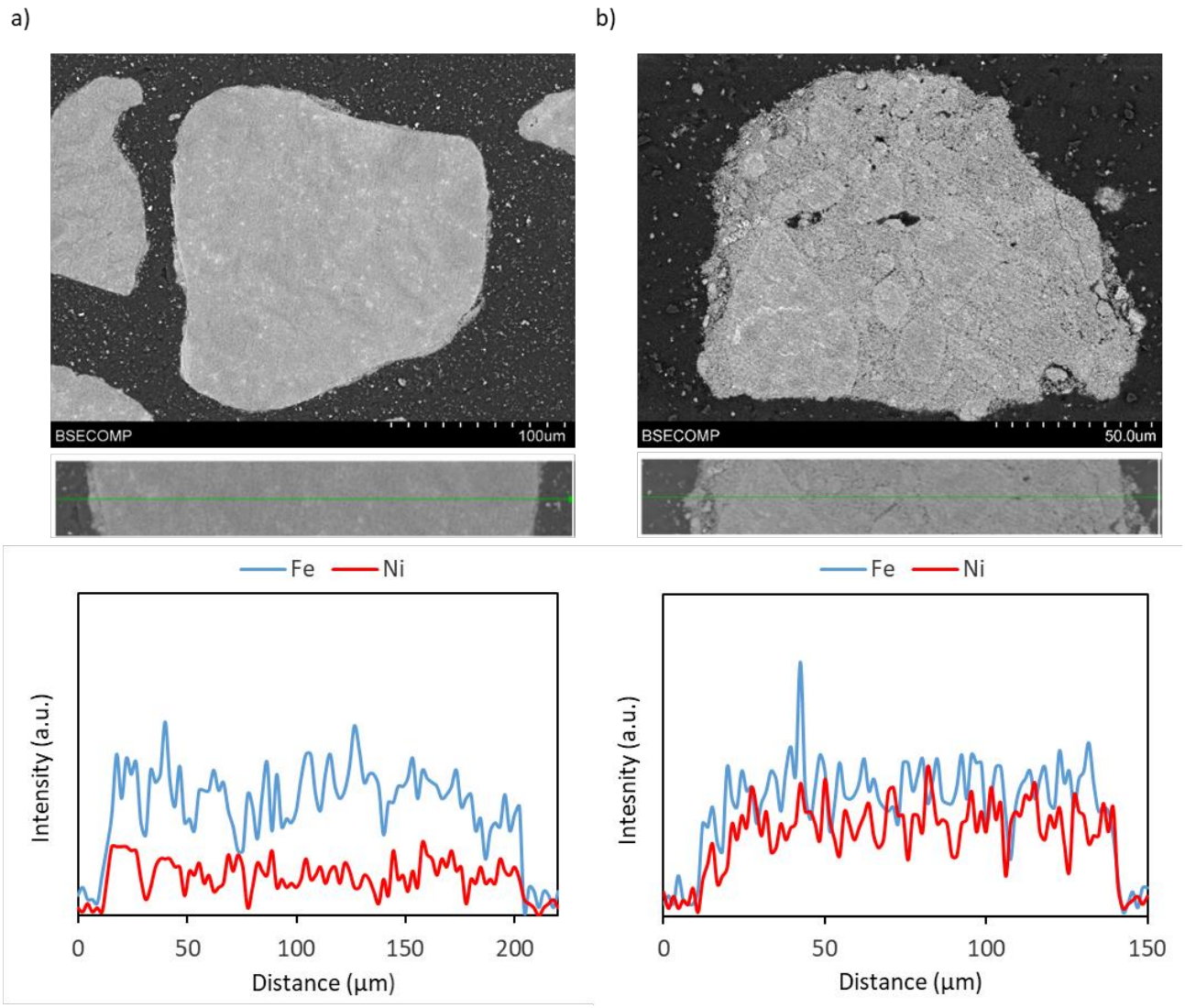

Figure 5.12. SEM images and EDX analysis with line-scan information for batch 1 (a) and batch 2 (b)

SEM pictures (Thermo Scientific Phenom ProX) of fresh batch 2 material and reduced after the 80 high-pressure cycles are compared in Figure 5.13. In general, the microstructure of the spent material does not display particular signs of stress in terms of increased cracks or voids formation compared to the fresh material. The presence of voids and cracks has been detected also in the fresh material and is probably associated with material synthesis and subsequent handling. Moreover, the particle size after reduction is almost preserved compared to the oxidized state.

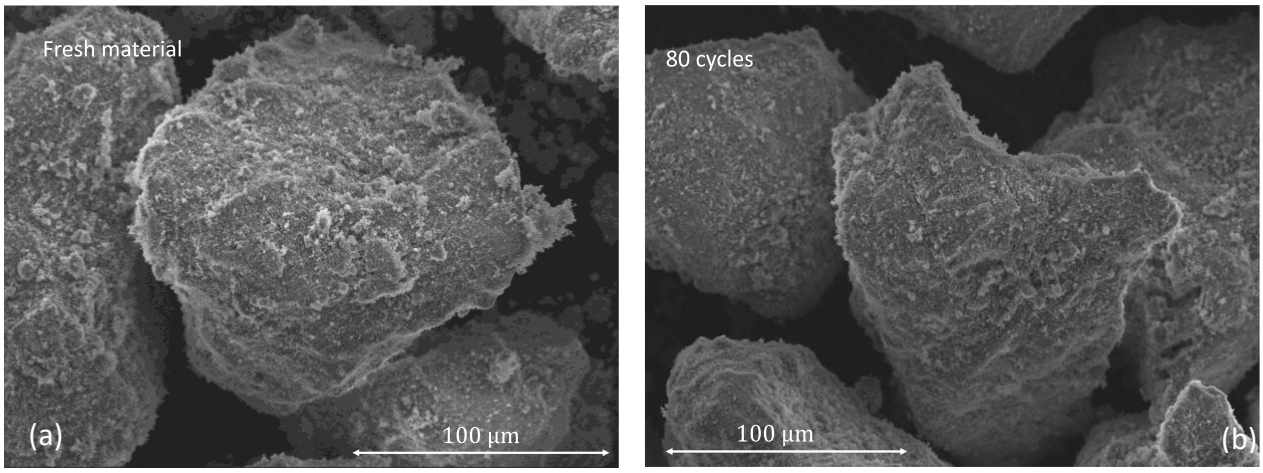

Figure 5.13. SEM pictures of fresh batch 2 NiFe aluminate (a) and reduced batch 2 after 80 high pressure cycles (b)

The XRD (Bruker D-8 Advance) patterns of the fresh and the reduced materials at ambient pressure conditions are displayed in Figure 5.14.

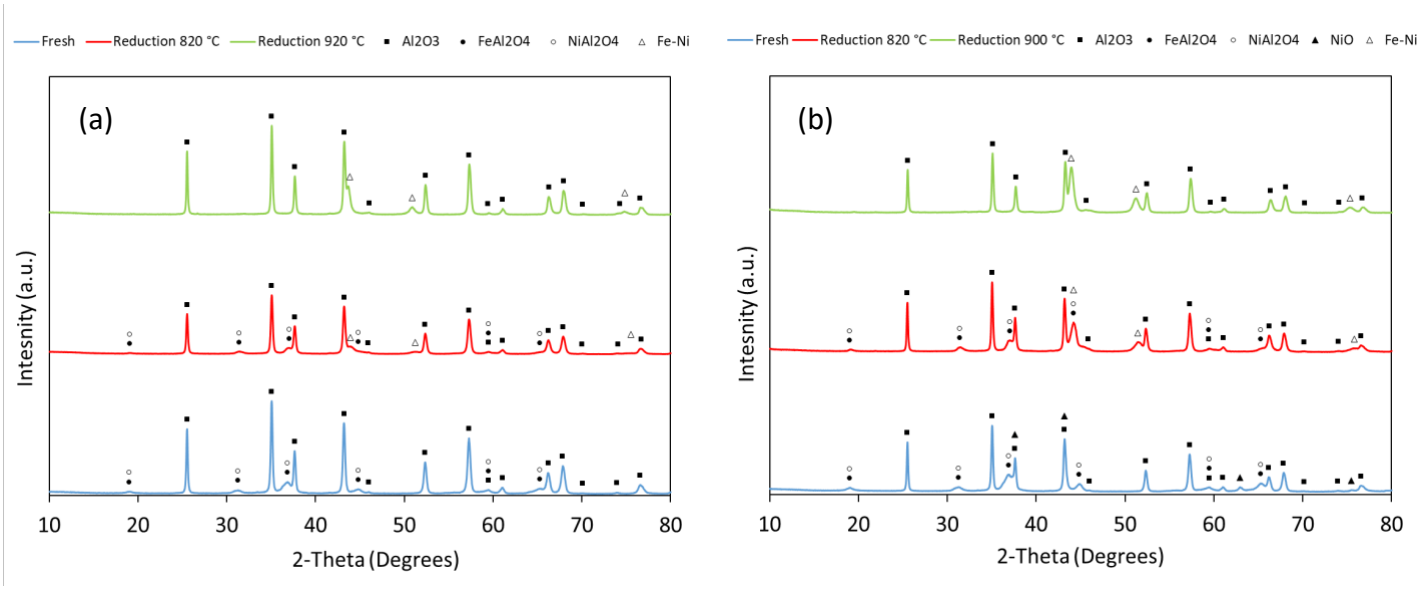

Figure 5.14. XRD patterns of batch 1 (a) and batch 2 (b) both fresh (oxidized) and reduced in H_2/N_2 at 820 °C and 900 °C or 920 °C

In both oxidized materials, the presence of Fe and Ni in aluminate form is appreciated, but in batch 2 (with a higher Ni content) NiO is also present as a Ni species. As the oxygen carriers have been submitted to a reduction atmosphere, peaks corresponding to an iron-nickel phase appear. XRD patterns corresponding to the materials reduced at 820 °C and 900-920 °C show the dependence of the reduction reaction with temperature. Samples reduced at the lowest temperature still have $FeAl_2O_4$ and $NiAl_2O_4$ peaks and Fe-Ni peaks of low intensity, while in samples reduced at high temperature the peaks corresponding to

aluminates disappear and more intense Fe-Ni peaks are present. This confirms that under high temperature conditions the material is completely reduced, while only partial reduction takes place at lower temperatures.

The XRD patterns (Rigaku MiniFlex) of the fresh and reduced material after long term tests (30 and 80 cycles) and at different pressure conditions (15 and 20 bar) are displayed in Figure 5.15. In both cases, complete reduction conversion is not achieved since the presence of aluminate phases peaks in all the reduced material patterns could be detected. The incomplete conversion can be again attributed to the detrimental effect of high-pressure operation. The patterns present a similar structure with three Fe-Ni peaks around 44°, 52° and 76°. From the fresh material pattern, the oxidized phase peaks at 31° and 59° reduce in intensity, while the shoulder at 37° and the peaks at 56° and 66° disappear. No significant differences can be observed between the patterns after cycles n.30 and n. 80, as well as between 15 and 20 bar patterns. Therefore, the reaction pathway does not change either with pressure or along multiple cycles.

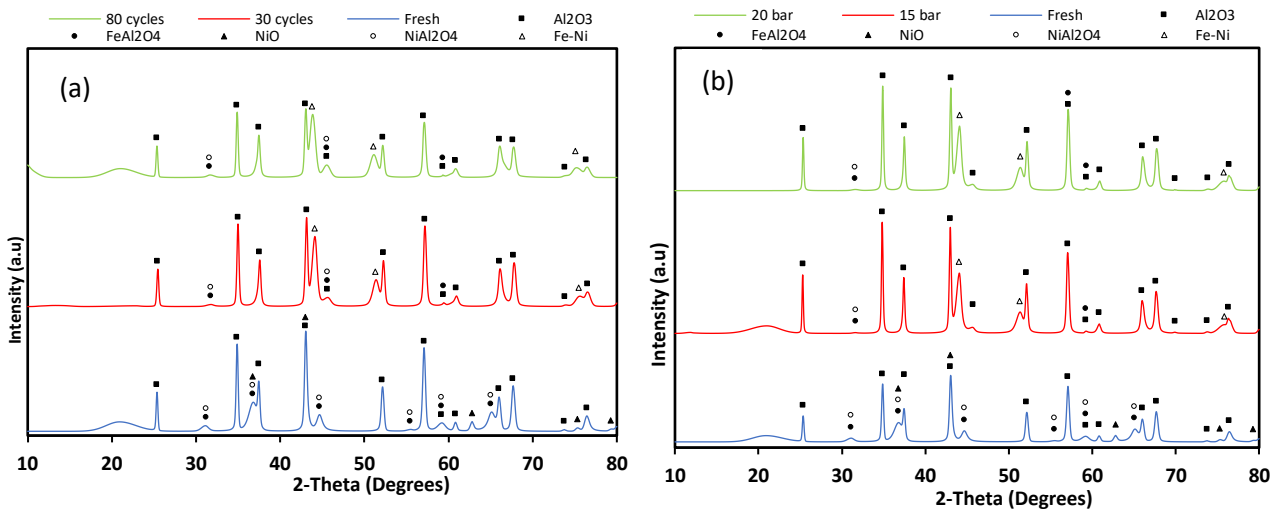

Figure 5.15. XRD patterns of batch 2 material fresh, reduced after 30 cycles and 80 cycles at 20 bar (a), fresh, reduced at 15 bar and 20 bar with p_{H2} = 10 bar

5.4 Chapter summary and conclusions

In this chapter, chemical looping cycles are carried out with two different setups to compare the reduction behaviour of two NiFe aluminates (batch 1 and 2) at ambient and high-pressure conditions. At ambient pressure conditions, the effect of different temperature levels on the oxygen transport capacity and on the reduction conversion of both materials is assessed. Each condition is tested for 20 reduction/oxidation cycles. It is shown that the oxygen transport capacity increases with the cycles for temperatures above 800 °C and that higher Ni loadings provide better reaction performances. Full reduction conversion is

achieved at 900 °C after 200 s of testing for the material with 12% wt Ni and 8.5% wt Fe. At high pressure conditions, the time variation of reduction conversion of batch 1 material is assessed under different operating conditions. The occurrence of external mass transfer limitations at 20 bar is preliminarily studied and prevented. In all tests, a general behaviour is observed where an initial fast kinetics is replaced by a plateau at high conversions. Increasing temperatures as well as higher H_2 contents improve the reaction kinetics and reach earlier a conversion plateau. However, the final conversion value is approximately the same above 800 °C or above 50% H_2 content. Total pressures show a negative effect on reaction kinetics. Batch 2 material with higher Ni loading is tested under different H_2 compositions and increased final conversion (depending on the specific condition) is observed when compared to batch 1 material. Long-term testing at both ambient and high-pressure conditions is then carried out on the former NiFe over 100 and 80 cycles, respectively. A reduction gain is observed throughout the cycles and full conversion is achieved after the 40th cycle at 900 °C and ambient pressure conditions. From characterization analyses, no significant changes in the microstructure of the material are observed and no difference between the diffraction patterns after 30 and 80 cycles are detected. Therefore, it can be concluded that the selected material composition in terms of active and inert species is able to ensure the continuous operation of the material over many cycles, while a higher Ni content in the spinel structure is indicated for better reduction performance and high cyclability in the process.

5.5 Nomenclature

CLC	Chemical Looping Combustion
CLR	Chemical Looping Reforming
c-YSZ	Yttria-Stabilized Cubic Zirconia
EDX	Energy Dispersive X-Ray
HP-TGA	High-Pressure Thermogravimetric Analyzer
ICP	Inductively Coupled Plasma
m_{ox}	Net sample mass at the end of the oxidation step after the basket signal removal
m_{red}	Completely reduced sample mass
m(t)	Net sample mass at time t after the basket signal removal
OTC	Oxygen Transport Capacity
SEM	Scanning Electron Microscopy
TGA	Thermogravimetric Analyzer
TPR	Temperature Programmed Reduction
t-PSZ	Partially Stabilized Tetragonal Zirconia
XRD	X-Ray Diffraction

Acknowledgments

This project has received funding from the European Union's Horizon 2020 Research and Innovation Program under grant agreement No 884197 (GLAMOUR).

5.6 References

[1] Muhich CL, Ehrhart BD, Al-Shankiti I, Ward BJ, Musgrave CB, Weimer AW. A review and perspective of efficient hydrogen generation via solar thermal water splitting. Wiley Interdiscip Rev Energy Environ 2015;5:261–87. https://doi.org/10.1002/wene.174.

[2] Abanades S, Flamant G. Thermochemical hydrogen production from a two-step solar-driven water-splitting cycle based on cerium oxides. Solar Energy 2006;80:1611–23. https://doi.org/10.1016/j.solener.2005.12.005.

[3] Tian H, Chaudhari K, Simonyi T, Poston J, Liu T, Sanders T, et al. Chemical-looping combustion of coal-derived synthesis gas over copper oxide oxygen carriers. Energy & Fuels 2008;22:3744–55.

[4] Mattisson T, Johansson M, Lyngfelt A. The use of NiO as an oxygen carrier in chemical-looping combustion. Fuel 2006;85:736–47.

[5] Yu Z, Yang Y, Yang S, Zhang Q, Zhao J, Fang Y, et al. Iron-based oxygen carriers in chemical looping conversions: A review. Carbon Resources Conversion 2019;2:23–34. https://doi.org/10.1016/j.crcon.2018.11.004.

[6] Hu J, Poelman H, Marin GB, Detavernier C, Kawi S, Galvita V V. FeO controls the sintering of iron-based oxygen carriers in chemical looping CO2 conversion. Journal of CO2 Utilization 2020;40:101216.

[7] Tijani MM, Aqsha A, Mahinpey N. Synthesis and study of metal-based oxygen carriers (Cu, Co, Fe, Ni) and their interaction with supported metal oxides (Al2O3, CeO2, TiO2, ZrO2) in a chemical looping combustion system. Energy 2017;138:873–82. https://doi.org/10.1016/j.energy.2017.07.100.

[8] Cabello A, Abad A, Mendiara T, Izquierdo MT, de Diego LF. Outstanding performance of a Cu-based oxygen carrier impregnated on alumina in chemical looping combustion. Chemical Engineering Journal 2022:140484.

[9] Abdalla A, Mohamedali M, Mahinpey N. Recent Progress in the Development of Synthetic Oxygen Carriers for Chemical Looping Combustion Applications. Catal Today 2022.

[10] Adánez J, De Diego LF, García-Labiano F, Gayán P, Abad A, Palacios JM. Selection of oxygen carriers for chemical-looping combustion. Energy and Fuels 2004;18:371–7. https://doi.org/10.1021/ef0301452.

[11] Gayán P, Luis F, Garc\'\ia-Labiano F, Adánez J, Abad A, Dueso C. Effect of support on reactivity and selectivity of Ni-based oxygen carriers for chemical-looping combustion. Fuel 2008;87:2641–50.

[12] Kidambi PR, Cleeton JPE, Scott SA, Dennis JS, Bohn CD. Interaction of iron oxide with alumina in a composite oxygen carrier during the production of hydrogen by chemical looping. Energy and Fuels, vol. 26, 2012, p. 603–17. https://doi.org/10.1021/ef200859d.

[13] Damizia M, Bracciale MP, Anania F, Tai L, De Filippis P, de Caprariis B. Efficient utilization of Al2O3 as structural promoter of Fe into 2 and 3 steps chemical looping hydrogen process: Pure H2 production from ethanol. Int J Hydrogen Energy 2023. https://doi.org/10.1016/j.ijhydene.2023.04.067.

[14] De Vos Y, Jacobs M, Van Der Voort P, Van Driessche I, Snijkers F, Verberckmoes A. Sustainable iron-based oxygen carriers for Chemical Looping for Hydrogen Generation. Int J Hydrogen Energy 2019;44:1374–91. https://doi.org/10.1016/j.ijhydene.2018.11.099.

[15] De Vos Y, Jacobs M, Van Driessche I, Van Der Voort P, Snijkers F, Verberckmoes A. Processing and characterization of Fe-based oxygen carriers for chemical looping for hydrogen production. International Journal of Greenhouse Gas Control 2018;70:12–21. https://doi.org/10.1016/j.ijggc.2018.01.007.

[16] Jerndal E, Mattisson T, Thijs I, Snijkers F, Lyngfelt A. Investigation of NiO/NiAl2O4 oxygen carriers for chemical-looping combustion produced by spray-drying. International Journal of Greenhouse Gas Control 2010;4:23–35. https://doi.org/10.1016/j.ijggc.2009.09.007.

[17] Dueso C, Abad A, García-Labiano F, De Diego LF, Gayán P, Adánez J, et al. Reactivity of a NiO/Al2O3 oxygen carrier prepared by impregnation for chemical-looping combustion. Fuel 2010;89:3399–409. https://doi.org/10.1016/j.fuel.2010.03.043.

[18] Bhavsar S, Veser G. Bimetallic Fe-Ni oxygen carriers for chemical looping combustion. Ind Eng Chem Res, vol. 52, 2013, p. 15342–52. https://doi.org/10.1021/ie400612g.

[19] Kuo YL, Hsu WM, Chiu PC, Tseng YH, Ku Y. Assessment of redox behavior of nickel ferrite as oxygen carriers for chemical looping process. Ceram Int 2013;39:5459–65. https://doi.org/10.1016/j.ceramint.2012.12.055.

[20] Evdou A, Zaspalis V, Nalbandian L. Ferrites as redox catalysts for chemical looping processes. Fuel 2016;165:367–78. https://doi.org/10.1016/j.fuel.2015.10.049.

[21] Huang Z, Deng Z, He F, Chen D, Wei G, Zhao K, et al. Reactivity investigation on chemical looping gasification of biomass char using nickel ferrite oxygen carrier. Int J Hydrogen Energy 2017;42:14458–70. https://doi.org/10.1016/j.ijhydene.2017.04.246.

[22] Wei G, He F, Zhao Z, Huang Z, Zheng A, Zhao K, et al. Performance of Fe-Ni bimetallic oxygen carriers for chemical looping gasification of biomass in a 10 kWth interconnected circulating fluidized bed reactor. Int J Hydrogen Energy 2015;40:16021–32. https://doi.org/10.1016/j.ijhydene.2015.09.128.

[23] Chen J, Zhao K, Zhao Z, He F, Huang Z, Wei G. Identifying the roles of MFe 2 O 4 (M=Cu, Ba, Ni, and Co) in the chemical looping reforming of char, pyrolysis gas and tar resulting from biomass pyrolysis. Int J Hydrogen Energy 2019;44:4674–87. https://doi.org/10.1016/j.ijhydene.2018.12.216.

[24] Wang X, Chen Z, Hu M, Tian Y, Jin X, Ma S, et al. Chemical looping combustion of biomass using metal ferrites as oxygen carriers. Chemical Engineering Journal 2017;312:252–62. https://doi.org/10.1016/j.cej.2016.11.143.

[25] Argyris PA, De Leeuwe C, Abbas SZ, Amieiro A, Poultson S, Wails D, et al. Chemical looping reforming for syngas generation at real process conditions in packed bed reactors: An experimental demonstration. Chemical Engineering Journal 2022;435:134883.

[26] de Leeuwe C, Abbas SZ, Argyris PA, Zaidi A, Amiero A, Poultson S, et al. Thermochemical syngas generation via solid looping process: an experimental demonstration using Fe-based material. Chemical Engineering Journal 2023;453:139791.

[27] Bracciale MP, Damizia M, De Filippis P, de Caprariis B. Clean Syngas and Hydrogen Co-Production by Gasification and Chemical Looping Hydrogen Process Using MgO-Doped Fe2O3 as Redox Material. Catalysts 2022;12. https://doi.org/10.3390/catal12101273.

[28] Ortiz M, de Diego LF, Abad A, Garcia-Labiano F, Gayan P, Adanez J. Catalytic activity of Ni-based oxygen-carriers for steam methane reforming in chemical-looping processes. Energy & Fuels 2012;26:791–800.

[29] Huang Z, He F, Chen D, Zhao K, Wei G, Zheng A, et al. Investigation on reactivity of iron nickel oxides in chemical looping dry reforming. Energy 2016;116:53–63.

[30] Antzara A, Heracleous E, Silvester L, Bukur DB, Lemonidou AA. Activity study of NiO-based oxygen carriers in chemical looping steam methane reforming. Catal Today 2016;272:32–41.

[31] Luo M, Yi Y, Wang S, Wang Z, Du M, Pan J, et al. Review of hydrogen production using chemical-looping technology. Renewable and Sustainable Energy Reviews 2018;81:3186–214. https://doi.org/10.1016/j.rser.2017.07.007.

[32] Deshpande N, Majumder A, Qin L, Fan LS. High-pressure redox behavior of iron-oxide-based oxygen carriers for syngas generation from methane. Energy and Fuels 2015;29:1469–78. https://doi.org/10.1021/ef5025998.

[33] Palone O, Hoxha A, Gagliardi GG, Di Gruttola F, Stendardo S, Borello D. Synthesis of Methanol From a Chemical Looping Syngas for the Decarbonization of the Power Sector. J Eng Gas Turbine Power 2023;145:21018.

[34] Pereira RJL, Argyris PA, Spallina V. A comparative study on clean ammonia production using chemical looping based technology. Appl Energy 2020;280:115874.

[35] Roshan Kumar T, Mattisson T, Rydén M. Techno-economic assessment of chemical looping gasification of biomass for Fischer–Tropsch crude production with net-negative CO2 emissions: part 2. Energy & Fuels 2022;36:9706–18.

[36] Osman M, Khan MN, Zaabout A, Cloete S, Amini S. Review of pressurized chemical looping processes for power generation and chemical production with integrated CO2 capture. Fuel Processing Technology 2021;214. https://doi.org/10.1016/j.fuproc.2020.106684.
[37] Zhang S, Xiao R, Zheng W. Comparative study between fluidized-bed and fixed-bed operation modes in pressurized chemical looping combustion of coal. Appl Energy 2014;130:181–9. https://doi.org/10.1016/j.apenergy.2014.05.049.
[38] Gallucci F, Hamers HP, Van Zanten M, van Sint Annaland M. Experimental demonstration of chemical-looping combustion of syngas in packed bed reactors with ilmenite. Chemical Engineering Journal 2015;274:156–68.
[39] Hamers HP, Gallucci F, Williams G, Cobden PD, van Sint Annaland M. Reactivity of oxygen carriers for chemical-looping combustion in packed bed reactors under pressurized conditions. Energy & Fuels 2015;29:2656–63.
[40] Garcia-Labiano F, Adánez J, de Diego LF, Gayán P, Abad A. Effect of pressure on the behavior of copper-, iron-, and nickel-based oxygen carriers for chemical-looping combustion. Energy & Fuels 2006;20:26–33.
[41] Lu X, Rahman RA, Lu DY, Ridha FN, Duchesne MA, Tan Y, et al. Pressurized chemical looping combustion with CO: Reduction reactivity and oxygen-transport capacity of ilmenite ore. Appl Energy 2016;184:132–9. https://doi.org/10.1016/j.apenergy.2016.09.107.
[42] Tan Y, Ridha FN, Duchesne MA, Lu DY, Hughes RW. Reduction Kinetics of Ilmenite Ore as an Oxygen Carrier for Pressurized Chemical Looping Combustion of Methane. Energy and Fuels 2017;31:7598–605. https://doi.org/10.1021/acs.energyfuels.7b01038.
[43] Nordness O, Han L, Zhou Z, Bollas GM. High-Pressure Chemical-Looping of Methane and Synthesis Gas with Ni and Cu Oxygen Carriers. Energy and Fuels 2016;30:504–14. https://doi.org/10.1021/acs.energyfuels.5b01986.
[44] San Pio MA, Gallucci F, Roghair I, van Sint Annaland M. Gas-solids kinetics of CuO/Al2O3 as an oxygen carrier for high-pressure chemical looping processes: the influence of the total pressure. Int J Hydrogen Energy 2017;42:12111–21.
[45] Díez-Martín L, Martínez I, Grasa G, Murillo R. Investigation of the reduction kinetics of high loaded CuO-based materials suitable for the Ca/Cu looping process. Fuel 2018;230:376–89. https://doi.org/10.1016/j.fuel.2018.05.054.
[46] Chiesa P, Lozza G, Malandrino A, Romano M, Piccolo V. Three-reactors chemical looping process for hydrogen production. Int J Hydrogen Energy 2008;33:2233–45.
[47] Coenen K, Gallucci F, Cobden P, van Dijk E, Hensen E, van Sint Annaland M. Chemisorption working capacity and kinetics of CO2 and H2O of hydrotalcite-based adsorbents for sorption-enhanced water-gas-shift applications. Chemical Engineering Journal 2016;293:9–23.
[48] Cabello A, Abad A, Gayán P, García-Labiano F, de Diego LF, Adánez J. Increasing energy efficiency in chemical looping combustion of methane by in-situ activation of

perovskite-based oxygen carriers. Appl Energy 2021;287. https://doi.org/10.1016/j.apenergy.2021.116557.

[49] Abad A, Cabello A, Gayán P, García-Labiano F, de Diego LF, Mendiara T, et al. Kinetics of CaMn0.775Ti0.125Mg0.1O2.9-δ perovskite prepared at industrial scale and its implication on the performance of chemical looping combustion of methane. Chemical Engineering Journal 2020;394. https://doi.org/10.1016/j.cej.2020.124863.

[50] Salhi N, Boulahouache A, Petit C, Kiennemann A, Rabia C. Steam reforming of methane to syngas over NiAl2O4 spinel catalysts. Int J Hydrogen Energy 2011;36:11433–9. https://doi.org/10.1016/j.ijhydene.2010.11.071.

[51] San Pio MA, Gallucci F, Roghair I, van Sint Annaland M. On the mechanism controlling the redox kinetics of Cu-based oxygen carriers. Chemical Engineering Research and Design 2017;124:193–201. https://doi.org/10.1016/j.cherd.2017.06.019.

Chapter 6

Techno-economic analysis of methanol and ammonia production by chemical looping hydrogen generation from waste plastic

This chapter is based on the following paper:
Palone, O., Gagliardi, G. G., Mechelli, M., Cedola, L., & Borello, D. (2023). Techno-economic analysis of sustainable methanol and ammonia production by chemical looping hydrogen generation from waste plastic. Energy Conversion and Management, 292, 117389.

Abstract

In this chapter, a techno-economic analysis is carried out on a novel plant configuration for the combined production of ammonia and methanol from chemical looping gases. The process presents advantages in terms of reduced dependency on market price fluctuations, thanks to the combined production of two chemicals, and optimal utilization of the chemical looping gases. The chemical looping plant is fed with recycled high-density polyethylene to enhance the carbon circularity of the process. In this case, part of the captured CO_2 is employed for methanol production with hydrogen from chemical looping, while hydrogen from electrolysis is used for ammonia production with nitrogen from the air reactor. Renewable electric energy supply ensures a carbon free power to fuel conversion. Several sensitivity analyses are carried out to assess the optimum process parameters combination, i.e. fuel flow rate, steam flow rate, oxygen carrier inlet temperature. The final production rate is divided between 174 kg/h of methanol and 910 kg/h of ammonia. An economic analysis is then carried out. Capital costs of 27 M€ and operating costs of 3 M€/y are computed for the system. Sensitivity analyses on the impact of the electricity input cost, the electrolytic oxygen selling price, the electrolyser capital cost and the internal rate of return are then carried out. The electricity demand is discovered to impact for the 68% of the total operating costs. For an electricity cost of 0.03 €/kWh, oxygen selling price of 0.07 €/kg_{O2} and internal rate of return of 8%, a final specific product (combined methanol and ammonia) cost of 0.76 €/kg is determined. The process achieves specific CO_2 emissions of 0.017 kg_{CO2}/kg_{prd}, which is significantly lower than the traditional processes (0.24 kg_{CO2}/kg_{CH3OH} and 1.66 kg_{CO2}/kg_{NH3}), and an energy intensity of 36 GJ/t_{prd}. The final selling price of the products is still not competitive with the traditional processes but is comparable with ammonia production from electrolysis and air separation, and methanol production from electrolysis and direct air capture.

6.1 Introduction

Hydrogen is an attractive energy carrier whose application ranges over several fields: power supply, energy-storage, energy-transport, heavy industry. However, the low volume energy density and the difficult handling of molecular H_2 complicates its usage and results in a high economic and energetic effort. Therefore, it seems more useful to convert H_2 (or more broadly a syngas) produced by renewable energy sources to an energy carrier or a chemical that can be easily transported and/or utilised (Power to X) [1].

6.1.1 Alternative routes for methanol and ammonia synthesis

Methanol, due to its high energy density [2,3], and ammonia, since it can be easily decomposed in H_2 [4], are believed to be a good chemical solution for energy storage and transportation [5,6]. Moreover, those compounds are two key chemical products used as a feedstock for the synthesis of many industrial chemicals.

In 2022, about 90 plants produced approximately 110 Mt of CH_3OH worldwide [7] and it is expected to increase up to 190 Mt/y by 2030 [8]. Methanol can be exploited as a raw material taking part in the production of valuable chemicals like dimethyl ether, formaldehyde, biodiesel and acetic acid. It is also a promising fuel for transportation or energy production purposes, as it can be directly injected or mixed up in motor vehicles without technical adjustments to the mechanical parts [9]. Conventional CH_3OH production is carried out through the following main steps: syngas production from natural gas reforming or coal gasification; syngas conditioning; CH_3OH synthesis and purification. Steam reforming technology is involved in 80% of the global CH_3OH production [10]. As explained in Chapter 1, the reforming step is generally carried out with pure oxygen injection from an air separation unit (ASU) to burn part of the fuel and provide heat to auto sustain the endothermic reforming reaction. The resulting syngas composition is adjusted by the water gas shift reaction and finally CO_2 capture is performed to achieve a $(H_2 - CO_2)/(CO + CO_2)$ molar ratio higher than 2 for optimal operation of the reactor. Methanol synthesis is generally performed in a multistage reactor followed by a series of separation steps with flash drums and distillation columns to obtain high purity CH_3OH. The unreacted gases are generally recycled back to the reactor. This process involves high energy consumption due to the ASU and the CO_2 capture units as well as considerable CO_2 emissions intrinsic to the process and from fossil-based electricity consumption. Recently, the combination of H_2 from different sources and captured CO_2 with renewable electricity supply has been proposed as an alternative and cleaner pathway for CH_3OH production [11]. However, the cost of these resources combined with the low efficiency of the catalyst is at the moment the main drawback hindering the commercialization of the process [12]. One of the most ambitious projects regarding CH_3OH production from CO_2 hydrogenation is the Liquid Sunshine in

China [13]. Recently, a 10 MW solar photovoltaic (PV) power plant has been built to supply energy for H_2 production from electrolysis [14]. Other relevant projects are the European MefCO_2 and FRESME, where CO_2 is captured from a coal power plant in Germany [15] and from steel mill gases [16], respectively, and reacted with H_2. In Iceland, a commercial-size plant is built for CH_3OH production from CO_2 hydrogenation [17]. In this case, the CO_2 is captured from a geothermal power plant and H_2 is produced by an electrolyser. The electricity for H_2 production is directly extracted from the grid, because the high percentage of renewable energy guarantees low emissions [18]. The plant has been working since 2012 with an average production of 4 kt/y of CH_3OH [18,19]. A CO_2 to CH_3OH plant has started production in Anyang, Henan Province, China. It can capture 160 kt of CO_2 emissions a year producing 110 kt of CH_3OH per year [20]. Within the Carbon2Chem® project, steel mill gases are valorised by producing CH_3OH. The integrated production of steel and CH_3OH showed greater benefit. A meta-LCA of CO_2-based CH_3OH production has shown a global warming impact value of 6.27 kg_{CO2eq}/kg_{MeOH} for the German grid mix, while when wind power is selected as energy supply this value becomes negative (–0.87 kg_{CO2eq}/kg_{MeOH}) [21].
Ammonia is a key chemical in the fertilizer industry. Currently, 88% of the whole NH_3 production is devoted to further processing into a fertilizer, such as urea or ammonium nitrate, while for the resting part it is employed as a working fluid or fuel in energy systems [22]. As explained in Chapter 1, conventional NH_3 production is carried out through the Haber-Bosch process, which involves H_2 production from a two-step methane reforming (first steam reforming and then autothermal reforming), syngas conditioning by high temperature and low temperature water gas shift, CO_2 absorption with amines and methanation. Nitrogen production is instead carried out in an ASU. The core of the plant is the NH_3 synthesis reactor, a three-bed quench converter operating at high pressure and temperature, generally 200 bar and 400 - 500 °C. The product gases are sent to a refrigeration station for NH_3 condensation and subsequent separation. Alternative NH_3 production processes can be grouped in two main routes: the biomass to NH_3 [23–25] and the power to NH_3 [26]. In the first solution, biomass is transformed into a syngas (principally composed of H_2, CO and CO_2) by gasification, which is then filtered and sent to water gas shift (WGS) units for conditioning and H_2 intensification. In the power to NH_3 pathway, H_2 is produced in an electrolysis unit while nitrogen is produced in an air separation unit (ASU). In recent years, Japan has become highly involved in green NH_3 production processes, due to its lack of energy resources. The most relevant project is promoted by the Cross-Ministerial Strategic Innovation Program of Japan with the aim of investigating the use of H_2, NH_3 and hydrides [27]. In the US, the Department of Energy has commissioned the Advanced Research Project Agency-Energy to investigate the conversion of energy into energy-dense carbon-neutral liquid fuels. A total of 32.7 M$ are destined to 16 projects, of which 13 are NH_3-related [27]. In Europe, Yara, the second biggest NH_3 producer, will install and test a

new 5 GW alkaline water electrolyser to supply 1% of H_2 to their conventional NH_3 plant in Porsgrunn, Norway. In addition, an agreement has been signed for the development of a first large-scale Power-to-Ammonia plant based on hybrid PV-wind power supply in Saudi Arabia [28]. Finally, the HØST PtX project in Esbjerg, Denmark, will power 1 GW electrolyser [29] and a conventional NH_3 plant through solar and wind technologies, leading to the production of about 600 kt/y of NH_3 [30].

6.1.2 Methanol and ammonia synthesis with chemical looping technology

As explained in previous Chapters, the three reactors chemical looping cycle (TRCL) is a process aiming at H_2 or syngas production. In that system the oxygen carrier is involved in three reaction steps: reduction, H_2/syngas production and oxidation [31]. The first step is endothermic, and it is conventionally performed with a fuel. The last two steps involve H_2 production from steam in an exothermic reaction and the oxygen carrier oxidation with ambient air, respectively. The main products of this process are CO_2 and H_2O from the reduction step, H_2 and H_2O from the H_2 generation step, and N_2 from the oxidation step. Since these gas species are the reactants of important chemical products (CH_3OH from H_2 and CO_2 and/or NH_3 from H_2 and N_2), their availability for further processing and the simultaneous CO_2 separation make chemical looping an attractive technology also in the chemical industry. In the literature several configurations propose CH_3OH production from chemical looping gases. In [32], Spallina et al. calculate that CH_3OH production from a chemical looping reforming plant provides 17-20% lower production cost than the conventional process, though the production efficiency is reduced by 4%. In [33], Yang et al. combine the three reactors chemical looping with CH_3OH synthesis from coal and coke oven gases observing reduced investment and production costs (by 23.3% and 7.5%, respectively) compared to the conventional process. Moreover, the internal rate of return (IRR) of the novel process increases by 9.1%, while the specific greenhouse emissions decrease from 2.86 to 0.78 $kg_{CO2equiv}/kg_{CH3OH}$. In [34], Sun et al. perform techno-economic analysis on the production of CH_3OH from algae with the two-step chemical looping combustion and with the three reactors chemical looping technology. The two configurations show similar global energy and exergy efficiencies of about 60%, while the three reactors configuration is more economically competitive in terms of levelized cost of CH_3OH, net present value (NPV), IRR and dynamic payback period (PBP).

Regarding NH_3 production from chemical looping processes, in [35] Pereira et al. consider a three-step chemical looping reforming cycle in which the oxygen carrier is first oxidized by air, providing a pure N_2 stream (with other gases in traces), undergoes reduction with low grade fuel gases separated in the process, providing CO_2 and H_2O at the outlet, and finally it catalyses methane reforming. The process provides 19% lower capital costs compared to the conventional configuration and a lower production cost. A negative CO_2

emissions avoidance cost of -5 $/t$_{CO2}$ is also computed. In [36], Miyahira et al. investigate NH_3 production from the three reactors chemical looping cycle with rice husk according to three possible configurations: direct chemical looping of rice husk with (1) H_2O or (2) CO_2 enhancers, (3) chemical looping of syngas from rice husk gasification. The effect of several process parameters such as reactor temperature, pressure, oxygen carrier flow rate and gas enhancer flow rate has been investigated and maximum H_2, NH_3 and power efficiencies of 51.8%, 38.09% and 0.65% have been found, respectively. In [37], Edrisi et al. consider a three reactors chemical looping cycle for NH_3 production and subsequent processing to urea by reaction of NH_3 with separated CO_2. An IRR between 11% and 60% is computed for the plant according to the considered scenario, making it an interesting and economic valuable solution for further research. In [38], Zhao et al. combine NH_3 and CH_3OH synthesis from coke oven gases and pulverised coal in a TRLC plant. The cogeneration of NH_3 and CH_3OH contributes to reduce the dependency on market fluctuation of each fuel. By utilizing 0.576 Mt/y of coke oven gases and 0.175 Mt/y of pulverized coal a final CH_3OH and NH_3 production of 0.44 – 0.86 Mt/y and 0 – 0.36 Mt/y, respectively, is achieved with an optimal H_2 utilization of 88.8%.

6.1.3 Objective of the study

Chemical looping can actively contribute to a more sustainable and carbon neutral society by intrinsically separating the CO_2 and the N_2 content from fuel oxidation. Furthermore, the combination of exothermic and endothermic reactions in the loop allows for autothermal operation of the chemical looping section. In this way, differently from the conventional syngas production where flue gases require further processing for CO_2 separation, the CO_2 content can be directly converted in an added value chemical or sent to permanent storage without further energy penalty for its separation or plant engineering complication.

The objective of this work is to analyse the techno-economic feasibility of a novel process for the sustainable and simultaneous production of CH_3OH and NH_3 from chemical looping gases. The combined production of two fuels represents an added value of this research, reducing the dependency on market prices fluctuations and at the same time optimising the chemical looping gases utilization. To the author's best knowledge, no works have presented and thoroughly analysed the combined production of these two high value chemicals through chemical looping processes. Detailed Aspen Plus simulations are carried out on the whole system. Recycled high density polyethylene (HDPE) is used as an innovative fuel in the chemical looping plant to promote the carbon circularity of the process. Preliminary sensitivity analyses on the effect of several parameters (the oxygen carrier inlet temperature to the fuel and steam reactors, the fuel flow rate to the fuel reactor and the steam flow rate to the steam reactor) are carried out to determine the optimal combination for maximising conversion through the chemical looping cycle. Efficiency and

environmental parameters are evaluated and compared with conventional and alternative production pathways. Subsequently, a series of sensitivity analyses are carried out to assess the effect on the levelized cost of electricity, the electrolytic oxygen selling price, the IRR and the cost of the electrolyser. Finally, a comparison with the selling prices from the conventional and green pathways is presented.

6.2 Materials and method

The proposed system is fully modelled with Aspen Plus V.11. The Redlich-Kwong-Soave equation of state with the Boston-Mathias correction is adopted to model the TRCL section, including the downstream processing, while for the NH_3 and CH_3OH synthesis plants the Redlich-Kwong-Soave model and the Redlich-Kwong-Soave with modified Huron-Vidal mixing rule model are used. The ambient air composition is assumed as 78.896% N_2, 21.00% O_2 and 0.004% CO_2 in volume. Pulverised high-density polyethylene is modelled as an Aspen Plus non-conventional component according to the specifications in Table 6.1.

Table 6.1. HDPE proximate and ultimate analysis [39]

Proximate [wt%]		Ultimate [wt%]		Sulphur [wt%]	
Moisture	0.25	C	78.18	Pyritic	0
Fixed carbon	0.55	H	12.84	Sulphate	0
Volatile matter	94.77	N	0.06	Organic	100
Ash	4.98	Cl	0		
		S	0.08		
		O	3.86		

6.2.1 Plant layout

The proposed process is composed of four main sections:

- the Three Reactors Chemical Looping plant (TRCL);
- the HRSG section with flue gas desulphurization and carbon capture units;
- the CH_3OH synthesis plant;
- the NH_3 synthesis plant.

The main material and energy flows in the system are synthetically represented in Figure 6.1.

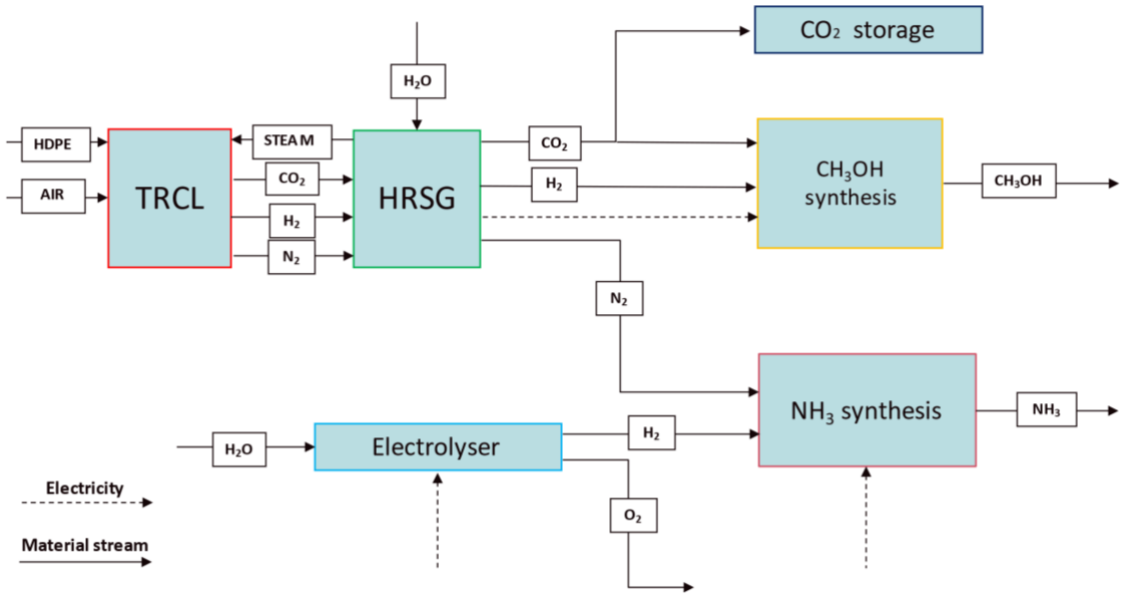

Figure 6.1. Schematic layout of the proposed plant

Pulverised high-density polyethylene is injected in the fuel reactor (FR) of the chemical looping plant as a reducing agent. Water steam from the HRSG is converted to H_2 in the steam reactor (SR), while air is injected in the air reactor (AR) to fully oxidize the oxygen carrier. The CO_2 produced in the fuel reactor and the H_2 from the SR are recovered and sent to the CH_3OH synthesis plant. To avoid the sulphur poisoning of the CH_3OH catalyst, a SO_2 removal unit is added before the CH_3OH synthesis plant. The exceeding part of the CO_2 is sent to storage. The depleted air stream coming from the air reactor unit is sent to the NH_3 plant, where it is mixed with H_2 produced from water electrolysis. Since the off-gases leaving the TRCL plant are at high temperature and pressure conditions, a HRSG section is located downstream, where steam at different pressure levels is produced and expanded in a turbine group for power production. In this way, part of the electricity demand is produced internally, while the remaining energy demand is satisfied by renewable energy sources. Compared to a traditional CH_3OH and NH_3 plant, the implementation of chemical looping hydrogen production simplifies the engineering application because it does not involve the ASU, the reforming section, the water gas shift and the CO_2 capture units. However, it is beyond the scope of this work to consider a system of buffers for H_2, CO_2 and N_2, suitably sized through a time-resolved model, to couple the renewable energy supply with the system.

6.2.2 TRCL section modelling

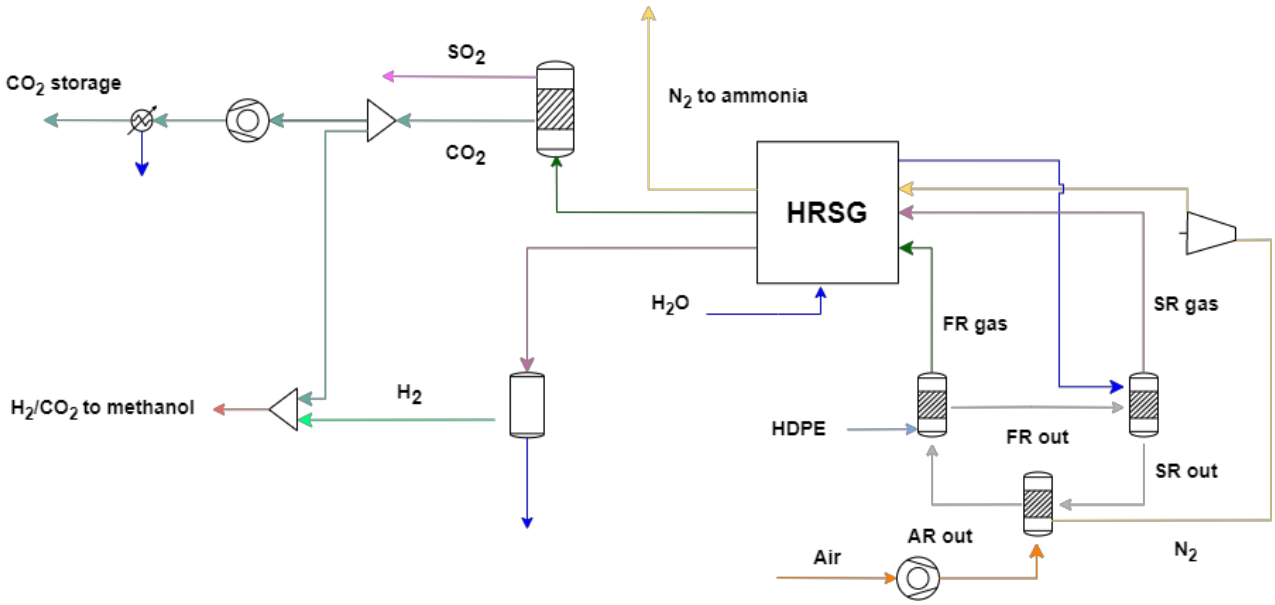

Figure 6.2. Simplified process flowsheet diagram (PFD) of the TRCL plant, the HRSG section and the CO_2 storage section

The PFD for the TRCL plant is displayed in Figure 6.2. The TRCL plant is modelled in Aspen Plus as an open cycle for simplicity. Iron oxides are selected as oxygen carriers, due to their low cost, high availability, and environmentally friendly nature [40]. However, support is necessary to ensure higher cyclability, thermal stability and autothermal operation in the reactors. A final composition of 30% wt iron oxide (Fe_2O_3/FeO) and 70% wt magnesium aluminate ($MgAl_2O_4$) is selected from other literature works [41,42]. The mechanism of the reduction process is not trivial since iron has different oxidation states and can produce many oxides, such as hematite (Fe_2O_3), magnetite (Fe_3O_4), and wustite (FeO). The reaction pathway across the chemical looping cycle is summarised in Table 6.2 [43]. In the fuel reactor, waste plastic undergoes thermal decomposition, gas-solid reaction with the volatiles (CO and H_2) and full fuel oxidation by solid-solid reaction with the oxygen carrier, while the inorganic content of the plastic is converted into ashes. The fate of the ashes has not been considered. Subsequently, in the steam reactor high purity H_2 is produced with Fe_3O_4 formation. Finally, oxidation with ambient air in the AR closes the loop and Fe_2O_3 is regenerated.

Table 6.2. Reaction scheme of the chemical looping section [43]

Reactor	Reactions	$\Delta H_{25°C}$ [kJ/mol]
	$HDPE \rightarrow Char + Volatiles + Ashes$	< 0
FR	$CO + 3Fe_2O_3 \rightarrow 2Fe_3O_4 + CO_2$	-48.27
	$H_2 + 3Fe_2O_3 \rightarrow 2Fe_3O_4 + H_2O$	-7.11

	$CO + Fe_3O_4 \rightarrow 3FeO + CO_2$	21.78
	$H_2 + Fe_3O_4 \rightarrow 3FeO + H_2O$	62.94
	$CO + FeO \rightarrow Fe + CO_2$	-10.95
	$H_2 + FeO \rightarrow Fe + H_2O$	30.21
	$C + 3Fe_2O_3 \rightarrow 2Fe_3O_4 + CO$	124.19
	$C + Fe_3O_4 \rightarrow 3FeO + CO$	194.24
	$C + FeO \rightarrow Fe + CO_2$	-121.48
SR	$3FeO + H_2O \rightarrow Fe_3O_4 + H_2$	-62.94
	$Fe + H_2 \rightarrow FeO + H_2O$	-513.87
AR	$4FeO + O_2 \rightarrow 2Fe_2O_3$	-562.84
	$4Fe_3O_4 + O_2 \rightarrow 6Fe_2O_3$	-469.44

An oxygen carrier mass flow rate of 22.1 t/h ensures full fuel combustion and prevents methane formation in the SR. The inlet temperature of the oxygen carrier to the FR is fixed to 930 °C, which guarantees the same temperature both at the outlet of the AR and at the inlet of the FR, i.e. closed cycle and autothermal operation. This is possible because the two exothermic reactions occurring in the SR and in the AR balance the endothermicity of the reaction occurring in the FR. All three reactors are modelled as fully adiabatic and without thermal losses, while pressurized operation is imposed according to typical literature values [42]. The FR and SR are modelled as moving bed reactors by using a series of five adiabatic RGIBBS reactors in counter-current configuration, as often found in the literature [34], [36], [44–47]. Moving bed configuration ensures a lower OC flow rate to fully oxidize the same amount of fuel compared to a fluidized bed configuration and can reach higher reaction extents of the iron oxides. Various studies in the literature have demonstrated that the counter-current moving bed configuration ensures a lower oxygen carrier flow rate [48]. The moving bed model validation is presented in Figure E1 and Table E1 of Appendix E. For the AR, a single adiabatic RGIBBS reactor is considered sufficient to reproduce fluidized/entrained bed conditions occurring in a riser [49]. The steam flow rate at the inlet of the SR is entirely produced in the HRSG, while the ambient air mass flow rate in the AR is tuned to reach high purity N_2 requirements for the NH_3 synthesis. A summary of the main thermodynamic conditions of the TRCL plant model is reported in Table 6.3.

Table 6.3. Specifications and assumptions for the TRCL plant modelling

Fe_2O_3 to FR	22062 kg/h
CL reactors pressure	AR-16 bar, FR-20 bar, SR-18 bar
CL reactors thermal	Adiabatic
NR. of Gibbs reactors	SR and FR – 5; AR – 1

Steam flow rate into SR	1009 kg/hr
Air flow rate in AR	1050 kg/hr
HDPE flow rate in FR	180 kg/hr
Compressor efficiency	0.98 mechanical; 0.85 isentropic

6.2.3 HRSG section modelling

The PFD of the HRSG section is displayed in detail in Figure E2 of Appendix E. The temperature and pressure values for the HRSG section modelling are taken from the work by Mansouri et al. [50]. Specifically, three nominal pressure levels are considered: high (136.2 bar), medium (11.7 bar) and low (3.447 bar). The HRSG unit is modelled following the scheme proposed by Chiesa et al. [41], where two different recovery units are proposed. The heat exchange between steam and exhaust gases coming from the CL plant is modelled using a total of eight heat exchanger units. The flows leaving the FR and SR and the flow leaving the AR exchange heat with the high and the intermediate-pressure section, respectively. The low-pressure section is doubled, so that all the tree streams leaving the reactors can exchange their duties at low temperature. Only the low- and high- pressure steam turbines groups are present, since steam at 20 bar is fed to the SR. To correctly reproduce the heat exchange with the FR and SR gases, the Aspen MHeatX block is used since it can simulate the exchange of heat between more than two streams (SHIP, SHHP, ECHP, EVLP, ECLP). On the contrary, a simple HeatX block is used for the heat exchange with the AR gases (IPEC, IPEV, IPSH, LPEV, LPEC, LPSH). The thermodynamic parameters for the heat exchange section modelling are reported in Table E2 of Appendix E.

6.2.4 SO_2 removal and CO_2 storage sections modelling

Before the CH_3OH synthesis plant, the gases from the HRSG section are subjected to a process of sulphur abatement, carried out by the wet flue gas desulphurization (FGD) system, to prevent the $Cu/ZnO/Al_2O_3$ catalyst poisoning. The FGD unit is simulated with a SEP unit and a complete SO_2 removal is assumed. Other sulphuric species such as H_2S are present in traces in the TRCL exhaust gases. After the desulphurization and the liquid water removal, the resulting gas stream is composed of high purity CO_2 which is subsequently split in two other streams: one is mixed with the H_2 coming from the SR, the other is compressed in a train of three intercooled compressors (40 bar, 60 bar and 80 bar) up to 80 bar and sent to permanent storage. The PFD of the CO_2 compression and storage unit is displayed in the red area of Figure E2 of Appendix E.

6.2.5 Methanol synthesis modelling

Methanol synthesis is carried out with H_2 and CO_2. The three main reactions considered for CH_3OH production are reported in Eqs. (6.1) to (6.3) [51]. The system can be described using

either the first and the third equations or the second and the third one [34], since they are independent between each other.

$$CO_2 + 3H_2 \rightleftharpoons CH_3OH + H_2O \qquad (\Delta H_{298\,K} = -40.9\ kJ/mol) \tag{6.1}$$

$$CO + 2H_2 \rightleftharpoons CH_3OH \qquad (\Delta H_{298\,K} = -90.7\ kJ/mol) \tag{6.2}$$

$$CO_2 + H_2 \rightleftharpoons CO + H_2O \qquad (\Delta H_{298\,K} = 49.8\ kJ/mol) \tag{6.3}$$

The PFD of the CH_3OH synthesis plant is represented in Figure 6.3.

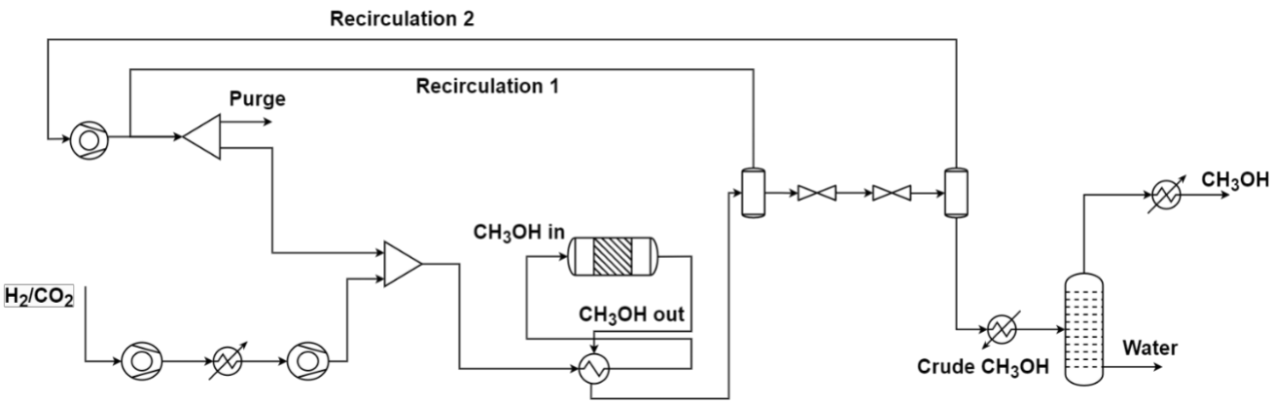

Figure 6.3. PFD of the CH_3OH synthesis plant

The gas stream coming from the HRSG unit is compressed in a train of intercooled compressors from the initial 18 bar to 80 bar. The resulting gas stream is then mixed with the recirculation flow of the non-reacted gases and heated to 250 °C. CH_3OH production is simulated with an isothermal RPLUG reactor operating at 250 °C and 80 bar. The reactor is designed with 7 tubes of 8 m length and 0.11103 m diameter [2] providing a gas space hourly velocity of about 10000 h^{-1}, as for commercial plants reactor [52]. The pressure drops are evaluated using the Ergun formula by imposing a pressure drop scaling factor of 1 and surface roughness of $4.572 \cdot 10^{-5}$ m. Regarding the $Cu/ZnO/Al_2O_3$ catalyst, the density is set to 1.5607 g/cm^3 with a particle diameter equal to 4.8 mm [12] and a bed void fraction equal to 0.42. The kinetics from Van den Bussche and Froment [53] model is implemented in the reactor model according to Eqs. (6.4) and (6.5).

$$r_{CH3OH} = \frac{k_1 p_{CO_2} p_{H_2} - k_2 p_{CH_3OH} p_{H_2O}/p_{H_2}^2}{\left(1 + K_1 p_{H_2O}/p_{H_2} + K_2 p_{H_2}^{0.5} + K_3 p_{H_2O}\right)^3} \quad \left[\frac{kmol}{kg_{cat} s}\right] \tag{6.4}$$

$$r_{RWGSR} = \frac{k_3 p_{CO_2} - k_4 p_{CO} p_{H_2O}/p_{H_2}}{\left(1 + K_1 p_{H_2O}/p_{H_2} + K_2 p_{H_2}^{0.5} + K_3 p_{H_2O}\right)} \quad \left[\frac{kmol}{kg_{cat} s}\right] \tag{6.5}$$

Where:

- p_i is the partial pressure of the i-th species;
- k_1, k_2, k_3, k_4, K_1, K_2, K_3 are the kinetic and adsorption constant, which are expressed as $\ln(k) = A + \frac{B}{T}$

The kinetic parameters values are taken from [54]. After leaving the MS reactor, the flow is sent to a cooler where the temperature drops to 30 °C and then is sent to a flash drum (30 °C and 65 bar), where most of the non-reacted gases is separated and recirculated to the reactor. The resulting liquid stream is then sent to two lamination valves for pressure reduction: the first one reduces pressure to 25 bar and the second to 14 bar. After lamination, the flow is sent to a second flash where pressure is set to 0.2 bar. The gases separated in the second flash drum are subsequently compressed to 80 bar and then recirculated. To ensure a low concentration of undesired components, a purge of 6% is set before mixing with fresh reactants and used for heat supply to the heaters. The liquid flow leaving the second flash is then heated to 85 °C and sent to a distillation column for CH_3OH and liquid water separation. A summary of the main parameters of the CH_3OH reactor and distillation column is reported in Table 6.4.

Table 6.4. Main modelling parameters of the CH_3OH reactor and the distillation column

MS reactor	250 °C, 80 bar; RPlug with 7 tubes of 8 m length and 0.11103 m diameter; catalyst: $Cu/ZnO/Al_2O_3$ with 1.5607 g/cm^3 density, 4.8 mm particle diameter and 0.42 bed void fraction; pressure drops with Ergun formula
Distillation column	20 stages [36]; Total condenser pressure, 1 bar; Reflux ratio 1.98; Distillate to feed ratio 0.44

6.2.6 Ammonia synthesis modelling

The PFD of the NH_3 production plant is shown in Figure 6.4.

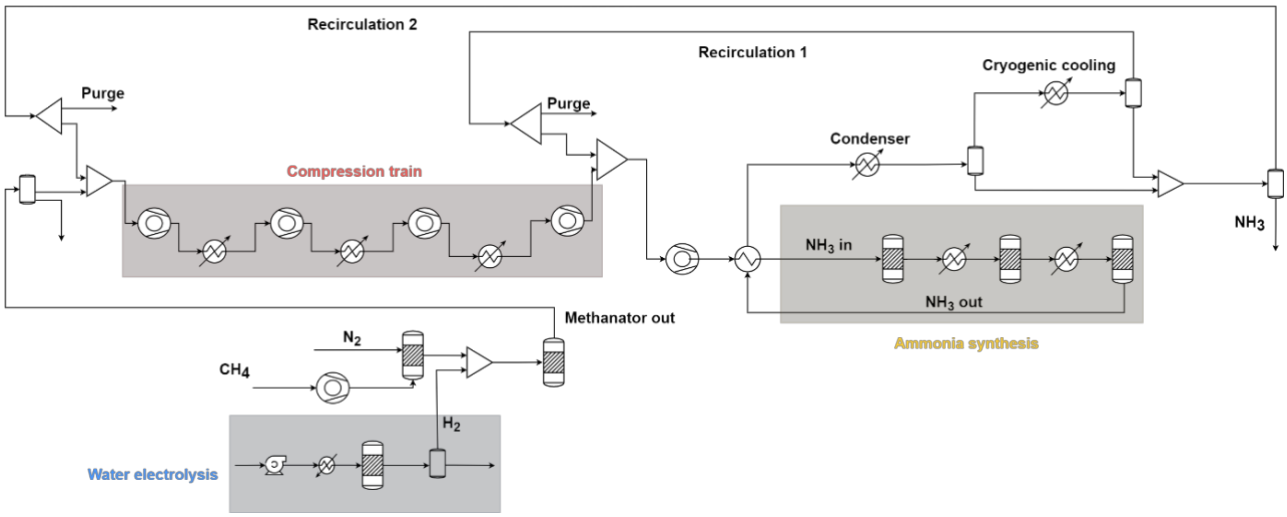

Figure 6.4. PFD of the NH_3 production plant

In this plant, H_2 production is carried out by water electrolysis. The electrolyser section is modelled with an RStoic unit. An alkaline electrolyser is selected due to its low temperature operation and its high technology readiness level. The electrolyser working temperature and pressure are set to 70 °C and 10 bar. The reaction conversion is set to 0.98. The water flow rate is evaluated to produce enough H_2 flow rate to react with the N_2 flow rate from the TRCL. After mixing with N_2, the H_2 stream is sent to a methanation unit for CO_2 removal, as industrially practiced in conventional ammonia plants [35]. Water from methanation is separated through molecular sieves or adsorption. The methanator is simulated with an RStoic block performing the reactions in Eqs. (6.6) and (6.7):

$$CO_2 + 4H_2 \rightarrow CH_4 + 2H_2O \tag{6.6}$$

$$CO + 3H_2 \rightarrow CH_4 + H_2O \tag{6.7}$$

The fractional conversion of CO_2 and CO is set to 1 for simplicity. The gases leaving the methanation unit are subsequently mixed with the recirculation stream and then sent to a train of five intercooled compressors to achieve a final pressure of 200 bar. Between the fourth and the fifth compressor, the fresh reactants stream is mixed with a second recirculating stream. Before entering the NH_3 reactor, the inlet gases exchange heat with the products of the reactor, which are then cooled down to 25 °C. The three-stage fixed catalytic bed reactor for NH_3 synthesis is simulated with a series of three adiabatic RGibbs reactors with intermediate cooling. The inlet temperature to each subsequent catalytic bed is fixed to 380 °C, 420 °C, 400 °C as reported in [35]. The final products are separated as follows: a first separation at high pressure condition is carried out in an adiabatic flash drum and then, since the separated gases are still rich in NH_3, cryogenic cooling to -25 °C is performed for

further flash separation. The two liquid phases from the flash drums are finally mixed and sent to a third flash separator operating at 18 bar and adiabatic condition. The separated gases are recirculated to the reactor. To maintain a low methane concentration in the reactants, a 4% purge is inserted on both the recirculating gas streams. A summary of the main thermodynamic conditions is reported in Table 6.5.

Table 6.5. Main thermodynamic conditions of the NH_3 synthesis plant

Block	Temperature [°C]	Pressure [bar]
Compressor	Isentropic	40, 80, 120, 160, 200
Electrolyser	70	10
Methanator	250	16
Preheating of the reactants	380	198
NH_3 reactors - Gibbs 1, 2 and 3	Adiabatic	193, 189, 187.3
Reactor cooling - 1, 2	420, 400	193, 189
Flash drum 1, 2 and 3	Adiabatic	183, 180, 18
Cooler after first separator	-25	180

6.2.7 Capital cost analysis

The purchased equipment cost C_p^0 is calculated for each component according to the polynomial cost functions in Eq. (6.8) provided by Turton et al. [55]

$$\log_{10}(\mathrm{Cp}^0) = \mathrm{K}_1 + \mathrm{K}_2 \cdot \log_{10}(\mathrm{A}) + \mathrm{K}_3 \cdot \log_{10}(\mathrm{A})^2 \tag{6.8}$$

Where:

- A is the capacity or size parameter;
- K_1, K_2 and K_3 are three correlation coefficients provided by Turton.

A correction is applied according to Eq. (6.9) when the size of the units is below the minimum value (S_{min}) indicated by Turton.

$$\mathrm{Cp}^0_{2022} = \mathrm{Cp}^0 \cdot \left(\frac{S}{S_{min}}\right)^{0.6} \tag{6.9}$$

In order to consider the effect of inflation, the purchased equipment cost is scaled to reference year (2020) with the Chemical Engineering Plant Cost Index (CEPCI).

$$\mathrm{Cp}^0_{2022} = \mathrm{Cp}^0 \cdot \left(\frac{\mathrm{CEPCI}_{2020}}{\mathrm{CEPCI}_{2002}}\right) \tag{6.10}$$

To account for different operating pressures and different materials employed for each component, the Bare Module Cost (BMC) is computed through Eq. (6.11).

$$BMC = C_P^0 \cdot F_{BM} = C_p^0 \cdot (B_1 + B_2 \cdot F_p \cdot F_M) \tag{6.11}$$

Where:

- F_{BM} is the bare module cost factor;
- B_1, B_2 are the bare module factors provided by Turton, function of the type of equipment;
- F_M is the material factor;
- F_p is the pressure factor, which accounts for the maximum pressure in the units.

Whenever a cooler is sized, the shell and tube configuration is selected with cooling water in the shell at 15 °C and 1 bar conditions. In the NH_3 plant, when the maximum gauge pressure is above 140 bar, a spiral tube heat exchanger configuration is used. The outlet temperature of the cooling water is always checked to be lower than 35 °C. Three cooling towers (one for each plant) are included to cool back the water to 15 °C.
Three possible cost scenarios are considered for the bare erected cost determination (BEC), i.e. optimistic, realistic, and pessimistic [12]. For the operating units with a high complexity level, such as the chemical looping reactors, the HRSG unit, the CH_3OH reactor etc., the BEC is evaluated by scaling according to Eq. (6.12).

$$BEC = BEC_{ref} \cdot \left(\frac{CEPCI_{2020}}{CEPCI_{ref}}\right) \cdot \left(\frac{A}{A_{ref}}\right)^m \tag{6.12}$$

Where:

- The BEC_{ref} is the bare erected cost taken from the literature for a reference unit;
- A is the capacity or size parameter of the component/unit under analysis;
- A_{ref} is the capacity or size parameter of the reference component/unit;
- m is a constant exponent taken from the literature for each component.

If no data are available from the literature, an exponent m equal to 0.6 is considered [56]. The reference values employed for the Total Overnight Cost (TOC) calculation are collected in Table 6.6. Whenever the reference costs taken from the literature corresponds to the BMC, the BEC is mathematically obtained by using the percentage values in Table 6.6.

Table 6.6. TOC estimation according to three scenarios [12,57]

Parameter	Optimistic	Realistic	Pessimistic
BMC_{main}	71.2%	68%	63.1%

Pipes, vales and fittings	18.0%	20.0%	23.0%
Process instruments and control	6.3%	7.0%	8.1%
Electric equipment and materials	4.5%	5.0%	5.8%
BMC_{tot}	100%	100%	100%
BMC_{tot}	71.2%	68%	63.2%
Erection and installation labour	21.6%	24%	27.6%
Buildings, materials, and labour	7.2%	8%	9.2%
BEC	100%	100%	100%
EPC contractor services (%BEC)	8.5%	10%	15%
Project and Process contingencies, PPC (%(BEC+EPC))	13.5%	20%	20%
Total Plant Cost (TPC)	BEC + EPC + PPC	BEC + EPC + PPC	BEC + EPC + PPC
Other owner's costs, OC (%TPC)	13.5%	15%	20%
TOC	TPC + OC	TPC + OC	TPC + OC

6.2.8 Operating cost analysis

A plant lifetime of 25 years is assumed with 85% capacity factor and 4 years of construction. The fixed operating costs are limited to the maintenance and insurance costs, which are evaluated as 2.5% and 1% of the TOC [58], respectively. Therefore, the administrative salaries and property rent cost voices are neglected. On the other side, the variable operating costs include:

1. The cost of the oxygen carrier make-up, evaluated by linearly scaling the literature data in [59];
2. The cost of the HDPE [60];
3. The water supply to the TRLC plant, the electrolyser and the make-up to the cooling towers (4% of the nominal water flow rate);
4. The FGD unit operating costs in terms of water and gypsum [61];
5. The CH_3OH ($Cu/ZnO/Al_2O_3$) and NH_3 (Fe) reactors catalyst replacement;
6. The alkaline electrolyser replacement. The electrolyser must be replaced in the 11th and in the 21st year of operation [62] with replacement costs according to Eq. (6.13).

   $$OC_{10} = \frac{2(C_{BM,WE} \cdot 0.4)}{3} \quad (6.13)$$

   where $C_{BM,WE}$ is the bare module cost of the water electrolyser.

7. The net electric power requested by compressors, pumps, alkaline electrolyser (50 kWh/kg_{H2} [58]), cooling towers (0.7143 MW_{el}/MW_{th}, calculated from [63]) and the cryogenic plant (0.7143 MW_{el}/MW_{th}, calculated from [64]).
8. The carbon transport and storage costs and the carbon tax. Currently, the carbon tax values in Europe range from less than 0.001 €/kg_{CO2} in Poland and Ukraine to above 0.1 €/kg_{CO2} in Sweden, Liechtenstein and Switzerland [65].

The cooling water and cryogenic refrigerant initial inventory costs are neglected. The oxygen produced by the electrolyser is an important source of revenue and three possible prices are considered according to Battaglia et al. [12]:

- 0 €/kg (the oxygen is vented);
- 0.07 €/kg (the oxygen is liquefied);
- 0.15 €/kg (the oxygen is compressed up to 30 bar).

The costs to treat the oxygen are neglected. A specific cost of electricity of 0.03 €/kWh is assumed considering the electricity costs of the Announced Pledges Scenario in the World Energy Outlook by IEA for 2050 [66]. A summary of the specific costs assumed for the indicated voices is provided in Table 6.7.

Table 6.7. Summary of the specific operating costs

Description	Specific Cost (€/scale)	Scale	Reference
Oxygen carrier	1.87	kg_{Fe2O3}	[59]
HDPE	0.0206	kg_{HDPE}	[60]
Process water	6	m^3	[57]
Cooling water	0.35	m^3	[57]
Flue Gas Desulphurization	0.095	kg_{SO2}	[61]
Electrolyser replacement	Eq. 6.14[3]	-	[62]
CH_3OH catalyst[4]	30	$kg_{catalyst}$	[57]
NH_3 catalyst	0.0015 (calc)	kg_{NH3}	[35]
Electricity	0.03	kWh	[67]
Carbon transport and storage	0.02	kg_{CO2}	[57]
Carbon tax	0.1	kg_{CO2}	[57]

6.3 Key performance indicators (KPI)

6.3.1 Energy and environmental parameters

The process energy and environmental performances are evaluated through a set of parameters. The first principle efficiency of NH_3 (η_{NH_3}) and CH_3OH (η_{CH_3OH}) production are computed according to Eqs. (6.14) to (6.16) and subsequently compared with other alternative pathways retrieved from the literature:

[3] Total replacement cost of the electrolyser

[4] Replacement every 3 years

$$\eta_{CH_3OH} = \frac{LHV_{CH_3OH} \cdot \dot{m}_{CH_3OH}}{LHV_{HDPE} \cdot m_{HDPE}} \tag{6.14}$$

$$\eta_{NH_3} = \frac{LHV_{NH_3} \cdot \dot{m}_{NH_3}}{W_{electrolyser}} \tag{6.15}$$

$$\eta_{comb} = \frac{LHV_{CH_3OH} \cdot \dot{m}_{CH_3OH} + LHV_{NH_3} \cdot \dot{m}_{NH_3}}{LHV_{HDPE} \cdot \dot{m}_{HDPE} + W_{electrolyser}} \tag{6.16}$$

Where:

- LHV_i is the lower heating value of the products;
- $\dot{m}_i$ is the flow rate of each species;
- $W_{electrolyser}$ is the electric power required by the electrolyser and provided by renewable sources.

Similarly, the process energy intensity EI is expressed as the ratio of the global energy consumption of the plant to the flow rates of the main products (CH_3OH and NH_3).

$$EI = \frac{LHV_{HDPE} \cdot \dot{m}_{HDPE} + W_{net,elec}}{\dot{m}_{CH_3OH} + \dot{m}_{NH_3}} \quad \left[\frac{GJ}{t}\right] \tag{6.17}$$

Where:

- $W_{net,elec}$ is the gross electric power demand subtracted by the electricity production in the HRSG.

Finally, on the environmental side the specific CO_2 emissions (SC), the carbon capture ratio (CCR) and the carbon conversion (CC) are evaluated according to Eqs. (6.18) to (6.20).

$$SC = \frac{\dot{m}_{CO_2,emitted}}{\dot{m}_{CH_3OH} + \dot{m}_{NH_3}} \tag{6.18}$$

$$CCR = \frac{\dot{m}_{CO_2,captured}}{\dot{m}_{CO_2,emitted} + \dot{m}_{CO_2,captured}} \tag{6.19}$$

$$CC = \frac{\dot{n}_{CH_3OH}}{\dot{n}_{HDPE} \cdot x_C} \tag{6.20}$$

Where:

- n_{CH_3OH} and n_{HDPE} are molar flow rates;
- x_C is the fixed carbon molar content in plastic.

In this work, only the direct CO_2 emissions associated with the process are considered. They are computed by summation of the CO_2 flow rates in the flue gases provided by Aspen Plus. In this case, part of the CO_2 is stored, meaning zero direct CO_2 emissions, while the rest is involved in CH_3OH production. The only contribution to the direct CO_2 emissions corresponds to the combustion of purge gases in the CH_3OH synthesis plant. Zero direct emissions are assumed for the renewable energy supply [68]. The indirect CO_2 emissions associated with raw materials extraction or preparation are not included and will be the focus of another work.

6.3.2 Economic parameters

A summary of the financial assumptions is provided in Table 6.8.

Table 6.8. Financial assumptions for the techno-economic analysis

Reference year	2020
Plant lifetime	25 years
Construction Period	4 years
Discount rate	8%
Capacity factor	85%

The levelized cost of methanol and ammonia (LCOAM) is defined as the combined fuels specific cost that zeros the NPV assuming an IRR of 8%. Nevertheless, the LCOAM cannot be compared directly with the conventional fuel production prices. To have a reference value for the economic discussion, the separate levelized cost of methanol (LCOM) and ammonia (LCOA) are also computed by considering the other product as a secondary revenue with an arbitrary specific cost. Comparisons are carried out with literature works reporting techno-economic analyses on the conventional plants for CH_3OH and NH_3 synthesis with same economical and financial assumptions as those in Table 6.8. In addition, the economic analysis is completed by evaluating the IRR and the PBP according to Eqs. (6.21) and (6.22).

$$\mathrm{IRR} = i : \sum_{k=0}^{n_{life}} \frac{FCF_k}{(1+i)^k} = \mathrm{NPV} = 0 \tag{6.21}$$

$$\mathrm{PBP} = \min\left\{k \mid -\|\mathrm{TOC}\| + \sum_{k=1}^{n} FCF_k > 0\right\} \tag{6.22}$$

6.4 Results and discussion

6.4.1 TRCL plant sensitivity analysis

Preliminary sensitivity analyses concerning the main parameters of the chemical looping plant are carried out to assess the validity of the process design. In general, the sensitivity intervals for the analyses are calibrated to show each phenomenon until a saturation limit or a plateau is achieved. The effect of the steam flow rate on the gases and solids composition from the SR is investigated in Figure 6.5.

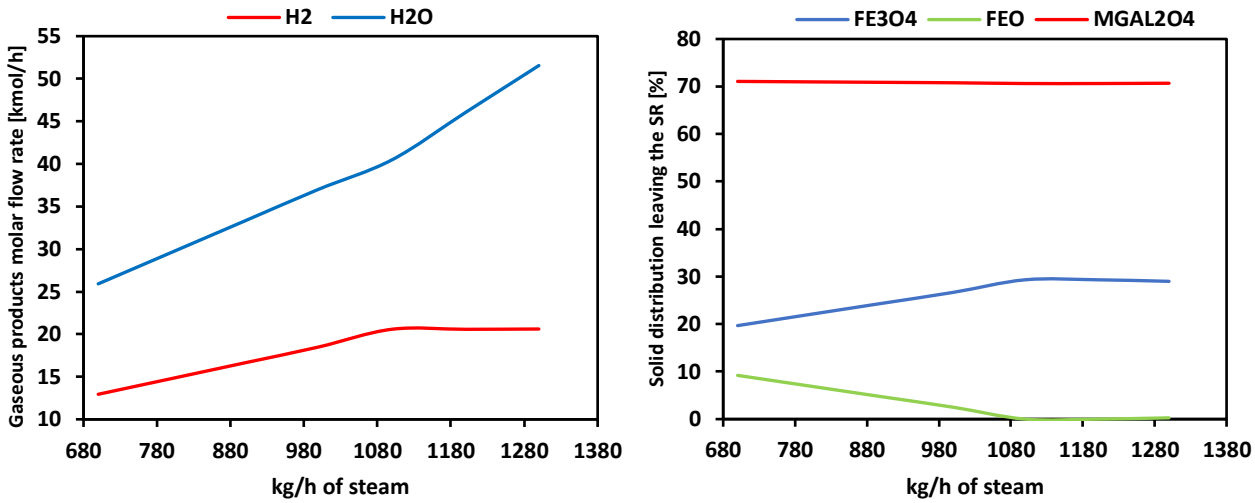

Figure 6.5. Effect of the steam flow rate on gases (left) and solids (right) composition leaving the SR

The analysis is conducted by varying the steam mass flow rate from 700 kg/hr to 1300 kg/hr, with a step of 100 kg/hr. The OC inlet temperature and flow rate are fixed to 840 °C and 21521 kg/hr, respectively. By increasing the steam flow rate, the H_2 production increases linearly up to about 1100 kg/h and then reaches a saturation limit, beyond which H_2 production is constant and unreacted water increases. Similarly, in Figure 6.5-right the oxidation of the iron oxides is shown to proceed for increasing steam flow rates until the saturation limit is reached, which corresponds to the complete oxidation of FeO to Fe_3O_4. Due to thermodynamic limitations, Fe_2O_3 formation cannot occur from FeO oxidation with steam. As expected, the support is not influenced by the increasing steam flow rate and the small detectable variation can be associated to the convergence error tolerance.

Two sensitivity analyses are then conducted on the FR to assess the influence of the fuel flow rate and of the oxygen carrier inlet temperature. In the first one, the HDPE flow rate is varied from 140 kg/hr to 240 kg/hr with a 20 kg/hr step, while the OC inlet temperature and flow rate are fixed to 930 °C and 22062 kg/hr, respectively. The resulting stream is principally composed of H_2O and CO_2, while other species such as CO, SO_2, H_2, N_2, H_2S and CH_4 are present in traces. As shown in Figure 6.6-left, considering low HDPE flow rates,

both steam and CO_2 grow linearly with an almost constant ratio of 1:1. From 180 kg/hr HDPE flow rate, a drastic reduction in CO_2 production is observed due to the inverse Boudard reaction among CO_2 and the accumulated carbon (C_s). The solids distribution in Figure 6.6-right shows that the iron oxides composition is significantly influenced by the fuel flow rate and in particular, between 140 kg/h and about 200 kg/h of HDPE, the oxygen carrier does not reach full reduction to FeO. Above 200 kg/h, the reduction step reaches completion with only FeO at the exit. By performing further simulations (not presented) it is observed that metallic Fe formation starts from around 320 kg/h of HDPE.

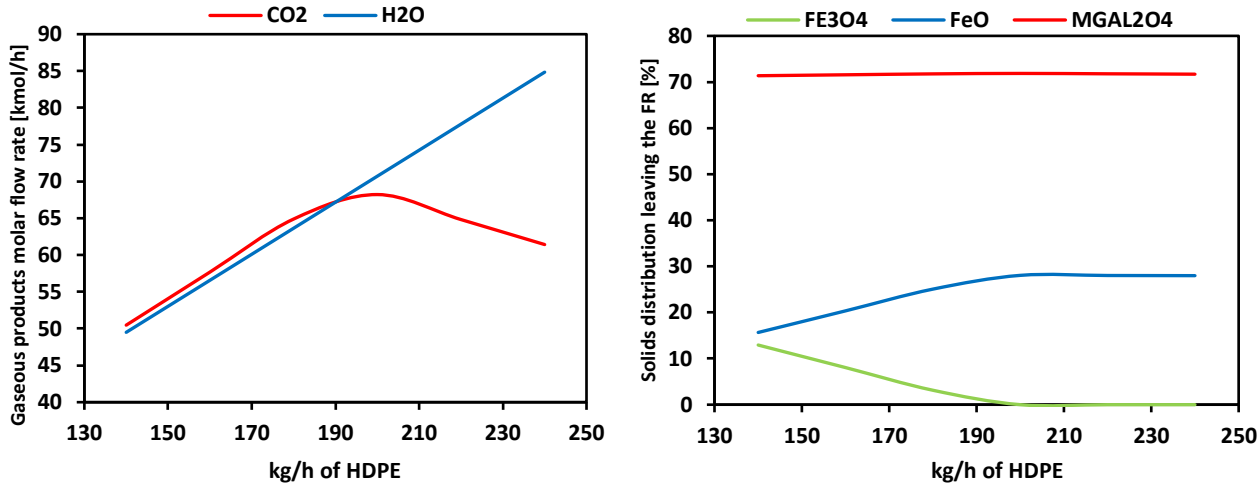

Figure 6.6.Effect of the HDPE flow rate on the gases (left) and solids composition (right) leaving the FR

Consequently, an HDPE flow rate of 180 kg/h can be considered optimal to ensure a deep reduction of the OC without intense carbon formation. The effect of the OC inlet temperature on the FR producibility is investigated in Figure 6.7. In this case, the flow rate of OC and HDPE are fixed to 22062 kg/hr and 180 kg/hr respectively, while the OC inlet temperature is varied from 730 °C to 1050 °C with a step of 40 °C. Between 730 °C and 900 °C, CO_2 production increases because a deeper reduction of the OC is achieved, as shown in Figures 6.7-a and 6.7-c. The steam molar flow rate in the off-gases is constant, indicating that the H_2 content of HDPE is more reactive than the carbon content and is immediately burnt. The solids distribution confirms that reduction continues up to about 860 °C and then is interrupted because a larger HDPE flow rate would be necessary to further reduce the iron oxides (Fe_3O_4 and FeO). This indicates that an inlet temperature above 900 °C ensures reduction of Fe_2O_3 to FeO with limited Fe_3O_4 residuals, as shown in Figure 6.7-b and 6.7-d.

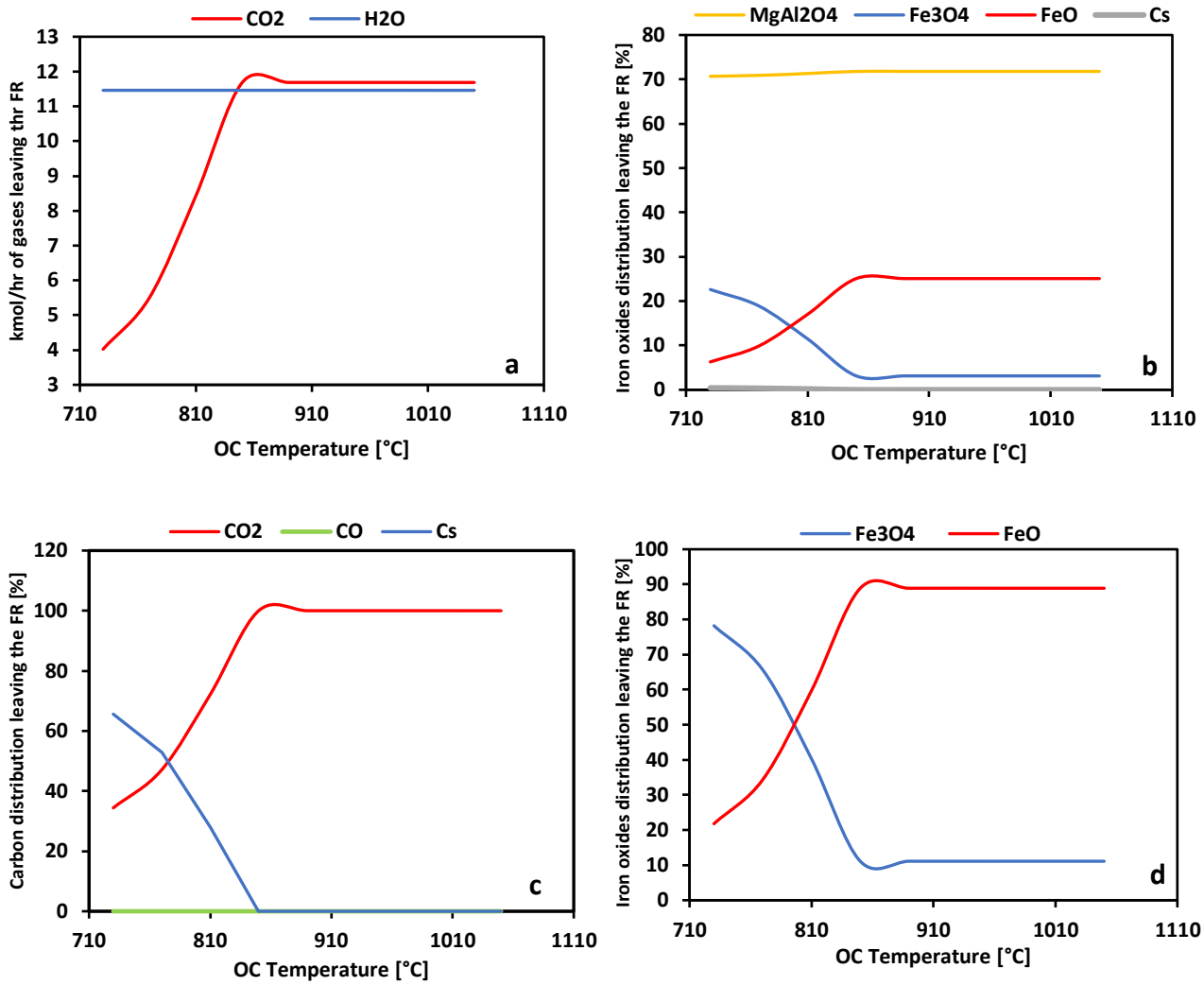

Figure 6.7.Effect of the OC inlet temperature on product gases distribution (a), total solids distribution (b), carbon distribution (c) and iron oxides distribution (d) leaving the FR

Finally, the effect of the OC inlet temperature on SR conversion efficiency is investigated in Figure 6.8. The OC flow rate is fixed to 21521 kg/hr, while 1009 kg/h of steam are injected at about 295 °C and 20 bar. In this case, since iron oxidation by H_2O is exothermic, lower temperatures promote H_2 production (Figure 6.8-left) and for an inlet temperature above 820 °C, unreacted FeO is detected in the solid distribution (Figure 6.8-right). Therefore, an

inlet OC temperature below 820 °C prevents FeO accumulation and increases H_2 production.

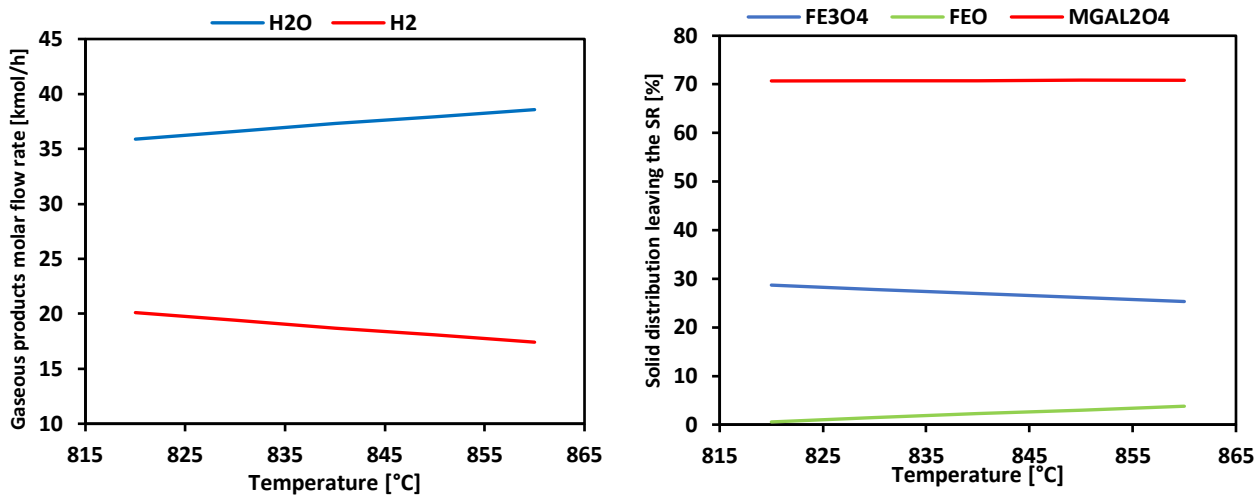

Figure 6.8. Effect of the OC inlet temperature on product gases distribution (left) and solids distribution (right) leaving the SR

6.4.2 Mass and energy balance results

In Table 6.9 the process main gas streams conditions are collected according to the nomenclature of Figures 6.2 to 6.4. More streams are collected in Tables E4 and E5 of Appendix E. Starting from the chemical looping plant, the gas flow leaving the FR is composed of 50.5% CO_2 and 49.5% H_2O with traces of other gases such as sulphur compounds and moisture. After the sulphur abatement and liquid water removal, part of the CO_2 content is used for CH_3OH production while the rest is compressed for storage or selling (final CO_2 purity of about 99.3% mol). On the contrary, the product gases leaving the SR are composed by 33% mol of H_2, with the remaining part being unreacted water. The steam conversion is limited by the relatively high temperature level occurring in the SR, being the reaction exothermic. The H_2 content of the gas stream is entirely employed for CH_3OH production and for this reason an alkaline electrolyser is present in the NH_3 plant. The purity of the N_2 leaving the AR is about 99.94% mol with the rest being CO_2 impurities that are converted to methane in the methanation reactor. The gas flow injected into the CH_3OH reactor is mainly composed of H_2 and CO_2, with a molar ratio (H_2/CO_2) of about 3.2 due to unreacted gases recirculation. The product stream leaving the reactor is at 250 °C and 79.59 bar due to pressure drops. The resulting single pass conversion of CO_2 is 20.2%, the CH_3OH yield is 19.98% and the CH_3OH selectivity is 98.9%. Crude CH_3OH leaves the distillation column with a total mass flow rate of about 174 kg/hr and a purity of 99.7% mol. On the other side, a final NH_3 production rate of about 910 kg/hr (99.9% mol purity) and a N_2 conversion per pass of 35% is achieved. A significant flow rate of oxygen is also produced

in the NH_3 plant by the electrolyser (1411.5 kg/hr). This is an important factor for the economic analysis of the plant since it represents a possible revenue.

Table 6.9. Main gas streams thermodynamic conditions

STREAM	P	T	$\dot{m}$	$\dot{N}$	Molar fraction									
	bar	°C	kg/hr	kmol/hr	CO_2	CO	H_2	H_2O	CH_3OH	NH_3	SO_2	N_2	O_2	CH_4
FR GAS	18	930	721.2	23.16	50.47	-	-	49.49	-	-	traces	traces	-	-
SR GAS	20	840.59	709.69	56.00	-	-	33.45	66.55	-	-	-	-	-	-
AR GAS	16	940.83	805.49	28.75	0.051	-	-	-	-	-	-	99.94	traces	-
CO_2 to storage	80	30	240.2	5.48	99.33	-	-	0.63	-	-	traces	0.033	-	-
N_2 to ammonia	16	626.45	805.49	28.75	0.051	-	-	-	-	-	-	99.94	traces	-
H_2/CO to methanol	18	83.30	325.48	25.70	24.26	-	72.88	2.85	-	-	-	-	-	-
CH_3OH in	80	250	1563.66	126.06	22.66	2.39	73.79	0.41	-	-	-	-	-	-
CH_3OH out	79.59	250	1563.66	114.65	19.88	2.68	66.15	5.76	5.43	-	-	traces	-	-
CH_3OH	1	25	173.86	5.42	0.23	-	-	traces	99.7	-	-	-	-	
NH_3 reactor IN	198	380	2635.95	306.59	-	-	74.21	-	-	1.01	-	24.70	-	0.081
NH_3 reactor OUT	187.3	467	2635.95	253.00	-	-	58.2	-	-	22.38	-	19.35	-	0.098
NH_3	18	13.90	909.77	53.43	-	-	0.045	-	-	99.91	-	0.031	-	-

In terms of energy flows, the electrolyser accounts for more than 90% of the global electricity consumption, as displayed in Table E6 of Appendix E. A part of the required electrical power is also internally produced by steam expansion from the HRSG. No thermal integration is carried out in the CH_3OH and NH_3 synthesis plants. An increase in first principles efficiency is expected by optimising the heating and cooling duties with pinch analysis or by the introduction of a steam cycle for each plant.

6.4.3 Energy and environmental parameters results

A comparison of the energy and environmental performance of the process is presented in Table 6.10. One alternative pathway for each product is considered: CH_3OH synthesis from amine absorption (ABS) of post-combustion gases and H_2 production from water electrolysis (EL) [12]; NH_3 synthesis with N_2 from air separation (ASU) and H_2 from water electrolysis [57]. The comparison shows that the process first principle efficiency is comparable with both the alternative pathways. For NH_3 synthesis the 5% difference in efficiency with the ASU+EL case can be attributed to the electrolyser efficiency choice and to small differences in the modelling. Similarly, the process energy intensity of 36.2 GJ/t_{prd} is intermediate between that of the ABS+EL and of the ASU+EL. Both the energy intensity and the first principle efficiency of this process are however not competitive with those of the benchmark plants, though the specific CO_2 emissions are significantly lower (0.017 kg_{CO2}/kg_{prd}) than the SMR-ATR (0.24 kg_{CO2}/kg_{CH3OH}) and NH_3 reference configurations (1.66 kg_{CO2}/kg_{NH3}). Compared to the ABS+EL and the ASU+EL routes, the CO_2 emissions are not zero and are associated to the purge gases combustion in the CH_3OH plant. Finally, as expected, the process is characterized by a high CR and a relatively low CC, since a significant part of the CO_2 content from the FR gases is sent to transport and storage.

Table 6.10. Energy and environmental efficiency comparison

Parameter	This work	CH_3OH (ABS+EL)	NH_3 (ASU + EL)	CH_3OH (SMR-ATR)	NH_3 (Ref.)
η_{CH_3OH} [-]	43.7%	42.5%	-	70.3%	65.5% [57]
η_{NH_3}[-]	55%	-	60%	-	-
EI $[GJ/t_{prd}]$	36.2	46.9	30.4	28	27.1
SC $[kg_{CO_{2,em}}/kg_{prd}]$	0.017	< 0	-	0.24	1.66
CCR [-]	93.1%	87%	-	-	-
CC [-]	46.4%	87%	-	-	-

6.4.4 Capital and operating cost analysis

The results of the capital cost analysis (TOC) are shown in Figure 6.9, divided according to the three cost scenarios.

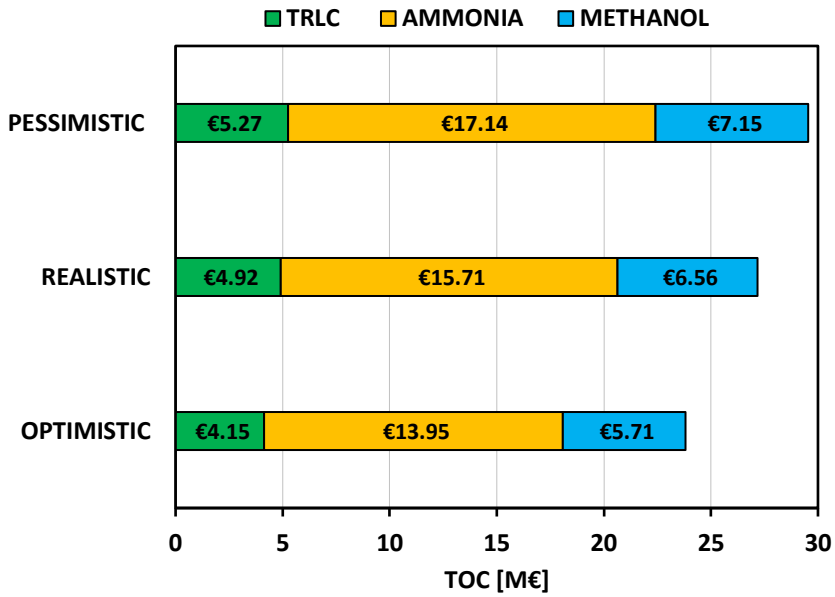

Figure 6.9: TOC in the three cost scenarios, i.e. optimistic, realistic, and pessimistic

The TRCL cost includes the cost of the HRSG, the FGD and the compression section for the carbon capture. In the optimistic scenario, the TOC amounts to about 27 M€ and increases to about 30 M€ in the pessimistic scenario. The major voice of cost is the NH_3 plant, since NH_3 production is dominant (910 kg/h) compared to the CH_3OH production of 174 kg/h. The cost allocation is such that:

- 18% is due to the TRCL section;
- 24% is due to the CH_3OH synthesis plant;
- 58% is due to the NH_3 plant.

On the operating costs side, the resulting OPEX cost (both fixed and variable) is about 3.1 M€/y. The energy source is the main voice of cost (68%), as evident in Figure 6.10. The second and third major cost voices are the maintenance cost (19%) and the insurance cost (8%). All the other voices, if combined, amount to only the 5%. For simplicity, the electrolyser replacement costs are annualized without considering any discount rate.

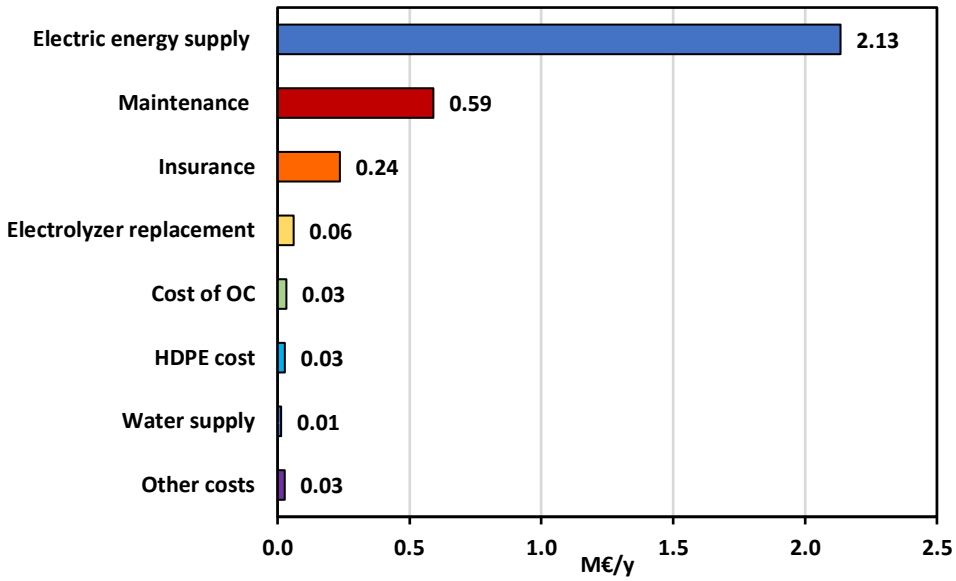

Figure 6.10: Operating costs breakdown

6.4.5 Economical sensitivities

Firstly, a sensitivity analysis is conducted to estimate the effect of different electricity costs on the LCOAM. In the following discussion, when not specified otherwise, the cost of oxygen is assumed equal to 0.07 €/kg. The results are displayed in Figure 6.11-left. The LCOAM linearly increases with the electricity cost from a minimum of 0.59 €/kg at 0.01 €/kWh to a maximum of 1.64 €/kg at 0.13 €/kWh. As previously stated, the electricity cost has an important impact on the final products cost due to the high energy demand of the electrolyser.

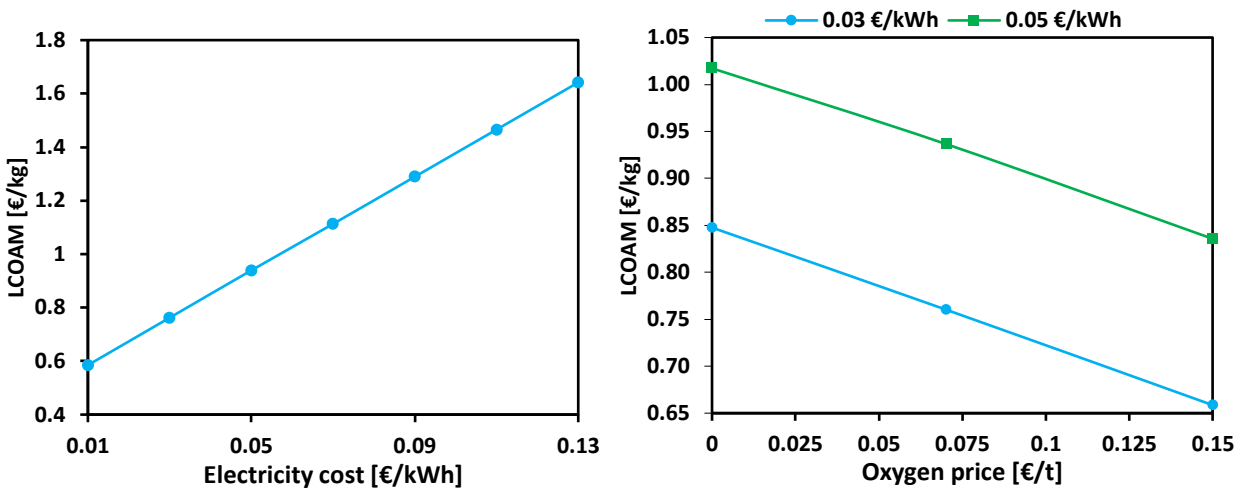

Figure 6.11: LCOAM variation with electricity costs (left) and with different oxygen selling prices (right)

On the other side, in Figure 6.11-right the effect of different oxygen selling prices is analysed. With a selling price of 0.15 €/kg and an electricity cost of 0.03 €/kWh, the LCOAM decreases by 13.4% to 0.66 €/kg. For higher electricity costs the effect of the oxygen selling price is analogous. The high cost (both capital and operational) of the alkaline electrolyser in the NH_3 plant is one of the most relevant drawbacks for the investment. Given the growing interest on this technology, it can be estimated that its capital cost will decrease overtime. To describe this decreasing cost trend, a learning curve has been proposed in the literature [69,70] according to Eq. (6.23).

$$C(t_2) = C(t_1) \cdot \left[\frac{V(t_2)}{V(t_1)}\right]^b \tag{6.23}$$

Where:

- $C(t_i)$ is the unit production cost at time t_i;
- $V(t_i)$ is the cumulative production volume at time t_i;
- b is the learning parameter, that can be evaluated from the learning rate (LR).

The learning rate (LR) is the percentual reduction of the cost of a single element once the production of the same technology is doubled and it is described by Eq. (6.24) [70].

$$LR = 1 - 2^{-b} \tag{6.24}$$

Where b is the learning parameter. According to the data available in the literature, the LR for the alkaline electrolyser is 8% [71] and the learning parameter b is 0.029. The total electrolyser target capacity set by the European Union for 2030 is 40 GW, starting from a

capacity of 0.135 GW in 2020 [70]. Assuming that the target is going to be achieved, the resulting cost of the alkaline electrolyser is going to be 4.87 M€, starting from an initial cost of 5.71 M€. No money depreciation is considered in this evaluation. As shown in Figure 6.12, if the selling price of the electrolytic oxygen is 0.15 €/kg the LCOAM decreases by about 15.8% (about 0.64 €/kg) from initial cost of 0.76 €/kg.

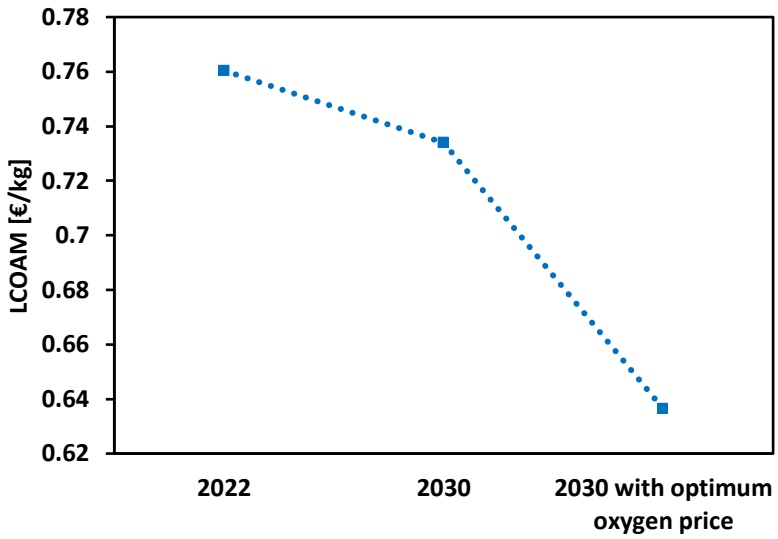

Figure 6.12: LCOAM evaluated for 2020 and 2030 according to the predicted electrolyser cost reduction

In Figure 6.13 the variation of the LCOAM and the PBP with the IRR is represented. No cost reduction for the electrolyser is considered in this analysis. In the previous sensitivities an IRR equal to 8% is assumed. As expected, the LCOAM increases with the IRR making the investment less competitive. Specifically, in the investigated range the LCOAM increases by 53% when the IRR passes from 8% to 18%. On the other hand, by increasing the IRR the PBP is reduced with a non-linear trend from 8 years to 4 years.

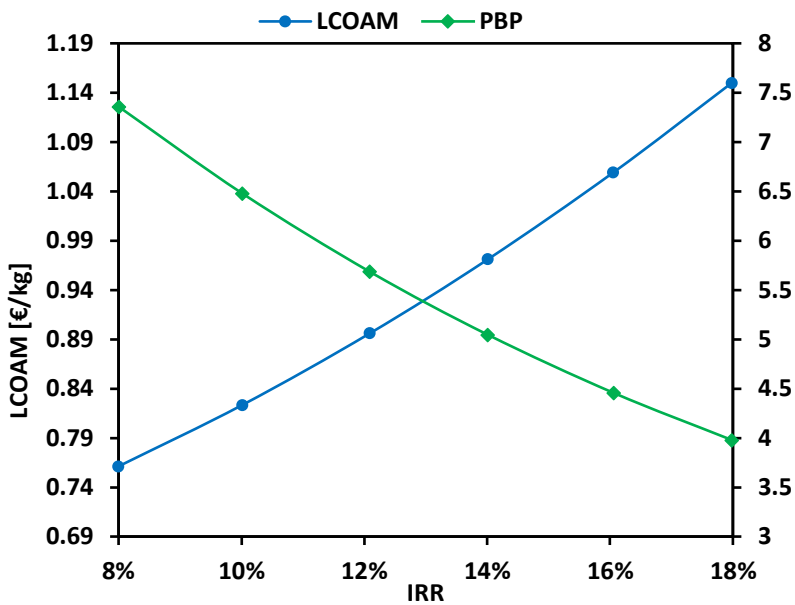

Figure 6.13: LCOAM and PBP variation with the IRR

Other sensitivity analyses assessing the effect on the LCOAM of the HDPE cost, the fixed OPEX costs and the lifetime of the plant are presented and discussed in Appendix E.

6.4.6 Comparison with benchmark technologies

For a complete analysis, the economic competitivity must be assessed by comparison with other clean processes and with the conventional pathways for CH_3OH and NH_3 synthesis. The green benchmark considers CH_3OH synthesis by direct air capture and water electrolysis [58], and NH_3 synthesis by air separation and water electrolysis [57]. The levelized costs correspond to a full renewable energy mix (optimized in GAMS) for Germany with the predicted energy costs for 2050 provided by the International Energy Agency [66]. The benchmarks are represented by the SMR-ATR [58] for CH_3OH synthesis and the Kellogg Brown & Root (KBR) for NH_3 synthesis [57]. To split the LCOAM into LCOM and LCOA the other product price had to be set. Four different cases are considered in Figure 6.14:

- case 1: LCOA equal to the green benchmark for LCOM evaluation;
- case 2: LCOM equal to the green benchmark for LCOA evaluation;
- case 3: LCOM equal to the LCOA with oxygen selling price of 0.07 €/kg;
- case 4: LCOM equal to LCOA with oxygen selling price of 0.15 €/kg.

In all cases the electrolyser expected cost reduction by 2030 is considered. In case 1 the LCOA is the same as the green one and the resulting LCOM is more competitive by about 30% compared to the green benchmark. In case 2, the LCOM is the same as the green case and, similarly to case 1, the resulting LCOA is more competitive. In case 3, both levelized

costs are competitive with the green process. However, in none of the presented scenarios the proposed process is competitive with the conventional ones, despite the introduction of 0.1 €/kg$_{CO2}$ carbon tax. When oxygen is sold at 0.15 €/kg, the LCOM and LCOA reduce by 13.7% but remain far from competitivity with the industrial processes. It must be added that no storage of either H_2 or chemicals (CH_3OH and NH_3) is considered in this work to compensate for the renewable energy source intermittency. This could determine a further increase in the final cost of the products for our process. However, the major contribution to the cost is the renewable electricity cost. The introduction of incentives and a higher carbon tax could be of support in the transition process to more sustainable production routes.

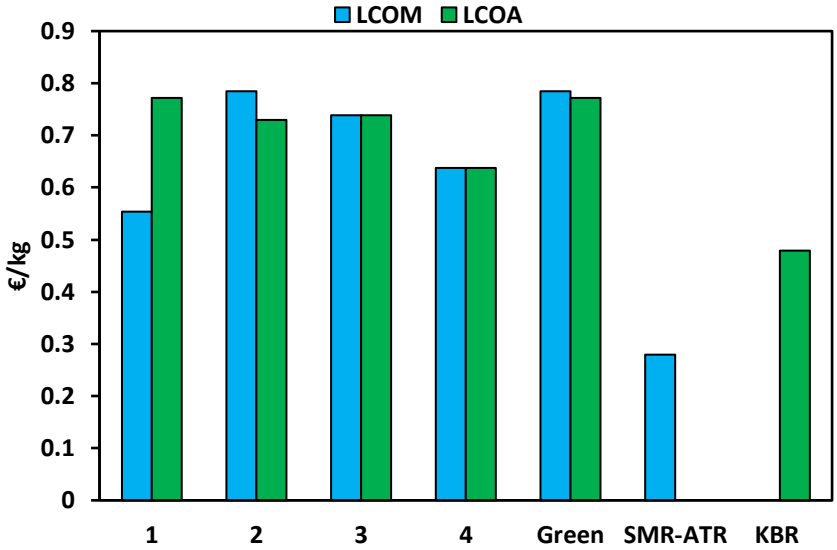

Figure 6.14: LCOA and LCOM comparison with green and conventional production pathways

6.5 Chapter summary and conclusions

In this chapter, a new approach to process synergy in system coupling design is proposed as a low-carbon alternative for the sustainable production of CH_3OH and NH_3 from chemical looping gases. The TRCL process is autothermal, regenerative and circular. The adopted fuel is recycled waste plastic. A sensitivity analysis on the chemical looping main parameters is firstly carried out to assess the best conditions for process design. The resulting values are used for the subsequent techno-economic analysis. The final production rate is divided between 174 kg/h of CH_3OH and 910 kg/h of NH_3. The process provides first principle efficiencies of 43.7% for CH_3OH production and 55% for NH_3 production; specific CO_2 emissions of 0.017 kg$_{CO2}$/kg$_{prd}$ and energy intensity of 36.2 GJ/t$_{prd}$. Compared to the benchmark processes, the specific CO_2 emissions are significantly lower while the first principle efficiencies and the energy intensity are higher, due to the high energy demand of

the electrolyser (responsible for more than 90% of the global electricity consumption). From the economic point of view, a capital cost of 27 M€ and an operating cost of 3.1 M€/y are determined in a realistic cost scenario. The electricity cost results as the major component of the operating expenses (66%). A combined levelized cost for CH_3OH and NH_3 (LCOAM) is developed, and several sensitivity analyses are carried out to assess the impact of different parameters on the final selling prices of the products: electricity input cost, oxygen selling price, electrolyser capital cost, internal rate of return etc. The electricity cost is proved to have a significant impact on the LCOAM. At an electricity cost of 0.03 €/kWh, the LCOAM decreases from 0.76 €/kg to 0.64 €/kg when the oxygen selling price is increased from 0.07 €/kg to 0.15 €/kg and by assuming the electrolyser cost reduction for 2030 with scale economies. Higher internal rates of return provide an increase in the LCOAM: from the initial 0.76 €/kg at 8% discount rate to a maximum of 1.15 €/kg at 18%. On the other side, the payback period is halved from 8 years to 4 years in the same range of discount rates. Finally, a comparison with clean (green) and conventional processes for CH_3OH and NH_3 production is carried out in terms of levelized cost of methanol (LCOM) and ammonia (LCOA). The LCOM and LCOA are derived by setting the selling price of the other product as a secondary revenue, i.e. for the LCOM computation the LCOA is set equal to the green benchmark in the comparison. In every considered scenario, economic competitivity with the electrolytic production of CH_3OH and NH_3 (separately) is observed, though the conventional industrial processes are far more convenient even with the highest oxygen selling price. High dependency on the electricity input cost is remarked. The introduction of incentives and a higher carbon tax values could represent a possible strategy to improve competitivity in the future.

6.6 Nomenclature

AR Air Reactor
ASU Air Separation Unit
BEC Bare Erected Cost
CAPEX Capital Expenditure
CEPCI Chemical Engineering Plant Cost
CSP Concentrated Solar Power
EBIT Earnings Before Interest and Taxes
EBITDA Earnings Before Interest Taxes and Depreciation
ECHP High-pressure economizer
ECLP Low-pressure economizer (first HRSG unit)
EPC Engineering Procurement and Construction
FCF Cash Flow

FGD Flue Gas Desulphurization
FR Fuel Reactor
HDPE High Density Polyethylene
HRSG Heat Recovery Steam Generation
LCOM Levelized Cost of Methanol
LCOAM Levelized Cost of Ammonia and Methanol
LPEC Low-pressure economizer (second HRSG unit)
LPEV Low-pressure economizer (second HRSG unit)
LPSH Low-pressure superheater
LR Learning Rate
OPEX Operating Expenditure
PBP Payback Period
PCC Process Contingencies Cost
PFD Process flow diagram
PV Photovoltaic
SHHP High-pressure superheater
SHIP Intermediate-pressure superheater (first HRSG unit)
SR Steam Reactor
TIC Total Investment Cost
TOC Total Overnight Cost
TPC Total Plant Cost

6.7 References

[1] Incer-Valverde J, Patiño-Arévalo LJ, Tsatsaronis G, Morosuk T. Hydrogen-driven Power-to-X: State of the art and multicriteria evaluation of a study case. Energy Convers Manag 2022;266:115814.
[2] Zhu Q-L, Xu Q. Liquid organic and inorganic chemical hydrides for high-capacity hydrogen storage. Energy Environ Sci 2015;8:478–512.
[3] Palone O, Hoxha A, Gagliardi GG, Di Gruttola F, Stendardo S, Borello D. Synthesis of Methanol From a Chemical Looping Syngas for the Decarbonization of the Power Sector. J Eng Gas Turbine Power 2023;145:21018.
[4] Wan Z, Tao Y, Shao J, Zhang Y, You H. Ammonia as an effective hydrogen carrier and a clean fuel for solid oxide fuel cells. Energy Convers Manag 2021;228:113729.
[5] Aziz M, Wijayanta AT, Nandiyanto ABD. Ammonia as effective hydrogen storage: A review on production, storage and utilization. Energies (Basel) 2020;13:3062.
[6] Schorn F, Breuer JL, Samsun RC, Schnorbus T, Heuser B, Peters R, et al. Methanol as a renewable energy carrier: An assessment of production and transportation costs for selected global locations. Advances in Applied Energy 2021;3:100050.
[7] Deka TJ, Osman AI, Baruah DC, Rooney DW. Methanol fuel production, utilization, and techno-economy: A review. Environ Chem Lett 2022:1–30.

[8] Initiative GCO. Global roadmap for implementing CO2 utilization. 2019.
[9] Tola V, Lonis F. Low CO2 emissions chemically recuperated gas turbines fed by renewable methanol. Appl Energy 2021;298:117146.
[10] Iaquaniello G, Centi G, Salladini A, Palo E, Perathoner S, Spadaccini L. Waste-to-methanol: Process and economics assessment. Bioresour Technol 2017;243:611–9.
[11] Lim D, Lee B, Lee H, Byun M, Lim H. Projected cost analysis of hybrid methanol production from tri-reforming of methane integrated with various water electrolysis systems: Technical and economic assessment. Renewable and Sustainable Energy Reviews 2021:111876.
[12] Battaglia P, Buffo G, Ferrero D, Santarelli M, Lanzini A. Methanol synthesis through CO2 capture and hydrogenation: Thermal integration, energy performance and techno-economic assessment. Journal of CO2 Utilization 2021;44:101407.
[13] Xu X, Liu Y, Zhang F, Di W, Zhang Y. Clean coal technologies in China based on methanol platform. Catal Today 2017;298:61–8.
[14] Shih CF, Zhang T, Li J, Bai C. Powering the future with liquid sunshine. Joule 2018;2:1925–49.
[15] Bowker M. Methanol synthesis from CO2 hydrogenation. ChemCatChem 2019;11:4238–46.
[16] Gentile G, Bonalumi D, Pieterse JAZ, Sebastiani F, Lucking L, Manzolini G. Techno-economic assessment of the FReSMe technology for CO2 emissions mitigation and methanol production from steel plants. Journal of CO2 Utilization 2022;56:101852. https://doi.org/10.1016/J.JCOU.2021.101852.
[17] Smith ER. Iceland–innovations in green energy production. The Carbon Cycle n.d.
[18] Sandalow D, Aines R, Friedmann J, McCormick C, McCoy S. Carbon Dioxide Utilization (CO2U) ICEF Roadmap 2.0. Draft October 2017. 2017.
[19] Hobson C, Márquez C, others. Renewable methanol report. Methanol Institute, Singapore 2018.
[20] World's largest CO2-to-methanol plant starts production 2022. https://www.carbonrecycling.is/news-media/worlds-largest-co2-to-methanol-plant-starts-production (accessed February 20, 2023).
[21] Thonemann N, Maga D. Life Cycle Assessment of Steel Mill Gas-Based Methanol Production within the Carbon2Chem® Project. Chemie Ingenieur Technik 2020;92:1425–30.
[22] Ash S. Mineral commodity summaries 2019 2019.
[23] Zhang H, Wang L, Maréchal F, Desideri U, others. Techno-economic comparison of green ammonia production processes. Appl Energy 2020;259:114135.
[24] Tunå P, Hulteberg C, Ahlgren S. Techno-economic assessment of nonfossil ammonia production. Environ Prog Sustain Energy 2014;33:1290–7.
[25] Arora P, Hoadley AFA, Mahajani SM, Ganesh A. Small-scale ammonia production from biomass: a techno-enviro-economic perspective. Ind Eng Chem Res 2016;55:6422–34.
[26] Ikäheimo J, Kiviluoma J, Weiss R, Holttinen H. Power-to-ammonia in future North European 100% renewable power and heat system. Int J Hydrogen Energy 2018;43:17295–308.

[27] Valera-Medina A, Xiao H, Owen-Jones M, David WIF, Bowen PJ. Ammonia for power. Prog Energy Combust Sci 2018;69:63–102.
[28] Fasihi M, Weiss R, Savolainen J, Breyer C. Global potential of green ammonia based on hybrid PV-wind power plants. Appl Energy 2021;294:116170.
[29] Singlitico A, Østergaard J, Chatzivasileiadis S. Onshore, offshore or in-turbine electrolysis? Techno-economic overview of alternative integration designs for green hydrogen production into Offshore Wind Power Hubs. Renewable and Sustainable Energy Transition 2021;1:100005.
[30] Green ammonia made in Denmark n.d. https://hoestptxesbjerg.dk/about-ptx/ (accessed February 20, 2023).
[31] Khan MN, Shamim T. Investigation of hydrogen generation in a three reactor chemical looping reforming process. Appl Energy 2016;162:1186–94.
[32] Spallina V, Motamedi G, Gallucci F, van Sint Annaland M. Techno-economic assessment of an integrated high pressure chemical-looping process with packed-bed reactors in large scale hydrogen and methanol production. International Journal of Greenhouse Gas Control 2019;88:71–84.
[33] Yang Q, Li X, Yang Q, Huang W, Yu P, Zhang D. Opportunities for CO2 utilization in coal to green fuel process: optimal design and performance evaluation. ACS Sustain Chem Eng 2019;8:1329–42.
[34] Sun Z, Aziz M. Comparative thermodynamic and techno-economic assessment of green methanol production from biomass through direct chemical looping processes. J Clean Prod 2021;321:129023.
[35] Pereira RJL, Argyris PA, Spallina V. A comparative study on clean ammonia production using chemical looping based technology. Appl Energy 2020;280:115874.
[36] Miyahira K, Aziz M. Hydrogen and ammonia production from low-grade agricultural waste adopting chemical looping process. J Clean Prod 2022;372:133827.
[37] Edrisi A, Mansoori Z, Dabir B. Urea synthesis using chemical looping process–Techno-economic evaluation of a novel plant configuration for a green production. International Journal of Greenhouse Gas Control 2016;44:42–51.
[38] Zhao Y, Zhao Y, Yi Q, Li T, Wang J, Bao W, et al. Highly flexible and energy-efficient process for converting coke-oven gas and pulverized coke into methanol and ammonia using chemical looping technology. Energy Convers Manag 2021;248:114796.
[39] Hu Q, Ok YS, Wang C-H. Sustainable and highly efficient recycling of plastic waste into syngas via a chemical looping scheme. Environ Sci Technol 2022;56:8953–63.
[40] Hoxha A, Palone O, Cedola L, Stendardo S, Borello D. Development of a novel carbon capture and utilization approach for syngas production based on a chemical looping cycle. Fuel 2022;325:124760. https://doi.org/10.1016/j.fuel.2022.124760.
[41] Chiesa P, Lozza G, Malandrino A, Romano M, Piccolo V. Three-reactors chemical looping process for hydrogen production. Int J Hydrogen Energy 2008;33:2233–45.
[42] Khan MN, Shamim T. Techno-economic assessment of a plant based on a three reactor chemical looping reforming system. Int J Hydrogen Energy 2016;41:22677–88.

[43] Martina Damizia. Pure hydrogen production by chemical looping technology: use of iron as redox element and bioethanol as renewable reductant. La Sapienza University of Rome , 2022.
[44] Li F, Zeng L, Velazquez-Vargas LG, Yoscovits Z, Fan L-S. Syngas chemical looping gasification process: Bench-scale studies and reactor simulations. AIChE Journal 2010;56:2186–99.
[45] Kuo P-C, Chen J-R, Wu W, Chang J-S. Hydrogen production from biomass using iron-based chemical looping technology: Validation, optimization, and efficiency. Chemical Engineering Journal 2018;337:405–15.
[46] Tong A, Sridhar D, Sun Z, Kim HR, Zeng L, Wang F, et al. Continuous high purity hydrogen generation from a syngas chemical looping 25 kWth sub-pilot unit with 100% carbon capture. Fuel 2013;103:495–505.
[47] Tong A, Zeng L, Kathe M V, Sridhar D, Fan L-S. Application of the moving-bed chemical looping process for high methane conversion. Energy & Fuels 2013;27:4119–28.
[48] Li F, Zeng L, Velazquez-Vargas LG, Yoscovits Z, Fan L-S, Lowrie WG. Syngas Chemical Looping Gasification Process: Bench-Scale Studies and Reactor Simulations 2009. https://doi.org/10.1002/aic.12093.
[49] Yang Q, Yan M, Zhang L, Xia X, Zhu Y, Zhang C, et al. Thermodynamic analysis of chemical looping coupling process for coproducing syngas and hydrogen with in situ CO2 utilization. Energy Convers Manag 2021;231:113845.
[50] Mansouri MT, Ahmadi P, Kaviri AG, Jaafar MNM. Exergetic and economic evaluation of the effect of HRSG configurations on the performance of combined cycle power plants. Energy Convers Manag 2012;58:47–58.
[51] Atsonios K, Panopoulos KD, Kakaras E. Investigation of technical and economic aspects for methanol production through CO2 hydrogenation. Int J Hydrogen Energy 2016;41:2202–14.
[52] Arab S, Commenge JM, Portha JF, Falk L. Methanol synthesis from CO2 and H2 in multi-tubular fixed-bed reactor and multi-tubular reactor filled with monoliths. Chemical Engineering Research and Design 2014;92:2598–608. https://doi.org/10.1016/J.CHERD.2014.03.009.
[53] Bussche KM Vanden, Froment GF. A steady-state kinetic model for methanol synthesis and the water gas shift reaction on a commercial Cu/ZnO/Al2O3Catalyst. J Catal 1996;161:1–10.
[54] Al-Malah KI. Aspen plus : chemical engineering applications. 2nd ed. New Jersey : Wiley ; 2022.
[55] Turton R, Bailie RC, Whiting WB, Shaeiwitz JA. Analysis, synthesis and design of chemical processes. Pearson Education; 2008.
[56] Orhan MF, Dincer I, Naterer GF. Cost analysis of a thermochemical Cu–Cl pilot plant for nuclear-based hydrogen production. Int J Hydrogen Energy 2008;33:6006–20.
[57] Arnaiz del Pozo C, Cloete S. Techno-economic assessment of blue and green ammonia as energy carriers in a low-carbon future. Energy Convers Manag 2022;255. https://doi.org/10.1016/j.enconman.2022.115312.

[58] Arnaiz del Pozo C, Cloete S, Jiménez Álvaro Á. Techno-economic assessment of long-term methanol production from natural gas and renewables. Energy Convers Manag 2022;266. https://doi.org/10.1016/j.enconman.2022.115785.
[59] Keairns D, Kuehn N, Newby R, Shah V. Guidance for NETL's oxycombustion R&D program: chemical looping combustion reference plant designs and sensitivity studies. 2014.
[60] Gracida-Alvarez UR, Winjobi O, Sacramento-Rivero JC, Shonnard DR. System Analyses of High-Value Chemicals and Fuels from a Waste High-Density Polyethylene Refinery. Part 1: Conceptual Design and Techno-Economic Assessment. ACS Sustain Chem Eng 2019;7:18254–66. https://doi.org/10.1021/acssuschemeng.9b04763.
[61] Hrastel I, Gerbec M, Stergaršek A. Technology optimization of wet flue gas desulfurization process. Chemical Engineering & Technology: Industrial Chemistry-Plant Equipment-Process Engineering-Biotechnology 2007;30:220–33.
[62] Shehzad MF, Abdelghany MB, Liuzza D, Mariani V, Glielmo L. Mixed logic dynamic models for MPC control of wind farm hydrogen-based storage systems. Inventions 2019;4. https://doi.org/10.3390/inventions4040057.
[63] Turner, Marc J. Cost and Performance Baseline for Fossil Energy Plants Volume 1a: Bituminous Coal (PC) and Natural Gas to Electricity Revision 3 OFFICE OF FOSSIL ENERGY. 2015.
[64] Luyben WL. Estimating refrigeration costs at cryogenic temperatures. Comput Chem Eng 2017;103:144–50. https://doi.org/10.1016/j.compchemeng.2017.03.013.
[65] 2022 Carbon Tax Rates in Europe | European Countries with a Carbon Tax n.d. https://taxfoundation.org/data/all/eu/carbon-taxes-in-europe-2022/ (accessed October 19, 2023).
[66] IEA. World Energy Outlook 2022 2022. https://www.iea.org/reports/world-energy-outlook-2022 (accessed June 8, 2023).
[67] IRENA. Renewable Power Generation Costs in 2021. 2022.
[68] Bi X, Yang J, Yang S. LCA-based regional distribution and transference of carbon emissions from wind farms in China. Energies (Basel) 2022;15. https://doi.org/10.3390/en15010198.
[69] Wei M, Smith SJ, Sohn MD. Experience curve development and cost reduction disaggregation for fuel cell markets in Japan and the US. Appl Energy 2017;191:346–57.
[70] Pastore LM, Basso G Lo, de Santoli MSL. Technical, economic and environmental issues related to electrolysers capacity targets according to the Italian Hydrogen Strategy: A critical analysis. Renewable and Sustainable Energy Reviews 2022;166:112685.
[71] Gül T, Kypreos S, Turton H, Barreto L. An energy-economic scenario analysis of alternative fuels for personal transport using the Global Multi-regional MARKAL model (GMM). Energy 2009;34:1423–37.

Chapter 7

Epilogue

7.1 Conclusions

In this work the integration of chemical looping technology within an industrial decarbonization scenario is proposed and assessed by modelling and experimental evaluations. Each step of the decarbonization strategy is studied individually starting from steel production, then focusing on chemical looping CO_2 splitting (through modelling and experimental evaluations), and finally investigating the techno-economic feasibility of liquid fuels production (methanol and ammonia) from the thermochemical syngas.

In **Chapter 1**, an initial overview is provided on the most relevant advances concerning oxygen carriers development. A general interest towards natural ores and waste materials with high Fe content is underlined. Subsequently, the technology is divided in its three main variants: combustion, reforming, and gasification. Chemical looping combustion is the most advanced version of this technology. Currently the main research topics are represented by the inherent cleaning of the combustion off-gases through the addition of alkaline metals and the development of optimal reactor configurations, such as interconnected fluidized beds, moving beds and internal circulating reactors. Chemical looping reforming is a very promising process with several advantages compared to benchmark processes. The presence of Ni in the oxygen carrier is crucial in this case, but its high toxicity and procurement costs are driving research towards alternatives or mixed materials. Finally, chemical looping gasification is shown as being competitive with conventional gasification, though it is at a lower TRL level compared to the previous chemical looping versions. Subsequently, the application of chemical looping in the power and chemical production sector is analysed. Chemical looping combustion is economically competitive with conventional systems such as natural gas combined cycles if they are retrofitted with carbon capture and storage systems. On the contrary, chemical looping reforming is already competitive in terms of hydrogen production costs and reforming efficiencies. Process research is currently focusing on systems coupling, as for instance chemical looping combustion processes feeding a conventional steam methane reformer, or combined hydrogen and power production in a chemical looping hydrogen production scheme.

In **Chapter 2**, a revamping methodology starting from conventional BF-BOF steel mills is proposed and assessed by Aspen Plus simulation. The methodology involves a four-steps transition to a more electrical and efficient production, based on the direct reduction – electric arc furnace technology (Energiron by Tenova and Danieli). In the first step the injection of 230 kt/y of waste plastic through the blast furnace tuyeres is considered as a carbon circularity strategy. As expected, a low impact on CO_2 emissions is observed. Subsequently, part of the BF-BOF lines are shut down and replaced with DR-EAF lines. In the third step, two DR-EAF lines are considered with 100% natural gas feeding and CO_2 emissions drop by 75% (0.45 t_{CO2}/t_{hrc}) compared to the initial configuration. Finally,

considering hydrogen as a reducing agent, CO_2 emissions drop by 92% and the energy flows reduce by 59.4%. However, this would entail the installation of 1.42 GW electrolyser to produce the required flow rate of hydrogen, with stable carbon-free electric energy supply, which is currently a particularly challenging task. The utilization of scrap material is also considered and a beneficial impact on electricity consumption is obtained due to the decrease in the direct reduction plant size. A linear correlation is also developed to predict the specific CO_2 emissions for the final steel mill configuration as a function of the scrap mass fraction sent to the EAF. The methodology establishes a line for guiding future governmental investments towards cleaner steel production and clarifies the main drawbacks associated within each step.

In **Chapter 3**, a process scheme integrating chemical looping syngas production downstream of a conventional BF-BOF steel mill is proposed. The process involves: a calcium looping cycle for separating the CO_2 content of BFG from the other gas species; a chemical looping cycle where syngas is produced from CO_2 and H_2O splitting and biogenic carbon is employed as a reducing agent such that the CO_2 emissions balance can be negative; a liquid fuel production section where thermochemical syngas is further processed. The main focus of the preliminary evaluations presented in Chapter 3 is on the chemical looping cycle, in order to assess the potentials of this technology as an effective carbon capture and utilization means. Mass balances supported by computational fluid dynamics simulation are thus carried out based on two oxygen carriers: nickel ferrites and iron oxides. A CO_2 flow rate of 1 t/h is considered, though this flow rate does not cover the total carbon content of conventional BFGs. To close the mass balances, assumptions on the oxygen carriers final conversion degree are made. For a fixed syngas mass flow rate (0.69 t/h with 50% H_2/CO in mol), lower mass flow rates are computed in the $NiFe_2O_4$ scenario. However, CFD simulations (with implemented reaction kinetics) are then carried out on a fluidized bed reactor with FeO particles, due to their lower toxicity and cost with respect to nickel ferrites. The CFD simulations indicate a complete conversion of the inlet gases to CO and H_2 over the first 15 seconds of simulation and validate the assumptions of unitary conversion of the reactants in the oxidation step. Based on the proposed process, in the subsequent chapters two crucial aspects for chemical looping syngas production cycles are identified and experimentally investigated: syngas production capabilities of a Fe bed, the effect of high pressure on NiFe oxygen carriers redox abilities.

In **Chapter 4**, experimental evaluation of the oxidation step of the proposed chemical looping syngas production process is carried out with a Fe bed at ambient pressure conditions. The objective is the identification of the optimal conditions to maximize syngas productivity. The syngas production step is encompassed in a process scheme for the reutilization of iron scrap, where the reduction step is replaced by the blast furnace of a conventional still mill. Initially, CO_2 splitting is investigated at different temperatures and

a maximum conversion of 37% is achieved at 1050 °C with 1 nl/min flow rate of CO_2. Then, for combined streams of CO_2 and H_2O the effect of flow rate, composition and Fe bed mass is assessed. By reducing the injected flow rates, the reactants dissociation increases for both species and below a certain threshold CO_2 dissociation (13%) is higher than that of H_2O_v (11%). By increasing the H_2O_v/CO_2 molar ratio in the 1-3 range at 37 L/min total flow rate, H_2 production is enhanced with respect to CO. The products molar ratio $CO/CO+H_2$ shows a linear dependency on reactants molar ratio CO_2/CO_2+H_2O, in agreement with experimental data on FeO oxidation reported in the literature. For H_2O/CO_2 molar ratios above 2 and low gas space velocity, the syngas compositions shows the best H_2 and CO volume percentages, ranging from 28% to 41% and 8.6 - 12.9%, respectively.

In **Chapter 5**, high pressure operation in a chemical looping cycle is experimentally evaluated on NiFe aluminates and compared with the ambient pressure behaviour. Two NiFe aluminates with different Ni loadings (4.3% wt. and 12% wt.) and similar Fe loadings (9.9% wt. and 8.5% wt.) are synthesized through a co-precipitation/impregnation route and tested in two thermogravimetric analysers. Higher temperatures show beneficial effect on conversion and at ambient pressure full conversion is achieved after 200 s at 900 °C for the material with higher Ni loadings. On the contrary, high total pressures (20 bar) show a negative effect on kinetics and a maximum of 75% conversion is achieved after 1200 s for the second material. The detrimental effect of high pressure is confirmed by XRD analyses on the spent samples from low and high-pressure tests after the reduction step. The long term cyclability is then investigated and a conversion gain over the cycles is observed both at low (100 cycles) and high pressure conditions (80 cycles). Microstructural characterization by SEM analysis does not display signs of deterioration after 80 high-pressure cycles compared to the fresh material. Similarly, XRD analyses do not display significant changes between the reduced spent material after 30 and 80 high-pressure cycles.

In **Chapter 6**, a techno-economic analysis of a system for the production of methanol and ammonia from chemical looping gases is carried out. The process involves waste plastic as reducing agent and pure hydrogen production from a chemical looping cycle with iron oxides as oxygen carriers. The chemical looping process involves two counter current-moving bed reactors (fuel and oxidation reactors) and a riser (air reactor). Process optimization is firstly carried out on the main parameters of the chemical looping unit. The final production rate is divided between 174 kg/h of methanol and 910 kg/h of ammonia. The process provides first principle efficiencies of 43.7% for CH_3OH production and 55% for NH_3 production; specific CO_2 emissions of 0.17 kg_{CO2}/kg_{prd} and energy intensity of 36.2 GJ/t_{prd}. A combined levelized cost for CH_3OH and NH_3 (LCOAM) is developed and several sensitivity analyses are carried out to assess the impact of different parameters on the final selling prices of the products: electricity input cost, oxygen selling price, electrolyser capital

cost evolution, internal rate of return etc. The electricity cost is demonstrated to have a significant impact on the LCOAM due to the presence of the electrolytic unit. From comparative analyses with other green alternatives, economic competitivity with the electrolytic production of CH_3OH and NH_3 (separately) is observed, while the benchmark processes remain more convenient, even assuming the highest selling price for electrolytic oxygen as a secondary revenue.

To summarise, in this doctoral thesis work chemical looping is demonstrated as a promising waste to energy and waste to fuel process with inherent abilities for CO_2 separation. Its flexibility allows the utilization of low grade fuels (biomass, waste plastic etc.) as reducing agents and the production of high purity hydrogen or syngas. The high temperature levels involved in the process enable combined power and fuel production, thus enhancing the economical competitivity with other clean technological alternatives. From the experimental evaluations, it is confirmed that to support the scale up of this technology more data should be collected on the activity of different oxygen carriers at industrially relevant operating conditions, such as high pressure and temperatures.

7.2 Developments and recommendations for future works

This work analysed in detail each step of a novel decarbonization strategy involving liquid fuels production from waste gases and solids reconversion by chemical looping processes. The presented results pave the way for further research questions on this topic. In this thesis, the oxidation step of a chemical looping syngas production cycle is experimentally analysed at ambient pressure. Further studies at higher pressure and in a close loop would complete the data hereby presented. Detailed analyses should be also carried out on an interconnected fluidized bed reactor configuration for chemical looping syngas production. The process performance should be analysed in terms of solid circulation rate, oxygen carrier conversion and chemical/mechanical stability over many cycles. The results could then support the design and construction of an experimental facility incorporating the chemical looping section and liquid fuels synthesis. Demonstration of autothermal operation would be crucial for the success of this technology. For instance, in the ongoing European Project "Glamour" the production of synthetic aviation fuels from Fischer-Tropsch and autothermal CLR of glycerol is attempted in a large-scale setup currently under construction at Eindhoven University of Technology [1]. The project aims to increase the TRL of this technology up to 5/6. The utilization of waste materials as oxygen carrier could be a further interesting research topic, because of the reduced operating costs and the limited impact on the environment compared to synthetic oxygen carriers, often containing elements such as nickel. Life cycle analyses comparing the utilization of synthetic and

natural or waste materials as oxygen carriers could be of help to define these environmental benefits.

Sideways to these aspects, other chemical looping processes would need further investigations, both from the experimental and modelling sides, such as the chemical looping ammonia production with nitrogen carriers and the chemical looping energy storage. The former process [2] should be compared with ammonia synthesis from chemical looping reforming [3] and with benchmark ammonia production. The environmental impact of the two technologies should also be assessed and compared. On the other hand, the chemical looping energy storage involves thermal solar energy (or other energy sources) to reduce the oxygen carriers during the charge periods and the release of the accumulated energy by simple air oxidation [4]. Currently, limited number of works deal with this topic and it would be of great interest to consider its integration in energy systems for balancing the intermittency of renewable energy sources.

7.3 References

[1] Glamour Project n.d. https://www.glamour-project.eu/ (accessed October 15, 2023).

[2] Lai Q, Cai T, Tsang SCE, Chen X, Ye R, Xu Z, et al. Chemical looping based ammonia production—A promising pathway for production of the noncarbon fuel. Sci Bull (Beijing) 2022;67:2124–38. https://doi.org/10.1016/J.SCIB.2022.09.013.

[3] Pereira RJL, Argyris PA, Spallina V. A comparative study on clean ammonia production using chemical looping based technology. Appl Energy 2020;280:115874.

[4] Diego ME, Abanades JC. Techno-economic analysis of a low carbon back-up power system using chemical looping. Renewable and Sustainable Energy Reviews 2020;132:110099. https://doi.org/10.1016/J.RSER.2020.110099.

Appendix

Appendix A

A.1 Model validation

Table A.1. Desulphurization unit model validation

Desulph.	Composition			Flow rates (kt/y)		
Element	**Simulation**	**Reference**	**Error**	**Simulation**	**Reference**	**Error**
Fe	94.62%	94.24%	-0.41%	3900.89	3894	-0.18%
C	4.86%	4.65%	-4.62%			
Si	0.51%	0.49%	-4.41%			

Table A.2. Sinter plant model validation

Composition				Flow rates (kt/y)		
Element	**Simulation**	**Reference**	**Error**	**Simulation**	**Reference**	**Error**
Fe	82.88%	82.63%	-0.30%	4455.28	4446	-0.21%
CaO	9.35%	9.45%	1.06%			
MgO	1.50%	1.50%	0.33%			
SiO_2	5.20%	5.25%	0.86%			
Al_2O_3	1.07%	1.04%	-2.87%			

Table A.3. Hot stoves model validation

Composition				Flow rates (kt/y)		
Element	**Simulation**	**Reference**	**Error**	**Simulation**	**Reference**	**Error**
O_2	24.13%	24.13%	0%	5364	5364	0%
N_2	73.88%	73.88%	0%			
H_2O	1.99%	1.99%	0%			

Table A.4. Coke oven model validation

Coke oven gas	Composition			Flow rates (kt/y)				Coke	Flow rates (kt/y)		
Element	**Simulation**	**Reference**	**Error (%)**	**Unit**	**Simulation**	**Reference**	**Error (%)**		**Simulation**	**Reference**	**Error (%)**
H_2	59.54%	59.53%	-0.02%	Hot stoves	12.21	12.34	1.03%		3397.73	3396.91	-0.02
N_2	5.76%	5.76%	0.00%	Sinter plant	7.93	8	0.93%				
CO_2	0.96%	0.96%	0.00%	BOF	143.96	145.96	0.93%				
CH_4	23.04%	23.04%	0.00%	Reheating	78.88	79.71	1.04%				
C_2H_4	2.69%	2.69%	0.00%								

Table A.5. Direct reduction plant validation

Element	Simulation	Reference	Error (%)
DRI (kt/y)	2531.91	2500	-1.28%
C%	4.32	4.30%	-0.42%

Fe%	87%	87.30%	0.34%
Metallization	96%	96%	0%
Gangue	4.0%	3.8%	-5.24%
T_{DRI} (°C)	600 °C	600 °C	0%
O_2 DRP (Nm^3/t_{DRI})	63.6	60	-5.65%

Table A.6. Correlation validation for specific CO_2 emissions with varying mass fraction on step 4

		Simulation [t/t_{hrc}]	**Correlation [t/t_{hrc}]**	**Error (%)**
Scrap wt%	10%	0.095882	0.0958	0.12%
	30%	0.093514	0.0936	- 0.050%
	60%	0.090193	0.0903	- 0.074%
	90%	0.087169	0.0870	0.24 %

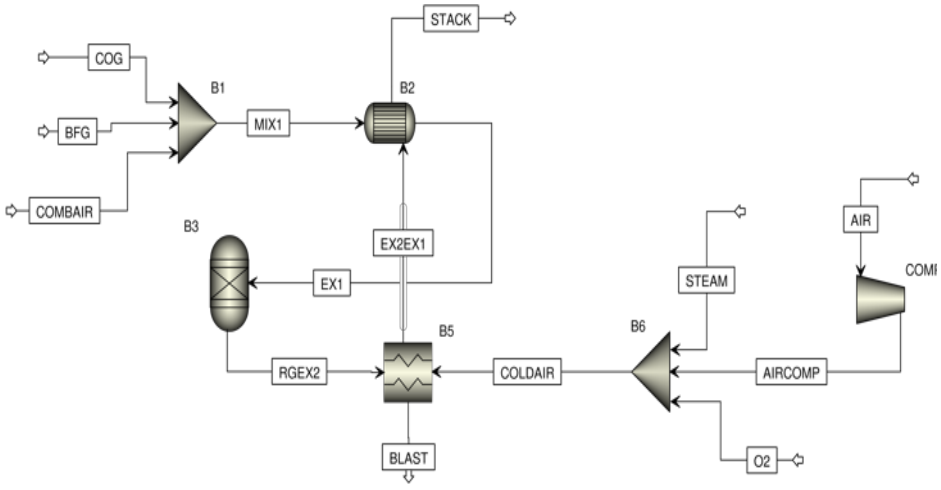

Figure A.1. Aspen Plus flowsheet of the hot stoves

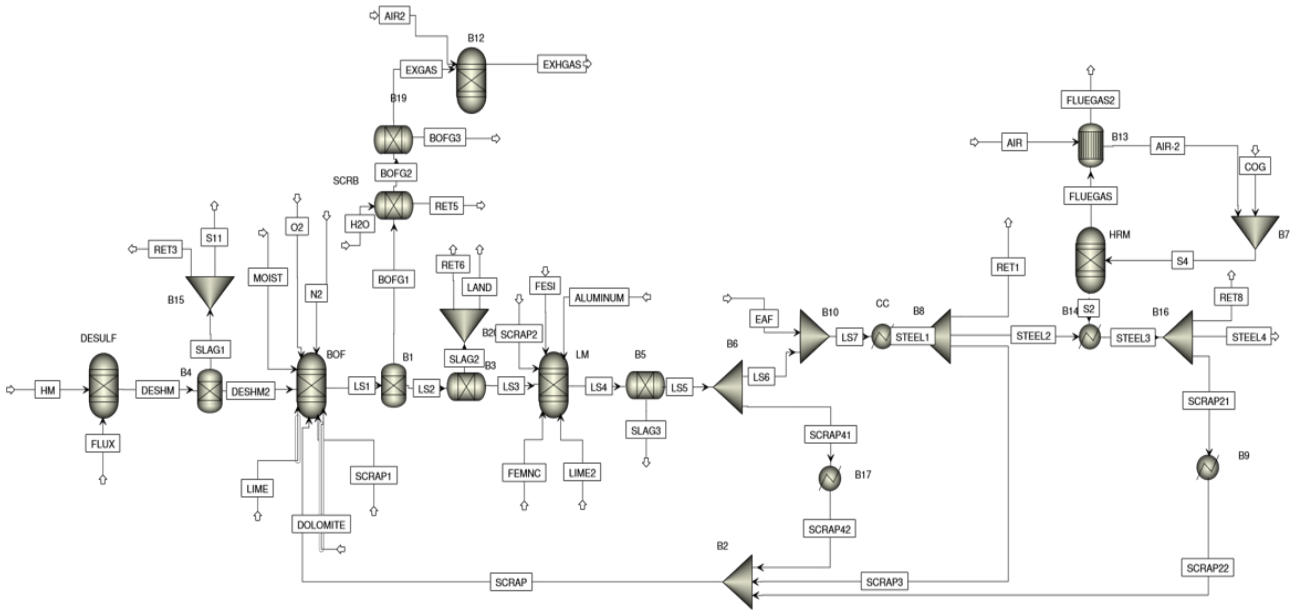

Figure A.2. Basic oxygen furnace and secondary steelmaking flowsheet

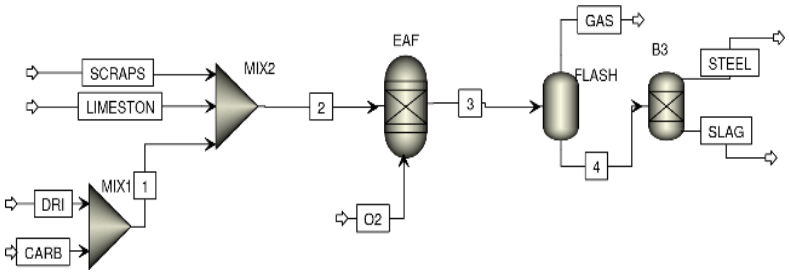

Figure A.3. Flowsheet of the EAF in Aspen Plus

BFG	Composition			Flow rates (kt/y)			**Pig iron**	Composition			Flow rates (kt/y)		
Elem.	Simulation	Ref.	Error	Sim.	Ref.	Error (%)	Element	Sim.	Ref.	Error (%)	Sim.	Ref.	Error (%)
H_2	3.59	3.75	**4.09%**	8810.91	8724.52	**-0.99%**	Fe	94.73%	94.15%	**-0.62%**	3975.85	3968.76	**-0.18%**
N_2	48.80	50.32	**3.02%**				C	4.77%	4.70%	**-1.42%**			
CO_2	23.75	22.81	**-4.08%**				Si	0.50%	0.50%	**0.00%**			
CO	23.74	23.07	**-2.90%**										

Table 2.9 of Chapter 2

BOFG	Composition			Flow rates (kt/y)			**Liq.steel**	Composition			Flow rates (kt/y)		
Element	Simulation	Reference	Error(%)	Simulation	Reference	Error(%)	Element	Simulation	Reference	Error(%)	Simulation	Reference	Error(%)
H_2	2.64%	2.64%	**0.00%**	453.752	448	**1.27%**	Fe	99.96%	99.90%	**-0.06%**	4432.72	4323	**-2.67%**
CO_2	14.44%	14.44%	**-0.28%**				C	0.04%	0.042%	**-5.00%**			
CO	56.90%	56.92%	**-0.04%**										
N_2	13.83%	13.83%	**0.00%**										
H_2O	12.18%	12.16%	**0.55%**										

Table 2.10 of Chapter 2

Appendix B

B.1 MATLAB flow diagram

The flow diagram of the MATLAB algorithm implementing both mass and energy balances is reported in the upper part of Figure B.1. The symbology employed in Figure B.1. has the following meaning:

- The "start" box identifies the start of the calculation process, equivalent to the "run" of the MATLAB script.
- The "end" circle represents the closure of a script. In fact, two distinct codes have been created, the first relating to mass and energy balances for the complete syngas production cycle, and the second relating to the design of a small-scale oxidizer reactor for the laboratory. The output of the first code is used as input in the second.
- The parallelogram-shaped boxes, in blue, represent the information entered by the user, i.e. inputs provided to the model according to the system conditions established during the design phase.
- The cylinder-shaped boxes, in blue, represent the data collected by the NIST database: the coefficients for the Shomate equation and the characteristics of the oxidizer compounds.
- The rectangular sections, in light blue, represent the MATLAB functions created to perform calculations outside of the main script.
- The rhomboid boxes represent the decision-making steps, i.e. the steps which perform the subsequent action according to the result of previous operations. They are used here to verify the presence of errors in the process and check the robustness of the model and the speed (flow) limits of the gases introduced in the oxidizer.

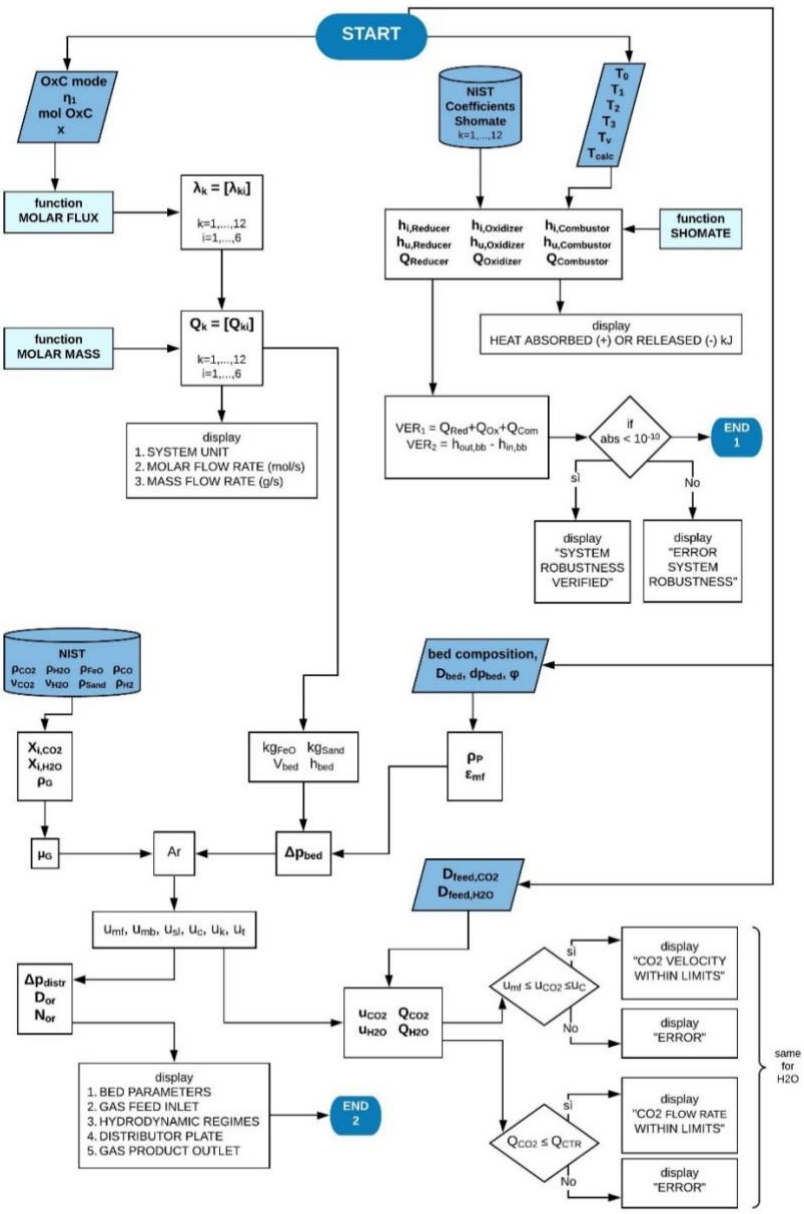

Figure B.1. Flow diagram of the MATLAB algorithm (upper half, mass and energy balances; lower half, bed parameters)

B.2 Split-fraction coefficients model

Figure B.2. shows the application of the split-fraction model to an illustrative process: each block constitutes a calculation module relating the outgoing flows of the chemical compounds with the input flows. The set of equations, describing the relations between the different modules, is defined by expressing the flow of any component in any outlet stream as a fraction of that component in the inlet stream.

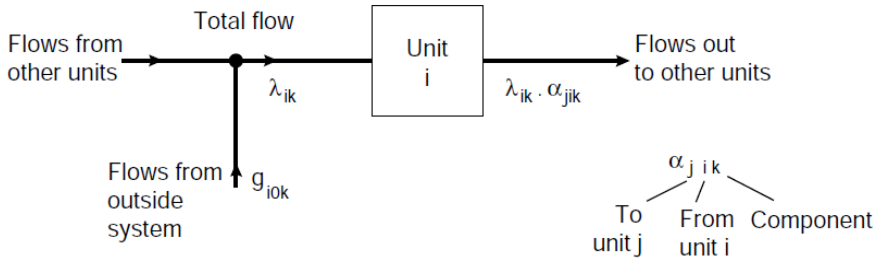

Figure B.2. Application of the split-fraction coefficients

In other words, the flow of a component k, from unit i to unit j, is expressed as the flow into i multiplied by the split-fraction coefficient:

$$\lambda_{j,i,k} = \lambda_{i,k} \cdot \alpha_{j,i,k} \tag{B.1}$$

Where:

- i is the number of the unit/module under consideration;
- k is the compound circulating in the system;
- $\lambda_{i,k}$ is the total flow rate (sum of different inputs) of the compound k entering unit i [mol/s];
- $\alpha_{j,i,k}$ is the split fraction coefficient of the compound k flowing from i to j [dimensionless, 0-1]. It is defined as the ratio of the flow of the compound k coming out of unit i and directed to unit j divided by the total flow of the compound k entering unit i;
- $g_{i,0,k}$ is the flow rate [mol/s] of the compound k coming from any source outside the system (dummy unit 0) and directed to module i. Furthermore, if a new compound is generated as a product from a unit, i.e. it is not part of the incoming flow of the generating unit, the flow of the new compound will be considered as an external flow for the destination unit.

The value attributed to each split-fraction coefficient depends on the nature of the reactor, the composition of the incoming flow and the distribution of the output flow [1]. The following units compose the thermochemical cycle of syngas production: Reducer (1), Oxidizer (2), Combustor (3), exit to Liquid Fuel synthesis unit (4), exit to CO_2 treatment (5), exit to N_2 treatment (6). The following chemical compounds are assumed: $Fe_2O_3/NiFe_2O_4$, Ni, FeO, $C_{biogenic}$, CO_2, $H_2O_{(v)}$, CO, H_2, NiO, Fe_3O_4, O_2, N_2 (for $k = 1, 2, 3, 4, 5, 6, 7, 8, 9, 10, 11, 12$, respectively).

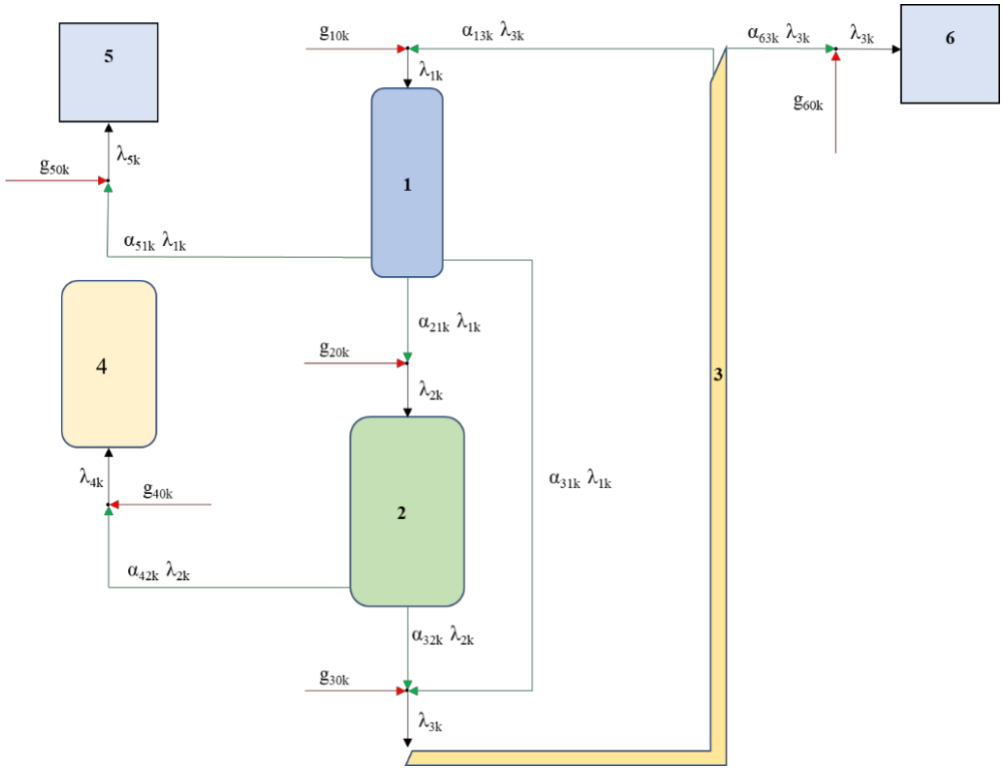

Figure B.3. Flow diagram of the split-fraction model for the thermochemical cycle

A mass balance equation is defined for each unit ($n = 6$, number of the units composing the system, $i = 1, \dots, n$) and then repeated for each chemical compound flowing in the system ($m = 12$, number of the compounds, $k = 1, \dots, m$).

$$\lambda_{1k} + 0 + \alpha_{13k} \cdot \lambda_{3k} + 0 + 0 + 0 = g_{10k} \quad \text{(B.2)}$$

$$\alpha_{21k} \cdot \lambda_{1k} + \lambda_{2k} + 0 + 0 + 0 + 0 = g_{20k} \quad \text{(B.3)}$$

$$\alpha_{31k} \cdot \lambda_{1k} + \alpha_{32k} \cdot \lambda_{2k} + \lambda_{3k} + 0 + 0 + 0 = g_{30k} \quad \text{(B.4)}$$

$$0 + \alpha_{42k} \cdot \lambda_{2k} + 0 + \lambda_{4k} + 0 + 0 = g_{40k} \quad \text{(B.5)}$$

$$\alpha_{51k} \cdot \lambda_{1k} + 0 + 0 + 0 + \lambda_{5k} + 0 = g_{50k} \quad \text{(B.6)}$$

$$0 + 0 + \alpha_{63k} \cdot \lambda_{3k} + 0 + 0 + \lambda_{6k} = g_{60k} \quad \text{(B.7)}$$

After the value attribution of every split-fraction coefficient $\alpha_{j,i,k}$ and external flow rates $g_{i,0,k}$ as described in [2], the mass balance can be solved to evaluate the unknown variables $\lambda_{i,k}$ for each compound k. If the set of equations is arranged for the whole system, the mass balance is reduced to:

$$\alpha \cdot \lambda = g \quad \text{(B.8)}$$

Where:

- A = 72, as the product of n and m.

- α [AxA] is a diagonal supermatrix composed of the m matrixes [nxn] of the split-fraction coefficients. Each matrix $\bar{\bar{A}}_1, \dots, \bar{\bar{A}}_m$ is referred to a specific compound k.
- λ [mx1] is the super vector composed of the m vectors [nx1] of the incoming flow rates. Each vector $\bar{\lambda}_1, \dots, \bar{\lambda}_m$ is referred to a specific compound k.
- g [mx1] is the super vector composed of the m vectors [nx1] of the external flow rates. Each vector $\bar{g}_1, \dots, \bar{g}_m$ is referred to a specific compound k.

$$\begin{pmatrix} \bar{\bar{A}}_1 & \bar{\bar{0}} & \bar{\bar{0}} & \bar{\bar{0}} & \bar{\bar{0}} \\ \bar{\bar{0}} & \bar{\bar{A}}_2 & \bar{\bar{0}} & \bar{\bar{0}} & \bar{\bar{0}} \\ \bar{\bar{0}} & \bar{\bar{0}} & \bar{\bar{A}}_3 & \bar{\bar{0}} & \bar{\bar{0}} \\ \bar{\bar{0}} & \bar{\bar{0}} & \bar{\bar{0}} & \dots & \dots \\ \bar{\bar{0}} & \bar{\bar{0}} & \bar{\bar{0}} & \dots & \bar{\bar{A}}_m \end{pmatrix} \begin{pmatrix} \bar{\lambda}_1 \\ \bar{\lambda}_2 \\ \bar{\lambda}_3 \\ \dots \\ \bar{\lambda}_m \end{pmatrix} = \begin{pmatrix} \bar{g}_1 \\ \bar{g}_2 \\ \bar{g}_3 \\ \dots \\ \bar{g}_m \end{pmatrix} \tag{B.9}$$

B.3 Lab-scale reactor modelling

The procedure to determine the oxidizer reactor design parameters is reported in the lower part of Figure B.1. The first part of the calculation procedure is devoted to insert the external inputs. Firstly, the operating conditions of the reactor are defined, so that the density and viscosity of the gas mixture can be inferred from thermodynamic tables. Then, some particles parameters are imposed, such as the average particle diameter d_p, the particle density ρ_p and the sphericity φ Moreover, both the bed diameter D_{bed} and the amount of oxygen carrier in the bed are set (FeO in this case). Lastly, the diameter of the oxidant distributor holes D_{or} and that of the feeding tubes carrying CO_2 and H_2O_v (at defined temperature and pressure conditions) are imposed.
Once the input data are provided, the code computes the thermo-physical properties of the gas mixture at operating conditions. The mixture density ρ_{mg} is computed as a weighted average of each species density:

$$\rho_{mg} = \sum_{i=1}^{N} x_i \rho_i \tag{B.10}$$

Where:

- x_i is the mass fraction of each gaseous species;
- ρ_i is the density of each species.

The viscosity of the mixture is computed as follows [3]:

$$\mu_g = \sum_{i=1}^{2} \frac{\mu_i}{1 + \frac{1}{x_i} \cdot \sum_{\substack{j=1 \\ j \neq i}}^{j=2} \frac{x_j \cdot \left[1 + \left(\mu_i/\mu_j\right)^{1/2} \left(MW_j/MW_i\right)^{1/4}\right]^2}{2\sqrt{2}\left(1 + MW_i/MW_j\right)^{1/2}}} \tag{B.11}$$

Where:

- μ_i is the viscosity of each gaseous species;
- MW_i is the molecular weight of each gaseous species.

Subsequently, the parameters of the bed are evaluated. Since the bed can include a certain amount of inert, the density of the bed is computed as:

$$\rho_{bed} = \rho_p \cdot c + \rho_{sand} \cdot (1 - c) \tag{B.12}$$

Where:

- ρ_p is the density of the oxygen carrier ;
- ρ_{sand} is the density of the inert;
- c is the percentage of oxygen carrier content with respect to the inert in the bed.

For the present case, no inert is assumed, i.e. $c = 0$. The porosity of the bed at minimum fluidized conditions ε_{mf} is evaluated according to [4]:

$$\epsilon_{mf} = 0.586 \cdot \varphi^{-0.72} \cdot \left(\frac{\mu_g^2}{\rho_g \cdot 9.81 \cdot (\rho_p - \rho_g) \cdot d_m^3}\right)^{0.029} \cdot \left(\frac{\rho_g}{\rho_p}\right)^{0.021} \tag{B.13}$$

Therefore, assuming that the porosity at minimum fluidization conditions is equal to that in fixed bed conditions, bed volume is derived from the following equation:

$$V_{bed} = \frac{\left(\frac{m_{OC}}{\rho_{OC}} + \frac{m_{sand}}{\rho_{sand}}\right)}{1 - \epsilon_{mf}} \tag{B.14}$$

Where:

- m_{OC} is the mass of oxygen carrier in the bed;
- m_{sand} is the mass of sand in the bed, obtained knowing the percentage of OC content with respect to the inert in the bed.

Therefore, the height of the bed h_{bed} at minimum fluidization conditions is equal to:

$$h_{bed} = \frac{V_{bed}}{A_{bed}} \tag{B.15}$$

Where A_{bed} is the cross section of the bed. The pressure drop due to the gaseous flow crossing the bed from the bottom to the top is then computed, according to the following equation [5]:

$$\Delta p_{bed} = h_{bed} \cdot (1 - \epsilon_{mf}) \cdot (\rho_{bed} - \rho_{mg}) \cdot 9.81 \quad \text{(B.16)}$$

Where:

- h_{bed} is the height of the bed, obtained by dividing V_{bed} by A_{bed};
- ρ_{mg} is the gas mixture density;
- ρ_{bed} is the density of the powder in the bed

By increasing the surface velocity of the gas passing through the solid particulate bed, different modes of interaction between the two phases are encountered: bubbly flow, slug flow, turbulent flow and pneumatic transport [6]. The minimum fluidization velocity is estimated by taking the arithmetic average of the expressions reported in [7–11]:

$$u_{mf} = \frac{\sum_{i=1}^{6} u_{m,i}}{6} \quad \text{(B.17)}$$

The starting velocities corresponding to other hydrodynamic regimes are also evaluated:

- Bubble flow, $u_{mb} = u_{mf}$ [12];
- Slug flow, u_{sl} [13];
- Turbulent regime, (starting transition velocity) u_c (ending transition velocity) u_k [14];
- Pneumatic drag, u_t [15].

For the turbulent regime, two velocities are computed, since the transition from slug flow to turbulent flow occurs throughout a range of velocities. To assess the occurrence of fluidization conditions and avoid the pneumatic drag, a verification step in the calculation code returns an error message if the gas velocities (deriving from the mass balance once the base area of the bed is known) do not fall within the accepted range ($u_{mf} < u_g < u_t$). The volumetric flow rates of the gas products are also computed by the code.
The pressure drop at the distributor is a fundamental parameter in defining the operating conditions of a fluidized bed reactor: a low-pressure drop causes an imbalance in the distribution of the gas flow, which will enter the bed following preferential paths [16]. The pressure drop through the distributor is computed as $1/3 \cdot \Delta P_b$ as it is considered optimal for fluidization. Assuming 2 mm holes diameter in the distributor plate, the required number of holes to have a uniform flow distribution with 0.03 moles/s of oxygen carrier processed by the chemical looping cycle and 436 Pa pressure drop is 18. Additional parameters of the distributor are computed by the code:

- The number of holes in the distributor $N_{or} = (u_g \cdot D_{distr}^2)/(u_{or} \cdot D_{or}^2)$ noting that D_{distr} is equal to D_{bed}.

- The percentage of empty surface ϵ_{sf} considering the distributor diameter as equal to that of the bed. According to [17], it should always be below 10%.

B.4 Eulerian-Eulerian model for multiphase flows

The governing equations for both phases (g for gas and S for solids) are written as follows:

- Conservation of mass

$$\partial(\alpha_g\rho_g) + \nabla\cdot(\alpha_g\rho_g\overrightarrow{u_g}) = S_{gs} \tag{B.18}$$

$$\partial(\alpha_S\rho_S) + \nabla\cdot(\alpha_S\rho_S\overrightarrow{u_S}) = S_{sg} \tag{B.19}$$

Where α, ρ and $\vec{u}$ are the volume fraction, density and velocity vector of the gaseous and solid phases, respectively. S_{gs} represents the mass source term due to heterogeneous reaction rate and $S_{gs} = -S_{sg}$.

- Conservation of momentum

$$\frac{\partial}{\partial t}(\alpha_g\rho_g\overrightarrow{u_g}) + \nabla\cdot(\alpha_g\rho_g\overrightarrow{u_g}\,\overrightarrow{u_g}) = -\alpha_g\nabla P + \nabla\cdot\overline{\tau_g} + \alpha_g\rho_g\vec{g} + K_{sG}(\overrightarrow{u_g} - \overrightarrow{u_s}) \tag{B.20}$$

$$\frac{\partial}{\partial t}(\alpha_S\rho_S\overrightarrow{u_S}) + \nabla\cdot(\alpha_S\rho_S\overrightarrow{u_S}\,\overrightarrow{u_S}) = -\alpha_S\nabla P - \nabla P_S + \nabla\cdot\overline{\tau_S} + \alpha_S\rho_S\vec{g} + K_{sg}(\overrightarrow{u_g} - \overrightarrow{u_s}) \tag{B.21}$$

Where ∇P is the fluid pressure gradient, ∇P_S the solids pressure gradient, $\bar{\tau}$ is the stress tensor and K_{gs} the interface momentum exchange coefficient. More specifically, the stress tensor is expressed as follows:

$$\overline{\tau_g} = \alpha_g\mu_g\left[\nabla\overrightarrow{u_g} + (\nabla\overrightarrow{u_g})^T\right] + \alpha_g\left(\lambda_g - \frac{2}{3}\mu_g\right)\nabla\cdot\overrightarrow{u_g}\,\bar{I} \tag{B.22}$$

$$\overline{\tau_S} = \alpha_S\mu_S[\nabla\overrightarrow{u_S} + (\nabla\overrightarrow{u_S})^T] + \alpha_S\left(\lambda_S - \frac{2}{3}\mu_S\right)\nabla\cdot\overrightarrow{u_S}\,\bar{I} \tag{B.23}$$

Where:

- μ is the shear viscosity
- λ the bulk viscosity
- $\bar{I}$ the identity matrix

The rheology of the granular phase is derived from the Kinetic Theory of Granular flows (KTGF), in which the kinetics of gases is applied to finite-sized solid particles [18]. Through this approach, the solid phase is characterized by a certain viscosity μ_s, pressure P_S and granular temperature θ_S. As for the solid viscosity μ_s, it is expressed as a combination of several terms:

$$\mu_s = \mu_{coll} + \mu_{kin} + \mu_{bulk} + \mu_{fric} \tag{B.24}$$

In the present work, the collisional μ_{coll} and kinetic μ_{kin} terms are evaluated according to Lun et al. [19] and Gidaspow [20], respectively:

$$\mu_{s,col} = \frac{4}{5}\alpha_S\rho_s d_s g_{0,ss}(1+e_{ss})\left(\frac{\theta_s}{\pi}\right)^{\frac{1}{2}} \tag{B.25}$$

$$\mu_{s,kin} = \frac{10 d_s \rho_s \sqrt{\theta_s \pi}}{96(1+e_{ss})g_{0,ss}}\left[1+\frac{4}{5}\alpha_S g_{0,ss}(1+e_{ss})\right]^2 \alpha_s \tag{B.26}$$

Where:

- $g_{0,ss}$ is the radial distribution function;
- e_{ss} is the coefficient of restitution for particle collision;
- θ_s is the granular temperature for the solid phase;
- d_s is the diameter of the solid phase.

As for the bulk viscosity μ_{bulk}, representing the response of the granular phase to a compression or expansion stress, it is evaluated with the Lun et al. model [19]:

$$\mu_{bulk} = \frac{4}{3}\alpha_S^2\rho_s d_s g_{0,ss}(1+e_{SS})\left(\frac{\theta_s}{\pi}\right)^{\frac{1}{2}} \tag{B.27}$$

In case of dense flows, a further component due to friction between particles is added to the viscosities and is evaluated here using the Schaeffer model [21], whose influence on bed dynamics is discussed in detail in [22]:

$$\mu_{friction} = \frac{P_{friction}\sin(\phi)}{2\sqrt{I_{2D}}} \tag{B.28}$$

Where:

- ϕ is the angle of internal friction;
- I_{2D} is the second invariant of the deviatoric stress tensor.

The frictional pressure $P_{friction}$ in the Schaeffer model is computed using the expression derived by Johnson and Jackson in [23]

$$P_{friction} = Fr\frac{(\alpha_s - \alpha_{s,min})^n}{(\alpha_{s,max} - \alpha_s)^p} \tag{B.29}$$

Where:

- Fr = 0.005
- n = 2

- $p = 5$
- $\alpha_{s,min}$ is the value of solids volume fraction above which the frictional viscosity is included in the model
- $\alpha_{s,max}$ is the packing factor, above which no further decrease in is allowed.

As for the solids pressure p_s, the expression by Lun et al. [19] is adopted:

$$p_s = \alpha_S \rho_S \theta_S + 2\rho_S(1 + e_{SS})\alpha_S^2 g_0 \theta_S \tag{B.30}$$

The radial distribution function g_o is a correction factor that adjusts the probability of particle-particle collision when the granular phase volume fraction is high and is expressed according to Lun et al. [19] for one solid phase:

$$g_0 = \left[1 - \left(\frac{\alpha_s}{\alpha_{s,max}}\right)^{\frac{1}{3}}\right]^{-1} \tag{B.31}$$

Where $\alpha_{s,max}$ is the volume fraction value where no further decrease in the spacing between particles can occur. The particle-particle restitution coefficient e_{SS} represents the extent to which the impacts between particles are close to a condition of complete elasticity ($e_{ss} = 1$) and is left at the default value of 0.9. This choice can be justified as follows: in first place, the lack of experimental data does not make it possible to identify a more proper value for the problem under analysis; secondly, the best agreement of simulation results to experimental data for Geldart A and B particles is observed when $e_{SS} = 0.9$ (as shown in [24,25]).
The solid phase is further characterized by a granular temperature θ_s, which is a measure of the fluctuation of solid particles kinetic energy and assumes the following expression:

$$\theta_S = \frac{1}{3} u'_{S,i} u'_{S,i} \tag{B.32}$$

Where $u'_{S,i}$ represents the i-th component of the fluctuating particle velocity. In the present study, rather than solving the full transport equation for this quantity, the temporal variation and the convective term in the transport equation of θ_s are ignored, so that an algebraic equation is obtained allowing for a significant reduction in the calculation time:

$$(-p_s \bar{I} + \bar{\tau}_s) : \nabla \overrightarrow{v_S} - \gamma_{\theta s} + \phi_{ls} = 0 \tag{B.33}$$

Where:

- $\gamma_{\theta s}$ is the collisional dissipation of energy
- ϕ_{ls} is the energy exchange between fluid L and solid s

This approach is valid for simulating fluidized beds, as discussed in [26]. Regarding to the interface momentum exchange drag coefficient K_{sg}, the Gidaspow model is adopted [20], having shown good consistency with the experimental results on dense fluidized beds in several past works [24,27,28]

$$K_{sg} = \frac{3}{4} C_D \left(\frac{\alpha_s \alpha_g \rho_g \left| \overrightarrow{v_s} - \overrightarrow{v_g} \right|}{d_S} \right) \alpha_g^{-2.65} \qquad \text{For } \alpha_g > 0.8 \qquad \text{(B.34)}$$

$$K_{sg} = \frac{150 \alpha_s (1 - \alpha_g) \mu_l}{\alpha_g d_s^2} + \frac{1.75 \rho_g \alpha_s |v_s - v_l|}{d_S} \qquad \text{For } \alpha_g < 0.8 \qquad \text{(B.35)}$$

Where:

$$C_D = \frac{24}{\alpha_g Re_s} \left[1 + 0.15 (\alpha_g Re_S)^{0.687} \right] \qquad \text{(B.36)}$$

Finally, the Gunn model [29] is employed to compute the heat exchange coefficient h_{sg} between the granular phase and the remaining phases:

$$Nu_s = \left(7 - 10\alpha_f + 5\alpha_f^2 \right)(1 + 0.7 Re_s^{0.2} Pr^{0.3}) + \left(1.33 - 2.4\alpha_f + 1.2\alpha_f^2 \right) Re_s^{0.7} Pr^{0.3} \qquad \text{(B.37)}$$

B.5 References

[1] Richardson JF. Coulson and Richardson's chemical engineering. 2002.

[2] Kranich WL. Material and energy balance computations, E. J. Henley and E. M. Rosen, John Wiley, New York, 577 pages. AIChE Journal 1969;15:642–793. https://doi.org/10.1002/aic.690150502.

[3] Wilke CR. A Viscosity Equation for Gas Mixtures. J Chem Phys 1950;18:517–9. https://doi.org/10.1063/1.1747673.

[4] Fogler HS. Elements of chemical reaction engineering. Third edition. Upper Saddle River, N.J. : Prentice Hall PTR, [1999] ©1999; n.d.

[5] Ergun S, Orning AA. Fluid Flow through Randomly Packed Columns and Fluidized Beds. Industrial & Engineering Chemistry 1949;41:1179–84. https://doi.org/10.1021/ie50474a011.

[6] Basu P, Fraser SA. Circulating fluidized bed boilers. Springer; 1991.

[7] Wen CY, Yu YH. A generalized method for predicting the minimum fluidization velocity. AIChE Journal 1966;12:610–2. https://doi.org/10.1002/aic.690120343.

[8] Author F, Harrison D. Fluidization. vol. 61. 1933.

[9] Saxena SC, Vogel GJ. Segregation and fluidization characteristics of a dolomite bed with a range of particle sizes and shapes. The Chemical Engineering Journal 1977;14:59–63. https://doi.org/10.1016/0300-9467(77)80023-3.

[10] Babu, Shah, Talwalkar. Fluidization correlation for coal gasification materials—minimum fluidization velocity and fluidized bed expansion ratio. AIChE Symposium Series 1978.

[11] Grace JR. Handbook of Multiphase Systems. vol. 8. Hemisphere Publishing Corp; 1982.

[12] Geldart D. The effect of particle size and size distribution on the behaviour of gas-fluidised beds. Powder Technol 1972;6:201–15. https://doi.org/10.1016/0032-5910(72)83014-6.

[13] Stewart PSB, Davidson JF. Slug flow in fluidised beds. Powder Technol 1967;1:61–80. https://doi.org/10.1016/0032-5910(67)80014-7.

[14] Horio M, Morishita K. Flow regimes of high velocity fluidization. Japanese journal of multiphase flow 1988;2:117–36. https://doi.org/10.3811/jjmf.2.117.

[15] Turton R, Clark NN. An explicit relationship to predict spherical particle terminal velocity. Powder Technol 1987;53:127–9. https://doi.org/10.1016/0032-5910(87)85007-6.

[16] Kumar VV, Batcha MF, Raghavan VR. Study of the fluid dynamic performance of distributor type in torbed type reactors. Engineering E-Transaction 2011;6:70–5.

[17] Kunii D, Levenspiel O. Fluidization engineering. Butterworth-Heinemann; 1991.

[18] Fan L-S. Multiphase flow and fluidization: Continuum and kinetic theory descriptions. By Dimitri Gidaspow, Academic Press, New York, 1994, 467 pp.,$69.50. AIChE Journal 1996;42:1197–8. https://doi.org/10.1002/aic.690420438.

[19] Lun CKK, Savage SB, Jeffrey DJ, Chepurniy N. Kinetic theories for granular flow: inelastic particles in Couette flow and slightly inelastic particles in a general flowfield. J Fluid Mech 1984;140:223–56. https://doi.org/10.1017/s0022112084000586.

[20] Gidaspow D, Bezburuah R, Ding J. Hydrodynamics of circulating fluidized beds: kinetic theory approach. 7th Fluidization Conference, 1992.

[21] Schaeffer DG. Instability in the evolution equations describing incompressible granular flow. J Differ Equ 1987;66:19–50. https://doi.org/10.1016/0022-0396(87)90038-6.

[22] Reuge N, Cadoret L, Coufort-Saudejaud C, Pannala S, Syamlal M, Caussat B. Multifluid Eulerian modeling of dense gas–solids fluidized bed hydrodynamics: Influence of the dissipation parameters. Chem Eng Sci 2008;63:5540–51. https://doi.org/10.1016/j.ces.2008.07.028.

[23] Johnson PC, Jackson R. Frictional–collisional constitutive relations for granular materials, with application to plane shearing. J Fluid Mech 1987;176:67. https://doi.org/10.1017/s0022112087000570.

[24] Geng S, Jia Z, Zhan J, Liu X, Xu G. CFD modeling the hydrodynamics of binary particle mixture in pseudo-2D bubbling fluidized bed: Effect of model parameters. Powder Technol 2016;302:384–95. https://doi.org/10.1016/j.powtec.2016.09.001.

[25] Gao X, Wu C, Cheng Y, Wang L, Li X. Experimental and numerical investigation of solid behavior in a gas–solid turbulent fluidized bed. Powder Technol 2012;228:1–13. https://doi.org/10.1016/j.powtec.2012.04.025.
[26] van Wachem BGM, Schouten JC, Krishna R, van den Bleek CM. Eulerian simulations of bubbling behaviour in gas-solid fluidised beds. Computers & Chemical Engineering 1998;22:S299–306. https://doi.org/10.1016/s0098-1354(98)00068-4.
[27] Taghipour F, Ellis N, Wong C. Experimental and computational study of gas–solid fluidized bed hydrodynamics. Chem Eng Sci 2005;60:6857–67. https://doi.org/10.1016/j.ces.2005.05.044.
[28] Guan Y, Chang J, Zhang K, Wang B, Sun Q. Three-dimensional CFD simulation of hydrodynamics in an interconnected fluidized bed for chemical looping combustion. Powder Technol 2014;268:316–28. https://doi.org/10.1016/j.powtec.2014.08.046.
[29] Gunn DJ. Transfer of heat or mass to particles in fixed and fluidised beds. Int J Heat Mass Transf 1978;21:467–76. https://doi.org/10.1016/0017-9310(78)90080-7.

Appendix C

The following properties and characterization results are extracted from the technical flowsheet of the iron powder provided by Alquera.

C.1 General properties of the iron powder

- Physical state: Solid
- Form: Powder
- Colour: Metallic
- Bulk density: 2.0 - 4.0 g/cm^3
- Specific gravity: 7.87 g/cm^3 at 20 °C
- Melting temperature: 1530 °C
- Ignition temperature in air: 290 °C in layer/ 320 °C in cloud
- Reaction temperature in N_2: 200 °C
- Minimum explosion concentration in air: 120 g/m^3

C.2 Grain size distribution

Table C.1. Grain size distribution

> 1.180 mm	0%
> 1.00 mm	<= 20%
> 0.5 mm	>= 90%
0.420 mm	>= 96%

C.3 Chemical composition

Table C.2. Chemical composition

C	0.80 – 1.20 %
Mn	0.60 – 1.20 %
Si	>= 0.40%
P	<= 0.05%
S	<= 0.05%

C.4 Microstructure

Martensitic

Appendix D

D.1 Setup validation tests

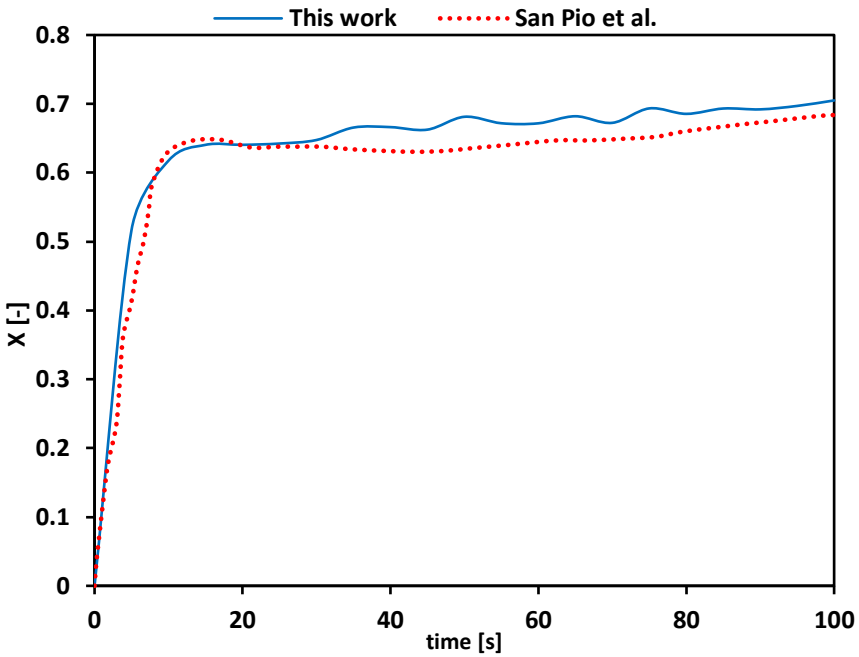

Figure D.1. Validation test with CuO/Al_2O_3 at 3 nl/min, 6 bar and 800 °C

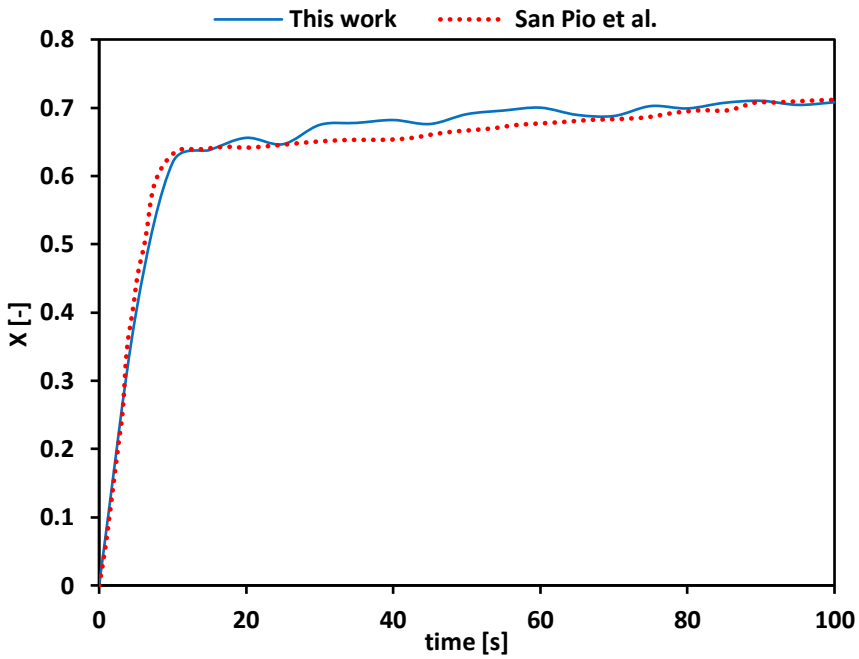

Figure D.2. Validation test with CuO/Al_2O_3 at 4 nl/min, 6 bar and 800 °C

Appendix E

E.1. Reducer and oxidizer validation

The counter current bed reactor model is validated in two steps, first for a moving bed reducer reactor with methane injection and then with biomass injection. In both cases, iron oxides are fed from the top. For the simulation, the Redlich-Kwong-Soave equation of state with Boston-Mathias correction is selected. The main species included in the model are H_2, H_2O, CO, CO_2, CH_4 for the gases and Fe_2O_3, Fe_3O_4, FeO and Fe for the solids.
For the methane reduction, the reactor thermodynamic conditions are fixed at 975 °C and 1 bar in all simulations. The final methane conversion is computed according to Eq (E.1).

$$X_{CH_4} = \frac{CO_2}{CO_2 + CO + CH_4} \tag{E.1}$$

Both the experimental and modelling results from [1] are plotted in Figure E.1. and compared with this work results. The model correctly predicts the methane conversion trend with increasing solid to gas weight ratios and shows the occurrence of complete oxidation for solid to gas weight ratios above 50.

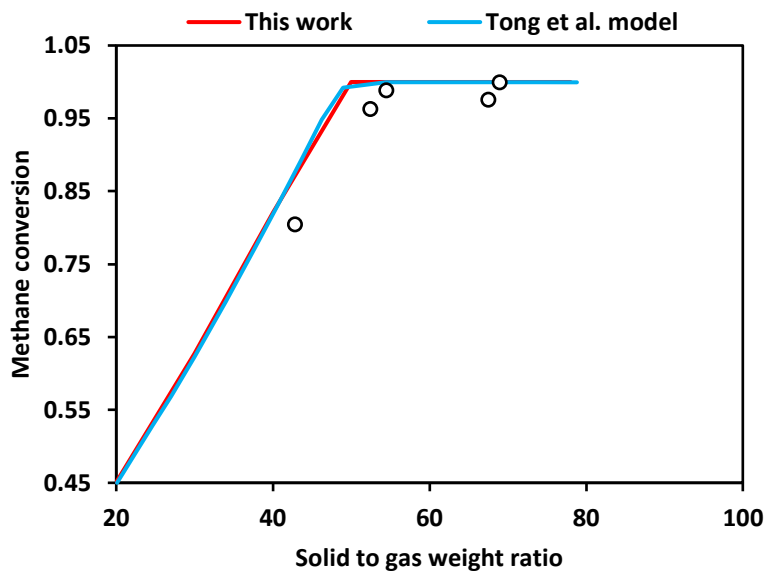

Figure E.1. Model validation with experimental results for a moving bed reactor fed by methane

Supported iron oxides (66.2% wt Fe_2O_3 and 33.8% wt SiC) and biomass (hybrid poplar) represent the feedstock of the second validation. Using the same input conditions (T = 900 °C, p = 1 atm, H_2O in the biomass 5%) of [2] the results indicate a good agreement between the models, as displayed in Table E.1.

Table E.1. Model validation of counter-current bed with biomass

	This work	Literature	Relative Error (%)
R	1.61	1.61	0%
x	0.866	0.849	-1.96%
C	0.422	0.434	-2.56%

Where

- R: molar ratio of Fe_2O_3 and the carbon content of biomass
- x: normalized oxygen content of the reduced oxygen carrier, i.e. the number of transferable oxygen atoms/the number of Fe atom.
- C oxygen carrier conversion, evaluated as 1-2x/3

E.2. Heat Recovery Steam Generator modelling

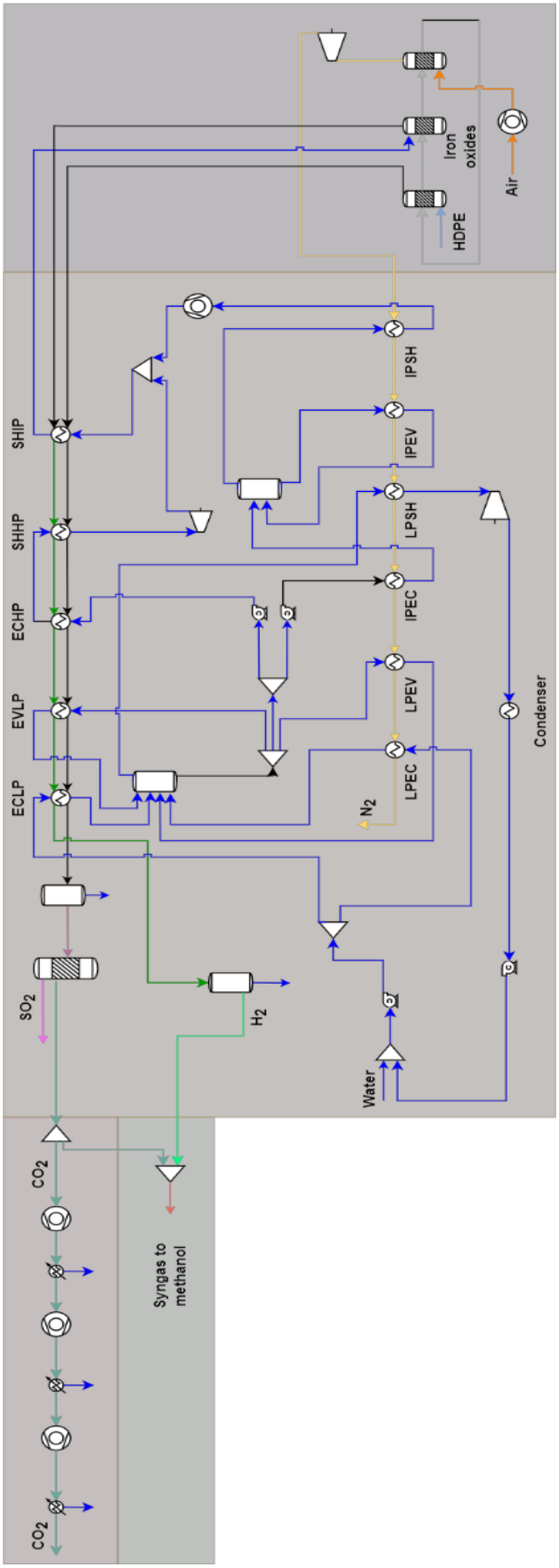

Figure E.2. PFD of the TRCL plant, HRSG section and CO_2 sequestration section

Table E.2. Specifications of the heat exchange parameters in the HRSG modelling

	Unit	H_2O Pressure	H_2O side variable	Value	FR side variable	Value	SR side variable	Value
SR and FR gases	ECLP	1.054 bar	T	92.5°C			Duty	-28.5 kcal/s
	EVLP	1.054 bar	Vapor frac	0.9	T	108 °C		
	ECHP	132.2 bar	T	329°C	Duty	-40 kcal/s		
	SHHP	127.7 bar	T	545°C			T	334°C
	LPEC	1.054 bar			DT	-5°C	DT	-4.5°C
AR gases	LPEV	1.054 bar	T	92.5°C				
	LPSH	2.667 bar	T	182.5°C				
	IPEC	11.35 bar	Vapor frac	0.9				
	IPEV	11.35 bar	T	210°C				
	IPSH	10.92 bar	Vapor frac	0.9				

E.3. Capital Cost analysis

Table E.3. Reference cost, scale and exponent values for BEC evaluation

Component	Unit	CEPCI	Reference cost	A_{ref}	m	Ref
HRSG	MW_{el}	542	16.25 M$	15.67	0.7	[3]
FR	t/hr of Fe_2O_3	542	2.15 M$	3723.4[5]	0.8	[3]
SR	t/hr of Fe_2O_3	542	1.23 M$	3723.4	0.8	[3]
AR	t/hr of Fe_2O_3	542	0.63 M$	3723.4	0.8	[3]
FGD	t/h of SO_2	499.6	8.31 M$	5.65	0.6	[4]
Cooling towers	t/min H_2O	603.5	0.037 M$	18.89	0.71	[3]
NH_3 reactor	t/h of NH_3	596.2	0.392 M$	76.67	0.6	[5,6]
Methanator	t/h	556.8	0.05 M$	3.07	0.6	[6]
Alkaline electrolyser	kg/h of H_2	541.7	1.59 M$	50	0.95	[7]
MS reactor	t/h gas feed	499.6	7.69 M€	87.5	0.6	[8]
Distillation column	t/h of CH_3OH	499.6	16.58 M€	6.75	0.7	[8]
Flash tank	kg/s gas feed	394.1	$\text{Installation (M€)} = 2.47 \cdot 983.2 \cdot 10^{-6} \cdot \left(\text{feed gas in } \frac{kg}{s}\right)^{0.8}$			[8]
Cryogenic unit	heat load (MW)	603.5	1.936 M$	1	0.6	[9]

E.4. Mass balance results

Table E.4. Summary of the gas streams thermodynamic conditions

STREAMS	P	T	$\dot{m}$	$\dot{N}$	Molar fraction									
	bar	°C	kg/hr	kmol/h	CO_2	CO	H_2	H_2O	CH_3OH	NH_3	SO_2	N_2	O_2	CH_4
FR GAS	18	930	721.2	23.16	50.47	-	-	49.49	-	-	traces	traces	-	-
SR GAS	20	840.59	709.69	56.00	-	-	33.45	66.55	-	-	-	-	-	-
AR GAS	16	940.83	805.49	28.75	0.051	-	-	-	-	-	-	99.94	traces	-
CO_2 to storage	80	30	240.2	5.48	99.33	-	-	0.63	-	-	traces	0.033	-	-
N2 to ammonia	16	626.45	805.49	28.75	0.051	-	-	-	-	-	-	99.94	traces	-
H_2/CO to methanol	18	83.30	325.48	25.70	24.26	-	72.88	2.85	-	-	-	-	-	-
CH_3OH in	80	250	1563.66	126.06	22.66	2.39	73.79	0.41	-	-	-	-	-	-
CH_3OH out	79.59	250	1563.66	114.65	19.88	2.68	66.15	5.76	5.43	-	-	traces	-	-
Recirc. 1 CH_3OH	65	30	1219.73	101.14	21.67	3.03	74.77	traces	0.28	-	-	traces	-	-
Recirc. 2 CH_3OH	0.2	10.10	43.65	1.30	59.69	0.87	16.82	3.61	18.98	-	-	-	-	-
Crude CH_3OH	2	85	300.29	12.22	traces	-	-	53.26	46.63	-	-	-	-	-
CH_3OH	1	25	173.86	5.42	0.23	-	-	traces	99.7	-	-	-	-	
H_2 for NH_3	10	70	173.85	86.24	-	-	1	-	-	-	-	-	-	-
Methanator out	16	250	114.96	979.34	-	-	75.75	0.025	-	-	-	24.21	-	0.012
NH_3 reactor IN	198	380	2635.95	306.59	-	-	74.21	-	-	1.01	-	24.70	-	0.081
NH_3 reactor OUT	187.3	467	2635.95	253.00	-	-	58.2	-	-	22.38	-	19.35	-	0.098
Recirc. 1 NH_3	178	15	1714.46	198.66	-	-	73.90	-	-	1.44	-	24.55	-	0.12
Recirc. 2 NH_3	18	13.90	11.69	0.91	-	-	40.22	-	-	41.34	-	17.98	-	0.46
NH_3	18	13.90	909.77	53.43	-	-	0.045	-	-	99.91	-	0.031	-	-

Table E.5. Summary of the solid streams thermodynamic conditions in the TRCL plant

STREAMS	P	T	ṁ	Ṅ	Molar fraction			
	bar	°C	kg/hr	kmol/h	Fe_2O_3	Fe_3O_4	FeO	MgAl2O4
FR out	18	840	21520.9	189.78	-	41.27	1.53	57.20
SR out	20	832.30	21820.6	140.97	-	18.30	4.96	77.00
AR out	16	940.83	22065.1	149.63	29.70	4.96	-	72.55

E.5. Electricity consumption in the plant

Table E.6. Electricity consumption in the plant

Unit	Power (kW)
Compressors	714
Pumps	6
Turbines	-173
Electrolyser	8692
Cooling towers	188
Cryogenic plant	128

E.6. Other economical sensitivity analyses

The effect of plastic cost on the LCOAM is evaluated in FigureE.3. The LCOAM varies linearly with the cost of plastic but, due to the limited flow rate of HDPE injected to the FR, the impact on the final products cost is limited: for a 21-fold increase in plastic cost, the LCOAM increases by only 8%.

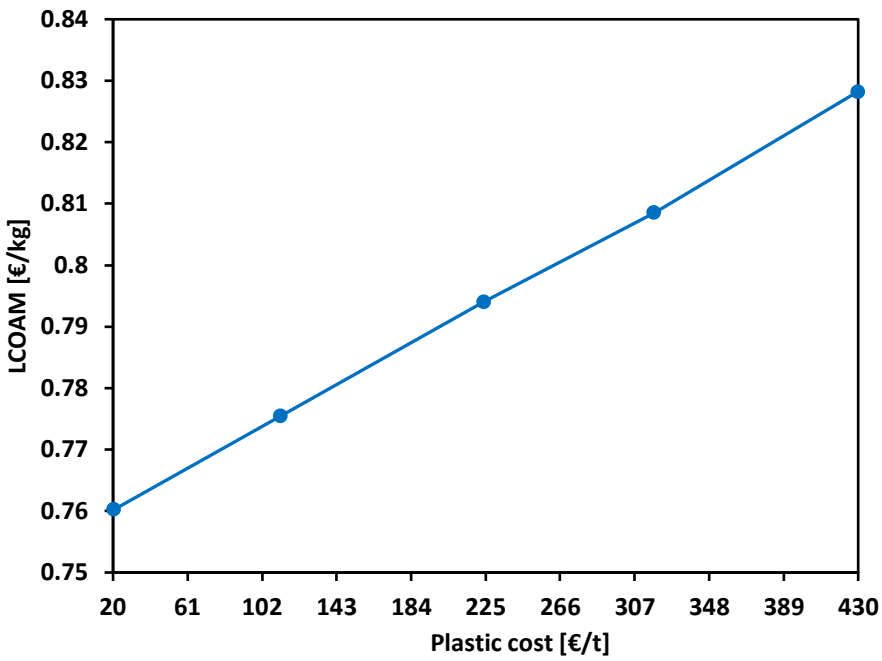

Figure E.3. Effect of fixed OPEX costs variation on the LCOAM [€/kg]

The effect of maintenance and insurance costs (fixed OPEX) on the LCOAM is assessed in Figure E.4. A correction factor is introduced to modify the fixed OPEX, ranging from 0.6 to 1.4. The resulting LCOAM ranges from a minimum of 0.72 €/kg to a maximum of 0.80 €/kg.

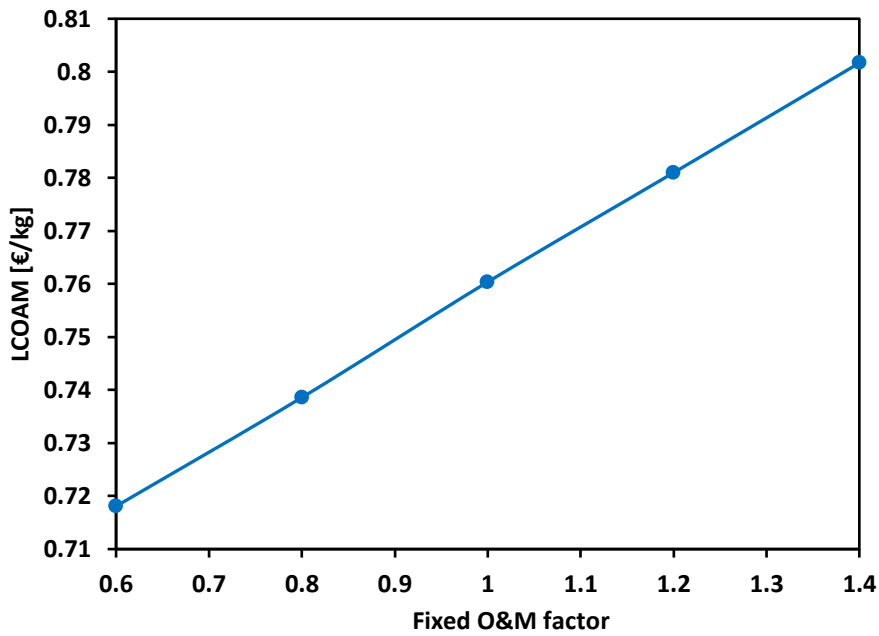

Figure E.4. Effect of fixed OPEX costs variation on the LCOAM [€/kg]

The effect of the plant lifetime is investigated in Figure E.5. The range is chosen between 15 and 35 years. Similarly to other works present in the literature [10–12], the aging of the plant

is not included in the economic evaluation. This assumption is less acceptable for longer lifetimes and therefore the relevance of such analysis is more related to the trend at the left of the 25 years lifetime. However, it can be observed that the LCOAM decreases significantly for longer plant lifetimes and at 35 years it amounts to 0.68 €/kg.

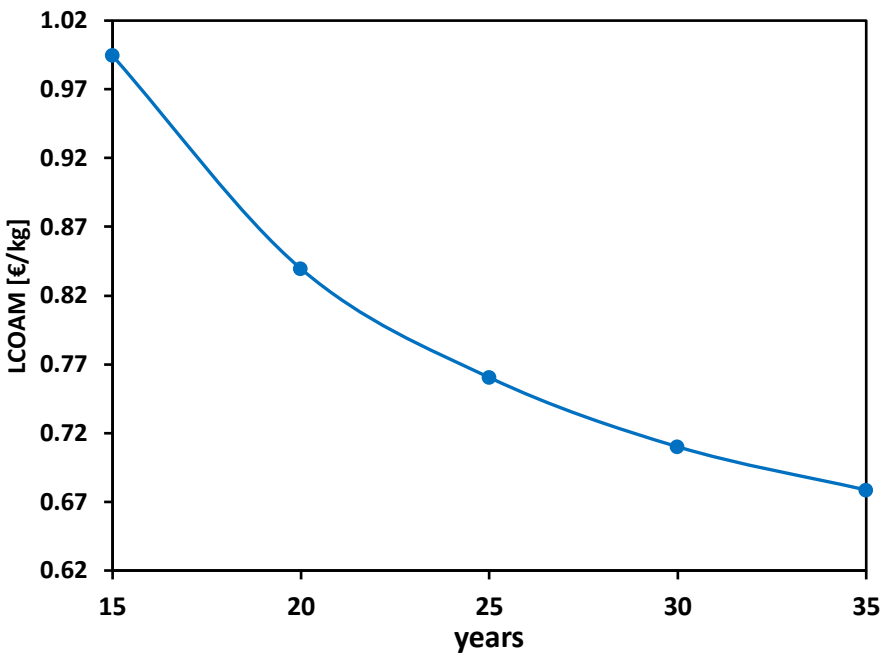

Figure 7.1. Effect of the plant lifetime on the LCOAM [€/kg]

E.7. References

[1] Tong A, Zeng L, Kathe M v, Sridhar D, Fan L-S. Application of the moving-bed chemical looping process for high methane conversion. Energy & Fuels 2013;27:4119–28.

[2] Li F, Zeng L, Fan LS. Biomass direct chemical looping process: Process simulation. Fuel 2010;89:3773–84. https://doi.org/10.1016/j.fuel.2010.07.018.

[3] Khan MN, Shamim T. Techno-economic assessment of a plant based on a three reactor chemical looping reforming system. Int J Hydrogen Energy 2016;41:22677–88.

[4] Hrastel I, Gerbec M, Stergaršek A. Technology optimization of wet flue gas desulfurization process. Chemical Engineering & Technology: Industrial Chemistry-Plant Equipment-Process Engineering-Biotechnology 2007;30:220–33.

[5] Osman O, Sgouridis S, Sleptchenko A. Scaling the production of renewable ammonia: A techno-economic optimization applied in regions with high insolation. J Clean Prod 2020;271:121627.

[6] Arora P, Hoadley AFA, Mahajani SM, Ganesh A. Small-scale ammonia production from biomass: a techno-enviro-economic perspective. Ind Eng Chem Res 2016;55:6422–34.

[7] Palys MJ, Daoutidis P. Using hydrogen and ammonia for renewable energy storage: A geographically comprehensive techno-economic study. Comput Chem Eng 2020;136:106785.

[8] Michailos S, McCord S, Sick V, Stokes G, Styring P. Dimethyl ether synthesis via captured CO_2 hydrogenation within the power to liquids concept: A techno-economic assessment. Energy Convers Manag 2019;184:262–76.

[9] Luyben WL. Estimating refrigeration costs at cryogenic temperatures. Comput Chem Eng 2017;103:144–50. https://doi.org/10.1016/j.compchemeng.2017.03.013.

[10] Battaglia P, Buffo G, Ferrero D, Santarelli M, Lanzini A. Methanol synthesis through CO_2 capture and hydrogenation: Thermal integration, energy performance and techno-economic assessment. Journal of CO_2 Utilization 2021;44:101407.

[11] Akbari M, Oyedun AO, Kumar A. Ammonia production from black liquor gasification and co-gasification with pulp and waste sludges: A techno-economic assessment. Energy 2018;151:133–43.

[12] Zhang H, Wang L, Perez-Fortes M, Maréchal F, Desideri U, others. Techno-economic optimization of biomass-to-methanol with solid-oxide electrolyzer. Appl Energy 2020;258:114071.

Curriculum Vitae

Born in Anzio (Rome) on the 11th of January 1996, after graduating from scientific high school at Liceo Scientifico Innocenzo XII, he started the bachelor's program in Energy Engineering of Sapienza University of Rome. He graduated on the 12th of October 2018 and then started the master's program in Energy and Nuclear Engineering. He graduated on the 19th of October 2020 with a thesis on liquid metals magnetohydrodynamics carried out under the supervision of Proff. Gianfranco Caruso and Alessandro Tassone. In the same year he was admitted to the XXXVI cycle of the engineering doctoral school in Energy and Environment under the supervision of Prof. Domenico Borello. Over the three years of his PHD he was one of the main investigators in the SFERO project, funded by the Italian Ministry of Economic Development, which involved the development and analysis of novel industrial decarbonization strategies. In Sapienza he had the chance of collaborating with wonderful people and scientists who helped him develop his talents and face his fears, especially of mistake. In September 2022 he started an eight-months visiting research period in Eindhoven University of Technology under the supervision of Dr. Rouzbeh Ramezani and Prof. Fausto Gallucci. There he grew both technically and personally, but above all he made wonderful friendships that hopefully will last forever.